



Universidad Autónoma de Madrid  
Departamento de Química Física Aplicada



Instituto de Química Física "Rocasolano"  
Grupo de Electroquímica

# Electrocatalysis and surface nanostructuring: atomic ensemble effects and non-covalent interactions

Memoria para optar al grado de doctor presentada por:

**María Escudero Escribano**

Director: **Ángel Cuesta Ciscar**

Investigador Científico

Instituto de Química Física "Rocasolano", CSIC

Tutora: **Pilar Ocón Esteban**

Catedrática de Universidad

Universidad Autónoma de Madrid

Madrid, octubre de 2011



# Contents

Abstract .....	7
Resumen .....	8
<b>1. Introduction .....</b>	<b>11</b>
1.1. Interfacial electrochemistry and single crystal electrodes .....	11
1.1.1. Adsorption on well-defined surfaces .....	13
1.2. Electrocatalysis .....	15
1.2.1. Electronic effects .....	16
1.2.2. Atomic ensemble effects .....	18
1.3. Fuel cells .....	19
1.3.1. Basic principles and classification .....	20
1.3.2. Anodic and cathodic electrocatalytic reactions .....	22
1.4. Surface nanostructuring .....	25
1.5. Scope of the research .....	27
<b>2. Experimental and theoretical methods .....</b>	<b>29</b>
2.1. Fabrication, orientation and flame treatment of Pt single-crystal electrodes .....	29
2.2. Experimental techniques .....	32
2.2.1. Cyclic voltammetry .....	32
2.2.1.1. <i>Electrochemical cell</i> .....	33
2.2.2. Rotating disk and rotating ring-disk electrodes .....	34
2.2.3. <i>In situ</i> scanning tunneling microscopy .....	35
2.2.3.1. <i>EC-STM cell</i> .....	40
2.2.4. <i>In situ</i> Fourier transform infrared spectroscopy .....	41

2.2.4.1.	<i>Spectroelectrochemical cell</i> .....	47
2.3.	Reagents and solutions .....	48
2.4.	Theoretical calculations.....	49
2.4.1.	Methodology .....	49
3.	<b>Cyanide-modified platinum surfaces: structure and stability.....</b>	<b>53</b>
3.1.	Introduction.....	53
3.2.	Cyanide-modified Pt(111) electrodes .....	54
3.2.1.	Cyclic voltammetry, FTIRS and EC-STM investigations.....	54
3.2.2.	Theoretical study of cyanide-modified Pt(111) surfaces.....	61
3.2.2.1.	<i>Structure of adsorbed cyanide on Pt(111) surfaces.....</i>	<i>62</i>
3.2.2.2.	<i>Adsorption of hydrogen on cyanide-modified Pt(111).....</i>	<i>69</i>
3.3.	Cyanide-modified polycrystalline Pt surfaces.....	72
3.4.	Conclusions and perspectives .....	73
4.	<b>Atomic ensemble effects in electrocatalysis .....</b>	<b>77</b>
4.1.	Introduction.....	77
4.2.	Nitric oxide electroreduction .....	78
4.2.1.	Nitric oxide electroreduction on Pt(111).....	78
4.2.2.	Nitric oxide reduction on cyanide-modified Pt(111) electrodes .....	81
4.2.3.	Mechanism of the NO electroreduction reaction on platinum .....	84
4.3.	Hydrogen oxidation reaction.....	88
4.3.1.	Hydrogen oxidation on cyanide-modified Pt(111) electrodes.....	92
4.4.	Formic acid electrooxidation reaction .....	94
4.4.1.	Formic acid oxidation on cyanide-modified Pt(111) electrodes .....	96
4.5.	Oxygen reduction reaction .....	103
4.5.1.	Oxygen reduction on cyanide-modified Pt(111) electrodes .....	104

---

4.6.	Conclusions and perspectives .....	111
5.	Cation-specific non-covalent interactions at the electrochemical double layer .....	115
5.1.	Introduction.....	115
5.2.	Experimental studies on the role of alkali cations on cyanide-modified Pt(111) in acidic solutions .....	116
5.2.1.	Voltammetric results .....	116
5.2.2.	Visualization of cations by electrochemical STM .....	122
5.3.	Theoretical calculations.....	125
5.4.	Conclusions .....	127
6.	Surface nanostructuring using a molecular pattern .....	129
6.1.	Introduction.....	129
6.2.	Cyclic voltammetry, FTIRS and EC-STM studies of the adsorption of copper on cyanide-modified Pt(111) electrodes .....	130
6.3.	Polymerization of aniline on cyanide-modified Pt(111) electrodes.....	145
6.4.	Conclusions and perspectives .....	148
7.	General conclusions .....	151
7.1.	Conclusiones generales.....	153
8.	References .....	156
	Appendix A. List of acronyms and symbols .....	166
	Appendix B. Publications and contributions in conferences .....	170
	Appendix C. Curriculum vitae.....	172



# Abstract

Probably the most important scientific challenge in the first decades of the XXI century is to make the transition from combustion-based energy conversion technologies to clean technologies possible. To do so, we need to develop new materials that allow efficient and cheap electrochemical energy conversion and storage, and enable less dependence on fossil fuels. These decades have also witnessed an increasing interest in the generation of nanometer-sized structures on surfaces, mainly (but not exclusively) driven by the need of microelectronics and information storage industries for device miniaturization.

The present PhD research is focused on the study of the role of geometric atomic ensembles in electrocatalysis, and on the fabrication of surface nanostructures guided by a self-ordered molecular pattern, namely cyanide-modified Pt(111). To achieve our purposes, we have used a combination of traditional electrochemical methods (mainly cyclic voltammetry) and non-electrochemical techniques (such as *in situ* scanning tunneling microscopy and Fourier-transform infrared spectroscopy).

Cyanide is spontaneously and irreversibly adsorbed on Pt(111) forming a  $(2\sqrt{3} \times 2\sqrt{3})R30^\circ$  ordered structure which consists of six cyanide groups adsorbed *on-top* of a hexagon of Pt atoms surrounding a central Pt atom. Cyanide groups act as a third body that blocks all the sites composed of three contiguous Pt atoms, while leaving unaffected the Pt atoms not directly bonded to a CN group, onto which some small molecules can adsorb. For this reason, cyanide-modified Pt(111) electrodes may be used as model surfaces to study atomic ensemble effects in electrocatalysis in the absence of significant simultaneous electronic effects. This research, instead of studying one reaction extensively, is aimed at interrogating a wide variety of reactions of relevance in fuel-cells with cyanide-modified Pt(111) electrodes.

Voltammetric and spectroscopic studies using cyanide-modified Pt(111) surfaces have allowed us to gain information on the mechanism of the electrooxidation of small molecules, such as hydrogen and formic acid. Furthermore, we have shown that a great enhancement of the catalytic activity for the oxygen reduction reaction can be achieved by efficiently blocking the sites necessary for the adsorption of 'spectator' anions (like (bi)sulphate or (hydrogen)phosphate). Finally, we have studied the adsorption of metal cations on cyanide-modified Pt(111) electrodes, and the role of this kind of non-covalent interactions in dictating the properties and the structure of the electrochemical double-layer. Non-covalent interactions have been used to fabricate periodic nanostructures on cyanide-modified Pt(111) surfaces and to metallize the cyanide adlayer.

## Resumen

Probablemente, el desafío científico más importante al que nos enfrentamos en las primeras décadas del S.XXI sea hacer posible el abandono de las tecnologías de conversión de energía basadas en procesos de combustión por tecnologías limpias, para lo cual necesitamos desarrollar nuevos materiales que nos permitan convertir y almacenar energía por procedimientos electroquímicos, posibilitando así disminuir la dependencia de los combustibles fósiles. Por otro lado, cada vez aumenta más el interés por el nanoestructurado de superficies, estimulado esencial, pero no exclusivamente, por la necesidad de las industrias microelectrónica y de almacenamiento de información por la miniaturización de dispositivos.

Esta Tesis Doctoral se ha basado en el uso de electrodos de platino (111) modificados con cianuro con el fin de estudiar el papel de los agrupamientos atómicos en electrocatálisis y fabricar nanoestructuras periódicas de dimensiones atómicas basadas en un patrón molecular. Para alcanzar estos objetivos, hemos combinado métodos electroquímicos tradicionales (principalmente voltametría cíclica) con técnicas no-electroquímicas (como la microscopía túnel de barrido *in situ* y la espectroscopía infrarroja por transformada de Fourier).

El cianuro se adsorbe de forma espontánea e irreversible sobre Pt(111), adoptando una estructura ordenada  $(2\sqrt{3} \times 2\sqrt{3})R30^\circ$  que consiste en grupos de 6 cianuros adsorbidos sobre 6 átomos de Pt formando un anillo hexagonal alrededor de un átomo de Pt central. Los grupos cianuro actúan como un tercer cuerpo que bloquea todos los sitios formados por tres átomos de Pt contiguos, y al mismo tiempo apenas afecta a la estructura electrónica de los átomos de Pt que no están directamente enlazados a un grupo CN, sobre los cuales se pueden adsorber algunas moléculas si son suficientemente pequeñas. Por ello, los electrodos de Pt(111) modificados con cianuro se pueden utilizar como superficies modelo con las que estudiar el efecto de los agrupamientos atómicos en electrocatálisis en ausencia de efectos electrónicos considerables. Este trabajo no se ha centrado en el estudio de una reacción concreta en profundidad, sino que tiene como objetivo investigar una amplia variedad de reacciones de interés en pilas de combustible usando electrodos de Pt(111) modificados con cianuro.

Los estudios voltamétricos y espectroscópicos que se han realizado sobre superficies de Pt(111) químicamente modificadas nos han proporcionado información sobre el mecanismo de electrooxidación de moléculas pequeñas como el hidrógeno y el ácido fórmico. Además, hemos demostrado que bloqueando los sitios necesarios para la adsorción de aniones "espectadores" (como, por ejemplo, (bi)sulfato o (hidrógeno)fosfato) se puede



conseguir un considerable aumento de la actividad catalítica para la reacción de reducción de oxígeno. Por último, hemos estudiado la adsorción de cationes metálicos sobre electrodos de Pt(111) modificados con cianuro, así como el efecto de este tipo de interacciones no-covalentes en las propiedades y la estructura de la doble capa electroquímica. Hemos utilizado estas interacciones no-covalentes para fabricar nanoestructuras periódicas sobre superficies de Pt(111) modificadas con cianuro y para metalizar la adcapa de cianuro.



# Chapter 1

## Introduction

### 1.1. Interfacial electrochemistry and single crystal electrodes

The interface between a metal electrode and an electrochemical solution plays a crucial role in many important technological processes like, for example, electrocatalytic reactions taking place at fuel cells. The scope of interfacial electrochemistry is the study of the interface between an electrode and an electrolyte, including the relationship between surface structure and surface reactivity, and the kinetics and the mechanism of the various processes taking place at the electrochemical interface [1-3]. Electrochemists have been able to study, interpret, describe and understand the electrode-electrolyte interface at the atomic scale only in the last 30 years. This has been possible essentially due to the development of characterization techniques which can probe the electrode surface and the interfacial region in the presence of a bulk electrolyte under potential control (such as *in situ* scanning probe microscopies, vibrational spectroscopies and synchrotron-based methods) as well as to the introduction in 1980 of the Clavilier's method, a simple method to prepare clean and structurally well-defined single-crystal electrodes [4]. All these techniques, in combination with the development in the same period of time of complementary theoretical methods, have made the study of the structure and reactivity of the electrochemical interface at the atomic scale possible.

The essential phenomenon in all electrochemical processes is the transfer of electrical charge, which occurs at the electrochemical interface. For this reason, the knowledge of the structure of the interface [1], which involves the species in the solution and the electrode surface, is extremely important. The structure of polycrystalline surfaces is not well defined, consisting of a mixture of facets, steps, kinks, and other defects, with different orientations, each of them with different local electronic structures (and, hence, with different local physical and chemical properties). As a consequence, their electrochemical behavior will be

the sum of all the contributions from the different individual sites, and these surfaces are not suitable for experimental and theoretical investigations at the atomic level. For a detailed understanding of electrochemical processes, it is desirable to use atomically well-defined surfaces with an ordered two-dimensional arrangement of atoms, obtained by cutting a single crystal along a given crystallographic plane, *i.e.*, single-crystal electrodes.

Figure 1.1 shows a schematic representation of the interface between a positively charged metal electrode and a concentrated electrolyte. In this figure, the inner Helmholtz plane (IHP) is defined by the geometrical centres of specifically adsorbed anions covalently bonded to the electrode surface, whereas the outer Helmholtz plane (OHP) is defined by the centres of solvated anions attached to the surface by purely electrostatic interactions. The electrode surface and the OHP define the electrochemical double layer [1,2], in which very intense electric fields of the order of  $10^9 \text{ V m}^{-1}$  can be easily attained.

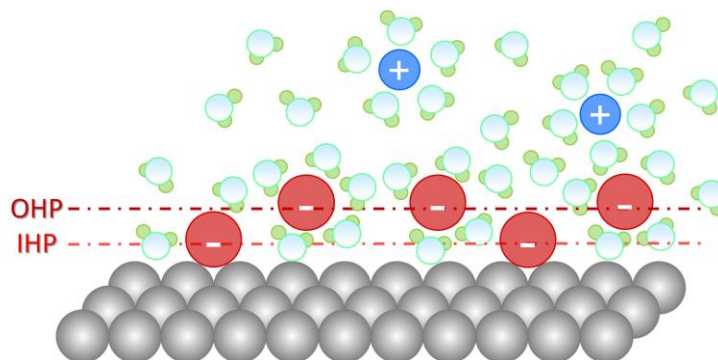


**Figure 1.1.** Scheme of the interface between a positively charged metal electrode and a concentrated electrolyte, with specifically adsorbed anions at the IHP and non-specifically adsorbed anions at the OHP that counterbalance the positive charge on the electrode. The bulk electrolyte is electrically neutral.

Most transition metals crystallize in the hexagonal system or in the cubic system. Metals crystallizing in the cubic system can adopt the body-centered cubic (*bcc*) structure, in which the unit cell is a cube with one atom at each corner and one additional atom at the centre of the cube, or the face-centered cubic (*fcc*) structure, in which the unit cell is a cube with one atom at each corner and one atom at the centre of each of the cube faces. The *fcc* structure is adopted by most of the metals of interest in electrocatalysis, like Pt, Pd, Rh or Ir, and by the coinage metals (Cu, Ag and Au) that have been often used as model surfaces in double-layer studies.

A single crystal surface is obtained by cutting a single crystal along a given plane. The generated surface may be defined by its Miller indices (*hkl*), which correspond to the

smallest three integers in the same ratio as the inverse of the fractional coordinates of the intersections of the plane with the crystallographic unit cell vectors. The three low Miller index surfaces of the *fcc* system, defining the vertices of a stereographic triangle, are (100), (110) and (111), with a square, rectangular and hexagonal arrangement of atoms at the surface, respectively.

This research is aimed at studying electrocatalytic reactions and fabricating nanostructures on chemically-modified Pt(111) surfaces, so I will focus on the (111) surface of the *fcc* systems (see Figure 1.2), *i.e.*, atomically flat surfaces with hexagonal symmetry obtained by cutting an *fcc* single crystal along a plane intersecting the *x*-, *y*- and *z*- axes at the same distance from the origin.

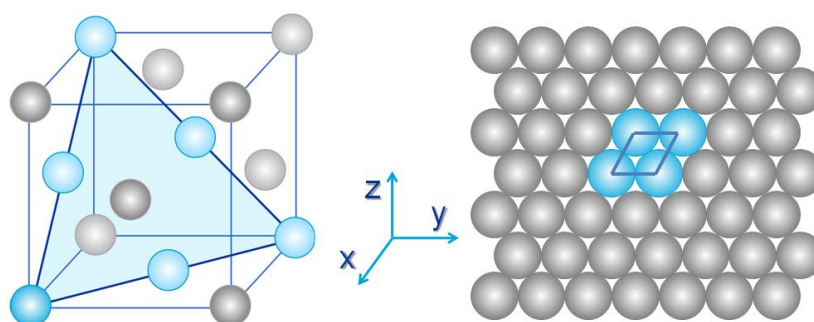


**Figure 1.2.** Unit cell of a face-centered cubic crystal (left) showing the position of the (111) plane, and atomic structure of the corresponding (111) surface (right).

### 1.1.1. Adsorption on well-defined surfaces

Many electrochemical processes, and all electrocatalytic reactions involve the adsorption of reactants and intermediates at surfaces [1]. For this reason, the study of adsorption is of paramount importance in surface electrochemistry. When adsorption involves the formation of chemical bonds between the adsorbate and the electrode surface, specific adsorption or chemisorption<sup>1</sup> occurs. Adsorption generally occurs at specific adsorption sites of the electrode surface.

---

<sup>1</sup> The term 'specific adsorption' is normally used for ions (particularly anions), while the term 'chemisorption' is used to describe the formation of a bond between a neutral molecule and the surface.

The *fcc* system can be described as the stacking of hexagonal atomic layers whose repetition pattern is ABC: the atoms of the second atomic layer (B) occupy half of the holes of the first one (A), and the atoms of the third atomic layer (C) are placed in those holes of layer B that coincide with the unoccupied holes in layer A. The atoms in the subsequent fourth layer occupy the same horizontal position as those in layer A. Adsorption on (111) surfaces of the *fcc* system may occur at the following positions: *on-top*, if the molecule is bonded to a single atom of the surface; *bridge*, when the molecule is adsorbed between two adjacent metal atoms, forming a bond with both of them; or *three-fold hollow* if the molecule is bonded to three contiguous surface atoms. There are two types of three-fold hollow sites on an *fcc*-(111) surface: *fcc-hollow*, if the threefold-hollow site coincides with a hole in the layer underneath, or *hcp-hollow*, if the three-fold hollow site coincides with an atom in the layer underneath (see Figure 1.3, left). The concept of adsorption is a rather static one, while reactions are dynamic processes. Accordingly, we have also often used the concept of the reaction site, understood as the number of atoms with which a molecule needs to interact for the reaction to proceed from the initial to the final state through the transition state. For small molecules like the ones studied in this work, reaction sites on an *fcc*-(111) surface can be composed of 1, 2 or 3 atoms.

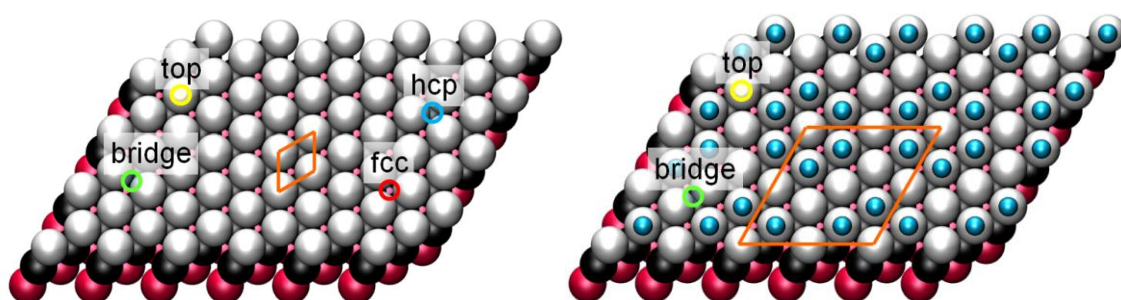


**Figure 1.3.** Ball models of the different adsorption sites on a Pt(111) surface (left) and the on a cyanide-modified Pt(111) surface (right).

Chemical modification of electrode surfaces has been proved to be very useful to study the mechanisms of certain electrochemical reactions or reaction steps (see, for example, [3]). The work presented here has been focused on the study of the role of the size and the geometry of atomic ensembles in electrocatalysis, and also on the fabrication of extended periodic nanostructures, both using a self-ordered molecular pattern, namely cyanide-modified Pt(111).

Cyanide adsorbs spontaneously and irreversibly on Pt(111) electrodes forming an ordered  $(2\sqrt{3} \times 2\sqrt{3})R30^\circ$  structure [5-7], which extends over the whole electrode surface. This structure was reported for the first time by Hubbard and co-workers [5], whose low-energy electron diffraction (LEED) experiments demonstrated that the  $(2\sqrt{3} \times 2\sqrt{3})R30^\circ$  structure formed by adsorbed cyanide on Pt(111) resists electrode emersion and transfer into a ultra-high vacuum (UHV) chamber, which is an indication of a very strong adsorption. The atomic, real space structure could be later elucidated by electrochemical scanning tunneling microscopy (EC-STM) [6,7]. The  $(2\sqrt{3} \times 2\sqrt{3})R30^\circ$  cyanide structure consists of hexagonally packed hexagons, each containing six CN groups adsorbed on top of a hexagon of Pt atoms surrounding a free Pt atom [7-9] (Figure 1.3, right). As can be observed, *three-fold hollow* adsorption sites and reaction sites composed of three contiguous Pt atoms have disappeared from the surface. Cyanide adsorption on Pt(111) has been intensively studied in acidic solutions by Huerta *et al.* [10-14] by means of cyclic voltammetry and spectroscopic techniques. They were the first to demonstrate, based on their voltammetric results [10], that cyanide-covered Pt(111) could be considered as a chemically-modified electrode.

## 1.2. Electrocatalysis

Similar to general heterogeneous catalysis, electrocatalysis involves the bonding of reactants to the surface of a catalyst, the formation of adsorbed reaction intermediates and the breaking and forming of bonds, yielding the reaction products. The term electrocatalysis, first introduced by W. T. Grubb in 1963 [15] to refer to the anodic and cathodic electrode reactions taking place in a fuel cell, defines the increase of the rate of a charge-transfer reaction by the electrode surface, which interacts specifically with some reactants and intermediates and reduces the activation energy barrier of the reaction, without being consumed in the reaction.

Electrocatalytic reactions are strongly dependent on the chemical composition and the structure of the electrocatalyst [3,16]. The rate at which an elementary reaction step proceeds on the surface of an electrocatalyst will therefore depend on its atomic structure, and also on the availability of atomic ensembles acting as active sites for the reaction or for the different reaction steps, *i.e.*, of sites with the required geometric arrangement to form the chemisorption bonds of reactants and/or reaction intermediates to the surface. In many cases, the structure-reactivity and structure-selectivity relationships, whose knowledge is crucial in the search for an active and selective electrocatalyst, are not completely

understood. The use of model electrocatalysts such as single-crystal metal surfaces is obviously essential to investigate and understand this structure-reactivity relationship.

Chemical modification of a surface can have an effect on its catalytic properties that can be divided into two main categories: (i) alteration of the electronic properties of the metal surface atoms (electronic effects), and (ii) modification of the available adsorption and reaction sites (purely geometric atomic ensemble effects). The study of these two difficult-to-separate effects is essential to gain a solid understanding of electrocatalysis. It is of paramount importance, therefore, to find adequate model electrodes to study electronic and atomic ensemble effects in electrocatalysis. This is particularly true in the case of the atomic ensemble effects, which have historically received much less attention than electronic effects. In the following sections, both electronic and atomic ensemble effects will be addressed.

### 1.2.1. Electronic effects

The electronic structure of an electrode surface determines its physical and chemical properties and plays, hence, a key role in electrocatalysis. A detailed knowledge of the electronic structure of the electrode, in particular of the potential of zero charge ( $E_{pzc}$ ) and of the local density of states (LDOS), is therefore required for understanding electrocatalytic reactions at the atomic-scale, and could be the basis for the design of more active and more selective catalysts [17].

The  $E_{pzc}$  of an electrode [1,18] is the potential at which the electrode surface has no excess charge density. The work function of the electrode, that is, the minimum energy required to take an electron from the highest occupied level (the Fermi level) inside the electrode to a place just outside the electrode surface, is linearly related with the  $E_{pzc}$  [19] and its knowledge is therefore very important in the study of the electronic properties of the electrode. The work function, and hence the  $E_{pzc}$ , contain a surface potential term that will be different for different surface structures, and, accordingly, they have different values for different single-crystal surfaces.

The LDOS describes the distribution of the electronic levels within an energy band. Figure 1.4 shows the LDOS of the  $d$ -band and the  $sp$ -band at the Pt(111) surface referred to the Fermi level energy. As can be observed, while the  $sp$ -band is broad and extends above the Fermi level, the  $d$ -band is narrower due to its strong localization. In order to study the reactivity of a metal surface, it has been shown that it is useful to treat the  $d$ -band as a single level, located at the  $d$ -band centre, interacting with an adsorbate [1,20], which determines the ability of the surface  $d$ -electrons to bind to a given adsorbate. All good



electrocatalysts, such as platinum and palladium, possess  $d$ -band centres near the Fermi level, where electron transfer happens [1,20]. In the case of Pt, the position of the  $d$ -band, which extends above the Fermi level in the case of Pt(111) (see Figure 1.4), explains its good catalytic properties in comparison with other metals.

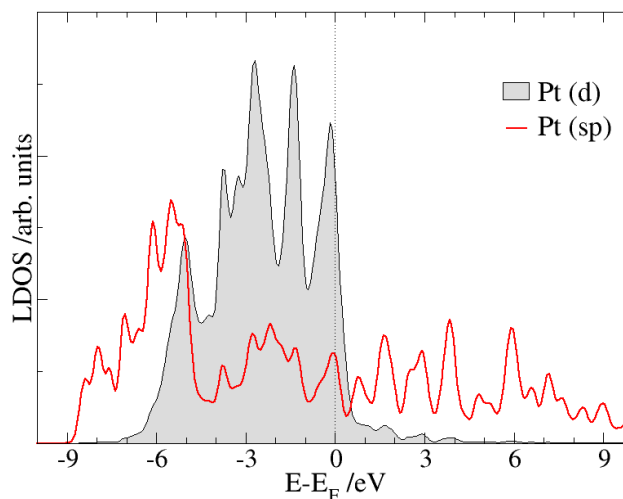


**Figure 1.4.** Density of states of the  $d$ -band and the  $sp$ -band projected on the Pt(111) surface.

The improvement of the catalytic or electrocatalytic properties of a metal surface upon addition of a second metal (bimetallic catalysis) has often been attributed to changes in the electronic structure of the surface atoms brought about by the interactions with the new, foreign atoms. Formation of bimetallic alloys [21] will affect the position of the  $d$ -band centre, due to the changes provoked by its new neighbors in the electronic state of an atom. For instance, alloying platinum with different transition metals, such as Co, Ni, Cr, Fe, Mn, V, W or Ti, has been shown to improve the activity of Pt for the oxygen reduction reaction (ORR) [22,23], due, at least in part, to changes in the electronic structure of the Pt surface atoms.

Deposition of a second metal on a metallic surface can lead to submonolayer (e.g., segregated adatom islands, as represented in Figure 1.5 A) formation on the surface. In the case of overlayers of a foreign metal formed on a substrate, strain effects [24,25], which happen when the atoms or the metal overlayer are forced to adopt positions different from their equilibrium positions in the corresponding bulk materials, provoke a rearrangement of the electron density, leading to changes in the electronic structure of the metal overlayer that can increase or decrease its reactivity towards a given reaction, as compared with the surface of the bulk material.

### 1.2.2. Atomic ensemble effects

The smallest group of atoms with a specific geometric configuration which acts as an active site for the adsorption of a reactant or a reaction step to take place (atomic ensemble) plays a relevant role in electrocatalysis. The study of atomic ensemble effects is very important, not only for understanding the mechanism of electrocatalytic reactions, but also for designing more efficient practical electrocatalysts.

The first studies of atomic ensemble effects were performed in UHV. By adding a second metal to the metallic surface, the kind and statistical distribution of atomic ensembles present on the surface can be altered, which can be very useful to study adsorption or reaction processes. UHV techniques made possible the preparation of ordered bimetallic surface structures, necessary for the study of atomic ensemble effects in heterogeneous catalysis. In 1969 Sachtler and Van Der Plank [26] dealt with the role of individual adatoms in heterogeneous catalysis in a study of hydrogen chemisorption by copper-nickel alloys. They observed changes in the catalytic activity of Cu-Ni alloy films for the hydrogenation of benzene, that were attributed to electronic ligand effects. In a subsequent study employing also Cu-Ni alloys [27], changes in the catalytic activity by the alloys due to both electronic and ensemble effects were found.

In some cases, ordered bimetallic surfaces can be prepared, which may be very useful for the study of atomic ensemble effects. For instance, the study of the adsorption of NO on the  $(\sqrt{3} \times \sqrt{3})$ -SnPt<sub>2</sub>/Pt(111) thin-film alloy (see Figure 1.5 B), in which three-fold hollow sites have been blocked [28], can be used to study the effect of this kind of sites on a variety of reactions. Unfortunately, as noted above, in ordered bulk, thin-film or surface bimetallic alloys geometric ensemble effects cannot be easily separated from electronic effects.

The first reports of purely geometric effects in electrocatalysis [29,30] precede Clavilier's development of the flame-annealing technique [4] to prepare clean and well-ordered single-crystal surfaces. Later, some atomic ensemble effects in electrocatalysis were identified from studies of the oxidation of formic acid and methanol on Pt single-crystal electrodes modified with antimony, selenium or bismuth adatoms [31]. These adatoms inhibit poisoning of the surface by adsorbed CO, promoting the reaction to proceed through the direct pathway and enhancing the rate of oxidation. However, in most of these cases, the increase in the catalytic activity can be attributed both to atomic ensemble and electronic effects, like, for example, in the case of the modification of Pt(100) electrodes with Sb adatoms [32], or in the case of the modification of Pt(111) and Pt(100) electrodes with Bi adatoms [33,34]. Leiva *et al.* [35] developed a simple model that allows distinguishing if the enhancement in the catalytic activity of an adatom-modified electrocatalyst is due to an

ensemble effect, to a ligand effect, or to a combination of both. An important contribution to the study of atomic ensemble effects was made by Maroun *et al.* [36], who used atomically flat PdAu(111) alloys and found that CO adsorption can take place on isolated Pd atoms, while pairs of Pd atoms are necessary for hydrogen adsorption.

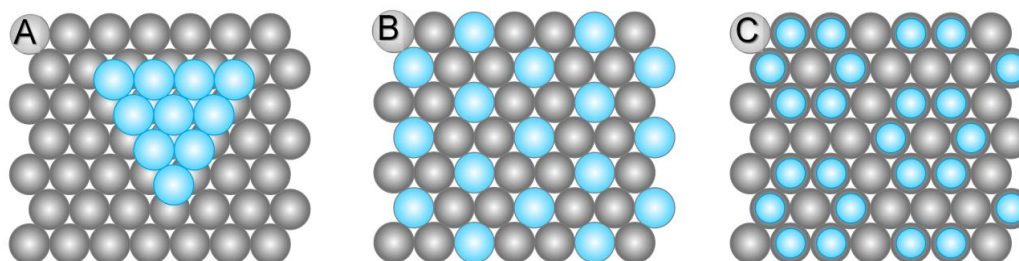


**Figure 1.5.** Ball models (top view) of typical alloy and adsorbate surface structures: A) Segregated smooth-edged  $p(1 \times 1)$  adisland of a foreign metal on a metal surface; B)  $(\sqrt{3} \times \sqrt{3})$ - $R30^\circ$ -(111) surface structure, typical both of ordered bulk alloys and of ordered thin-film and surface alloys, for example  $M_2Sn/M(111)$  thin-film alloys ( $M=Pt, Ni, Cu$ ); C)  $(2\sqrt{3} \times 2\sqrt{3})$ - $R30^\circ$  structure of  $CN_{ads}$  on  $Pt(111)$  surfaces.

Surface modification in such a way that only one kind of sites is removed without modifying the electronic structure of the rest of the surface (the site-knockout strategy [31]) is particularly useful to study the role of geometric atomic ensembles in electrocatalysis. The determination of the smallest number of surface atoms necessary for an electrochemical reaction or a reaction step to occur can help us to identify the rate-determining transition state [37], and thus unveil the reaction mechanism. In addition, this knowledge can be used to channel a reaction through a desired pathway (if there is more than a possible one). Cyanide-modified Pt(111) electrodes (Figure 1.5 C), from which pure Pt three-fold hollow sites and trigonal (or larger) reaction sites have been removed, are excellently suited for this purpose [31,38].

### 1.3. Fuel cells

Fossil fuels supply most of our current energy requirements and are the main sources of pollution of our planet. They are the main cause of the dramatic increase experienced by human emissions of greenhouse gases in the last decades, especially from electric power

plants and from private vehicles. Furthermore, the global energy demand for power generation and for automotive propulsion is increasing rapidly. In order to slow down global warming and improve our quality of life, it is urgent to switch to clean technologies. To achieve this global goal, it is essential to develop new materials that may solve the challenging problems of clean energy production, conversion and storage as alternatives to fossil fuel use.

Fuel cells are electrochemical devices that convert chemical energy directly into electricity. If hydrogen is used as fuel, fuel cells are a zero-emission technology (although, obviously, from a global point of view, this will depend on the hydrogen source). Fuel cells were invented by Sir William Grove, who in 1839 generated an electric current by passing hydrogen and oxygen over two platinum electrodes immersed in sulphuric acid and placed in separate compartments [39]. However, the abundance and cheapness of fossil fuels (and the fuel-cell requirements of large amounts of expensive Pt) made them unquestionable energy sources until the 1950s, when renewed interest on fuel cells arose due to the emerging USA space flight programs, which chose alkaline fuel cells (AFCs) over nuclear power to provide on-board electric power for space vehicles [40]. In 1966, General Motors designed and developed the world's first fuel-cell electric vehicle, which was equipped with an AFC [41]. In the late 1990s, the technology was reintroduced and, since then, many companies have launched low-temperature prototype fuel-cell powered vehicles. The development of fuel cell technology has become more and more important, not only to produce zero-emission cars, but also to power buses, boats, trains, planes and motorcycles. In addition to this, fuel cells can provide electric power supply for buildings or portable electronic devices, among a wide range of applications. They have turned into interesting alternative solutions for sustainable development, and are expected to play a key role in the future energy landscape. These reasons have sparked renewed interest in electrocatalysis during the last decades [3,18,40,42-45].

### 1.3.1. Basic principles and classification

Fuel cells, like batteries, are electrochemical energy conversion devices which convert the energy released in a chemical reaction directly into electrical energy [40,46]. These devices consist of two electrodes -the anode and the cathode- separated by an electrolyte and connected through an external circuit. The direct oxidation of a fuel (e.g., hydrogen, methanol, ethanol, formic acid, etc.) occurs at the anode while the reduction of an oxidant (oxygen) takes place at the cathode. Ions travel across the electrolyte and electrons flow through the external circuit, creating an electric current. The efficiency of a fuel cell, like

that of any other electrochemical energy conversion device, is not limited by the Carnot cycle and, hence, is higher than that of internal combustion engines, or of any other device that converts heat into work. Additionally, in contrast to batteries, energy is generated as long as the fuel and the oxygen are supplied at sufficient quantities. In a hydrogen-oxygen fuel cell (Figure 1.6) with a proton conducting membrane electrolyte (proton exchange membrane fuel cells, PEMFCs), hydrogen is oxidized at the anode, releasing protons and electrons. Protons and electrons are transported (the former across the membrane and the latter across the electrical circuit) to the cathode, where oxygen is reduced to water (the only waste product). Electricity is produced and heat is supplied to the surroundings.

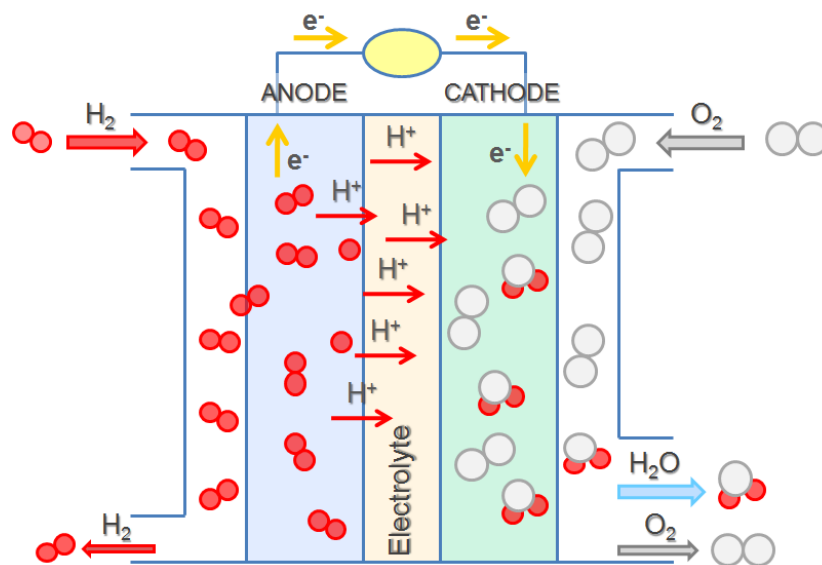


**Figure 1.6.** Hydrogen-oxygen fuel cell scheme.

Fuel cells are classified into two groups, depending on the operation temperature: low-temperature fuel cells, which operate at temperatures lower than 250 °C, and high-temperature fuel cells, which operate above 600 °C. Low-temperature fuel cells have the advantage of achieving faster start-up times and are therefore more attractive for portable applications, especially for vehicle propulsion, where fast response times and start-times are required. On the contrary, high-temperature fuel cells have the advantage that they can burn practically any fuel, because electrocatalysis does not play a limiting role. Fuel cells are also additionally classified, either according to the electrolyte employed in the cell, or to the fuel used. Low-temperature fuel cells are PEMFCs, phosphoric acid fuel cells (PAFCs) and AFCs. As fuel they can use hydrogen, alcohols (direct alcohol fuel cells, DAFCs) or formic acid (direct formic acid fuel cells, DFAFCs). Some other alternative fuels, like hydrazine [47,48] or

sodium borohydride [49] have also been proposed. In all the cases, the fuel-cell stacks are built up from hundreds of single cells in series.

Each fuel cell type has its own advantages and potential applications. AFCs, which use concentrated KOH as electrolyte, exhibit faster ORR kinetics than fuel cells with acid electrolytes and the highest electrical efficiencies. However, pure H<sub>2</sub> and pure O<sub>2</sub> are required, since formation of carbonate from traces of CO<sub>2</sub> in reformed fuels reduces the electrolyte's ion mobility. This requirement increases their costs and limits their applications. In contrast, PEMFCs, which can use oxygen from air, combine a high power density with high energy conversion efficiency and low operating temperatures.

An important problem of hydrogen-fueled FCs is the production, transportation and storage of hydrogen, that has the largest energy density per unit mass but a very low energy density per unit volume. These problems led to consider small organic molecules, such as formic acid, methanol and ethanol, as fuels, because, being liquid at operating temperatures, their energy density per unit volume is higher than that of hydrogen, and, in addition, can use the currently available petroleum distribution network, reducing the barriers to commercial implementation. Their higher volume-referred energy density makes them particularly suitable for low power, portable applications. However, the overpotential required for the oxidation of these small organic molecules is higher than that required for hydrogen oxidation, and catalyst poisoning by adsorbed carbon monoxide formed during the electrooxidation reaction is a common problem.

Finally, PAFCs, which use Pt-based catalysts for both anode and cathode, have the highest level of commercial implementation amongst fuel cells, probably due to their thermal and chemical stability and to the low volatility of the electrolyte at operating temperatures. Power plants based on PAFCs are being installed worldwide, supplying cities and buildings with electricity, central heating and hot water.

### 1.3.2. Anodic and cathodic electrocatalytic reactions

In a fuel cell the fuel is oxidized at the anode and oxygen is reduced at the cathode. Pt-based electrocatalysts are usually employed for both the anode and the cathode. The hydrogen oxidation reaction (HOR, Reaction 1.1) is the most fundamental electrocatalytic reaction and it has been intensively studied [3]. This reaction involves either the homolitic chemisorption of hydrogen onto the surface (Reaction 1.2, Tafel reaction) or the heterolitic electrochemical adsorption of hydrogen (Reaction 1.3, Heyrovsky reaction), followed by the oxidation of adsorbed hydrogen and the desorption of the resulting proton (Reaction 1.4, Volmer reaction).



The oxidation of formic acid and the ORR are the more important electrocatalytic reactions studied in the work reported here. As explained above, methanol and formic acid are promising liquid fuels with some advantages over hydrogen. The oxidation of these fuels typically proceeds by the so-called dual path mechanism (represented in Figure 1.7 for the case of the formic acid oxidation reaction, FAOR), in which  $\text{CO}_2$  and water are formed either directly or through a poisoning intermediate [50,51]. Formic acid oxidation has been extensively studied during the last decades, both because it is the fuel in DFAFCs and because it appears as an intermediate in the methanol oxidation reaction (MOR). The advent of *in situ* infrared reflectance spectroscopy at the beginning of the 1980s allowed the identification of CO as the poisoning intermediate in both the MOR and FAOR [52,53]. More recently, *in situ* surface enhanced infrared reflection absorption spectroscopy in the attenuated total reflection mode (ATR-SEIRAS) has allowed Osawa and co-workers to identify bridge-bonded adsorbed formate as the intermediate in the reactive pathway of the FAOR [54-57] and the MOR [58]. Cuesta *et al.* have very recently demonstrated that adsorbed formate is also the intermediate in the indirect path of the FAOR (*i.e.*, in the dehydration of formic acid to yield adsorbed CO) and is, hence, the bifurcation point in the dual-path mechanism of the FAOR [59] (see Figure 1.7). The mechanism of the direct path of the FAOR has been recently unveiled thanks to an ATR-SEIRAS study with Au thin-film electrodes [60], onto which CO does not adsorb in CO-free acidic solutions.

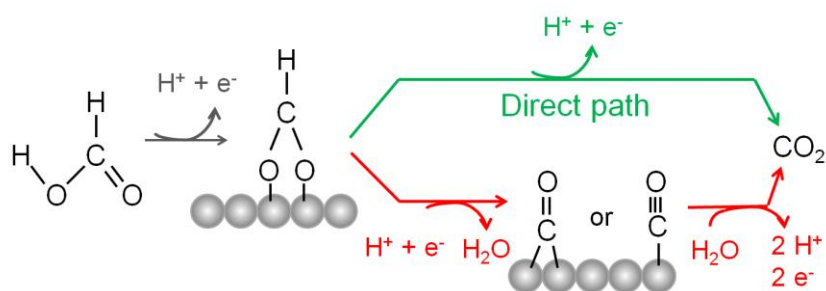
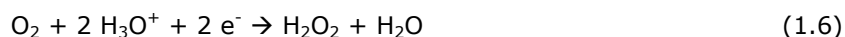


**Figure 1.7.** Schematic representation of the dual path mechanism for formic acid electrooxidation on Pt electrodes.

ORR is the most intensively investigated electrocatalytic reaction [3,24,26,44,45,61, 62], because the high overpotential necessary to make this reaction proceed at an acceptable rate is the main responsible for the high platinum loadings necessary at the cathode in order to achieve acceptable power densities. Oxygen can be either totally reduced (four-electrons reduction), with water as the product in acidic media (Reaction 1.5), or partially reduced (two-electrons reduction), with hydrogen peroxide as product in acidic media (Reaction 1.6). Obviously, hydrogen peroxide can be further reduced to the final product (Reaction 1.7). The complete, four-electron reduction is preferable, because  $\text{H}_2\text{O}_2$  is an aggressive chemical that can damage the polymer electrolyte membrane, and producing  $\text{H}_2\text{O}_2$  instead of  $\text{H}_2\text{O}$ , leads to the conversion of only a fraction of the available chemical energy. However,  $\text{H}_2\text{O}_2$  is a valuable chemical, and fuel cells producing  $\text{H}_2\text{O}_2$  at the cathode have been recently proposed as a way to produce a commercially valuable product using a clean technology and releasing electrical energy as a byproduct [63].



The maximum open circuit voltage of a fuel cell is given by the difference between the equilibrium potential of the cathodic and anodic reactions, but as soon as the fuel cell starts to operate the voltage will decrease, due to potential drops in the fuel cell that include resistive losses and transport limitations [40]. However, kinetic losses (kinetic overpotential) due to the slow kinetics of the ORR are responsible for about 70% of the total loss [22]. This makes a very high Pt loading in the cathode absolutely necessary, preventing fuel cells from being economically competitive (or even viable) with other, conventional, energy conversion devices. Well-defined surfaces are used as model catalysts to gain an understanding of adsorption and reaction processes occurring during the ORR (*i.e.*, about the reaction mechanism) that could help us to design more active real cathode fuel-cell catalysts [3].

In order to improve the kinetics for the ORR and/or decrease the price of the cathode material we need to develop more active and selective catalysts. This is particularly challenging, because any suitable catalyst must counterbalance two opposite requirements: it must be noble enough to minimize the adsorption of poisonous spectator species, and at the same time it must be active enough to break the O-O bond and produce the four-electron reduction of oxygen at potentials that are as close as possible to the ORR reversible potential. So far, there are two basically different approaches to the development of more active and selective catalysts. The first strategy consists of tuning the electronic properties of the metal surface atoms. The success of this approach has been demonstrated in the



development of PEMFCs catalysts [43], mostly with Pt alloys [23,44] or by de-alloying some alloys of Pt [64] as well as by synthesizing Pt core-shell catalysts [65-67]. The second strategy is based on a systematic alteration of the components and structure of the electrochemical double layer, thus affecting the properties of the entire interfacial region. In this approach, emphasis has been placed on understanding how variations in non-covalent interactions between covalently bonded adsorbed OH, located at the IHP, and hydrated alkali metal cations that are located at the OHP may affect the reactivity [68].

## 1.4. Surface nanostructuring

In the last decades we have witnessed a trend towards device miniaturization, mainly led by the need of the microelectronics, data storage and communication industries for even smaller feature sizes [69]. Lithographic techniques using beams of particles, ions or electrons allow the drawing of nanostructures on surfaces with a resolution of 50 nm. Although it could be possible to reduce this barrier, it would be at the expenses of large cost increases and a large decrease in the size of the substrates. For this reason, it is necessary to develop new techniques that allow us to create structures on surfaces with a size of only some nanometres.

In 1959, at the annual meeting of the American Physical Society, the Physics Nobel Prize winner Richard P. Feynman lectured his classic conference entitled *There is plenty of room at the bottom* [70], which brought about the starting point of nanoscience. In this visionary lecture, he talked about 'the problem of manipulating and controlling things on a small scale'. He predicted exciting phenomena such as writing books on the head of a pin, seeing and manipulating atoms and miniaturizing computers to improve their speeds and decrease the energy consumption. For more than two decades, however, due to the lack of appropriate tools, building structures composed of a group of molecules or atoms remained an inaccessible dream. This changed in 1981, after the development by Gerd Binnig and Heinrich Rohrer of the scanning tunnelling microscope (STM) [71], an instrument which makes possible not only the visualization of surfaces with atomic resolution, but also the modification of surfaces and the control of matter down to the atomic level, by manipulating single atoms with the STM tip [72-74].

In the early 1990s, when STM had already brought about a revolution in surface science, it began to be applied in situ in electrochemistry [2]. The ability to easily create and control very intense electric fields at the electrode-electrolyte interface makes electrochemical methods very promising for surface nanostructuring. In contrast to lithographic methods,

electrodeposition processes are accessible and inexpensive. Nanostructures on surfaces may be produced, for example, by preferential electrodeposition of a metal at monoatomic step edges separating atomically flat terraces on highly ordered pyrolytic graphite (HOPG) electrodes [75], by underpotential-deposition of admetals on stepped Pt single crystal electrodes [76], or by creating Au-Cd alloy nanowires by preferential deposition of the alloy at the *hcp* regions between the sets of soliton walls of the reconstructed Au(111) surface [77]. In all the previous examples, STM was used to visualize the structure of the surface. In other cases, the tip of the STM has been the tool used to create the nanostructures on a surface. A very interesting method developed by Kolb's group [78], consists on transferring Cu predeposited on the STM tip to the surface of a Au(111) electrode, by applying an externally generated voltage pulse directly to the z piezo, leading to an appropriate approach of the STM tip to the surface. In combination with a microprocessing unit, various patterns and cluster arrays (including geometric and artistic drawings) can be easily and reproducibly created.

Conducting polymers such as polyanilines, polypyrroles and polythiophenes have received special attention for applications in molecular electronic devices. Therefore, it is extremely interesting to study the electrochemical polymerization of conducting polymers on ordered metal surfaces and to characterize their conformations and structures on a molecular level using *in situ* STM. Aniline molecules adsorb forming highly ordered arrays on Au(111) electrodes in sulphuric acid solutions at 0.55 V and 0.85 V vs. RHE [79], forming conducting polyaniline (PANI) with well-defined molecular conformations at potentials above 0.95 V vs. RHE [79,80].

We aim at using cyanide-modified Pt(111) electrodes as a molecular pattern to produce periodic surface nanostructures by metal adsorption or electrodeposition, as well as by the polymerization of adequate organic molecules. The typical dimensions of copper deposits on silicon formed by the damascene process are of the order of 100 nm wide, whereas in our case, the line width of the searched-for nanostructures would be one atom or one molecule, *i.e.*, approximately three orders of magnitude thinner (in addition to being periodic with a large long-range order, what could impart them interesting collective electronic properties).

## 1.5. Scope of the research

This Doctoral Thesis has addressed the use of a self-ordered molecular pattern, namely cyanide-modified Pt(111), as a model surface to study the role of geometric atomic ensembles in electrocatalysis and to fabricate extended nanostructures (of only one atomic diameter). The main objectives pursued in this research are shown below.

One objective has been to use a combination of electrochemical methods, non-electrochemical *in situ* techniques (such as electrochemical scanning tunneling microscopy (EC-STM) and external-reflectance Fourier-transform infrared spectroscopy (FTIRS)) and theoretical calculations to gain an understanding on the fundamental properties of cyanide-modified Pt(111) electrodes. The experimental techniques employed and their theoretical foundations are described in Chapter 2, and Chapter 3 presents a combined experimental and theoretical study concerning the stability and the geometric and electronic structure of cyanide-modified Pt(111) surfaces.

Cyanide-modified Pt(111) electrodes may be used to study the kinetics and the mechanisms of important electrocatalytic reactions, like the electrooxidation of oxygenated C1 molecules, in which atomic ensemble effects can be used to inhibit catalyst poisoning and channel the reaction exclusively through the reactive path [38]. Similarly, the catalytic activity of Pt-based electrocatalysts for the ORR can be increased by blocking the sites needed for the adsorption of spectator anions (e.g. sulphates or phosphates). Atomic ensemble effects in electrocatalysis are addressed in Chapter 4. First, the suitability of cyanide-modified Pt(111) electrodes as model surfaces to study atomic ensemble effects was tested with the NO-reductive stripping reaction (Chapter 4.2). Then, cyanide-modified Pt(111) surfaces were used to investigate atomic ensemble effects in fuel-cell electrocatalytic reactions, such as the hydrogen (Chapter 4.3) and formic acid oxidation (Chapter 4.4), or the oxygen reduction (Chapter 4.5).

Finally, this Thesis aimed at developing a new simple method to produce periodic nanostructures extending over the whole surface of an electrode, irrespective of its size. Chapter 5 illustrates the role of non-covalent interactions between alkali metal cations and adsorbed cyanide in dictating the electrochemical double layer properties. Copper ions attached non-covalently to the surface of a cyanide-modified Pt(111) are shown in Chapter 6 to be the precursor for the metallization of the cyanide adlayer. The formation of polyaniline on cyanide-modified Pt(111) surfaces is also addressed in this Chapter.



## Chapter 2

### Experimental and theoretical methods

#### 2.1. Fabrication, orientation and flame treatment of platinum single-crystal electrodes

In 1980 Clavilier *et al.* [4] adapted a previously existing method to fabricate platinum single crystals [81,82] and demonstrated that simple flame annealing leads to clean and well-ordered single-crystal surfaces, bringing about a revolution in surface electrochemistry.

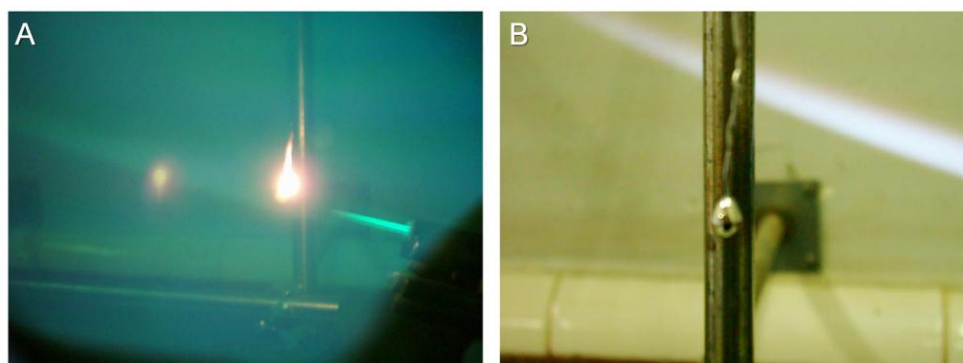


**Figure 2.1.** Melted Pt bead, hanging from a Pt wire, in the flame of a  $O_2/C_4H_{10}$  burner (A) and solidified Pt bead (B).

In the Group of Electrochemistry of the Institute of Physical Chemistry 'Rocasolano' (Madrid), Clavilier's method, adapted from the Alicante Group version, is used to fabricate Pt single-crystal electrodes. Briefly, the extremity of a platinum wire is melted using an  $O_2/C_4H_{10}$  burner until formation of a bead, which grows fed by the wire (see Figure 2.1). The bead is allowed to crystallize and is then placed in the centre of a three-circle goniometer, located on an optical bench at the other extreme of which there is a He-Ne laser aligned with the bench and pointing to the single crystal (see Figure 2.2). The laser beam is reflected by

the small (111), and (100) facets present on the surface of the bead. Measuring the angle between the different reflections (*i.e.*, the angle between the facets) it is possible to determine if the bead is well crystallized, and the plane parallel to which we wish to cut the crystal can be found and placed perpendicular to the axis of the optical bench. The goniometer is then fixed and the crystal attached to the goniometer is introduced in a polypropylene cylindrical mold (Figure 2.2), which is then filled with an epoxy resin. When the resin has solidified (after *ca.* 8 hours) the resin cylinder, with the oriented crystal (the desired plane of which is now parallel to the circular base of the resin cylinder) embedded in it, can be separated from the goniometer and transferred to a *Phoenix Beta* polishing machine with an electrically-driven *Vector* power head (Buehler). The resin cylinder containing the oriented Pt single crystal is then grinded until the bead has been cut to its maximum diameter. The crystal is then polished with alumina (final particle size: 0.05  $\mu\text{m}$ ) until a mirror-like surface is obtained and, finally, the resin cylinder is introduced in dichloromethane overnight, in order to dissolve the epoxy resin and extract the oriented cut and polished single crystal.

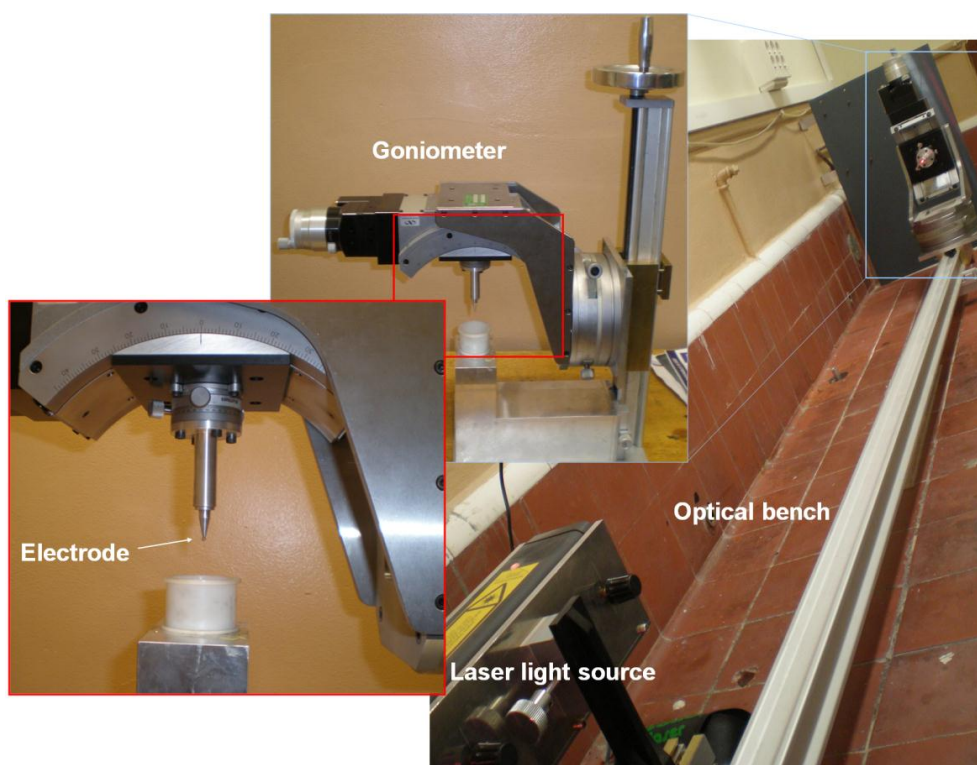


**Figure 2.2.** Set-up used for the orientation of single crystal beads in the laboratories of the Electrochemistry Group at the Institute of Physical Chemistry 'Rocasolano'.

After polishing, the single-crystal surface is disordered and contaminated and it is necessary to anneal it (using, e.g., the flame of a Bunsen burner) in order to obtain a clean and well-ordered Pt single-crystal surface. Originally, after annealing the electrode was quenched in ultrapure water [4], but the method was later improved by allowing the electrode to cool in a reducing atmosphere (Ar and H<sub>2</sub>) before attaching a protecting drop of ultrapure water to the surface [83].

The working Pt electrodes used in this work for cyclic voltammetry and Fourier transform infrared (FTIR) experiments were bead-type platinum single crystals (*ca.* 2 and *ca.* 4 mm in diameter, respectively) prepared according to the method described above, oriented and polished parallel to the (111) plane. The Pt(111) electrode used for STM experiments was a single crystal disk (10 mm in diameter) purchased from MaTeck (Jülich, Germany). In our laboratories, newly fabricated single-crystal electrodes are typically annealed in the flame of a Bunsen burner during at least 30 min. After this first treatment, the electrode is annealed only for a few minutes in the flame of a Bunsen burner before performing each experiment. After annealing, the electrode is cooled in a reducing H<sub>2</sub> + N<sub>2</sub> atmosphere and, once at room temperature, CO is introduced in the cooling vessel for *ca.* 5 min, in order to form a saturated CO adlayer on the electrode surface, which is then protected with a droplet of ultrapure water saturated with CO and transferred to the electrochemical cell, where it is put in contact with the electrolyte using the hanging meniscus configuration. The CO adlayer survives the contact with atmospheric oxygen during the transfer, protects the platinum surface from contamination and, due to its hydrophobic nature, allows the easy formation of a good and reproducible meniscus without wetting the sidewalls of the bead. After stripping the CO adlayer in the first positive potential sweep, well ordered Pt single-crystal surfaces with large, atomically flat terraces are obtained, as demonstrated by the cyclic voltammograms obtained in 0.1 M H<sub>2</sub>SO<sub>4</sub> (Figure 2.3).

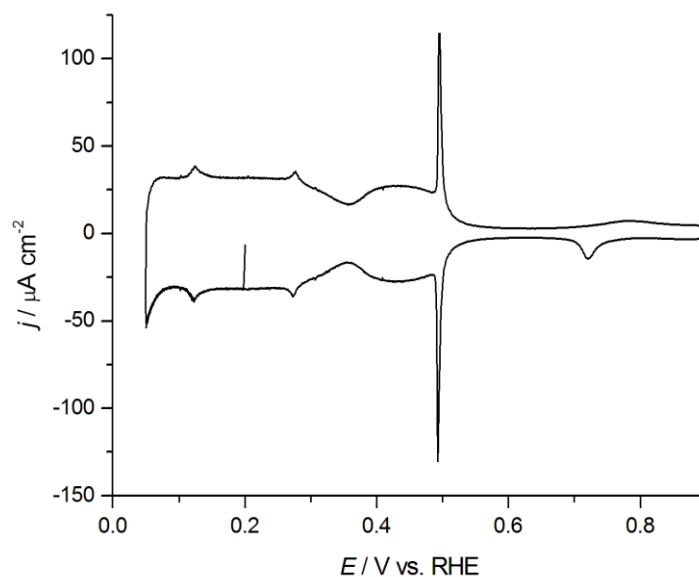


**Figure 2.3.** Cyclic voltammogram at  $50 \text{ mV s}^{-1}$  of Pt(111) in  $0.1 \text{ M H}_2\text{SO}_4$ .

## 2.2. Experimental techniques

### 2.2.1. Cyclic voltammetry

Cyclic voltammetry is probably the technique most commonly employed to characterize electrode surfaces and to study processes occurring at the electrode-electrolyte interface. It consists of recording the current flowing through the working electrode upon applying a triangular cyclic sweep of the electrode potential with a constant scan rate ( $\nu = dE/dt$ ). The resulting current density ( $j$ ) versus potential ( $E$ ) plot is called a cyclic voltammogram (CV), and is characteristic of the structure and the chemical nature of the electrode surface, and of the composition of the electrolyte. In the case of a single crystal surface, its shape often gives details of the quality and cleanliness of the surface. Cyclic voltammetry can provide thermodynamic and kinetic information of the processes occurring at the electrode-electrolyte interface, although in the latter case care must be taken, since potential and time change simultaneously during a CV.

CVs can be often considered 'fingerprints' of surfaces. For this reason, cyclic voltammetry is widely used for initial electrochemical studies of new systems. In addition to this, in the case of platinum single-crystal electrodes it is a routine technique for surface characterization, showing if the crystal has the desired orientation and being able to detect a



very small number of defects. Other *ex situ* (e.g., low-energy electron diffraction, LEED) and *in situ* (e.g. surface X-ray scattering, SXS, or scanning tunneling microscopy, STM) surface characterization techniques are often necessary for a detailed characterization of the surface, but these are more complex physical techniques requiring an equipment much more expensive (including a UHV chamber in the case of LEED, or a synchrotron in the case of SXS) than the modest (in terms of price) potentiostat required for cyclic voltammetry.

In this research, the usual three-electrode configuration (Working Electrode, Reference Electrode and Auxiliary Electrode) was used. A *CHI 600* digital potentiostat was used to control the potential difference between the working and reference electrodes and to measure the current passing through the working and auxiliary electrodes. The auxiliary electrode was a platinum wire, and a reversible hydrogen electrode (RHE), to which all of the potentials in this work are referred, was used as reference.

#### 2.2.1.1. Electrochemical cell

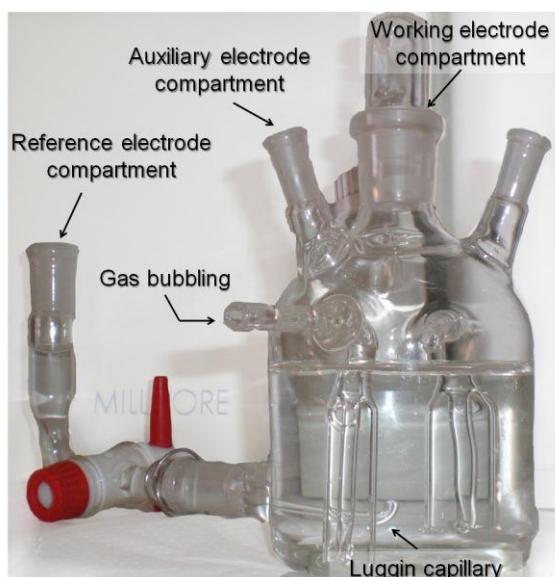


**Figure 2.4.** Electrochemical cell used in the Electrochemistry Group at the Institute of Physical Chemistry 'Rocasolano'.

The electrochemical cell used for voltammetric experiments was made of Pyrex glass in the workshops of the Institute of Physical Chemistry 'Rocasolano'. The electrode holder is made of Teflon and fits in the central cone of the glass cell, allowing the approach of the working electrode to the surface to form a hanging meniscus, so that only the polished face

of the bead, with the desired orientation, touches the solution. The auxiliary electrode, which is a Pt wire, fits in one of the smaller lateral cones of the glass cell, the other one allowing, if necessary, to fit a tube that leads the gases from the cell to a fume (Figure 2.4) The reference electrode is placed in a separate compartment ending in a Luggin capillary located as close as possible to the electrode surface, in order to minimize the ohmic drop due to the electrolyte resistance. Two tubes bended upwards, protected by a bell-shaped chamber opened at its bottom and with a small lateral circular aperture, allow to bubble gases through the solution without disturbing it.

### 2.2.2. Rotating disk and rotating ring-disk electrodes

The rotating disk electrode (RDE) is a hydrodynamic electrochemical technique very useful for the study of electrochemical kinetics. It induces forced convection of the electrolyte, making the study of electrochemical reactions under well-defined mass-transport conditions possible. The working electrode is a disk embedded in a rod of an insulating material, and rotates at a controlled rate. Mass transport of the reacting species to the electrode surface is convective up to a small diffusion layer, whose thickness ( $\delta_{RDE}$ ) depends exclusively on the rotation rate for a given system, as can be observed in Equation 2.1.

$$\delta_{RDE} = 1.61D^{1/3}\nu^{1/6}\omega^{-1/2} \quad (2.1)$$

where  $D$  is the diffusion coefficient of the reactant in the electrolyte,  $\nu$  the kinematic viscosity of the electrolyte and  $\omega$  the rotation rate (in  $\text{rad s}^{-1}$ ). Two important advantages of hydrodynamic methods [84] are that time-independent mass flow of the electroactive species to the electrode and steady-state currents are attained very quickly, and are controlled by the rotation rate.

If the reaction rate of the electrode is much larger than the rate at which the reactant diffuses to the electrode, the surface concentration of the reactant is essentially zero, and the current is diffusion limited. The diffusion-limited current density on a RDE can be calculated with the Levich equation:

$$j_l = nFc_0 \frac{D}{\delta} = 0.62nFc_0 D^{2/3} \nu^{-1/6} \omega^{1/2} \quad (2.2)$$

where  $n$  is the number of electrons transferred in the reaction,  $F$  is the Faraday constant and  $c_0$  is the bulk concentration of reactants.

On an RDE the electrode is uniformly accessible, so that, during a reaction, the flux, and hence the current density, is the same across the entire disk surface. The RDE has been

widely used as a tool for studying electrode processes occurring at fuel cells by means of polarization curves (current density vs. potential plots).

Rotating ring-disk electrodes (RRDE) utilize a metal (usually Pt) ring as a second independent electrode which is placed around the disk electrode, with an insulating gap separating them, to detect products formed at the disk electrode. In a RRDE the polarization curves of the disk are unaffected by the presence of the ring. RRDE experiments require the use of a bi-potentiostat to separately control the potential of the disk and the potential of the ring.

Both RDE and RRDE experiments were performed in a three-compartment electrochemical cell, using an *Autolab PGSTAT 302N* bi-potentiostat and rotation control (Pine Instruments), at Prof. Markovic's laboratories at Argonne National Laboratory (United States Department of Energy, Illinois). A saturated calomel electrode (SCE), separated by an electrolytic bridge from the main cell compartment, was used as reference electrode, and a Pt mesh was used as auxiliary electrode. Argon or oxygen was bubbled through the electrolyte using a glass tube ending in a glass frit.

### 2.2.3. *In situ* scanning tunneling microscopy

In 1981 Binnig and Rohrer, then at the IBM laboratories in Zurich, developed a powerful instrument able to image surfaces in real space and real time with atomic resolution: the scanning tunneling microscope (STM) [71,85]. Only five years later they were awarded with the Nobel Prize in Physics for this invention. The STM is based on the combination of two physical effects: quantum tunneling and the piezoelectric effect. Quantum tunneling is a phenomenon by which a subatomic particle can go through a potential barrier of a height higher than its energy, something impossible from the point of view of classical mechanics. The piezoelectric effect, discovered by Pierre Curie and Jacques Curie in 1880 (about 100 years before the invention of the STM) is the ability of some materials (e.g., quartz and some ceramics) to expand or contract when a voltage is applied across them (or, inversely, to develop a potential difference across them when subjected to a compressive or expansive pressure). The combination of both effects allows the control with a precision of less than 1 Å of the vertical and the lateral movement of a tip in relation to a sample.

In STM, a metallic conducting tip is approximated within a few tenths of a nanometer to a conducting or semiconducting surface (sample), and a potential difference (potential bias), usually of the order of a few hundreds of millivolts, is applied between tip and sample.

When the tip is biased positively relative to the sample, electrons can tunnel from the sample to the tip if there is an overlap between filled electronic states at the sample and empty states at the tip. If the tip is negatively biased, electrons can tunnel from the tip to the sample if there is an overlap between filled electronic states at the tip and empty electronic states at the sample (see Figure 2.5).

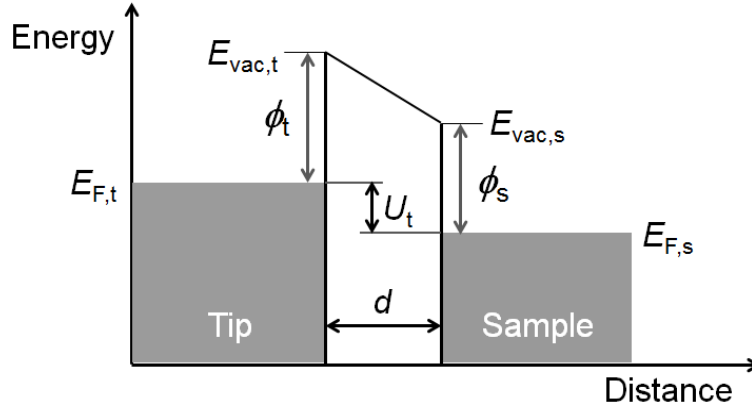


**Figure 2.5.** Schematic representation of the quantum tunneling effect: a negative potential bias ( $U_t$ ) is applied between the tip and the sample, and electrons tunnel from the tip to the sample.  $E_{F,t}$  and  $E_{F,s}$  are the Fermi levels of the tip and the sample, respectively,  $\phi_t$  and  $\phi_s$  are the work functions of the tip and the sample, respectively, and  $d$  is the separation between tip and sample.

The flow of tunneling electrons generates a tunneling current ( $i_t$ , typically of a few nanoamperes), whose magnitude decays exponentially with the distance between tip and sample ( $d$ ) according to Equation 2.3.

$$i_t \propto U_t \cdot \rho_s(0, E_F) \exp(-Ad\sqrt{\phi}) \quad (2.3)$$

where  $U_t$  is the potential bias,  $\rho_s(0, E_F)$  is the local density of states (LDOS) at the Fermi level,  $\phi$  is the potential barrier and  $A$  is a constant. The value of  $1/(A\sqrt{\phi})$  is of the order of a few tenths of a nanometer, which allows a very high vertical resolution. Obviously, since sub-Angstrom distances are involved in maintaining a constant tunneling current, the motion of the tip must be very precisely controlled. For this purpose, a piezoelectric tube scanner [86] with the tip attached to its bottom is used to control the motion of the STM tip. The top of the piezoelectric tube is held fixed relative to the sample. The piezoelectric tube is covered inside and outside with a metal coating in order to allow for the connections with the controlling electrodes, as shown in Figure 2.6. The outer coating is divided into four sections, while the inner coating covers the inside of the tube completely. As explained above, a

piezoelectric material expands or contracts when a voltage is applied across it. The vertical  $z$  motion is controlled by the voltage applied between the inner and the outer electrodes, while the lateral motion is controlled by the voltage difference between opposed sections of the outer metallic coating. The deformation of the piezoelectric in a given direction depends on its dimensions, the applied voltage and the piezoelectric coefficient [87]. Typically, the contraction or expansion of the piezoelectric is of a few  $\text{nm V}^{-1}$  in each direction [86], allowing for the STM's high lateral resolution. The lateral tip movement (scanning rate) is controlled by the instrument electronics, and is fixed by the researcher.

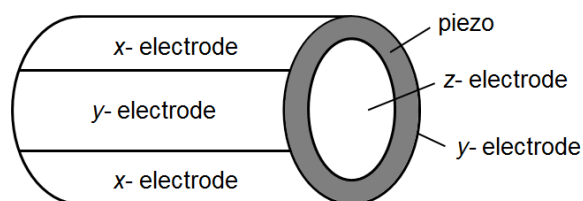


**Figure 2.6.** Schematic representation of the piezoelectric tube.

The STM may be used in two scanning modes: the 'constant current' mode, in which a feedback is used to readjust the separation between the tip and the substrate whenever the tunneling current deviates from a predetermined value, or the 'constant height' mode, where the tunneling current is monitored while the tip is scanned at a fixed distance from the sample. Figure 2.7 shows a schematic representation of the constant current imaging mode, the most frequently employed and the one used in the work reported here.

In the constant current mode the scanning process is controlled by a computer and the corresponding software, which applies to the piezoelectric tube the voltage necessary to move the tip to any desired  $x$ - $y$  position. The image is obtained point by point as the tip is scanned line by line across the sample. The control electronics measure the tunneling current at each point of the scan and compare it to the user-determined reference current, adjusting the voltage that controls the  $z$  motion of the piezoelectric in order to move the tip away from or towards the sample. The vertical distance travelled by the tip (proportional to the change in the  $z$  voltage applied to the piezo) when the tip moves from one position to the next is a direct measure of the difference in height between the corresponding points on the surface (please note that, in the case of images with atomic resolution, the apparent corrugation reflects differences in the LDOS, rather than the surface topography). While this scanning mode yields directly a topographic map of the surface, no further treatment of the acquired data being necessary, it suffers from a low time resolution, associated to the time constant of the feedback circuit.

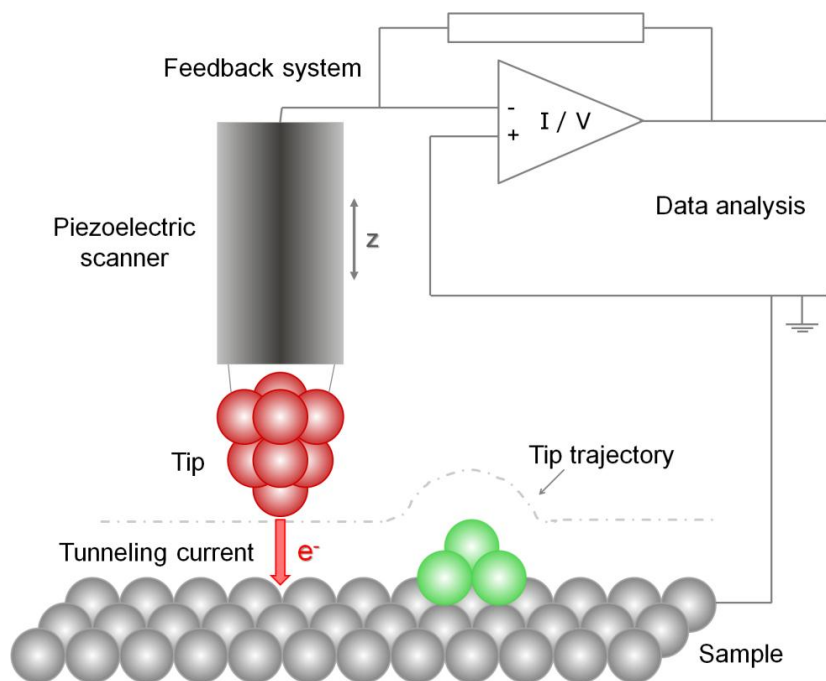


**Figure 2.7.** Schematic representation of the constant current mode of operation of a STM.

A STM provides three-dimensional images of the surface of a conducting or semiconducting material in real time and real space. Typically, a gray or color scale is used for the vertical dimension, brighter areas corresponding to higher ones. As indicated above, high-resolution STM images are maps of the LDOS of the surface. In many cases, each maximum in the density of electronic states corresponds to one atom, but this is not necessarily so. For example, in high-resolution STM images of highly ordered pyrolytic graphite (HOPG) typically only half of the surface carbon atoms are imaged, the other half remaining invisible. When polyatomic ions or molecules are present on the surface, the appearance of the image will depend strongly on their electronic structure (which might be affected by the bonding of the molecule or the ion to the surface), which is often reflected in the STM image. In these cases, the registered image may change when switching the tunneling potential, due to the change in the molecular orbitals to or from which electrons tunnel.

Our EC-STM measurements were performed with tungsten tips, electrochemically etched from a polycrystalline tungsten wire in 2 M NaOH. The tungsten wire was connected to the positive end of a DC power supply and was placed in the centre of a gold wire ring connected to the negative end of the DC power supply. A lamella of the etchant solution was then suspended from the gold ring and a constant potential of 2.5 V was applied between the

ring and the tungsten wire (see Figure 2.8). Under these conditions, the tungsten wire dissolves. Due to the geometry of this electrolytic cell, dissolution of the tungsten wire proceeds faster in the part of the wire located at the centre of the lamella, creating a neck which becomes thinner and thinner until the wire breaks. With the help of a feedback loop that interrupts the circuit whenever there is a sudden change in the current, the etching of the wire stops as soon as the wire breaks, and both the upper and the lower part of the tungsten wire can be used as tips for STM experiments.

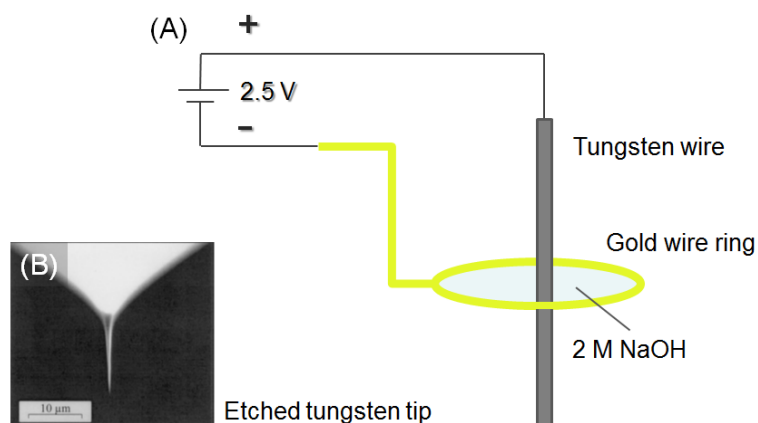


**Figure 2.8.** (A) Schematic representation of the setup used for the fabrication of tungsten tips by electrochemical etching of a tungsten wire. (B) Scanning electron microscopy image of an electrochemically etched tungsten tip, adapted from reference [88].

Even with an appropriate selection of the tip potential ( $E_t$ ), faradaic currents (which are proportional to the area of the electrode) from a bare metal wire immersed in an electrolyte can easily be of the order of mA, while tunneling currents are typically of the order of nA. For this reason, the area of the tip exposed to the solution must be minimized, covering all but the very end of the tip with an insulating and chemically inert material. We have used polyethylene glue (ethyl-vinyl-acetate) from a polyethylene-glue gun or an electrophoretic paint. The latter was electrodeposited by applying a constant potential of 80 V between a Pt wire and the tungsten tip during 3 minutes, followed by baking the resulting coated tungsten tip in a furnace at 200 °C for 10 minutes.

A PicoLE Molecular Imaging STM with a PicoScan 2100 Controller was used for *in situ* STM experiments and a tunneling current of 2 nA was typically applied. The microscope head is placed on a platform suspended from four elastic bands and located inside an acoustically isolated chamber that sits on a second, *ca.* 200 kg heavy, platform pending from four steel

springs. An adequate mechanical and acoustic isolation is a critical element for achieving atomic resolution with the STM [89].

### 2.2.3.1. EC-STM cell

The EC-STM cell (Figure 2.9) has to be mechanically stable in order to obtain high-resolution images. The cell used by the Electrochemistry Group at the Institute of Physical Chemistry 'Rocasolano', made of Kel-F, has a central hole with an O-ring (Kalrez) that must be placed on top of the working electrode (a disk *ca.* 10 mm in diameter). A drop of the desired solution covering the electrode surface acts as supporting electrolyte, and two Pt wires immersed into the electrolyte serve as quasi-reference electrode and auxiliary electrode, respectively. The cell is suspended from three magnetic rods in the STM head, and the tip approaches the electrode surface from above (see Figure 2.7). The potentials of the sample ( $E_s$ ) and the tip ( $E_t$ ) are controlled independently with a bipotentiostat with respect to the reference electrode.

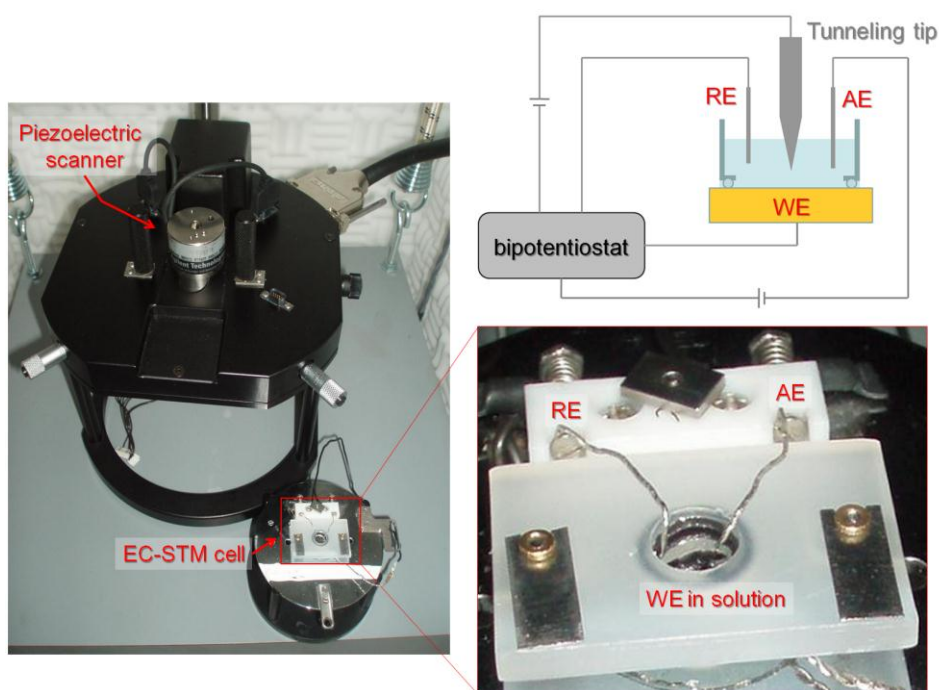


**Figure 2.9.** STM head (left) and EC-STM cell (bottom, right) used by the Electrochemistry Group at the Institute of Physical Chemistry 'Rocasolano'. The figure on the top-right corner shows a schematic representation of the EC-STM cell.



#### 2.2.4. *In situ* Fourier transform infrared spectroscopy

Infrared spectroscopy (IRS) is a powerful technique for studying adsorbed molecules at the solid/gas as well as the solid/liquid interfaces. The infrared radiation of structural and analytical interest covers the zone of the spectrum between 4000 and 600  $\text{cm}^{-1}$ , an energy that matches the separation between the vibrational levels of molecules.

IRS is a technique widely used by electrochemists to examine the electrode-electrolyte interface at the molecular level [90]. IRS involves the absorption of a fraction of the incident light by molecules present at the interface. Light may be absorbed when photons matching the energy corresponding to the separation between consecutive vibrational levels of a molecule interact with it, and an examination of the wavelengths at which absorption occurs and of the number of photons absorbed provides information about the different vibrational modes of the molecule and about the number of molecules present in the sample, respectively. IRS at electrochemical interfaces can be used to study species adsorbed at the electrode surface and species in a thin layer of solution adjacent to the electrode, yielding information on the chemical nature of the species present at the interface, on the adsorption site and the orientation of adsorbed molecules, and on the lateral interactions between adsorbates.

A usual observation in electrochemical IRS, due to the huge electric fields (*ca.*  $10^9 \text{ V m}^{-1}$ ) typically attained at the electrochemical double layer, is the variation of the absorption frequency of a band with the potential, often called the electrochemical Stark effect [91]. The Stark effect can be explained either by the potential-induced variations in the electronic density involved in the chemical bond between the surface and the adsorbed molecule, or by the interaction between the electric field at the interface and the dynamic dipole moment associated to the vibrational mode. It can be demonstrated that these two effects are one and the same thing, and cannot be separated from each other [91].

Polyatomic molecules containing  $N$  atoms will have  $3N$  degrees of freedom,  $(3N - 5)$  vibrational modes if they are linear and  $(3N - 6)$  vibrational modes if they are non-linear molecules. Stretching vibrations involve changes in the bond lengths and bending vibrations involve changes in the bond angles. Librational modes (wagging, twisting and rocking) appear in a spectral region well below the spectral range accessible with fluorite, Si or ZnSe windows. Selection rules [92] limit the observable vibrational transitions to those corresponding to vibrational modes with an associated dynamic dipole moment  $\neq 0$  that involve a transition between a vibrational quantum level and the immediately lower or upper levels ( $\Delta v = \pm 1$ ). The latter rule is based on the Born-Oppenheimer approximation, that assumes that the electronic and vibrational states are completely independent. Since this is not strictly true, harmonics corresponding to  $\Delta v = \pm 2$  or even higher can sometimes be

observed, although with much less intensity than the fundamental transition. The IR vibrational spectra of a molecule will be composed of the absorption bands corresponding to the vibrational modes allowed by the selection rules. Using the harmonic oscillator model, the vibrational frequency of a normal vibration mode of a molecule can be calculated by Equation 2.4, where  $\mu$  is the reduced mass and  $k$  the force constant of the oscillator (associated to the bond strength).

$$\nu = \frac{1}{2\pi} \sqrt{\frac{k}{\mu}} \quad (2.4)$$

In infrared reflection absorption spectroscopy (IRRAS) the spectrum is obtained by detecting the changes in the intensity of a beam reflected from a metallic surface as a consequence of the absorption of light by molecules present at the interface. For a description of IRRAS, it is desirable to outline the basic principles of the reflection of light from a surface.

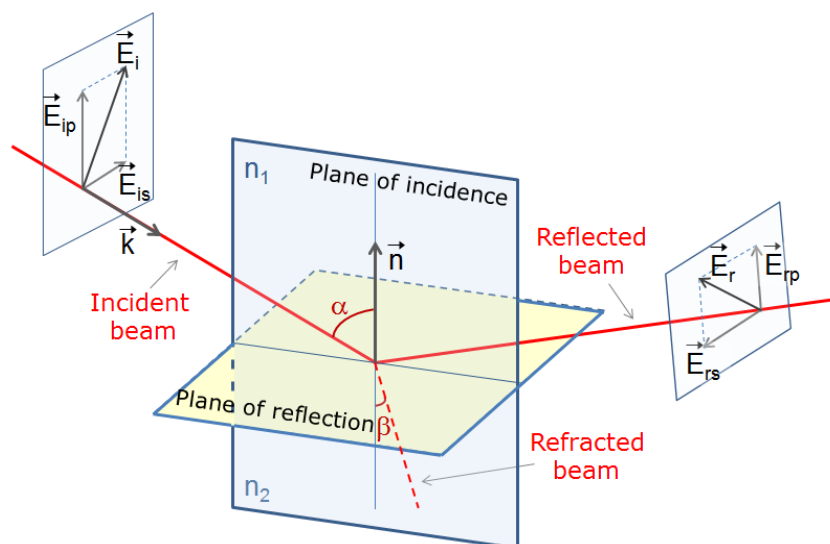


**Figure 2.10.** Schematic representation of an electromagnetic wave being reflected at the boundary between two homogeneous media of different refractive index.

When light is reflected at the surface separating two homogeneous, isotropic phases both the intensity and the state of polarization are affected [92]. Figure 2.10 shows a schematic representation of the reflection of an electromagnetic wave at the boundary between two homogeneous media of different refractive index.  $\vec{E}_i$  and  $\vec{E}_r$  are the electric field vectors of the incident and the reflected waves, respectively. They oscillate perpendicularly to the direction of propagation, that is parallel to the wave vector  $\vec{k}$ . The

latter, together with the unit vector  $\vec{n}$  perpendicular to the plane of reflection, define the plane of incidence. The electric field vectors can be decomposed into two mutually perpendicular components:  $\vec{E}_p$  (p-polarization), which lies in the plane of incidence, and  $\vec{E}_s$  (s-polarization), which is perpendicular to the plane of incidence (see Figure 2.10).

The amplitude and the phase angles of the s- and p-polarized components of the radiation can change upon reflection, as shown by Fresnel equations (2.5 and 2.6).

$$E_{rp} = -E_{ip} \frac{\operatorname{tg}(\alpha - \beta)}{\operatorname{tg}(\alpha + \beta)} \quad (2.5)$$

$$E_{rs} = -E_{is} \frac{\sin(\alpha - \beta)}{\sin(\alpha + \beta)} \quad (2.6)$$

The angle of refraction ( $\beta$ ) depends on the angle of incidence ( $\alpha$ ) and on the refractive indices of the two phases ( $n_1$  and  $n_2$ , respectively), and can be calculated using Snell's law (Equation 2.7).

$$n_1 \sin \alpha = n_2 \sin \beta \quad (2.7)$$

For highly reflecting surfaces, the changes in phase angle are 0 for the component of the electric field oscillating perpendicular to the surface and  $\pi$  for the component of the electric field oscillating parallel to the surface, *i.e.*, at the surface, the incident and reflected waves tend to cancel out for s-polarization and for the component of the p-polarized beam parallel to the surface, while both waves add in phase for the component of the p-polarized light perpendicular to the surface. As a consequence, for adsorbed species, only the excitation of vibrational modes whose associated dynamic dipole moment has a non-zero component perpendicular to the surface is possible. This restriction constitutes the surface selection rule for IRRAS [92,93], a consequence of which is that p-polarized light probes both solution and adsorbed species, while s-polarized light only probes solution species (which are randomly oriented). Therefore, we can distinguish between the contribution from solution and adsorbed molecules by comparing spectra obtained using p- and s-polarized infrared light.

A second consequence is that the intensity of the reflected s-(p-)polarized infrared beam increases (decreases) exponentially with the distance from the surface until its value in the bulk phase, a consequence of which is that, for solution species present in a thin layer of electrolyte adjacent to the surface, the absorption bands are also more intense when p-polarized light is used.

A third consequence is that, on highly reflecting surfaces, while the intensity of the stationary electric field on the surface is always null for s-polarized light, it increases with the angle of incidence for p-polarized light, following the increase of its component perpendicular to the electrode surface with increasing angle of incidence. The angle of incidence becomes thus a critical parameter in IRRAS. The intensity of the stationary electric field (normalized to the amplitude of the electric field of the incident beam) generated at the electrode surface upon reflection of an IR beam shows a maximum, for p-polarization at an angle of incidence of *ca.* 88° [92]. Taking into account that the absorption intensity is given by the product between the amplitude of the electric field and the dynamic dipole moment of the vibrational mode, this is the most adequate value of the angle of incidence, and is indeed the one used at the gas-metal interface or at the metal-UHV interface. However, in electrochemical environments the angle of incidence must be below the critical angle of the window-electrolyte interface ( $\mathcal{G}_c$ ), *i.e.*, the angle of incidence at which light, when going from an optically more dense medium (phase 2, refractive index  $n_2$ ) to an optically less dense medium (phase 1, refractive index  $n_1$ ,  $n_1 > n_2$ ) is totally reflected.  $\mathcal{G}_c$  is given by Equation 2.8.

$$\mathcal{G}_c = \arcsin \frac{n_2}{n_1} \quad (2.8)$$

The refractive index of fluorite ( $n_2$ ) is 1.40 at 2000  $\text{cm}^{-1}$ , and that of water ( $n_1$ ) is 1.26 at 2000  $\text{cm}^{-1}$ , yielding a critical angle at the fluorite/water interface at 2000  $\text{cm}^{-1}$  of *ca.* 64°.

If using a flat window, the angle of incidence at the air-window interface must be as close as possible to the Brewster angle,  $\theta_B$ , which is given by Equation 2.9, and is the angle at which p-polarized light will not be reflected when closing the interface from a less to a more optically dense medium, the reflected light being entirely s-polarized.

$$\theta_B = \arctan \frac{n_1}{n_2} \quad (2.9)$$

The Brewster angle for the air ( $n_2 = 1.0$ )/fluorite interface is *ca.* 54° at 2000  $\text{cm}^{-1}$ . If this angle is used with a flat fluorite window, the angle of incidence at the electrode/electrolyte interface would be, at 2000  $\text{cm}^{-1}$ , *ca.* 40°, at which the gain in the signal-to-noise ratio achieved by maximizing the transmission of p-polarized light at the air/fluorite interface is cancelled by the low value of the stationary electric field at the electrode surface. The best signal-to-noise ratio with a flat fluorite window is achieved at an

incidence angle at the air-fluorite interface of  $68^\circ$ , for which the angle of incidence at the electrode-electrolyte interface, at  $2000\text{ cm}^{-1}$ , is of *ca.*  $50^\circ$ .

The system can be improved using a triangular fluorite window. In this case, if the IR beam comes into contact with one of the prism faces at normal incidence, it will come out of the prism through one of the adjacent faces with an angle of incidence that will coincide with the angle formed by the faces. The optimum experimental set up would, hence, consist of an isosceles triangular prism with the two equal angles slightly lower than the critical angle, attached to the bottom of the spectroelectrochemical cell. The practical assembly makes use of an equilateral triangular prism. Using this configuration, the angle of incidence at the electrode/electrolyte interface is, at  $2000\text{ cm}^{-1}$ , *ca.*  $74^\circ$ . In addition, since both the incident and reflected beams reach the air/fluorite interface at normal incidence, energy losses due to reflection are minimized.

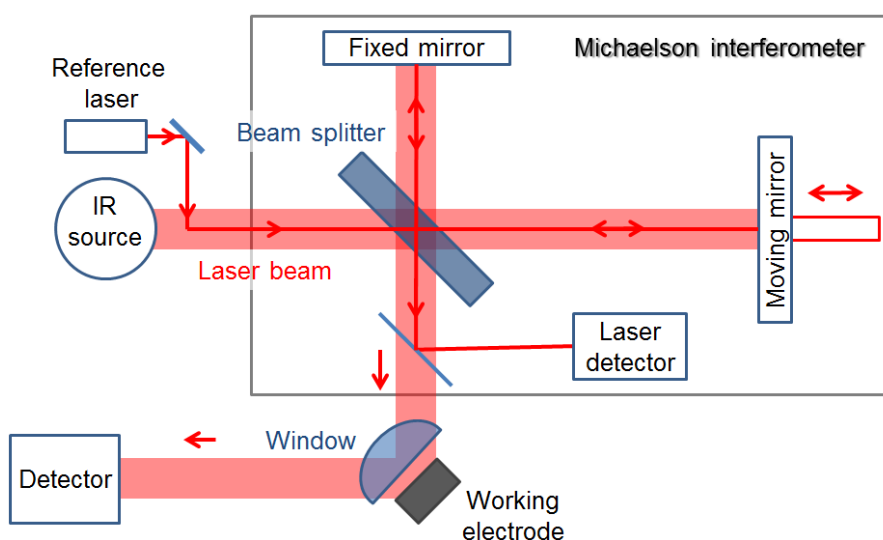


**Figure 2.11.** Schematic representation of an *in situ* FTIR spectrometer. Adapted from reference [94].

Fourier transform infrared spectroscopy (FTIRS) uses an interferometer [94] instead of a monochromator. The interferometer consists, briefly, of a beam splitter, a fixed mirror and a mobile mirror. IR radiation is sent from the source to the beam splitter, that divides the beam into two ideally identical beams, each one of which is sent to one of the mirrors, that reflects it back to the beam splitter and to the detector (see Figure 2.11). Depending on the position of the mobile mirror, the reflected beams will interfere constructively or destructively at the beam splitter.

A plot of the intensity of the radiation that reaches the detector as a function of the position of the mobile mirror is called an interferogram, and typically has a central maximum, the intensity decreasing very quickly (although with oscillations) and symmetrically at both sides. The interferogram can be mathematically expressed by Equation 2.10, where  $I(\bar{\nu})$  is the light intensity as a function of the wavenumber  $\bar{\nu}$ , *i.e.*, the searched-for spectrum.

$$F(x) = \int_0^{+\infty} I(\bar{\nu}) \cos(2\pi x \bar{\nu}) d\bar{\nu} \quad (2.10)$$

By applying the Fourier-transform the spectrum can be obtained:

$$I(\bar{\nu}) = \int_{-\infty}^{+\infty} F(x) \cos(2\pi \bar{\nu} x) dx \quad (2.11)$$

To maximize the signal to noise ratio each spectrum is typically obtained from the addition of several interferograms: noise (which is a random fluctuation) is cancelled with consecutive additions, while the signal increases with the number of added interferograms.

The main obstacle when working in electrochemical environments is the strong absorption of IR light by water. In order to overcome this difficulty, the distance that the infrared beam has to travel across the electrolyte must be minimized. In the external reflection approach this is achieved by trapping a thin layer of electrolyte (1-25  $\mu\text{m}$ ) between the working electrode and the IR transparent window, commonly a fluorite prism, by pressing the electrode surface against the prism. This introduces some problems, the most important ones being (i) that diffusion from the electrolyte into the thin layer is severely hindered and (ii) that the thin layer has a high resistance, provoking large ohmic (*IR*) drops when a current flows and a very large time constant of the cell (*RC*), that severely limits the time resolution of the experiments. An additional obvious problem is that, even if the thickness of the thin layer were homogeneous, non-homogeneous current distributions result.

Each IR spectrum from the electrochemical interface is usually obtained from the difference between two spectra, in order to cancel the bands corresponding to the solvent and other species whose concentration does not change during the experiment, and that would otherwise obscure the bands corresponding to the species of interest. The intensity of the bands can be given as the relative variation of reflectance (Equation 2.12) or as absorbance (Equation 2.13).

$$\frac{\Delta R}{R} = \frac{R_s - R_r}{R_r} = \frac{R_s}{R_r} - 1 \quad (2.12)$$

$$Abs. = -\log\left(\frac{R_s}{R_r}\right) \quad (2.13)$$

where  $R_s$  and  $R_r$  are the intensities of the radiation reflected from the surface in the sample and the reference spectrum, respectively. According to Equation 2.13, positive absorption bands correspond to species present at the interface when the sample spectrum was recorded and absent when the reference spectrum was recorded, while negative absorption bands correspond to species present at the interface when the reference spectrum was recorded and absent when the sample spectrum was recorded. Bipolar bands would correspond to species present in both the sample and reference spectra, but whose frequency changed due to potential and/or coverage variations.

The experiments reported here were carried out in a *Perkin Elmer 1725X* spectrophotometer, using a homemade reflectance accessory and a homemade spectroelectrochemical cell, described in next section.

#### 2.2.4.1. Spectroelectrochemical cell

The *in situ* IR experiments discussed in this work were performed in a three-electrode spectroelectrochemical cell made of Teflon, which has a central body connected to a Teflon square piece at the bottom that is attached to the fluorite equilateral triangular prism. There is a tube that allows the bubbling of  $N_2$  and another tube that leads the gases out of the cell. The reference and the auxiliary electrodes are introduced through small holes at the sides of the central tube. The working electrode holder is a Teflon rod that fits in the central tube and is used to push the electrode against the  $CaF_2$  window, leaving a thin film of electrolyte between the two surfaces (thin layer configuration). The spectroelectrochemical cell is placed in a *Perkin Elmer 1725X FT-IR* spectrometer equipped with a liquid-nitrogen-cooled narrow-band mercury-cadmium-telluride (MCT) detector. Each spectrum typically consisted of 100 interferograms, collected with a spectral resolution of  $8\text{ cm}^{-1}$ .

## 2.3. Reagents and solutions

All the solutions were prepared using ultrapure water (18 M $\Omega$ , 2-4 ppb TOC) from a Milli-Q Gradient A-10 water purification system fed with deionized water produced by a Rios-5 reverse osmosis unit, both from Millipore.

Cyanide-modified Pt(111) electrodes were prepared by immersion of a clean and well-ordered Pt(111) surface in a 0.1 M KCN (Merck, p.a.) or a 0.1 M NaCN (Sigma-Aldrich, p.a.) solution for approximately 3 min, after which the electrode was rinsed with ultrapure water and transferred to the electrochemical or spectroelectrochemical cell containing the cyanide-free solutions.

0.1 M H<sub>2</sub>SO<sub>4</sub> and 0.1 M HClO<sub>4</sub> solutions were prepared using ultrapure water and concentrated H<sub>2</sub>SO<sub>4</sub> (Merck, Suprapure) or HClO<sub>4</sub> (Merck, p.a.), respectively.

NO-saturated adlayers were prepared *ex situ* by immersion of the clean and well-ordered Pt(111) electrode in a 0.1 M HClO<sub>4</sub> solution containing 0.01 M KNO<sub>2</sub> (Merck, p.a.) for 3 min. Applying the same procedure to a cyanide-modified Pt(111) electrode yielded mixed CN-NO adlayers. After formation of the NO adlayer, the electrode was rinsed with ultrapure water and transferred to the electrochemical or spectroelectrochemical cell containing 0.1 M HClO<sub>4</sub>.

Oxygen reduction reaction experiments were performed in 0.1 M HClO<sub>4</sub>, 0.05 M H<sub>2</sub>SO<sub>4</sub> (both EMD), 0.05 M H<sub>3</sub>PO<sub>4</sub> and 0.1 M KOH (both Sigma-Aldrich) solutions. In these experiments, the electrode was immersed at 0.27 V vs. RHE in a solution saturated with oxygen. After five cycles between 0.07 V and 1.05 V the polarization curve for the ORR was recorded. Then, oxygen was purged out of the solution and the voltammetric response was recorded in argon-purged solutions.

Formic acid was supplied by Fluka (88-91%, puriss. p.a.). LiClO<sub>4</sub>, Na<sub>2</sub>SO<sub>4</sub>, KClO<sub>4</sub>, K<sub>2</sub>SO<sub>4</sub>, CsClO<sub>4</sub> and Cs<sub>2</sub>SO<sub>4</sub> (p.a.) were supplied by Sigma-Aldrich. High-purity KClO<sub>4</sub> was obtained by recrystallization of commercial KClO<sub>4</sub>: a flask containing 500 mL of ultrapure water and 13.9 g of KClO<sub>4</sub> was heated on a hot plate until complete dissolution of the salt, and was then allowed to cool slowly to room temperature. The supernatant liquid was decanted, and the precipitated KClO<sub>4</sub> crystals were rinsed with ultrapure water and dried overnight in an oven at 80–100 °C. CuSO<sub>4</sub> was supplied by Merck (p.a.) and aniline by Sigma-Aldrich (ACS).

The auxiliary electrode was a platinum wire. Either a reversible hydrogen electrode (RHE) (CV and FTIR experiments), or a platinum wire (STM experiments) was used as reference or quasi-reference electrodes, respectively. All the potentials in the text are referred to the RHE.



## 2.4. Theoretical calculations

Quantum mechanical properties of many-atoms systems may be obtained by solving the Schrödinger equation, but, due to their complexity, approximations must be introduced for most systems. Probably the most popular of them is density-functional theory (DFT), which was formulated by Hohenberg and Kohn [95] in 1964, and is a powerful tool widely used by physicists and chemists to study the electronic structure of many-body systems. Kohn was awarded by the Chemistry Nobel Prize in 1998 [96] for his contributions to this field.

DFT may be employed to describe the total energy of many-atoms systems by using energy functionals of the electron density. This method replaces the N-electron wave function and the associated Schrödinger equation by a formulation based on the simpler electron density,  $\rho(r)$ , *i.e.*, the number of electrons per unit volume in a given state, to obtain the ground state energy (the lowest-energy state) of a given system.

### 2.4.1. Methodology

Theoretical calculations for the ( $2\sqrt{3} \times 2\sqrt{3}$ ) Pt(111) slab were performed using three platinum layers. The bottom two were kept fixed at the next-neighbor distance corresponding to the Pt bulk (calculated to be 4.00 Å in agreement with the experimental value, 3.92 Å [97]) and the top layer was allowed to relax. The calculated surface energy ( $\sigma$ ) and work function ( $\Phi$ ) were only 0.03 eV and 0.06 eV smaller, respectively, when four layers were used instead of three, as can be seen in table 2.1.

**Table 2.1.** Values of the surface energy and of the work function of the Pt fcc(111) surface calculated using different numbers of layers.

Number of layers	$\sigma$ (eV)	$\Phi$ (eV)
2	0.65	5.72
3	0.66	5.80
4	0.63	5.74
5	0.64	5.72
6	0.63	5.76

Smaller unit cells were computed for DFT calculations involving CN adsorbed on Pt(111) adopting different configurations ( $\theta_{\text{CN}}$  between 0.25 and 1). The adsorption of hydrogen was studied using DFT on Pt(111) and on Pt(111) with various CN coverages in different configurations. Convergence was considered to be achieved when the total forces were less than 0.01 eV/Å.

The calculations were performed with DACAPO [98], a total energy program based on DFT code. The electron-ion interactions were accounted for through ultrasoft pseudopotentials [99], while the valence electrons were treated within the generalized gradient approximation (GGA) in the version of Perdew and Wang [100,101]. Special care was taken for the parametrization of the energy cutoff and the k-points sampling of the Brillouin zone based on the Monkhorst-Pack grid [102]. Both parameters were increased systematically in a Pt bulk system with the optimized lattice constant until the change in the absolute energy was less than 20 meV. An energy cutoff of 400 eV and a grid of 12 x 12 x 12 satisfy the energy accuracy.





## Chapter 3

# Cyanide-modified platinum surfaces: structure and stability

### 3.1. Introduction

The adsorption of cyanide on single-crystal platinum electrodes has been intensively investigated over the last two decades, partly because cyanide and carbon monoxide are isoelectronic [6-14,38,103], but also because adsorbed cyanide is the main strongly adsorbed intermediate generated during the oxidation of amines [104] and amino acids [105,106] on Pt.

Voltammetric and spectroscopic studies show that cyanide is irreversibly adsorbed on Pt single-crystal electrodes. Adsorption of cyanide is extremely sensitive to the surface structure of Pt, the cyanide adlayer being very stable on Pt(111) in acidic solutions in a wide range of potentials [10-14], while on Pt(100) and Pt(110) it is only stable in a narrow potential region [11]. The adsorption of cyanide on Pt(111) single-crystal electrodes is particularly interesting, due to the spontaneous formation, upon immersion of Pt(111) in a cyanide-containing solution, of an ordered  $(2\sqrt{3} \times 2\sqrt{3})R30^\circ$  structure composed of hexagonally packed hexagons, each of them containing six  $CN_{ads}$  groups adsorbed *on top* of a hexagon of Pt surface atoms surrounding a free Pt atom.

Although many fundamental studies of the adsorption of cyanide on Pt single-crystal surfaces have been performed in the last two decades, more experimental and theoretical studies concerning the spatial and electronic structure, as well as the stability of cyanide-modified Pt(111) surfaces, are needed due to the interest of employing this system to study atomic ensemble effects in electrocatalysis [31] and as a template to fabricate periodic nanostructures on surfaces.

This chapter presents a broad, combined theoretical and experimental study, which tries to understand more deeply the structure of adsorbed cyanide on Pt(111) electrodes and the adsorption phenomena occurring on these chemically-modified surfaces, as well as some preliminary voltammetric results on the adsorption of cyanide on polycrystalline Pt electrodes.

## 3.2. Cyanide-modified Pt(111) electrodes

Cyanide adsorbs spontaneously and irreversibly on Pt(111) electrodes forming an ordered  $(2\sqrt{3} \times 2\sqrt{3})R30^\circ$  structure [5-7], which extends over the whole electrode surface, as represented in Figure 3.1. This structure was observed for the first time using LEED by Hubbard and co-workers [5], who demonstrated that the  $(2\sqrt{3} \times 2\sqrt{3})R30^\circ$  structure formed by adsorbed cyanide on Pt(111) resists electrode emersion and transfer into an UHV chamber. The atomic, real space structure could be later elucidated by electrochemical STM [6,7].

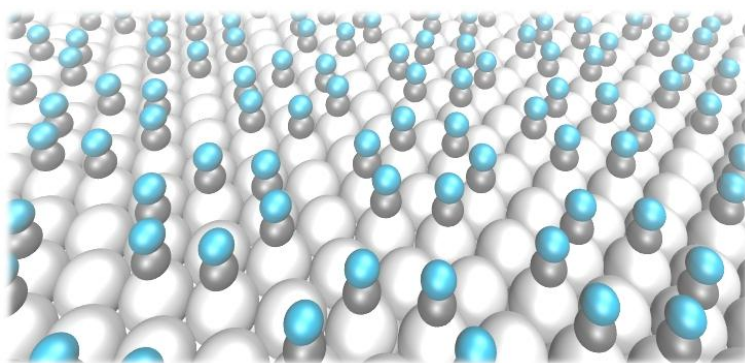


**Figure 3.1.** Three dimensional view of a cyanide-modified Pt(111) surface. Cyanide hexagons are formed by six cyanide groups adsorbed through its carbon end (dark grey balls), with the nitrogen atom (blue balls) facing the solution side.

### 3.2.1. Cyclic voltammetry, FTIRS and EC-STM investigations

Cyanide adsorption on Pt(111) in acidic solutions has been intensively studied by Huerta *et al.* [10-14] by means of cyclic voltammetry and spectroscopic techniques. They have shown that the cyanide adlayer on Pt(111) is remarkably stable, no change being observed in the CVs of the cyanide-covered electrode upon repetitive cycling between 0.05 V

and 1.00 V. Adsorption of hydrogen on Pt(111) in sulphuric acid solutions (Figure 3.2) between 0.05 V and 0.35 V (historically denoted as underpotential deposited hydrogen,  $H^+ + e^- = H_{\text{upd}}$ , *i.e.*, hydrogen adsorbed at potentials more positive than the equilibrium potential for the hydrogen evolution reaction) is followed first by adsorption of (bi)sulphate anions between 0.35 and 0.60 V, then by a so-called double layer region and, finally, by a small pseudocapacitance between 0.70 V and 1.00 V that corresponds to OH adsorption [107]. In contrast, on cyanide-modified Pt(111), both in sulphuric acid (Figure 3.2) and in perchloric acid solutions (Figure 3.3), a broad feature between 0.10 V and 0.60 V is followed by the double layer charging region from 0.60 V to 0.80 V and by a Nernstian process at approximately 0.90 V that has been suggested to correspond to the adsorption of OH or other oxygenated species [11]. Based on all the previous observations, Huerta *et al.* [10] suggested that the cyanide-covered Pt(111) could be considered as a chemically-modified electrode. Furthermore, as can be observed in Figures 3.2 and 3.3, CVs of cyanide-modified Pt(111) in  $HClO_4$  and in  $H_2SO_4$  solutions are qualitatively very similar. This is an indication of the insensitivity of the chemically-modified surface to the anions present in the supporting electrolyte, *i.e.*, adsorbed cyanide acts as a third-body which selectively blocks the sites necessary for the adsorption of tetrahedral anions, such as sulphate, on Pt, but leaves unaffected the CN-free Pt atoms onto which OH [14] or CO [103] can adsorb.

The double layer-corrected voltammetric charge in the hydrogen adsorption region of a cyanide-modified Pt(111) electrode (from the onset of hydrogen adsorption to 0.1 V) amounts to *ca.*  $80 \mu\text{C cm}^{-2}$ , which is the charge expected for the adsorption of atomic hydrogen on two thirds of the Pt atoms left free upon modification of the Pt(111) electrode with cyanide, in very good agreement with Huerta *et al.* [11], who suggested that adsorbed cyanide blocks only some of the sites available for hydrogen adsorption. Interestingly, as can be observed in Figures 3.2 and 3.3, the hydrogen adsorption region is shifted positively by *ca.* 0.20 V and the OH adsorption region is shifted positively by *ca.* 0.25 V with respect to unmodified Pt(111) electrodes. This implies that  $\Delta G_0$  of  $H_{\text{upd}}$  ( $\theta_H = 0$ ) is *ca.*  $19 \text{ kJ mol}^{-1}$  more negative, and  $\Delta G_0$  of  $OH_{\text{ads}}$  ( $\theta_{OH} = 0$ ) *ca.*  $24 \text{ kJ mol}^{-1}$  more positive, than on Pt(111). Furthermore, and since hydrogen adsorption extends over a potential region that is *ca.* 1.5 times larger for the cyanide-modified Pt(111) electrode than for the clean Pt(111), the repulsions between the adsorbed hydrogen atoms must be *ca.* 1.5 times larger in the former than in the latter case. Although this could be taken as an indication of a modification of the electronic structure of the free Pt atoms in the cyanide-modified Pt(111) structure, we will show below that this is not the case.

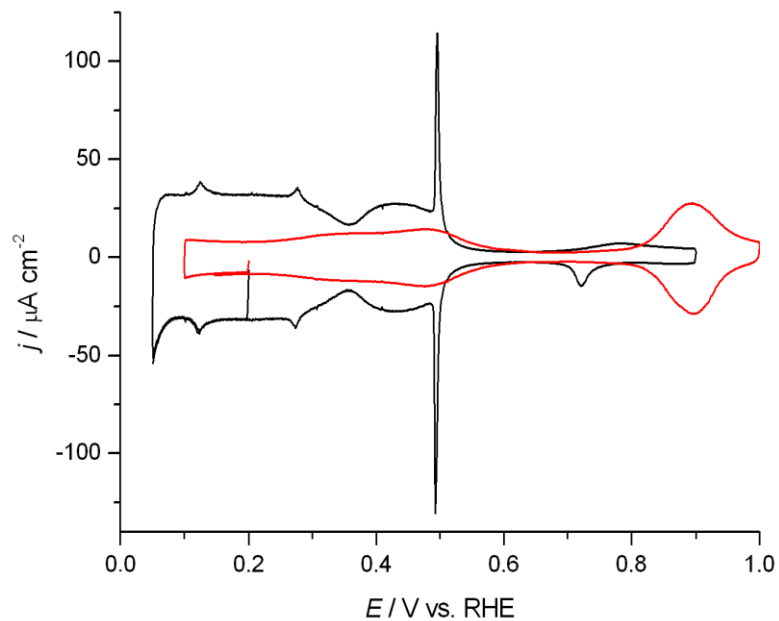


**Figure 3.2.** Cyclic voltammogram at  $50 \text{ mV s}^{-1}$  of Pt(111) (black) and of cyanide-modified Pt(111) (red) in  $0.1 \text{ M H}_2\text{SO}_4$ .

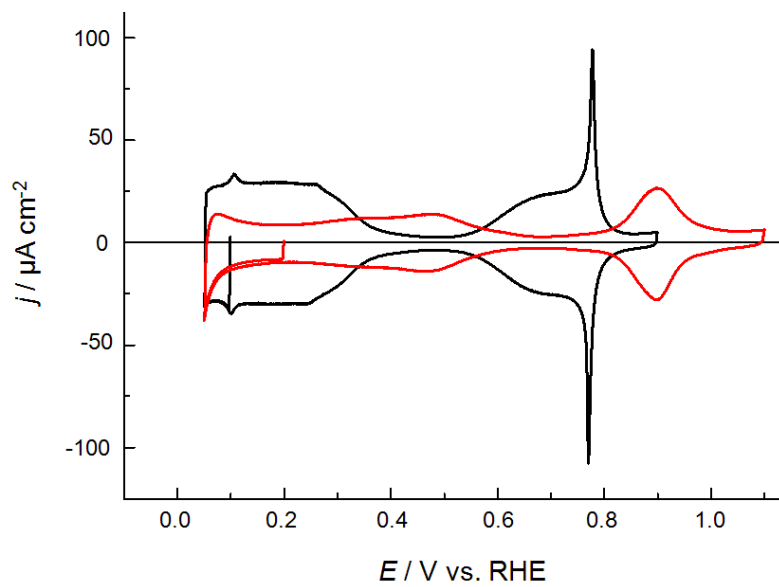


**Figure 3.3.** Cyclic voltammogram at  $50 \text{ mV s}^{-1}$  of Pt(111) (black) and of cyanide-modified Pt(111) (red) in  $0.1 \text{ M HClO}_4$ .



The shift in the onset of hydrogen adsorption can be explained by the formation in the  $H_{\text{upd}}$  region of adsorbed isocyanide,  $\text{CNH}_{\text{ads}}$ , instead of  $H_{\text{ads}}$  directly bonded to the Pt atoms. This idea had been already proposed by Schardt *et al.* [108], who suggested that the  $\text{CNH}_{\text{ads}}$  adlayer behaves as a polyprotic acid. The formation of  $(\text{CN}_{\text{ads}})_x\text{-H}$  (with  $x$  decreasing with decreasing potential within the H adsorption region) corresponding to  $(\text{CN}_{\text{ads}})_x\text{-H}$  stoichiometries with particular stabilities would explain all the previous experimental facts. As illustrated in Figure 3.4, the charge density at the broad peak at 0.48 V in the  $H_{\text{upd}}$  region is ca.  $20 \mu\text{C cm}^{-2}$  ( $\theta_{\text{CNH}} = 1/6^{\text{th}} \text{ ML}$ )<sup>2</sup>, which might correspond to a stoichiometry  $(\text{CN}_{\text{ads}})_6\text{-H}$ . The minimum of current density at ca. 0.40 V corresponds to a charge density about  $32 \mu\text{C cm}^{-2}$  ( $\theta_{\text{CNH}} = 0.25 \text{ ML}$ ), coinciding with the charge expected for the formation of  $(\text{CN}_{\text{ads}})_4\text{-H}$ . Finally, at 0.37 V and ca. 0.20 V, the charge densities are  $40 \mu\text{C cm}^{-2}$  ( $\theta_{\text{CNH}} = 1/3^{\text{rd}} \text{ ML}$ ) and  $64 \mu\text{C cm}^{-2}$  ( $\theta_{\text{CNH}} = 0.5 \text{ ML}$ ), respectively. The former might correspond to a  $(\text{CN}_{\text{ads}})_3\text{-H}$  stoichiometry (honeycomb structure), and the latter to a  $(\text{CN}_{\text{ads}})_2\text{-H}$  stoichiometry (kagome structure).

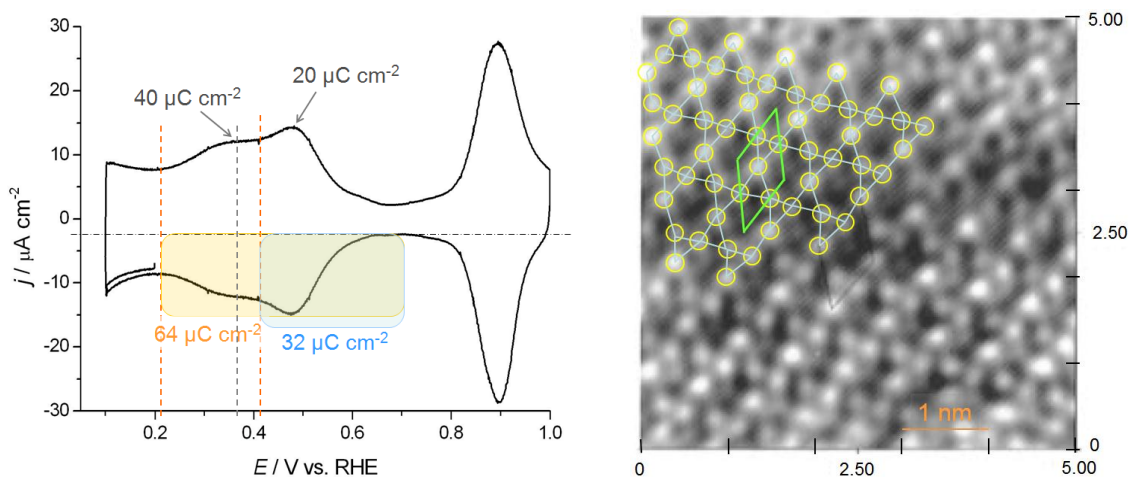


**Figure 3.4.** Left: Cyclic voltammogram at  $50 \text{ mV s}^{-1}$  of CN-modified Pt(111) in  $0.1 \text{ M HClO}_4$ . Right:  $5 \times 5 \text{ nm}^2$  STM image obtained at  $0.3 \text{ V}$ , adapted from reference [9]. The image can be interpreted as a kagome structure corresponding to a  $(\text{CN}_{\text{ads}})_2\text{-H}$  stoichiometry.

<sup>2</sup> The charge for a full monolayer on a Pt(111) surface for a process involving one electron transfer per Pt atom is  $Q_{\text{Pt}} = eN_{\text{Pt}} = 240 \mu\text{C} \cdot \text{cm}^{-2}$ . Since the coverage of  $\text{CN}_{\text{ads}}$  is 0.5, the charge for 1 ML of  $\text{CNH}_{\text{ads}}$  would correspond to  $120 \mu\text{C cm}^{-2}$ .

Itaya and co-workers [7] attributed the STM images of a cyanide-modified Pt(111) electrode obtained at 0.30 V vs. RHE (well within the  $H_{\text{upd}}$  region) in perchloric acid solutions to a  $(\sqrt{7} \times \sqrt{7})R19^\circ$  structure, but this is in contradiction with the absence in the cyclic voltammogram of any feature indicating a phase transition, as would be expected for a change from a long-range ordered  $(2\sqrt{3} \times 2\sqrt{3})R30^\circ$  structure to a long-range ordered  $(\sqrt{7} \times \sqrt{7})R19^\circ$  structure. As shown in Figure 3.4, right, the structure found by Itaya and co-workers can also be interpreted as a kagome structure with a  $(2\sqrt{3} \times 2\sqrt{3})R30^\circ$  unit cell, in excellent agreement with our analysis above, based on the charge density measured in the corresponding CV.

It must be noted that, as can be observed in Figure 3.3, hydrogen evolution does not seem to be affected by the presence of  $\text{CN}_{\text{ads}}$  on cyanide-modified Pt(111) electrodes. *On-top* sites, thought to be the active ones in the evolution of  $\text{H}_2$  on Pt(111) electrodes, are perfectly available on cyanide-modified Pt(111). If these sites remain electronically unaltered, hydrogen evolution would be expected to coincide on both Pt(111) and cyanide-modified Pt(111) electrodes, as in Figure 3.3. On the other hand, the weakening of the  $\text{Pt-OH}_{\text{ads}}$  bond may be understood as being due to electrostatic through-space repulsive interactions between the electronegative  $\text{CN}_{\text{ads}}$  adlayer and the large dipole moment associated with  $\text{OH}_{\text{ads}}$ .

In contrast to acidic solutions, in 0.1 M KOH (Figure 3.5) the onset of hydrogen adsorption is shifted negatively *ca.* 0.20 V while there is essentially no change in the peak position of adsorbed OH. It can also be observed that the coverage of adsorbed H has decreased significantly in alkaline solution as compared to acidic media.

The results found in KOH solutions are probably due to the presence of a high concentration of  $\text{K}^+$ , and may be interpreted in terms of non-covalent interactions between the solvated potassium cation and the adsorbed CN. The effect of non-covalent interactions between hydrated metal cations ( $\text{M}^+$ ) and adsorbed OH has been recently discussed for the methanol oxidation and oxygen reduction reactions [68], and the consequent formation of  $\text{M}^+(\text{H}_2\text{O})_x\text{-OH}_{\text{ads}}$  clusters has been shown to inhibit the access of reactants to the surface during these electrocatalytic reactions [68]. In the case of cyanide-modified Pt(111) surfaces, a possible explanation for the decrease of the charge in the  $H_{\text{upd}}$  region in alkaline solutions could accordingly be the formation of  $\text{K}^+(\text{H}_2\text{O})_x\text{-CN}_{\text{ads}}$  clusters by electrostatic interactions between the electronegative  $\text{CN}_{\text{ads}}$  adlayer and hydrated  $\text{K}^+$ , that would act as site blockers for the formation of the  $H_{\text{upd}}$  adlayer. Cyclic voltammetry (Figure 3.5) indicates that the process is very reversible, *i.e.*, the negative shift is due to a thermodynamic effect. The variation of the potential of zero charge ( $E_{\text{pzc}}$ ) with solution pH, as found by Ramírez *et al.* [109] with self-assembled mercaptoalkanoic acid monolayers deposited on Au(111) could explain this potential shift. If this were the case, a plot of the  $E_{\text{pzc}}$  vs. pH would be equivalent

to a titration curve of the cyanide-modified Pt(111) surface, and would allow the determination of the  $pK_a$  of the cyanide adlayer.

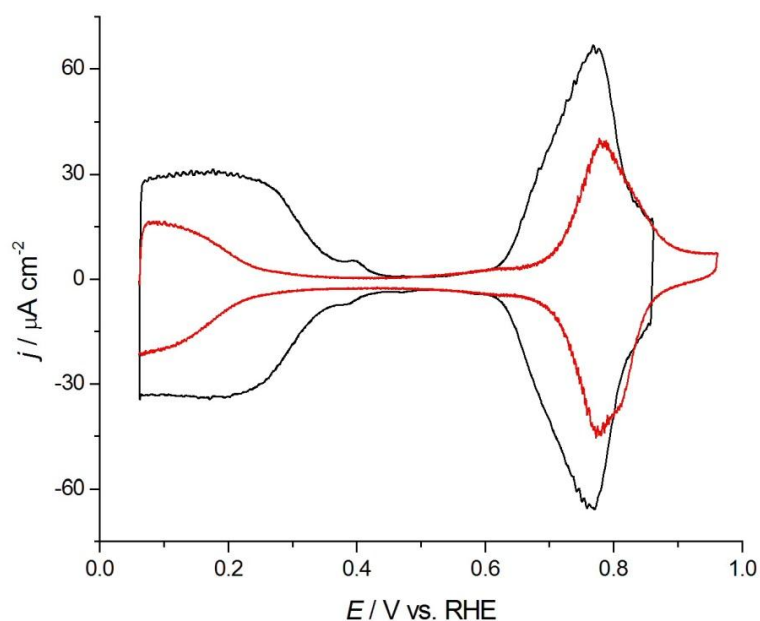


**Figure 3.5.** Cyclic voltammogram at  $50 \text{ mV s}^{-1}$  of Pt(111) (black) and of cyanide-modified Pt(111) (red) in  $0.1 \text{ M KOH}$ .

The IR spectra of cyanide adsorbed on Pt(111) electrodes has been intensively studied both in acidic [10,11] and in alkaline solutions [6,9,110,111]. The spectra show a single vibrational band corresponding to the stretching vibration of a CN group adsorbed *on-top* of a platinum atom through its carbon atom [6,9-11]. Our FTIR spectra show that, in perchloric acid solutions, the frequency of the stretching vibration of the CN band increases with potential from  $2085 \text{ cm}^{-1}$  at  $0.10 \text{ V}$  to  $2123 \text{ cm}^{-1}$  at  $1.10 \text{ V}$ . Figure 3.6 shows the potential dependence of the stretching frequency of CN adsorbed *on-top* ( $\text{CN}_L$ ) on the cyanide-modified Pt(111) electrode.

As can be observed, the plot of the  $\text{CN}_L$  band of cyanide-modified Pt(111) shows two clearly different slopes: at  $E \leq 0.5 \text{ V}$  the  $\text{CN}_L$  stretching frequency increases with potential with a slope of  $82 \text{ cm}^{-1} \text{ V}^{-1}$ , this being significantly smaller than that of ca.  $100 \text{ cm}^{-1} \text{ V}^{-1}$  reported by Huerta *et al.* [10,11], while for  $E \geq 0.60 \text{ V}$  the slope is  $25 \text{ cm}^{-1} \text{ V}^{-1}$  in good agreement with the literature [10,11]. Some authors have attributed this change in the Stark tuning rate to a change from N-bound CN at  $E \leq 0.50 \text{ V}$  to C-bound CN at  $E > 0.50 \text{ V}$  [10,11,112], and this assignment was supported by theoretical calculations of Pt-CN<sup>-</sup> and Pt-

NC<sup>-</sup> vibrational systems [113,114]. On the contrary, Paulissen and Korzeniewski suggested that the changes in the Stark tuning rate correspond to the conversion from Pt-CN to Pt-CNH species [8]. Naturally, due to bond order conservation, the adsorption of hydrogen on the nitrogen atoms of adsorbed cyanide should weaken the carbon-nitrogen bond and, hence, provoke a decrease in the corresponding C-N stretching frequency. A comparison with the CV of the cyanide-modified Pt(111) electrode (Figures 3.2 and 3.3) strongly suggests that the high slope at  $E \leq 0.50$  V must be due to the presence of adsorbed hydrogen on the nitrogen atoms of adsorbed cyanide. Therefore, our hypothesis is that, over the whole frequency range between 2085 and 2123  $\text{cm}^{-1}$ , the band corresponds to C-bound CN adsorbed on-top on Pt(111), and that the change in the Stark tuning rate of the CN stretching frequency at ca. 0.50 V, coinciding with the onset of hydrogen adsorption in the cyclic voltammogram, can be explained by the formation of  $(\text{CN}_{\text{ads}})_x\text{-H}$ .

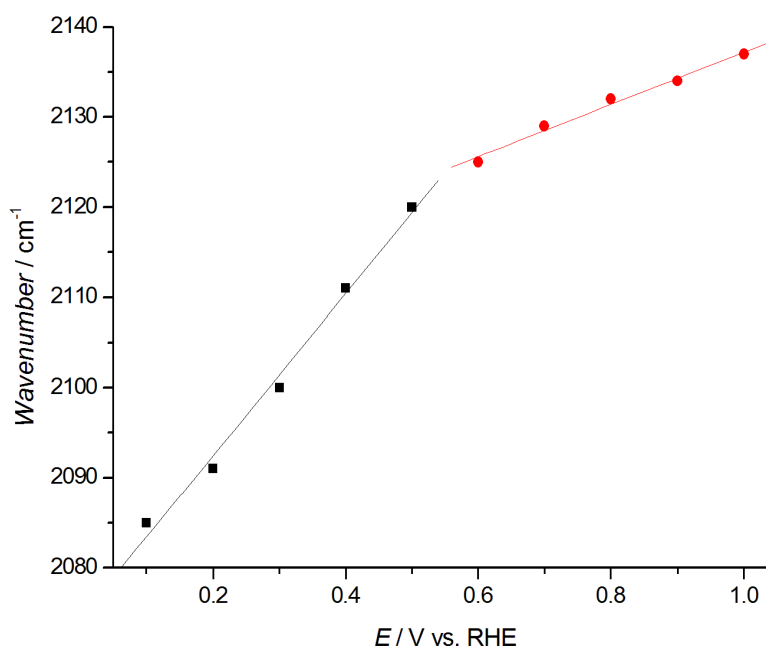


**Figure 3.6.** Plot of the C-N stretching frequency of a cyanide-modified Pt(111) electrode vs. the electrode potential in 0.1 M  $\text{HClO}_4$ .

*In situ* STM studies revealed the real-space structure of cyanide-modified Pt(111) electrodes [6,7]. We have observed the same long-range-ordered structure in acidic solutions by *in situ* STM (Figure 3.7), although, instead of the six individually-resolved  $\text{CN}_{\text{ads}}$  groups forming the hexagonal rings, a single tunnelling spot with a slight depression at its centre was observed. Figure 3.7, right, shows two translational domains of the  $(2\sqrt{3} \times 2\sqrt{3})R30^\circ$  structure, and the domain boundary separating them.

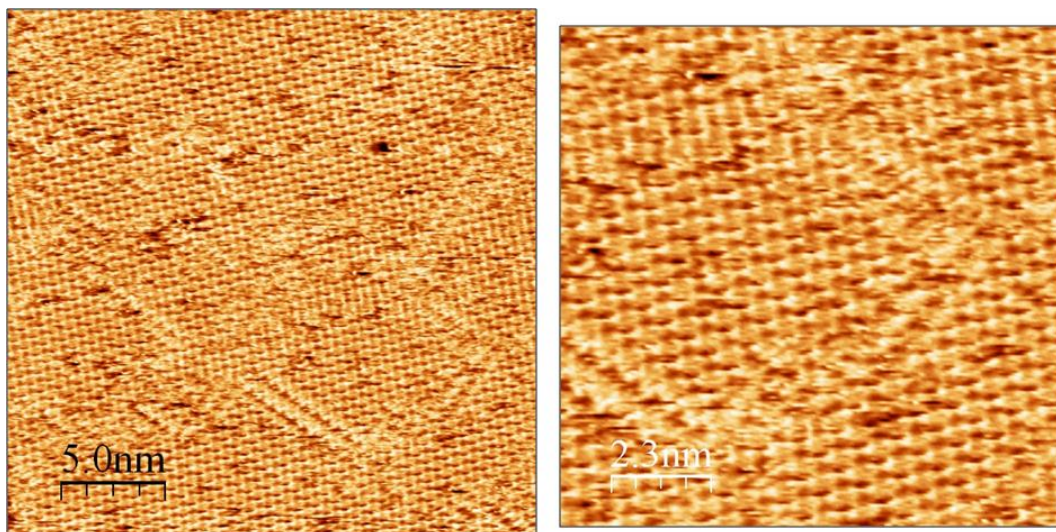


**Figure 3.7.** Left: STM image ( $25 \times 25 \text{ nm}^2$ ) of a cyanide-modified Pt(111) electrode in  $0.1 \text{ M HClO}_4 + 0.1 \text{ M KClO}_4$  at  $E_s = 0.65 \text{ V vs. RHE}$ . Right: zoom into the  $11.5 \times 11.5 \text{ nm}^2$  area enclosed by the square in the image on the left.  $U_T = 0.37 \text{ V}$  (tip negative);  $i_T = 2 \text{ nA}$ .

Cyanide is so strongly adsorbed on Pt(111) that CO adsorption and subsequent stripping on a cyanide-modified Pt(111) electrode does not affect the pre-adsorbed cyanide adlayer [103]. Using the exact thermodynamic double-layer correction, obtained with the help of CO-charge displacement measurements, it has been demonstrated that the CO coverage at saturation of a cyanide-modified Pt(111) electrode is  $\theta_{\text{CO}} = 0.25$  [103]. Interestingly, hydrogen adsorption after adsorption of CO to saturation on cyanide-modified Pt(111) electrodes is not completely blocked [14,103,115], this being in agreement with our hypothesis that, on cyanide-modified Pt(111), the  $H_{\text{upd}}$  region corresponds to the formation of  $(\text{CN}_{\text{ads}})_x\text{-H}$ .

### 3.2.2. Theoretical study of cyanide-modified Pt(111) surfaces

Although the structure of adsorbed cyanide on Pt(111) electrodes has been elucidated by LEED [5] and *in situ* STM [6,7], and although many unique properties of these chemically-modified electrodes have been experimentally proved [10-14,103], there is a lack of theoretical studies concerning the structure and the configuration adopted by adsorbed cyanide on Pt(111) surfaces. In this section we will describe, using DFT calculations, the adsorption of cyanide on Pt(111) surfaces, considering different adsorption sites forming

different geometries. Theoretical calculations are particularly necessary in order to understand the experimental results regarding the adsorption of hydrogen on cyanide-modified Pt(111). For these reasons, we have studied the adsorption of hydrogen on the nitrogen end of adsorbed CN as well as on the free Pt atoms of the surface.

### 3.2.2.1. Structure of adsorbed cyanide on Pt(111) surfaces

In order to study the dependence of the adsorption energy of cyanide on the coverage of  $CN_{ads}$  we have calculated the adsorption energy of adsorbed CN on Pt(111) surfaces for different adsorption sites (*on-top*, *bridge*, *fcc-hollow* and *hcp-hollow* sites) and different configurations in the coverage interval between 0.25 and 1. Figure 3.8 shows *on-top* views of the configurations for which the adsorption energy of cyanide on Pt(111) at different coverages, with all the CNs occupying *on-top* sites, has been calculated. Figure 3.8(A) corresponds to  $\theta_{CN} = 0.25$  in a  $2 \times 2$  unit cell, Figure 3.8(B) to  $\theta_{CN} = 0.50$  in a  $2 \times 2$  unit cell forming a *zig-zag* structure, which resulted after relaxation of a linear distribution of cyanide, Figure 3.8(C) to  $\theta_{CN} = 0.75$  in a  $2 \times 2$  unit cell, and Figure 3.8(D) to  $\theta_{CN} = 1$  in a  $1 \times 1$  unit cell. Calculations for the same cyanide coverages with all the CN in *bridge*, *fcc-hollow* or *hcp-hollow* sites were performed with the same structures by simply shifting the CN groups to the corresponding adsorption sites. It must be noted that none of these ideal structures have been experimentally observed.

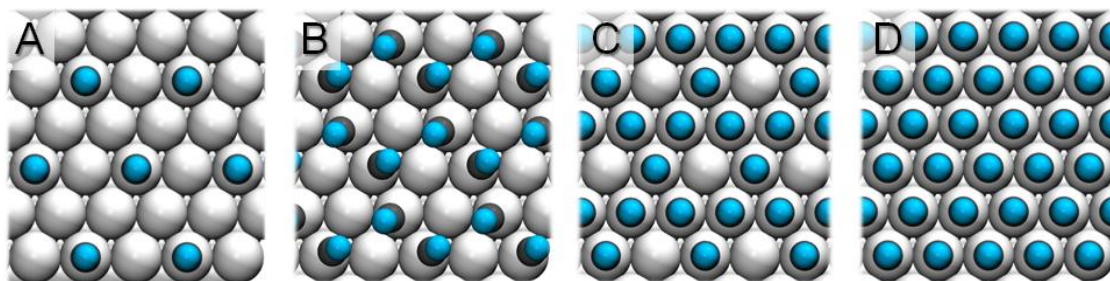


**Figure 3.8.** Top views of the different ideal structures for which the adsorption energy of cyanide on-top on Pt(111) at different coverages has been calculated: A)  $\theta = 0.25$ ; B)  $\theta = 0.50$ ; C)  $\theta = 0.75$ ; D)  $\theta = 1$ .

The adsorption energy of cyanide on Pt(111) was calculated taking the substrate and the radical adsorbate as reference (3.1):

$$E_{ads} = E_{CN-Pt(111)} - (E_{CN} + E_{Pt(111)}) \quad (3.1)$$



Figure 3.9 shows the coverage dependence of the adsorption energy of cyanide *on-top* and at *fcc-hollow* sites for the four ideal configurations of coverages 0.25, 0.50, 0.75 and 1 shown in Figure 3.8.

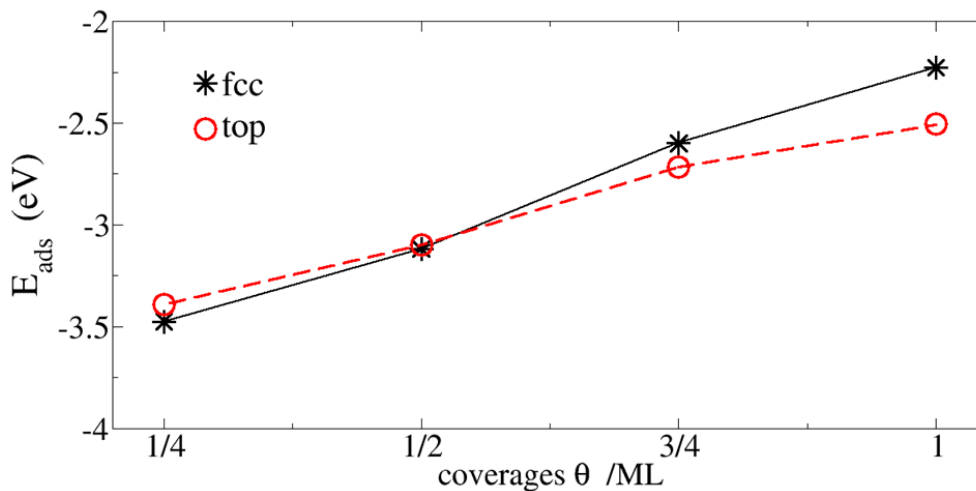


**Figure 3.9.** Adsorption energy of  $\text{CN}_{\text{ads}}$  on Pt(111) at different coverages from 0.25 to 1, with all the  $\text{CN}_{\text{ads}}$  occupying either *fcc-hollow* sites (black stars) or *on-top* sites (red circles).

Obviously, the adsorption energy becomes less negative as the coverage increases due to the repulsion between adsorbed CN groups. The major contribution to the repulsion comes from the negatively charged nitrogen. Interestingly, Figure 3.9 shows that the *fcc-hollow* and the *on-top* curves intercross, the *fcc-hollow* site being the preferred one for CN adsorption at lower coverages, while at 1 ML CN the *on-top* site is favoured over the *fcc-hollow* site by *ca.* 0.3 eV. The higher stability of the *on-top* site at  $\theta_{\text{CN}} = 1$  is due to the longer distance and the consequent lower repulsion between the large electronic density of the nitrogen atoms and that of the Pt(111) surface.

Figure 3.10 shows the total electronic density versus the distance from the metal surface ( $z$ ) for  $\text{CN}_{\text{ads}}$  coverages of 0.25 and 1. At  $\theta_{\text{CN}} = 0.25$ , the charge density initially decreases fast with the distance from the surface, and then remains more or less constant until it vanishes at distances longer than the nitrogen-surface separation. In contrast, at  $\theta_{\text{CN}} = 1$ , there is a local maximum at the location of the nitrogen atoms. This electron accumulation is large enough as to produce charge repulsion with the electrons of the Pt(111) surface. Since in the case of CN adsorbed *on-top* nitrogen atoms are located farther from the surface, the repulsion is lower, as noted above. This result suggests that CN

adsorption on Pt(111) implies a competition between two types of forces: a chemical force, that tends to locate  $CN_{ads}$  on the *fcc* site, and an electrostatic force that tends to push the  $CN_{ads}$  further from the surface and favors adsorption *on-top*.

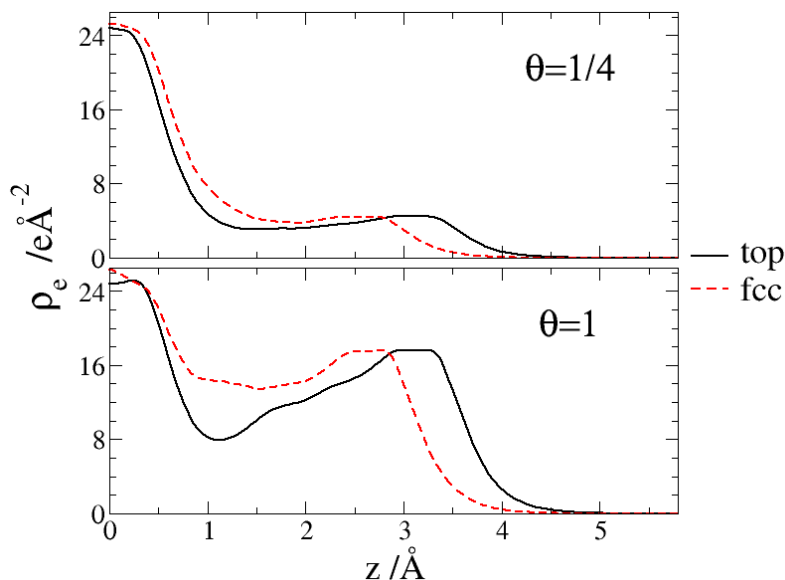


**Figure 3.10.** Total electronic density ( $\rho_e$ ) as a function of the distance ( $z$ ) from the metal surface for a cyanide-modified Pt(111) surface. The Pt surface corresponds to  $z = 0$ . The total charge density for adlayers with all the CNs at *fcc*-hollow and at *on-top* sites are compared for  $\theta_{CN} = 0.25$  and  $\theta_{CN} = 1$ .

As can be seen in Figure 3.11, after relaxation of the experimentally observed  $(2\sqrt{3} \times 2\sqrt{3})R30^\circ$  structure the nitrogen atoms of the adsorbed cyanide groups forming the cyanide-modified Pt(111) structure tend to be as far from each other as possible, causing the CN groups not to be perpendicular to the metal surface (see Figure 3.11, right).



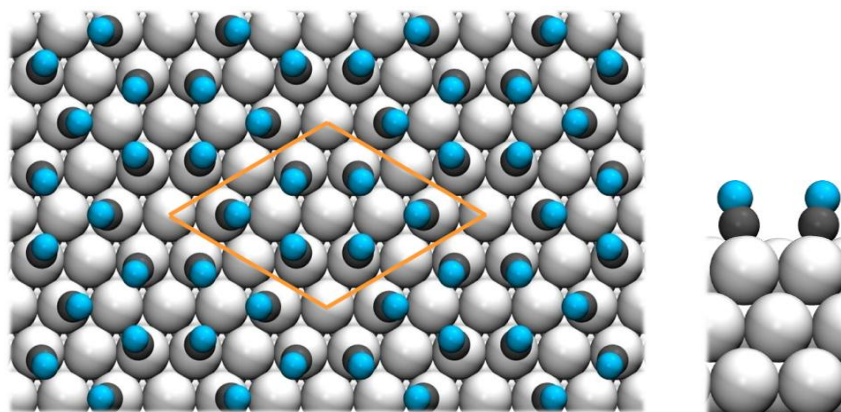


**Figure 3.11.** Top (left) and side views (right) of the configuration resulting after relaxation of the experimentally observed  $(2\sqrt{3} \times 2\sqrt{3})R30^\circ$  structure of CN adsorbed on Pt(111).

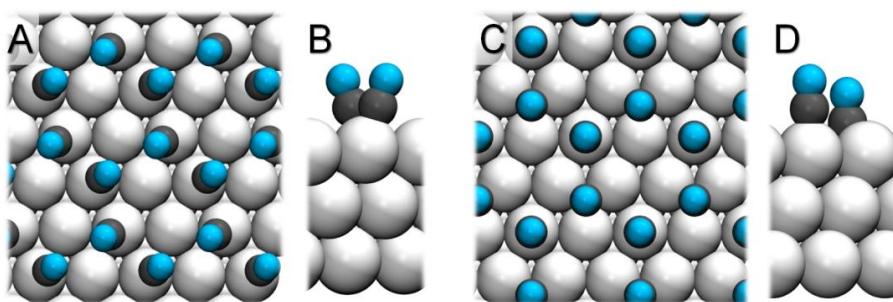


**Figure 3.12.** Top and side views of a  $2 \times 2$  top zig-zag configuration (A and B) and a  $2 \times 2$  top-fcc mix configuration for cyanide adsorbed on Pt(111). These two structures have the same coverage, 0.5 ML, as the  $(2\sqrt{3} \times 2\sqrt{3})R30^\circ$  structure observed experimentally, and are nearly isoenergetic with it, as revealed by DFT calculation of the adsorption energy of  $CN_{ads}$ .

For the particular case of 0.5 ML of cyanide adsorbed on Pt(111), we have calculated the adsorption energy of cyanide for different configurations, including the  $(2\sqrt{3} \times 2\sqrt{3})R30^\circ$  structure, that is the only one observed experimentally. The adsorption energy calculated for the  $(2\sqrt{3} \times 2\sqrt{3})R30^\circ$  structure is  $-3.17$  eV. We have found two configurations (see Figure 3.12) which are almost isoenergetic with the  $(2\sqrt{3} \times 2\sqrt{3})R30^\circ$  structure: a *zig-zag* distribution with all the CN groups adsorbed *on-top* (Figure 3.8 B, and Figures 3.12 A and B,  $E_{ads} = -3.10$  eV) and a *mix* structure in which half of the CN groups are adsorbed *on-top* and the other half are adsorbed on *fcc* sites (Figures 3.12 C and D,  $E_{ads} = -3.22$  eV). The *zig-zag* structure resulted after relaxation of a linear distribution of cyanide in a  $2 \times 2$  unit cell, due

to the repulsion between nitrogen atoms of neighboring CN groups, while the *mix* structure, which is slightly more stable than the *zig-zag* and the  $(2\sqrt{3} \times 2\sqrt{3})R30^\circ$  structures, resulted after relaxation of a  $2 \times 2$  unit cell in which cyanide was adsorbed in the *three-fold hollow* (*fcc* or *hcp*) sites. The higher stability of this structure is due, at least in part, to the absence of bond constrains and, more importantly, to the location of the CN groups at different heights above the metal surface (see Figure 3.12 D), which lowers the repulsion between N atoms of two neighboring CN groups.

From a thermodynamical point of view, equilibrium between the three structures described above should be expected. However, as explained above, only the  $(2\sqrt{3} \times 2\sqrt{3})$  structure has been experimentally observed. A cation located at the centre of each hexagonal cyanide ring of the  $(2\sqrt{3} \times 2\sqrt{3})$  structure, as suggested by Itaya and co-workers based on their STM images [7] in solutions containing  $K^+$  or  $Na^+$ , could explain the tendency of  $CN_{ads}$  to group forming an ordered array of hexagons instead of distributing themselves randomly over the surface. DFT calculations concerning the adsorption of alkaline metal (Na and K) cations (approximated as neutral metals) on different adsorption sites indicate, however, that the centre of the CN hexagonal rings (one adsorbed cation per unit cell, Figure 3.13 A) is the less favoured site [116]. The other examined adsorption sites were a cation surrounded by four  $CN_{ads}$  groups (Figure 3.13 B) and a cation surrounded by three  $CN_{ads}$  (Figure 3.13 C), yielding a kagome structure with three cations per unit cell and a honeycomb structure with two cations per unit cell, respectively. Both *in situ* STM images and theoretical calculations [116] show that the honeycomb structure is the most stable configuration. Results regarding the adsorption of alkali metal cations on cyanide-modified Pt(111) electrodes will be explained in more detail in Chapter 5.

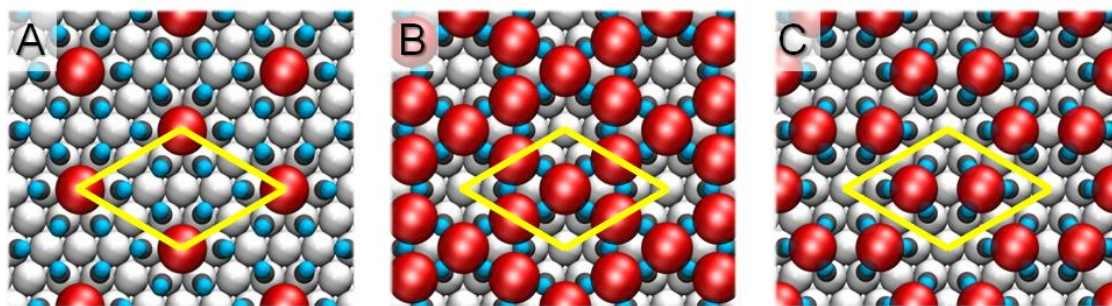


**Figure 3.13.** Top view of the structures resulting from cation adsorption in the three possible cavity sites of the  $(2\sqrt{3} \times 2\sqrt{3})R30^\circ$  cyanide adlayer on Pt(111): A)  $(CN_{ads})_6$ , B)  $(CN_{ads})_4$  and C)  $(CN_{ads})_3$ .

Our hypothesis is that cations, that are always present during the experimental formation of the cyanide adlayer, may play an important role in determining the structure of cyanide-modified Pt(111) electrodes. Experimental evidence of the presence of cations attached to the cyanide-modified Pt(111) has been reported even under UHV conditions by *ex situ* LEED experiments [5]. A comparison of the *zig-zag* and the *mix* structures with the  $(2\sqrt{3} \times 2\sqrt{3})$  structure makes us think that the size of the different cavities available for the adsorption of cations plays a crucial role in determining the finally adopted configuration. The *mix top-fcc* arrangement, which is the most stable according to the theoretical calculations, does not seem a stable candidate for the adsorption of cations due to the large size of the cavity formed by a trigonal arrangement of Pt atoms (see Figure 3.12 C). As for the *zig-zag* structure, although the cavity in this case is quite similar to that of the experimentally observed structure, in the presence of counter-ions the CN groups will probably tend to rearrange, rendering a distribution less stable than the  $(2\sqrt{3} \times 2\sqrt{3})$  structure.

According to theoretical calculations, the chemisorption of  $\text{CN}_{\text{ads}}$  *on-top* through its carbon atom is driven by the prevailing tendency to donate electronic density from the  $\text{CN}_{\text{ads}}$  to the empty *d*-band of the metal surface, forming a  $\sigma$  bond, rather than by the backdonation from the metal to the  $\pi$  antibonding orbitals of  $\text{CN}_{\text{ads}}$ , forming a  $\pi$  bond [117-119]. We have studied the local density of states (LDOS) in order to analyze the electronic factors that control the adsorption of CN on Pt(111) surfaces. By the analysis of the LDOS, the orbitals involved in the bond of adsorbed cyanide to the Pt(111) surface can be identified. Figure 3.14 shows the LDOS projected on the carbon atom of a  $\text{CN}_{\text{ads}}$  and on the Pt atom of the cyanide-modified Pt(111) surface bonded to it. As can be observed, there is a coincidence of peaks at around -16 eV, where the 2sp states of carbon and 6sp states of platinum clearly overlap. There is also an overlap at around -7.5 eV, where the *d* band of platinum contributes to the bond.

The LDOS projected on the *d*-band of the surface Pt atoms of a cyanide-modified Pt(111) electrode with the  $(2\sqrt{3} \times 2\sqrt{3})\text{R}30^\circ$  structure (Figure 3.15), shows that the DOS of the Pt atoms directly bonded to the  $\text{CN}_{\text{ads}}$  is shifted to lower energies as compared to clean Pt(111), this being consistent with a strong bonding. On the other hand, the DOS projected on the *d*-band of the free Pt atoms remains nearly identical to the DOS of the Pt atoms of the clean (111) surface, supporting the notion that  $\text{CN}_{\text{ads}}$  acts as an inert site blocker. Hence, the positive shift in the onset potential for hydrogen adsorption cannot be explained by an electronic disturbance of the free Pt atoms of the cyanide-modified Pt(111) surface.

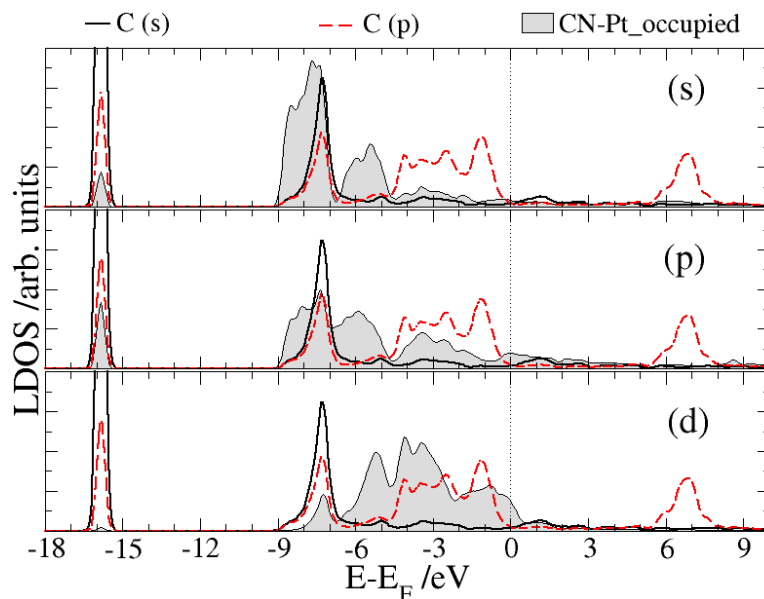


**Figure 3.14.** LDOS projected on the C atom of a  $\text{CN}_{\text{ads}}$  group of the  $(2\sqrt{3} \times 2\sqrt{3})R30^\circ$  structure and on the Pt atom bonded to it. The  $sp$  states of carbon are contrasted with, from top to bottom, the  $s$ ,  $p$ , and  $d$  valence states of the metal.

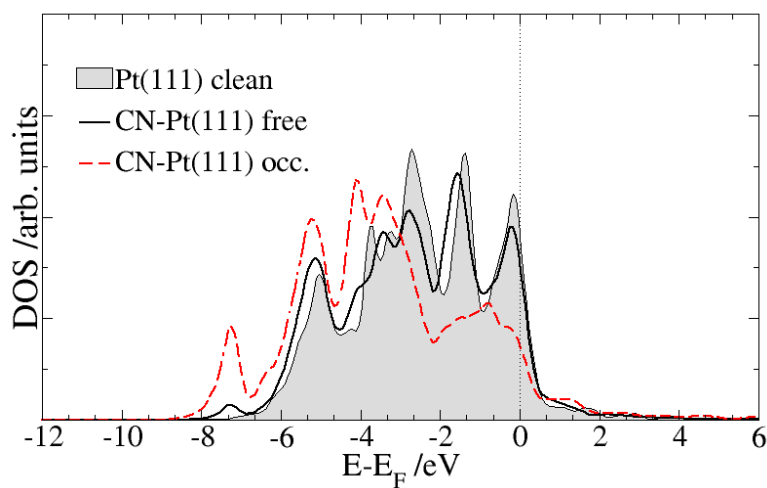


**Figure 3.15.** LDOS of the  $d$  band projected on the surface atoms of a clean  $\text{Pt}(111)$  and of a cyanide-modified  $\text{Pt}(111)$  surface with the  $(2\sqrt{3} \times 2\sqrt{3})R30^\circ$  structure. For the cyanide-modified  $\text{Pt}(111)$  surface, Pt free atoms (not bonded to adsorbed cyanide) are distinguished from the Pt atoms directly bonded to CN (Pt occupied).

### 3.2.2.2. Adsorption of hydrogen on cyanide-modified Pt(111)

We have studied the adsorption energy of CNH on Pt(111), given by Equation 3.2, and have compared it with the adsorption energy of CN on Pt(111), given by Equation 3.1. We have also computed the changes in the work function induced by the adsorption of  $\text{CN}_{\text{ads}}$  and  $\text{CNH}_{\text{ads}}$  on a Pt(111) surface (Table 3.1), given by Equation 3.3. The sub-index *adsorbate* in Equation 3.3 is referred either to  $\text{CN}_{\text{ads}}$  or  $\text{CNH}_{\text{ads}}$ . The work function of the Pt(111) surface is  $\Phi_{\text{Pt}(111)} = 5.80$  eV.

$$E_{\text{ads}} = E_{\text{CNH-Pt}(111)} - (E_{\text{CNH}} + E_{\text{Pt}(111)}) \quad (3.2)$$

$$\Delta\Phi = \Phi_{\text{adsorbate-Pt}(111)} - \Phi_{\text{Pt}(111)} \quad (3.3)$$

Interestingly, as can be observed in Table 3.1, in all the configurations used for calculating the work function at different CN coverages (including the  $(2\sqrt{3} \times 2\sqrt{3})R30^\circ$  structure observed experimentally), the change in the work function upon adsorption of cyanide is higher when *on-top* sites are occupied than when CN adsorbs on *fcc-hollow* sites, due to the larger dipole moment of  $\text{CN}_{\text{ads}}$  in the former case. The latter will also favour the solvation of CN by water molecules, and will therefore contribute to the experimentally observed preference of the CN groups to be adsorbed *on-top* (see Table 3.1), although the calculated adsorption energies of adsorbed cyanide are very similar for the different adsorption sites at the same cyanide coverage.

**Table 3.1.** Adsorption energy ( $E_{\text{ads}}$ ) and work function difference ( $\Delta\Phi$ ) in eV for different CN and CNH configurations and coverages on Pt(111) surfaces.

$\theta_{\text{adsorbate}}$	Adsorption site	$E_{\text{ads}(\text{CN})} / \text{eV}$	$E_{\text{ads}(\text{CNH})} / \text{eV}$	$\Delta\Phi_{(\text{CN})} / \text{eV}$	$\Delta\Phi_{(\text{CNH})} / \text{eV}$
0.25	<i>top</i>	-3.39	-1.86	2.75	-2.66
0.25	<i>fcc</i>	-3.47	-2.11	1.67	-0.88
0.50	<i>top (exp.)</i>	-3.17	-	3.56	-
0.50	<i>top (zig-zag)</i>	-3.10	-1.43	3.48	-3.37
0.50	<i>top (linear)</i>	-3.02	-1.60	3.48	-2.23
0.50	<i>fcc (linear)</i>	-3.04	-1.81	2.09	-0.86
0.50	<i>top-fcc (mix)</i>	-3.23	-1.87	3.24	-2.38
1	<i>top</i>	-2.51	-1.04	3.82	-2.69
1	<i>fcc</i>	-2.23	-0.96	3.33	-1.63

Table 3.1 shows that  $\text{CNH}_{\text{ads}}$  inverts the surface dipole moment with respect to  $\text{CN}_{\text{ads}}$ . As happens with  $\text{CN}_{\text{ads}}$ , for the same coverage large differences in the work function are found for  $\text{CNH}_{\text{ads}}$  in the different configurations studied, in contrast with the small changes in the adsorption energy.

The adsorption energy of hydrogen on  $\text{CN-Pt(111)}$ , both on the nitrogen atom of adsorbed cyanide (Figure 3.16) and on the Pt atoms of the  $\text{Pt(111)}$  surface (Figure 3.17), has also been calculated according to Equations 3.4 and 3.5. The results are summarized in Table 3.2.

$$E_{\text{ads}}^{\text{H-N}} = E_{\text{CNH-Pt(111)}} - \left( \frac{E_{\text{H}_2}}{2} + E_{\text{CN-Pt(111)}} \right) \quad (3.4)$$

$$E_{\text{ads}}^{\text{H-P}} = E_{\text{CNH-HPt(111)}} - \left( \frac{E_{\text{H}_2}}{2} + E_{\text{CNH-Pt(111)}} \right) \quad (3.5)$$

Although the *zig-zag* arrangement is one of the most stable configurations for adsorbed CN on  $\text{Pt(111)}$ , for  $\text{CNH}_{\text{ads}}$  it becomes unfavourable, as can be seen in Table 3.1, because formation of hydrogen bonds between neighbouring CNH groups in a linear configuration (Figures 3.16 C and D), that cannot be formed in the *zig-zag* configuration, adds additional stability to the adlayer.

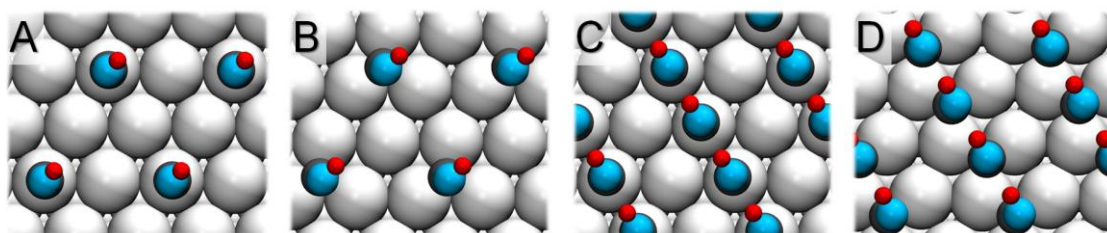


**Figure 3.16.** Top view of the different configurations for which the adsorption energy of hydrogen on the nitrogen atoms of  $\text{CN}_{\text{ads}}$  of  $\text{CN-Pt(111)}$  surfaces has been calculated.

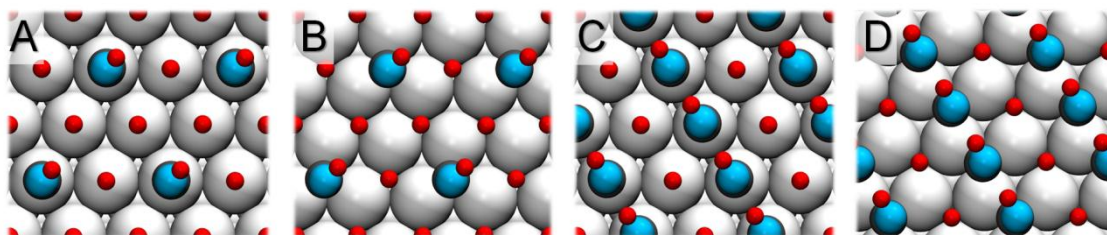


**Figure 3.17.** Top view of the different configurations for which the adsorption energy of hydrogen on the free Pt atoms of  $\text{CNH-Pt(111)}$  surfaces has been calculated.



**Table 3.2.** Adsorption energy and work function difference in eV for H adsorbed on N (H-N) or on the Pt surface (H-Pt) forming different configurations and coverages on Pt(111) surfaces.

$\theta_{adsorbate}$	Adsorption site	$E_{ads}^{H-N} / eV$	$E_{ads}^{H-Pt} / eV$	$\Delta\Phi_{(H-N)} / eV$	$\Delta\Phi_{(H-Pt)} / eV$
0.25	<i>top</i>	-1.10	-0.31	-2.66	-2.84
0.25	<i>fcc</i>	-1.26	-0.33	-0.68	-1.16
0.50	<i>top (linear)</i>	-0.95	-0.40	-2.23	-2.33
0.50	<i>fcc (linear)</i>	-1.31	-0.28	-0.86	-0.90
0.50	<i>top-fcc (mix)</i>	-1.26	-	-	-

As already deduced from the results of the calculation of the *d*-band LDOS (Figure 3.15), the results shown in Table 3.2 corroborate that the adsorption of hydrogen on the free Pt atoms of the different structures of Pt(111) with  $CN_{ads}$  is very close in energy to the adsorption on unmodified Pt(111) (-0.4 eV for the *on-top* linear configuration of  $H_{ads}$ ). These results show that adsorbed hydrogen on nitrogen is much more stable (*ca.* 1 eV) than adsorbed hydrogen ( $H_{upd}$ ) on the free Pt atoms of the Pt(111) surface, and strongly support the hypothesis that the  $H_{upd}$  region on cyanide-modified Pt(111) is due to the formation of  $(CN_{ads})_x-H$  (see Figure 3.18). It must be noted that the values of  $E_{ads}^{H-Pt}$  in Table 3.2 correspond to the adsorption of H on the free Pt atoms of Pt(111)- $CNH_{ads}$ , *i.e.*, when hydrogen is already adsorbed on the nitrogen atom of the CN groups. We have checked that the difference of these results with respect to  $E_{ads}^{H-Pt}$  on Pt(111)- $CN_{ads}$  is negligible (lower than 0.1 eV). Although none of these ideal structures have been experimentally observed, they allow to calculate, in a first approximation, the adsorption energy of hydrogen on the different adsorption sites forming different configurations. DFT calculations concerning the adsorption of hydrogen on the  $(2\sqrt{3} \times 2\sqrt{3})R30^\circ$  structure observed experimentally, both on the nitrogen atoms of the cyanide groups (see Figure 3.17) and on the Pt atoms of the surface are currently in progress.

As can be observed in Figure 3.18, the formation of  $(CN_{ads})_x-H$  is probably stabilized by the formation of hydrogen-bonds between nitrogen atoms of neighboring cyanide groups in the hexagonal ring, as happens with the linear configuration (Figure 3.17 C and D). Theoretical calculations show that hydrogen adsorption *on-top* of the free Pt atoms of the cyanide-covered Pt(111) surface ( $\theta_{CN} = 0.5$ ) is also exothermic for all the configurations analyzed. This supports the idea that, in the potential region between 0.6 V and 0.1 V, hydrogen adsorbs on the nitrogen atoms of the cyanide groups, but, at sufficiently negative

potentials, *on-top*  $H_{\text{ads}}$  can also be formed. It must be noted that, on Pt(111),  $H_{\text{ads}}$  occupies *fcc-hollow* sites in the upd region, but, on cyanide-modified Pt(111), three-fold hollow sites surrounded by free Pt atoms are absent.

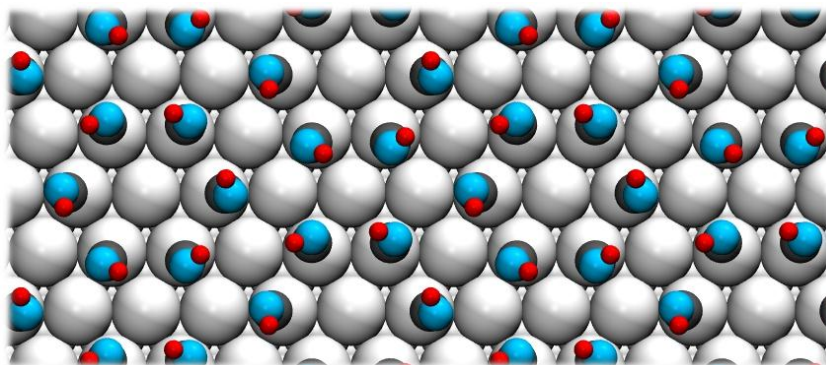


**Figure 3.18.** Top view of the most stable configuration for hydrogen adsorbed on the nitrogen atoms of the CN groups of the  $(2\sqrt{3} \times 2\sqrt{3})R30^\circ$  structure of cyanide-modified Pt(111) surfaces.

### 3.3. Cyanide-modified polycrystalline Pt surfaces

The electrochemical behaviour of platinum surfaces covered by adsorbed cyanide in acidic solutions is strongly dependent on the atomic structure of the electrode surface [11]. While the cyanide adlayer is very stable on Pt(111) in the potential region between 0.1 and 1.0 V, the other two low-index single-crystal surfaces (Pt(100) and Pt(110)) exhibit a more complex behaviour, the cyanide adlayer being oxidized at more negative potentials [11] and being therefore only stable in a narrow potential region. However, interestingly, cyclic voltammograms of cyanide-modified polycrystalline Pt in 0.1 M  $\text{HClO}_4$  solutions (Figure 3.19) show that cyanide is spontaneously and irreversibly adsorbed on polycrystalline Pt electrodes, and that the cyanide adlayer is very stable in the potential region between 0.1 V and 0.8 V vs. RHE, no change being observed in the cyclic voltammograms upon repetitive cycling in this potential region.

The shape of the CV obtained for cyanide-modified polycrystalline Pt is qualitatively very similar to that obtained for cyanide-modified Pt(111) electrodes (Figures 3.2 and 3.3). Figure 3.19 shows that the onset of hydrogen adsorption is positively shifted (*ca.* 0.25 V), as happens on cyanide-modified Pt(111) electrodes, and, as in that case, this can be explained by the formation of  $(\text{CN}_{\text{ads}})_x\text{-H}$  in the  $H_{\text{upd}}$  region.



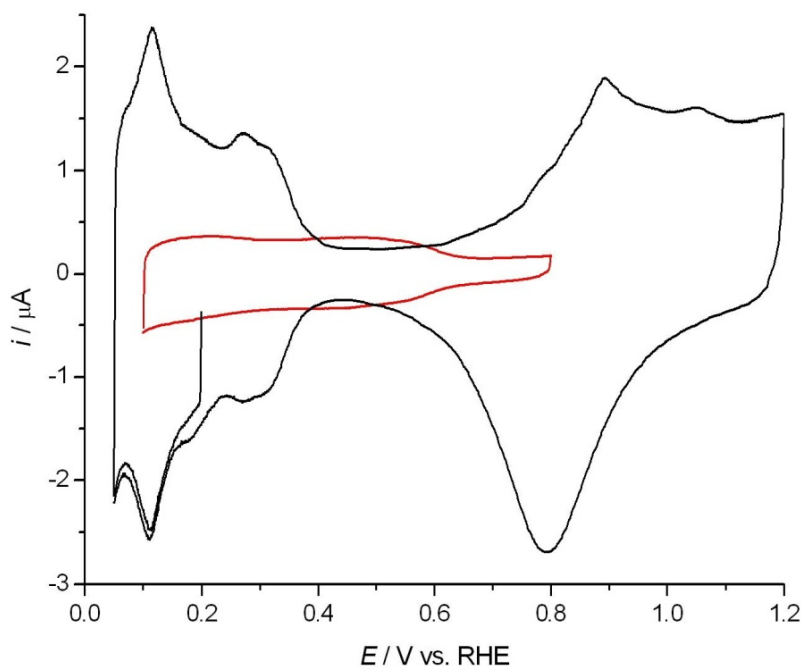


**Figure 3.19.** Cyclic voltammogram at  $50 \text{ mV s}^{-1}$  of cyanide-free (black) and cyanide-modified (red) polycrystalline Pt in  $0.1 \text{ M HClO}_4$ .

The stability of the CV on cyanide-modified polycrystalline Pt in the potential region between  $0.1 \text{ V}$  and  $0.8 \text{ V}$  indicates that polycrystalline Pt behaves similar to Pt(111) in this potential region, defect sites and (100) and (110) facets being probably completely blocked by adsorbed cyanide. The lower potential of the positive limit of the potential region of stability of the cyanide adlayer for cyanide-modified polycrystalline Pt also suggests that the presence of an excessive amount of defects on Pt(111) single-crystal electrodes may affect negatively the stability of cyanide adlayers on Pt(111) surfaces at potentials above  $0.8 \text{ V}$ .

### 3.4. Conclusions and perspectives

We have shown, by means of cyclic voltammetry and FTIRS, that cyanide-modified Pt(111) electrodes are very stable. We have performed DFT calculations in order to study the spatial and electronic structure of cyanide adsorbed on Pt(111), as well as the adsorption of hydrogen on these surfaces. The most important conclusions reached are summarized below.

DFT calculations suggest that adsorption of cyanide forming a  $(2\sqrt{3} \times 2\sqrt{3})R30^\circ$  structure is driven by the presence of cations, the other nearly isoenergetic ideal structures studied presenting cavities with inappropriate sizes or geometries for the adsorption of cations.

The positive shift in the onset of the hydrogen adsorption region in the CV can be explained by the formation of  $(\text{CN}_{\text{ads}})_x\text{-H}$  instead of  $\text{H}_{\text{upd}}$  bonded to the unmodified Pt atoms. An analysis of the FTIR spectra shows that the Stark tuning rate of the CN stretching frequency of cyanide-modified Pt(111) changes at a potential coinciding with the onset of hydrogen adsorption in the corresponding CV, which can also be explained by the formation of  $(\text{CN}_{\text{ads}})_x\text{-H}$ . According to DFT calculations, the adsorption of hydrogen on the nitrogen atoms of  $\text{CN}_{\text{ads}}$  of a cyanide-modified Pt(111) surface is more favored than the adsorption on top of a Pt atom.

Furthermore, regarding the electronic structure of cyanide-modified Pt(111) surfaces, the LDOS of the  $d$ -band of the free Pt atoms remains nearly identical than that of the Pt atoms of the unmodified surface, which demonstrates that  $\text{CN}_{\text{ads}}$  acts as an inert site blocker. For this reason, cyanide-modified Pt(111) electrodes are unique for studying atomic ensemble effects in electrocatalysis, as we will discuss in the following chapter.

Finally, preliminary voltammetric results on cyanide-modified polycrystalline Pt show that the cyanide adlayer is very stable in the potential region between 0.1 V and 0.8 V vs. RHE and the CVs are qualitatively very similar to those obtained with cyanide-modified Pt(111) electrodes. These results let us host some hope that highly sensitive ATR-SEIRAS studies can be undertaken with cyanide-modified Pt(111)-like surfaces.





## Chapter 4

# Atomic ensemble effects in electrocatalysis

### 4.1. Introduction

A good electrocatalyst must have high activity and selectivity. Improved catalysts can be designed by modifying the electronic properties of the surface atoms (electronic effect) and/or by modifying the size and the geometric structure of the different sites present on the surface (atomic ensemble effect). A very appropriate way to study the role of geometric atomic ensembles in electrocatalysis is to modify the surface in such a way that only one kind of sites is removed without modifying the electronic structure of the rest of the surface (the site-knockout strategy [31]). Single-crystal surface modification by adsorption of atoms or molecules that block the sites to which they are bonded but do not affect their neighbors (third body effect) can provide us with information regarding the critical atomic ensemble needed for an electrocatalytic reaction or a reaction step to proceed.

Cyanide-modified Pt(111) electrodes, from which all the sites composed of three contiguous atoms have been removed, are very useful to study the role of this kind of sites in several electrocatalytic reactions, and have been used as model surfaces to investigate the size and geometric arrangement of the smallest group of atoms necessary for an electrocatalytic reaction or reaction step to occur [31]. The suitability of these chemically-modified surfaces to study the role of atomic ensembles in electrocatalysis was demonstrated, for the first time, in the study of the role of atomic ensembles in the electrooxidation of methanol on Pt electrodes [38], whose dehydrogenation to adsorbed carbon monoxide was shown to require at least three contiguous platinum atoms.

This chapter addresses the study of atomic ensemble effects in electrocatalysis. The study of the mechanisms of nitric oxide reduction, that can be considered as a test case for checking the suitability of cyanide-modified Pt(111) electrodes to investigate atomic ensemble effects in electrocatalysis is presented first. This is followed by a study, using cyanide-modified Pt(111) electrodes, of atomic ensemble effects on the hydrogen and formic

acid electrooxidation reactions, from which important conclusions regarding the reaction mechanism could be obtained. Finally, we have used cyanide-modified Pt(111) surfaces to study the oxygen reduction reaction (ORR). Some of these studies (atomic ensemble effects on the electroreduction of NO and on the electrooxidation of HCOOH) had already been initiated when the work reported in this PhD Thesis began, but my contributions and the work performed previously are shown here as a whole for the sake of completeness.

## 4.2. Nitric oxide electroreduction

Nitric oxide, like carbon monoxide, is a simple molecule that can serve as a model adsorbate, or as a molecular probe in vibrational spectroscopy. NO has only one electron more than CO, both molecules having a similar size. For this reason, NO is expected to fit, like CO, within the troughs of the  $(2\sqrt{3} \times 2\sqrt{3})R30^\circ$  cyanide-modified Pt(111) structure. NO appears as an intermediate in many important catalytic reactions such as ammonia oxidation and nitrate and nitrite reduction. Furthermore, it is an important pollutant, present in the exhaust gases of automobile engines, that causes acid rain. As a consequence, the adsorption of NO at the metal/gas and metal/electrolyte interfaces has been extensively studied [120-128].

### 4.2.1. Nitric oxide electroreduction on Pt(111)

NO electroreduction on Pt(111) has been studied previously in detail [126,129-131]. We present here an analysis of the behaviour of irreversibly adsorbed nitric oxide ( $\text{NO}_{\text{ads}}$ ) adlayers on Pt(111) electrodes in perchloric acid solutions. Figure 4.1 shows the cyclic voltammogram of Pt(111) in 0.1 M  $\text{HClO}_4$  (solid line) and the reductive stripping of an irreversibly adsorbed NO adlayer on Pt(111) during a slow ( $2 \text{ mV s}^{-1}$ ) potential scan down to the onset of hydrogen evolution (dotted line). Ammonium has been identified as the product of the reductive stripping process by voltammetric and *in situ* FT-IRRAS experiments [123,126,129-131]. The NO coverage can be obtained from the charge under the reduction peaks, after subtraction of the double layer correction, which corresponds to the charge that must flow to form the double layer once the NO adlayer has been reduced and, as demonstrated by the Alicante group, can be obtained from CO charge-displacement measurements [132]. The charge under the dotted line in Figure 4.1, after double layer correction, amounts to  $563 \mu\text{C cm}^{-2}$ , and corresponds to a coverage  $\theta_{\text{NO}} = 0.47$  (assuming total reduction to ammonium, 5 electrons transferred), in very good agreement with the

values reported previously [132]. Rosca *et al.* [131] demonstrated, using CV and FTIRS, that the cathodic peak at ca. 0.28 V and its shoulder at ca. 0.34 V correspond to the reductive stripping of NO adsorbed *on-top* ( $\text{NO}_L$ ), while the cathodic peak appearing at ca. 0.15 V corresponds to the reductive stripping of NO adsorbed at *threefold-hollow* sites ( $\text{NO}_M$ ).

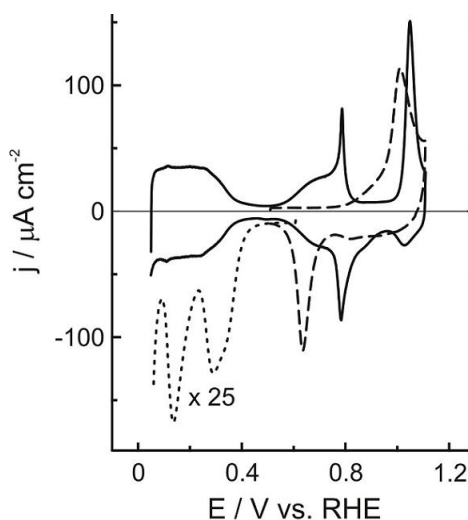


**Figure 4.1.** Reductive stripping of  $\text{NO}_{\text{ads}}$  at  $2 \text{ mV s}^{-1}$  (dotted line) and CV at  $50 \text{ mV s}^{-1}$  between 0.51 V and 1.11 V (dashed line) after *ex situ* formation of a saturated NO adlayer on Pt(111). The solid line corresponds to the CV at  $50 \text{ mV s}^{-1}$  of a clean Pt(111) electrode. The electrolyte was 0.1 M  $\text{HClO}_4$  in all cases.

The dashed line in Figure 4.1 corresponds to the CV in 0.1 M  $\text{HClO}_4$  at  $50 \text{ mV s}^{-1}$ , between 0.51 V and 1.11 V, of Pt(111) after *ex situ* formation of a saturated NO adlayer. The anodic peak at 1.01 V has been assigned to a monoelectronic surface redox process, in which adsorbed NO is reversibly oxidized to adsorbed nitrite [129] or adsorbed nitrous acid [130], and the cathodic peak at 0.64 V to the reverse process. The charges obtained by integration, without double layer correction, of the anodic sweep between 0.51 V and 1.11 V and of the cathodic sweep between the potential at which the current starts to be negative and 0.51 V, are  $304 \mu\text{C cm}^{-2}$  and  $300 \mu\text{C cm}^{-2}$ , respectively. This is clearly larger than the  $120 \mu\text{C cm}^{-2}$  expected for oxidation of ca. 0.5 ML of adsorbed NO to adsorbed  $\text{NO}_2^-$  or  $\text{HNO}_2$ . According to Beltramo and Koper [130], this is due to OH adsorption and desorption within the  $\text{HNO}_2$  adlayer. However, if the positive integration limit is reduced to 0.75 V (a potential at which we assume that desorption of OH has been completed) integration of the reduction peak yields, after double layer correction,  $121 \mu\text{C cm}^{-2}$ , in excellent agreement with the value of  $120 \mu\text{C cm}^{-2}$  expected for the reduction of 0.5 ML of  $(\text{HNO}_2)_{\text{ads}}$  or  $(\text{NO}_2^-)_{\text{ads}}$  to  $\text{NO}_{\text{ads}}$ , and also

coinciding with the value reported by Rodes *et al.* [126] for this redox couple (these authors did not indicate the integration limits).

Momoi *et al.* [127] and Casero *et al.* [133] have proposed that oxidation of NO proceeds further, up to adsorbed NO<sub>2</sub>, and that there is no OH adsorption. Therefore, the double layer-corrected charges obtained by integration of the anodic sweep between 0.51 V and 1.11 V (220 μC cm<sup>-2</sup>), and of the cathodic sweep between the potential at which the current starts to be negative and 0.51 V (216 μC cm<sup>-2</sup>), would correspond to 0.45 ML. This coverage is nearly twice as high as the NO coverage of 0.25 ML estimated by both Momoi *et al.* [127] and Casero *et al.* [133], probably because the authors, who did not indicate the integration limits, used a lower positive integration limit.

Figure 4.2 shows a sequence of differential FTIR spectra of the NO adlayer irreversibly adsorbed on the Pt(111) electrode in 0.1 M HClO<sub>4</sub>, with the reference spectrum recorded at 0.06 V and the sample spectra recorded sequentially between 0.60 V and 0.10 V (potential jump of 0.10 V). The main feature in the spectrum is the positive band around 1675 cm<sup>-1</sup>, which corresponds to NO<sub>L</sub> [125-127,129,131]. This band is often difficult to observe in external reflectance FTIRS, because it can be easily obscured or deformed by the bending mode of liquid water (*ca.* 1645 cm<sup>-1</sup>), in the case of small changes in the thickness of the thin electrolyte layer between the electrode and the infrared transparent window, this being the reason why external reflectance FTIR spectra of NO adsorbed on metal electrodes have often been measured using D<sub>2</sub>O as solvent. The broad negative band around 1460 cm<sup>-1</sup> was attributed to NH<sub>4</sub><sup>+</sup>, formed upon reduction of the adsorbed NO [131].

A small band around 1400 cm<sup>-1</sup> can also be observed in Figure 4.2. The same experiment using *s*-polarized light (not shown) only revealed the bands corresponding to NH<sub>4</sub><sup>+</sup> and to uncompensated water, the band at *ca.* 1675 cm<sup>-1</sup> and the feature around 1400 cm<sup>-1</sup> being completely absent, a clear indication that these two bands correspond to an adsorbed species. A band at frequencies between 1395 cm<sup>-1</sup> and 1440 cm<sup>-1</sup> has been observed before for sub-saturated irreversibly adsorbed NO adlayers on Pt(111) by Gómez *et al.* [129], who assigned it to bridge bonded NO<sub>ads</sub> (NO<sub>B</sub>). On the contrary, Weaver *et al.* [134], assigned both the band at higher frequencies (1670-1680 cm<sup>-1</sup>) and the band at lower frequencies (1395-1440 cm<sup>-1</sup>) to NO<sub>M</sub> with different N-O bond lengths (shorter in the case of the higher frequency band). We assign the band observed by us around 1400 cm<sup>-1</sup> to NO<sub>M</sub>.



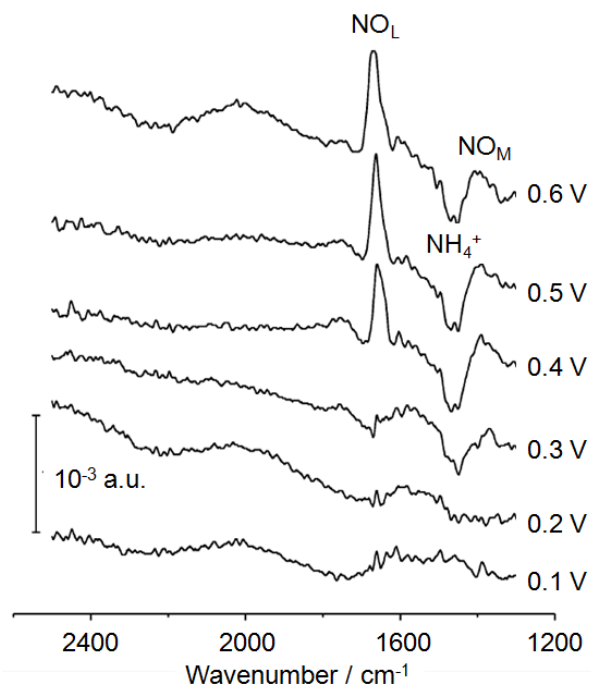


**Figure 4.2.** FTIR spectra of the NO adlayer irreversibly adsorbed on Pt(111) in 0.1 M  $\text{HClO}_4$ . The reference spectrum was recorded at 0.06 V.

As can be observed in Figure 4.2, at 0.30 V the band corresponding to  $\text{NO}_L$  has already disappeared, while the band assigned to  $\text{NO}_M$  can still be observed at this potential, and has disappeared at 0.20 V. This behaviour is in agreement with the hypothesis suggested by Rosca *et al.* [131], according to which the cathodic peak at *ca.* 0.28 V and the shoulder at *ca.* 0.34 V correspond to the reductive stripping of  $\text{NO}_L$ , while the cathodic peak appearing at *ca.* 0.15 V corresponds to the reductive stripping of  $\text{NO}_M$ .

#### 4.2.2. Nitric oxide reduction on cyanide-modified Pt(111) electrodes

Figure 4.3 (A) shows the voltammetric behaviour of NO adsorbed on a cyanide-modified Pt(111) electrode in 0.1 M  $\text{HClO}_4$ . The solid line corresponds to the CV of cyanide-modified Pt(111), which coincides with the voltammetric profiles reported previously [10-14,103]. After immersion of the cyanide-modified Pt(111) in a 0.1 M  $\text{HClO}_4$  solution containing 0.01 M  $\text{KNO}_2$  for 3 min, only a very small double layer-charging current, suggesting a decrease of the interfacial capacity due the presence of a new adsorbate, can be observed in the positive scan between 0.51 V and 0.85 V, and the anodic peak at 0.80 V

completely disappears (Figure 4.3 (A), dashed line). When the potential is scanned in the negative direction at  $2 \text{ mV s}^{-1}$  (Figure 4.3 (A), dotted line), only one reduction peak at  $0.28 \text{ V}$  appears in the voltammogram, instead of two as in the case of unmodified Pt(111) covered by an irreversibly adsorbed adlayer of NO. The charge under this peak, without double layer correction, amounts to  $160 \mu\text{C cm}^{-2}$ , indicating that, at the most, only one of every four free Pt atoms on the cyanide-modified Pt(111) surface is covered by an  $\text{NO}_{\text{ads}}$  molecule, which would correspond to a NO coverage of only 0.13, at the most. Due to this low coverage, a weak band around  $1620 \text{ cm}^{-1}$ , attributable to  $\text{NO}_L$  adsorbed within the CN adlayer, was only occasionally discerned in the corresponding differential FTIR spectra. One of these spectra obtained with reference and sample potentials of  $0.60 \text{ V}$  and  $0.20 \text{ V}$ , respectively, is shown in Figure 4.4 (A), where, besides the bipolar band of linearly adsorbed cyanide also observed in the spectrum in Figure 4.4 (A) (top), an additional band at  $1626 \text{ cm}^{-1}$ , corresponding to  $\text{NO}_L$ , can be observed. The band is positive, since at  $0.20 \text{ V}$  no nitric oxide remains on the surface (see Figure 4.3). The negative broad band around  $1460 \text{ cm}^{-1}$ , corresponding to  $\text{NH}_4^+$  produced by reduction of  $\text{NO}_{\text{ads}}$  at  $0.20 \text{ V}$ , is hardly observable, due to the small amount of  $\text{NO}_{\text{ads}}$  on the cyanide-modified Pt(111) electrode.

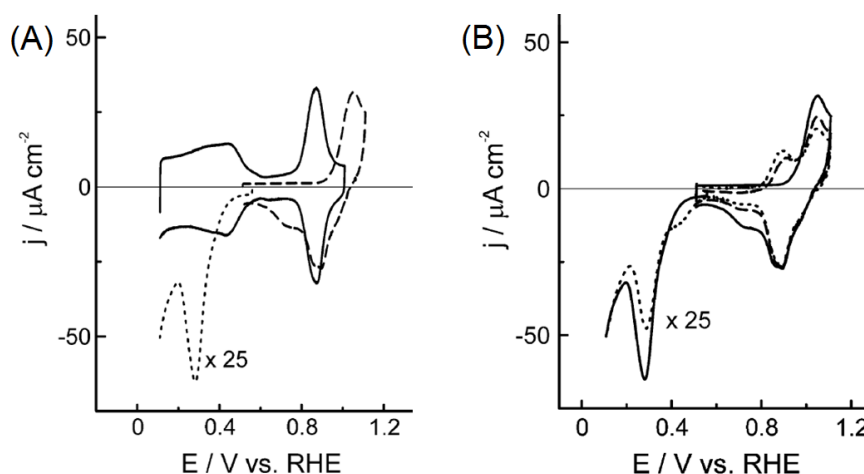


**Figure 4.3.** (A) CV at  $50 \text{ mV s}^{-1}$  of cyanide-modified Pt(111) (solid line), reductive stripping at  $2 \text{ mV s}^{-1}$  of  $\text{NO}_{\text{ads}}$  on cyanide-modified Pt(111) (dotted line), and CV at  $50 \text{ mV s}^{-1}$  between  $0.51 \text{ V}$  and  $1.11 \text{ V}$  of NO-covered cyanide-modified Pt(111) (dashed line). (B) First (solid line), second (dashed line) and third (dotted line) CVs between  $0.51 \text{ V}$  and  $1.11 \text{ V}$  of NO-covered cyanide-modified Pt(111), and reductive stripping at  $2 \text{ mV s}^{-1}$  of a freshly prepared NO adlayer (solid line) and of a NO adlayer submitted to three cycles between  $0.50 \text{ V}$  and  $1.11 \text{ V}$  (dotted line). The electrolyte was  $0.1 \text{ M HClO}_4$  in all cases.

In order to confirm that the band at  $1626\text{ cm}^{-1}$  corresponds to  $\text{NO}_L$  adsorbed within the CN adlayer, we performed a square-wave FTIR experiment (SW-FTIR), in which we alternatively collected 20 spectra (each of them consisting of 100 interferograms) at the reference potential (0.50 V) and 20 at the sample potential (0.80 V). Then, spectra collected at the same potential were co-added, thus improving the signal-to-noise ratio. Figure 4.4 (B) shows SW-FTIR spectra of the cyanide-modified Pt(111) electrode in 0.1 M  $\text{HClO}_4$  (top) and cyanide-modified Pt(111) in 0.1 M  $\text{HClO}_4$  after immersion in a 0.1 M  $\text{HClO}_4$  solution containing 0.01 M  $\text{KNO}_2$  (bottom). A weak but discernible band can be observed in the latter case around  $1620\text{ cm}^{-1}$ , supporting that the band at  $1626\text{ cm}^{-1}$  in the bottom spectrum of Figure 4.4 (A) is due to  $\text{NO}_L$  adsorbed within the CN adlayer.

The reductive stripping voltammogram of the NO-covered cyanide-modified Pt(111) electrode confirms the assignment by Rosca *et al.* [131] of the more positive cathodic peak in the negative scan of an NO-covered Pt(111) electrode to the reduction of  $\text{NO}_L$  to  $\text{NH}_4^+$ , while the more negative peak would correspond to the reduction of  $\text{NO}_M$ : since  $\text{NO}_M$  cannot exist on cyanide-modified Pt(111), the more negative reduction peak is absent. An interesting aspect is that the NO reduction peak on the cyanide-modified Pt(111) electrode (Figure 4.3) has a symmetric shape, in contrast with unmodified Pt(111) electrodes, onto which the first reduction peak, corresponding to the reduction of  $\text{NO}_L$ , shows a shoulder at positive potentials. Rosca *et al.* [131] attributed the latter behavior to the presence of two different local environments of the  $\text{NO}_L$  species (well-ordered two-dimensional domains and disordered domains). This interpretation is consistent with the results reported here for cyanide-modified Pt(111) electrodes, since in this case all the NO molecules will have a similar environment.

An oxidation-reduction process with peaks at 1.05 V (anodic) and 0.74 V (cathodic) (Figure 4.3 (A), dashed line), similar to that of NO oxidation and  $\text{HNO}_2$  reduction observed for the NO adlayer on the unmodified Pt(111) electrode with anodic and cathodic peaks at 1.01 and 0.64 V, respectively (Figure 4.1, dashed line), can also be observed for NO adsorbed on the cyanide-modified Pt(111) electrode. We assign them to the same redox process. As for the cathodic peak appearing at 0.89 V after oxidation of the NO adlayer up to 1.11 V (Figure 4.3 (A), dashed line), it coincides with that of OH desorption observed in the absence of adsorbed NO (Figure 4.3 (A), solid line), which suggests that, in the case of the cyanide-modified Pt(111) electrode, accommodation of the bulky  $\text{HNO}_2$  in the one-atom wide, two-atoms deep trenches of free Pt is hindered. This is clearly demonstrated in Figure 4.3 (B), where three successive sweeps between 0.50 V and 1.11 V are shown. As can be seen, successive cycling provokes a decrease of both the anodic peak at 1.05 V and the cathodic peak at 0.74 V, and the emergence of an anodic peak around 0.90 V, this coinciding with the potential of OH adsorption on an NO-free cyanide-modified Pt(111) electrode (see

Figure 4.3 (A), solid line). Reduction of the NO coverage during this redox process is confirmed by the fact that, if an NO-reduction stripping sweep is performed (Figure 4.3 (B), dashed line) after having carried out three NO oxidation – HNO<sub>2</sub> reduction cycles between 0.50 V and 1.11 V, the charge involved in the process is clearly smaller than that involved in the reduction of an unperturbed NO adlayer (Figure 4.3 (B), solid line), and a shoulder between 0.6 V and 0.4 V appears in the stripping voltammogram, probably owing to the adsorption of hydrogen on sites made accessible after partial desorption of NO.

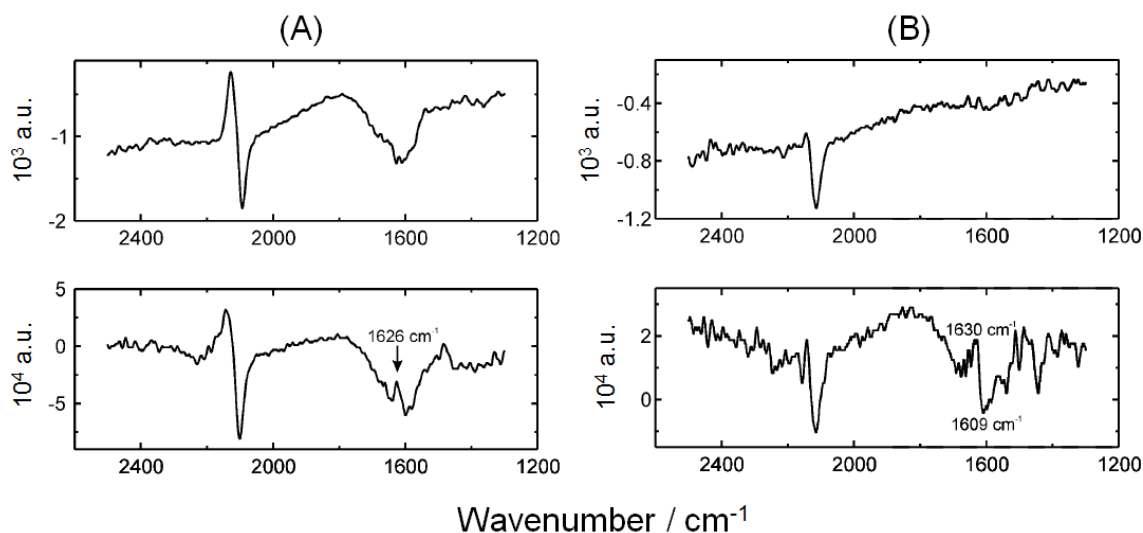


**Figure 4.4.** (A) Differential FTIR spectra, with sample and reference spectra recorded at 0.60 V and 0.20 V, respectively, of cyanide-modified Pt(111) in 0.1 M HClO<sub>4</sub> (top) and NO-covered cyanide-modified Pt(111) in 0.1 M HClO<sub>4</sub> (bottom). (B) SW-FTIR spectra of cyanide-modified Pt(111) in 0.1M HClO<sub>4</sub> (top) and NO-covered cyanide-modified Pt(111) in 0.1M HClO<sub>4</sub> (bottom). The reference and sample potentials were 0.50 V and 0.80 V, respectively.

#### 4.2.3. Mechanism of the NO electroreduction reaction on platinum

The coincidence between the potential of the peak attributed to the reductive stripping of NO<sub>L</sub> on Pt(111) electrodes (Figure 4.1) and the potential of the peak in the reductive stripping of NO<sub>ads</sub> on cyanide-modified Pt(111) (Figure 4.3 (A), dotted line) are the same suggests that NO reduction follows the same mechanism in the two cases. Figure 4.5 shows the potential of the peak of the reductive stripping of NO<sub>L</sub> on Pt(111) (dotted line in Figure 4.1) and on cyanide-modified Pt(111) versus the logarithm of the scan rate. The Tafel slope for the reductive stripping of NO<sub>L</sub> on Pt(111) is 46 mV (Figure 4.5, circles), in

agreement with the value reported by Beltramo and Koper [130], while the same process on cyanide-modified Pt(111) electrodes has a Tafel slope of 62 mV (Figure 4.5, squares).

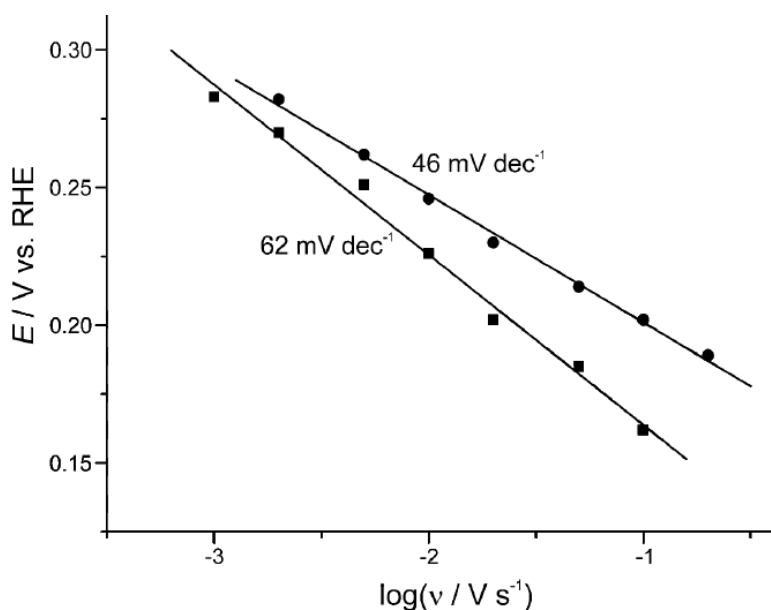


**Figure 4.5.** Semilogarithmic plot of the dependence on the scan rate of the peak potential of the reductive stripping of  $\text{NO}_L$  on Pt(111) (circles) and on cyanide-modified Pt(111) (squares).

The transfer coefficient,  $\alpha$ , is the inverse of the Tafel slope in dimensionless form:

$$b = \frac{2.3RT}{\alpha F} = \frac{59mV}{\alpha} \quad (4.1)$$

where  $b$  is the Tafel slope,  $R$  is the gas constant ( $R = 8.314 \text{ J K}^{-1} \text{ mol}^{-1}$ ),  $T = 298 \text{ K}$ , and  $F$  is the Faraday constant ( $F = 96485 \text{ C mol}^{-1}$ ). If the rate-determining step (*rds*) of the reaction is a chemical step,  $\alpha$  is determined by Equation 4.2:

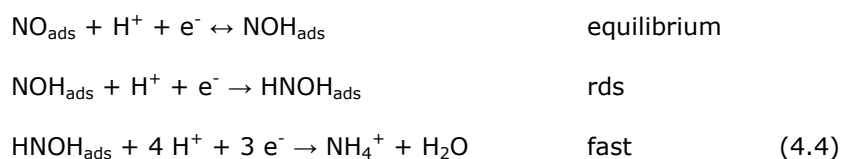
$$\alpha = \frac{n_b}{\nu} \quad (4.2)$$

in which  $n_b$  is the number of electrons being transferred before the *rds* and  $\nu$  is the stoichiometric coefficient, *i.e.*, the number of times that the *rds* must take place for the overall reaction to occur once. If the *rds* of the reaction is electrochemical,  $\alpha$  is given by Equation 4.3:

$$\alpha = \frac{n_b}{\nu} + \beta \quad (4.3)$$

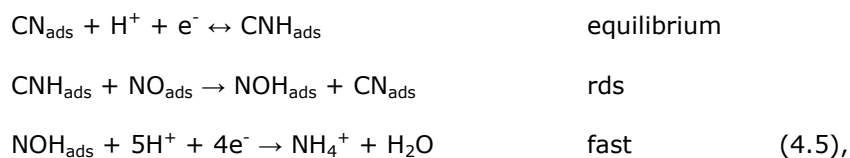
where  $\beta$  is the symmetry factor of the electrochemical *rds* (*i.e.* the fraction of the potential drop across the interface that is felt by the activated state), that is commonly assumed to have a value of 0.5.

A Tafel slope of *ca.* 40 mV (see Figure 4.5) suggests an electrochemical-electrochemical (EE) mechanism, consisting of an electrochemical equilibrium followed by a rate-determining electrochemical step (reaction mechanism 4.4).



Beltramo and Koper [130] proposed this same mechanism, with  $\text{HNO}_{\text{ads}}$  in the first step, instead of  $\text{NOH}_{\text{ads}}$ , because gas-phase HNO is *ca.* 100 kJ mol<sup>-1</sup> more stable than gas-phase NOH [135]. In this process the *rds* is an Eley-Rideal (ER) reaction<sup>3</sup>, involving a direct proton transfer from the solution to adsorbed NO. Beltramo and Koper [130] noted that, since NO reduction on clean Pt(111) starts in a potential region where no or very little adsorbed hydrogen is present on the surface (see Figure 4.2), the first two steps should involve instead a direct proton transfer from the solution to the adsorbed species.

On the contrary, and as has been noted in Chapter 3, on a cyanide-modified Pt(111) electrode hydrogen adsorption starts at a potential about 0.20 V more positive than on clean Pt(111), and, hence, NO reduction on a cyanide-modified Pt(111) electrode occurs in a potential region where  $\text{CNH}_{\text{ads}}$  is present. Accordingly, in agreement with the observed Tafel slope of 60 mV, we suggest that, in this case, the reduction of adsorbed NO follows an electrochemical-chemical mechanism:




---

<sup>3</sup> An Eley-Rideal reaction is a particular type of bimolecular catalytic reaction, in which one of the reacting species is adsorbed on the catalyst surface and the other one comes from the bulk of the gas or solution phase.

where the *rds* is a Langmuir-Hinshelwood (LH) reaction<sup>4</sup>. The slower formation of NOH<sub>ads</sub> on cyanide-modified Pt(111) as compared to the reaction on Pt(111) may be due to the sterical hindrance by adjacent CNH<sub>ads</sub> groups.

We suggest that the reduction of NO<sub>ads</sub> on Pt in acidic medium can proceed through any of the two mechanisms described above, depending on the availability of adsorbed hydrogen. If there is no or very little adsorbed hydrogen present on the surface, the reaction will follow path (4.4), characterized by a Tafel slope of *ca.* 40 mV, as in the case of Pt(111) electrodes. If, on the contrary, there is a considerable amount of adsorbed hydrogen, the reaction will follow path (4.5), characterized by a Tafel slope of *ca.* 60 mV, as in the case of cyanide-modified Pt(111) electrodes. In intermediate cases, both paths can occur simultaneously, yielding Tafel slopes intermediate between 40 and 60 mV, as in the case of Pt(554) [130] and Pt(poly) [131]. In the two mechanisms proposed above, N-O bond breaking occurs after the *rds*, which, as noted by Beltramo and Koper [130], is consistent with the lack of structure sensitivity observed for this reaction [130,131,136].

Although it is difficult to unravel the nature of the elementary steps occurring after the *rds*, some considerations can be made. Focusing first on mechanism 4.3, hydrogenation of the N atom of HNOH<sub>ads</sub> would yield hydroxylamine, but, in the absence of NO in the solution, only ammonia has been detected as the product of NO reduction [126,129,130,136], and so we believe that the *rds* is followed by a third hydrogenation process which involves breaking of the N-O bond, yielding H<sub>2</sub>O and adsorbed imide:



Two more hydrogenation processes would yield adsorbed amide and, finally, ammonia, which upon desorption would immediately be ionized to NH<sub>4</sub><sup>+</sup> in the acidic medium. Regarding mechanism 4.5, and by analogy to mechanism 4.4, we propose that, after the *rds*, hydrogenation of HNO<sub>ads</sub> yields HNOH<sub>ads</sub>, which then follows the path described above.

---

<sup>4</sup> A Langmuir-Hinshelwood reaction is a particular type of catalytic bimolecular reaction in which both reacting species are adsorbed on the catalyst surface.

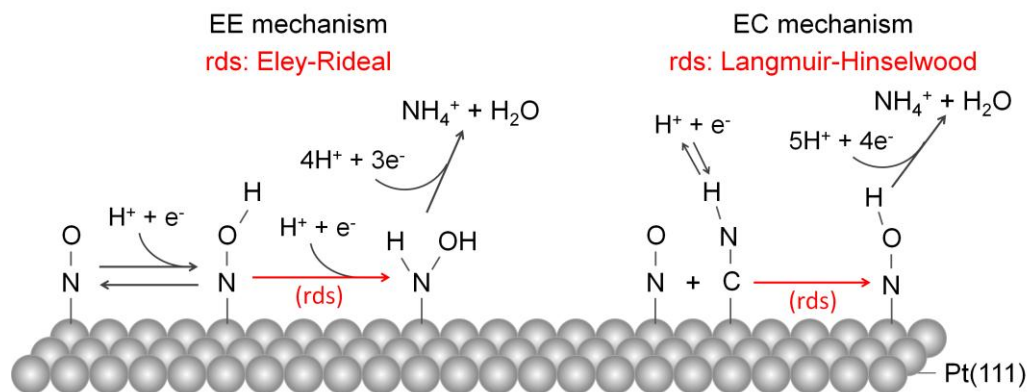


**Figure 4.6.** Reaction mechanisms proposed for the NO electroreduction reaction on Pt(111) and on cyanide-modified Pt(111) electrodes.

Finally, the results shown in this section demonstrate unequivocally that the reduction to ammonia of NO irreversibly adsorbed on Pt electrodes requires the presence of not more than two adjacent Pt atoms.

### 4.3. Hydrogen oxidation reaction

The hydrogen oxidation reaction (HOR) is one of the simplest, if not the simplest, electrocatalytic reactions and it has intensively been studied over the past decades [3], not only due to its fundamental interest, but also to its technological relevance in hydrogen-based fuel cells such as PEMFCs, PAFCs and AFCs. Platinum is the most active single-metal catalyst for the HOR both in acidic and in alkaline solutions. Regarding the use of hydrogen in fuel cells, Pt is so active that a very low Pt loading is necessary in the anode, and the development of alternative catalysts is not necessary when pure hydrogen is used as a fuel. However, when hydrogen is obtained by reforming of hydrocarbons, the Pt electrocatalyst is very easily poisoned by CO present in the fuel feed [137-139], CO concentrations as low as 10 ppm in the anode feed gas being required [139]. The development of CO-tolerant anode catalysts [140-142] is, hence, very important if fuel cells are to be fed with cheap hydrogen produced by reforming of hydrocarbons.

The HOR involves either the dissociative chemisorption of hydrogen onto the electrode surface (Tafel reaction, 4.7) or the electrochemical (one-electron oxidation) chemisorption of hydrogen (Heyrovsky reaction, 4.8), followed by the oxidation of adsorbed



hydrogen and the desorption of a proton (Volmer reaction, 4.9). Accordingly, the HOR may occur via a Tafel-Volmer (steps 4.7 and 4.9) or a Heyrovsky-Volmer (steps 4.8 and 4.9) mechanism. As can be observed, the Tafel reaction requires two contiguous Pt atoms, while a single surface Pt atom is enough for the Heyrovsky reaction to proceed. The hydrogen evolution reaction (HER) will obviously involve the same sequence of steps but in the inverse order (Volmer-Tafel or Volmer-Heyrovsky).



$\text{H}_{\text{ads}}$  is the reactive intermediate in the HOR and the HER (see Equations 4.6–4.8), and therefore, the kinetics of these two reactions are governed by the interaction of  $\text{H}_{\text{ads}}$  with the surface Pt atoms. Hydrogen adsorption on Pt is a structure sensitive reaction [3,143–147], due to the different adsorption sites and states available on surfaces with different structures and, consequently, Pt surfaces with different structures will show different activities towards the HOR and the HER. Figure 4.7 shows a schematic representation of the three reactions that can be involved in the HOR and the HER on Pt(111) electrodes.

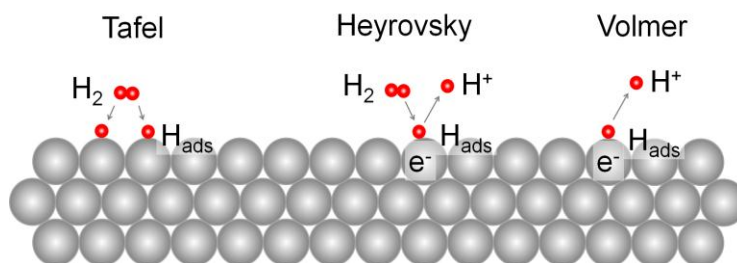


**Figure 4.7.** Schematic representation of the steps that can be involved in the HOR and the HER on Pt electrodes.

Even if the HOR and the HER consist of the same couple of reactions, their Tafel slopes will not necessarily have the same values, because the reaction sequence is inverted (in other words, a Tafel plot is not necessarily symmetric around the equilibrium potential).

- i. In the case of a Tafel-Volmer (HOR) or a Volmer-Tafel (HER) mechanism, assuming that the Tafel step is at equilibrium (*i.e.*, the Volmer step is rate-determining), the reaction rate will be given by  $j_{\text{HOR}} = k_3 \exp\left(\frac{\beta F \eta}{RT}\right) \theta_{\text{H}}$  and  $j_{\text{HER}} = k_{-3} \exp\left(\frac{-(1-\beta)F\eta}{RT}\right) c_{\text{H}}$  for the HOR and the HER, respectively, where  $\eta$  is the overpotential and  $\beta$  is the symmetry factor of the Volmer step. Assuming that  $\theta_{\text{H}}$  can be described by the Langmuir isotherm, at low coverage,

$$\theta_{\text{H}} = \sqrt{\frac{k_1}{k_{-1}}} c_{\text{H}_2} \quad (4.10)$$

and the reaction rate for the HOR will be given, hence, by:

$$j_{\text{HOR}} = k_3 \sqrt{\frac{k_1}{k_{-1}}} c_{\text{H}_2} \exp\left(\frac{\beta F \eta}{RT}\right) \quad (4.11)$$

Accordingly, for a mechanism composed of the Tafel and the Volmer reactions, with the Volmer step as the *rd*s and assuming  $\beta = 0.5$ , the Tafel slope will be 120 mV for both the HER and the HOR.

- ii. If the mechanism is composed of the Tafel and the Volmer reactions, but the Tafel reaction is not at equilibrium, the reaction rate of the HOR will depend only on the hydrogen concentration,  $j_{\text{HOR}} = k_1 c_{\text{H}_2}$ . In the case of the HER, the hydrogen coverage will be given, at low coverage and assuming that a Langmuir electroadsorption isotherm applies, by:

$$\theta_{\text{H}} = \frac{k_{-3}}{k_3} c_{\text{H}^+} \exp\left(\frac{F \eta}{RT}\right) \quad (4.12)$$

The reaction rate for the HER will be, hence, given by:

$$j_{\text{HER}} = k_{-1} \theta_{\text{H}}^2 = \frac{k_{-1} k_{-3}^2}{k_3^2} c_{\text{H}^+}^2 \exp\left(\frac{2F \eta}{RT}\right) \quad (4.13)$$

Accordingly, for a mechanism composed of the Tafel and the Volmer reactions, the Tafel slope will be infinite for the HOR and 30 mV for the HER if the Tafel step is not in equilibrium.

- iii. When the mechanism is composed of the Heyrovsky and the Volmer reactions and the Heyrovsky step is at equilibrium (*i.e.*, the Volmer step is the *rd*s),  $\theta_{\text{H}}$  at low coverage will be given, assuming that a Langmuir electroadsorption isotherm applies, by:

$$\theta_{\text{H}} = \frac{k_2}{k_{-2}} \frac{c_{\text{H}_2}}{c_{\text{H}^+}} \exp\left(\frac{F\eta}{RT}\right) \quad (4.14)$$

And, hence, the current density for the HOR and the HER will be:

$$j_{\text{HOR}} = k_3 \frac{k_2}{k_{-2}} \frac{c_{\text{H}_2}}{c_{\text{H}^+}} \exp\left[\frac{(1+\beta)F\eta}{RT}\right] \quad (4.15)$$

And,

$$j_{\text{HER}} = k_{-3} c_{\text{H}^+} \exp\left(\frac{-(1-\beta)F\eta}{RT}\right) \quad (4.16)$$

Accordingly, for a mechanism composed of the Heyrovsky and the Volmer reactions, the Tafel slope will be 40 mV for the HOR and 120 mV for the HER if the Volmer step is the *rds*.

- iv. On the contrary, if the mechanism is composed of the Heyrovsky and the Volmer reactions and the Heyrovsky reaction is not in equilibrium, the current density for the HOR and the HER will be:

$$j_{\text{HOR}} = k_2 c_{\text{H}_2} \exp\left(\frac{\beta_2 F\eta}{RT}\right) = k_3 \theta_{\text{H}} \exp\left(\frac{\beta_3 F\eta}{RT}\right) \quad (4.17)$$

And,

$$j_{\text{HER}} = k_{-2} c_{\text{H}^+} \theta_{\text{H}} \exp\left(\frac{-(1-\beta_2)F\eta}{RT}\right) \quad (4.18)$$

$\theta_{\text{H}}$  will be given by the Volmer equilibrium, so, assuming that a Langmuir electroadsorption isotherm applies, at low coverage:

$$\theta_{\text{H}} = \frac{k_{-3}}{k_3} c_{\text{H}^+} \exp\left(\frac{F\eta}{RT}\right) \quad (4.19)$$

Accordingly, in this case the Tafel slope will be 40 mV for the HER and 120 mV for the HOR.

The role of  $\text{H}_{\text{upd}}$  on the kinetics of the HOR remains unclear on Pt(111). Markovic and co-workers [145-147] proposed that both  $\text{H}_{\text{upd}}$  and  $\text{H}_{\text{opd}}$  compete for the same sites at potentials near the Nernst potential and that  $\text{H}_{\text{upd}}$  blocks the adsorption of hydrogen on active Pt sites. In contrast, Conway and Tilak [148] and Watanabe and co-workers [149] suggested that  $\text{H}_{\text{upd}}$  is the reactive intermediate on Pt surfaces.

The site-knockout strategy using cyanide-modified Pt(111) electrodes [31] may throw some light on the mechanism of the HOR on Pt(111) electrodes. Particularly interesting is the study of the HOR on CO-saturated cyanide-modified Pt(111) surfaces, onto which the CO coverage is 0.25 and hydrogen adsorption is not completely blocked [103].

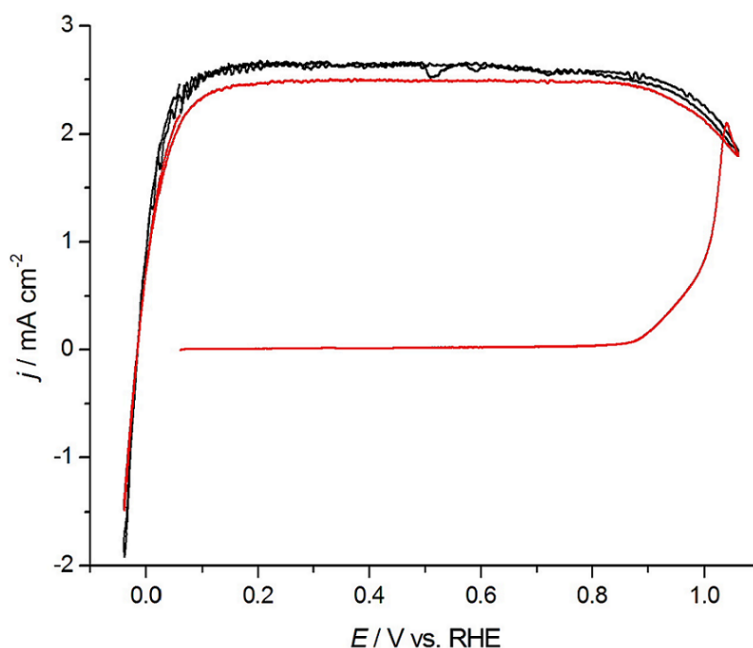
### 4.3.1. Hydrogen oxidation on cyanide-modified Pt(111) electrodes

Figure 4.8 shows the polarization curves during HOR on cyanide-modified Pt(111) electrodes with (red curve) and without (black curve) a saturated CO adlayer. As can be observed, cyanide-modified Pt(111) electrodes are as active for the HOR as unmodified Pt(111). Starting at 0.0 V in the positive direction, the HOR is first under mixed kinetic-diffusion control, and above ca. 0.1 V diffusion-limited currents are observed. This potential is slightly lower than the potential at which diffusion control is reached on unmodified Pt(111) surfaces [3,146,147]. Diffusion-limited current for the HOR is still observed at more positive potentials than on unmodified Pt(111) electrodes, due to the positive shift of the onset potential for OH adsorption on cyanide-modified Pt(111) electrodes. Hydrogen adsorption occurs at *fcc-hollow* sites on unmodified Pt(111) in the  $H_{\text{upd}}$  region. Since these sites have been shown in Chapter 3 to be unfavorable on cyanide-modified Pt(111), this result is a clear proof that three-fold hollow  $H_{\text{ads}}$  is not the intermediate in the HOR (and probably not in the HER, either).

Adsorption of CO on a cyanide-modified Pt(111) electrode does not block hydrogen adsorption completely [14,103], but there remains a current plateau in the corresponding CV extending from 0.05 V to 0.60 V, with a superimposed surface process with anodic and cathodic peaks at 0.31 V and 0.21 V, respectively [103]. Taking into account our new interpretation, based on a combination of experimental results and theoretical calculations, of the process occurring in the hydrogen adsorption region of a cyanide-modified Pt(111) electrode (see Chapter 3), we can now safely attribute the current measured between 0.05 V and 0.60 V in the CV of a cyanide-modified Pt(111) electrode covered by a saturated CO adlayer to the formation of  $\text{CNH}_{\text{ads}}$ , that has been affected by the presence of CO adsorbed within the troughs of the  $(2\sqrt{3} \times 2\sqrt{3})$  cyanide structure.

The black curve in Figure 4.8 shows that the HOR is completely blocked on cyanide-modified Pt(111) electrodes covered by a saturated CO adlayer, the activity being restored when adsorbed CO is oxidized to  $\text{CO}_2$ . An accurate determination of the CO coverage at saturation on a cyanide-modified Pt(111) electrode [103] yields a value of 0.25 ML, *i.e.*, there is one adsorbed CO molecule every two cyanide-free Pt atoms of the cyanide-modified Pt(111) electrodes. This result might suggest that isolated Pt atoms are inactive for the HOR,

whose first step should be, hence, the adsorption of hydrogen on two adjacent Pt atoms and the rupture of the H-H bond to yield two adsorbed H atoms (Tafel reaction). However, FTIR spectra of CO chemisorbed on cyanide-modified Pt(111) electrodes show the presence on the surface of both linearly and bridge-bonded adsorbed CO. A structure in which 50% of the  $\text{CO}_{\text{ads}}$  molecules on the surface of a cyanide-modified Pt(111) electrodes occupy bridge positions would block all the cyanide-free Pt atoms in this surface. Accordingly, and in the absence of STM images that can show us the spatial arrangement of the adsorbed CO molecules within the troughs of the cyanide-modified Pt(111) surface, no conclusion regarding the size of the atomic ensemble necessary for the HOR and, consequently, about the first step of the HOR being a Tafel or a Heyrovsky step, can be reached from this result.



**Figure 4.8.** RDE polarization curves at 1600 rpm and  $50 \text{ mV s}^{-1}$  recorded with a cyanide-modified Pt(111) electrode (black line) and with a cyanide-modified Pt(111) electrode covered with a saturated CO adlayer (red line, CO-free solution) in  $\text{H}_2$ -saturated 0.05 M  $\text{H}_2\text{SO}_4$ .

The absence of any activity for the HOR on cyanide-modified Pt(111) electrode covered by a saturated CO adlayer lets us, however, reach the important conclusion that the H in the  $\text{CNH}_{\text{ads}}$  groups (that can still be formed in the presence of co-adsorbed CO) cannot be the intermediate in the HOR. Once excluded both hydrogen adsorbed in the *fcc* threefold-hollow sites and H in the  $\text{CNH}_{\text{ads}}$  groups, the only possible intermediate in the HOR is hydrogen

adsorbed *on-top* of a Pt atom, in good agreement with previous spectroscopic studies [149-151].

Based on the results found on cyanide-modified Pt(111) surfaces, we can conclude that, contrary to the suggestions by Conway and Tilak [148] and Watanabe and co-workers [149],  $H_{\text{upd}}$  adsorbed at *fcc* threefold-hollow sites is not the reactive intermediate, but could have, on the contrary, a site-blocking effect, as suggested by Markovic and co-workers [145-147]. This might explain why on cyanide-modified Pt(111) electrodes, onto which  $H_{\text{upd}}$  adsorbed at threefold-hollow sites is absent, the diffusion-limited current is reached at more negative potentials than on unmodified Pt(111) electrodes.

## 4.4. Formic acid electrooxidation reaction

Direct formic acid fuel cells (DFAFCs) are very promising alternative energy conversion systems, especially for portable electronic devices, having the advantages over hydrogen fuel-cells of ease of handling of the fuel and flexibility in cell operation [152]. In addition, HCOOH is the simplest possible C1 oxygenated organic fuel, and its electrooxidation has often been considered as a model reaction in electrocatalysis. As a consequence, the electrooxidation of formic acid on Pt electrodes has attracted great interest over the past decades. This section is aimed at studying formic acid electrooxidation on cyanide-modified Pt(111) electrodes using cyclic voltammetry, Fourier transform infrared spectroscopy, and differential electrochemical mass spectrometry (DEMS). The latter experiments were performed by the supervisor of this Thesis during a short stay in the laboratories of Prof. Baltruschat at the University of Bonn (Germany), and have been included here for the sake of completeness.

It is well-known that the electrooxidation of oxygenated C1 molecules on platinum and other metal electrodes follows a dual-path mechanism [153,154], composed of a slow reaction pathway in which a poisoning species, adsorbed CO [53], is formed, and a direct path leading to  $\text{CO}_2$  without formation of the electrocatalytic poison. The electrooxidation of methanol and formaldehyde, which are also of great technological importance, through the direct pathway follows a sequential mechanism in which the formation of formic acid precedes the complete oxidation to  $\text{CO}_2$  [155]. For this reason, the identification of the intermediates formed during the electrocatalytic oxidation of formic acid is also essential in order to unveil the details of the reaction mechanisms of the oxidation of more complicated molecules on metal electrodes [58,156,157]. Osawa and co-workers [54-58] have shown by ATR-SEIRAS that the reactive intermediate in the oxidation of formic acid is bridge-bonded

adsorbed formate, and the details of the reaction mechanism of the direct pathway have been described by Cuesta *et al.* [60]. Very recently, Cuesta *et al.* have demonstrated that adsorbed formate is also the intermediate in the indirect path [59].

From a fundamental point of view, the determination of the smallest number of surface atoms necessary for a given reaction to proceed can be of the utmost importance when trying to solve its mechanism. From an applications perspective, if the reaction proceeds through two parallel paths, the knowledge of the smallest number of surface atoms required by each of them could help us to channel the reaction through the desired pathway, by fabricating a surface lacking those sites necessary for the undesired pathway and containing only those sites required for the desired one. In order to gain more information about the mechanism of the formic acid oxidation reaction, we performed voltammetric and spectroscopic studies on Pt(111) and cyanide-modified Pt(111) surfaces in acidic solutions containing different concentrations of formic acid.

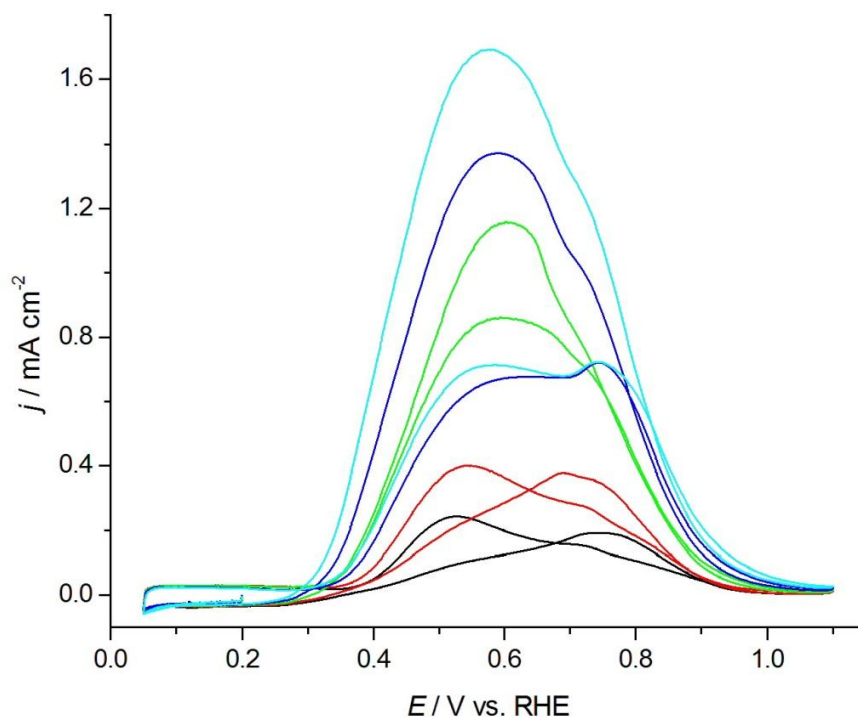


**Figure 4.9.** Cyclic voltammograms at  $50 \text{ mV s}^{-1}$  of a Pt(111) electrode in  $0.1 \text{ M HClO}_4 + x \text{ M HCOOH}$ ;  $x = 10^{-3}$  (black),  $2 \times 10^{-3}$  (red),  $0.01$  (green),  $0.02$  (blue) and  $0.1$  (cyan). The scan starts at  $0.20 \text{ V}$  in the negative direction.

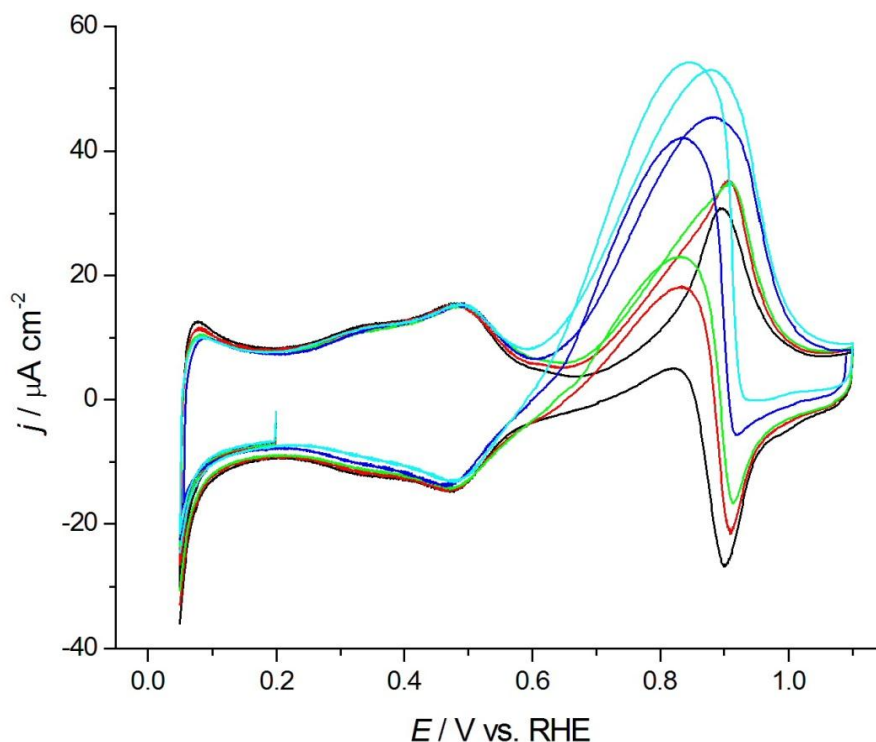
Figure 4.9 shows cyclic voltammograms on Pt(111) surfaces in 0.1 M perchloric acid solutions containing different concentrations of formic acid from 1 mM to 0.1 M. As can be observed, adsorbed hydrogen ( $E < 0.30$  V vs. RHE) blocks the adsorption of formate, which is the first step in HCOOH oxidation on Pt(111). The voltammograms show a clear hysteresis between positive-going and negative-going scans due to the formation of adsorbed CO at low potentials during the positive-going scan. At potentials above 0.75 V  $\text{CO}_{\text{ads}}$  is oxidized, and the surface remains free from adsorbed CO during the initial portion of the negative scan. All the surface sites are available for the direct oxidation reaction and, therefore, currents are higher than in the positive-going scan. It must be noted that the differences between the positive-going and the negative-going scans are higher in perchloric acid than in sulphuric acid solutions [158], due to the presence in the latter of (bi)sulphate anions, which in part inhibit  $\text{CO}_{\text{ads}}$  formation.

#### 4.4.1. Formic acid oxidation on cyanide-modified Pt(111) electrodes

Cyclic voltammograms on cyanide-modified Pt(111) in 0.1 M perchloric acid solutions containing different concentrations of formic acid from 1 mM to 0.2 M are shown in Figure 4.10. The first clear difference with the voltammograms in the presence of formic acid of unmodified Pt(111) is that the hydrogen adsorption region ( $E < 0.55$  V) is unaffected by HCOOH, indicating that, contrary to what happens with Pt(111) electrodes (at potentials above 0.30 V), formation of the poisoning species does not occur in this potential region. Formic acid oxidation starts at *ca.* 0.55 V, a potential at which there is no adsorbed hydrogen. As can be observed, and contrary to unmodified Pt(111) electrodes (Figure 4.9), there is no hysteresis between the positive and the negative sweeps. This indicates that the amount of  $\text{CO}_{\text{ads}}$  formed on cyanide-modified Pt(111) electrodes must be very small, if any. The lack of hysteresis is not observable at low concentrations of HCOOH due to the very low oxidation currents, that overlap with the OH adsorption-desorption feature.

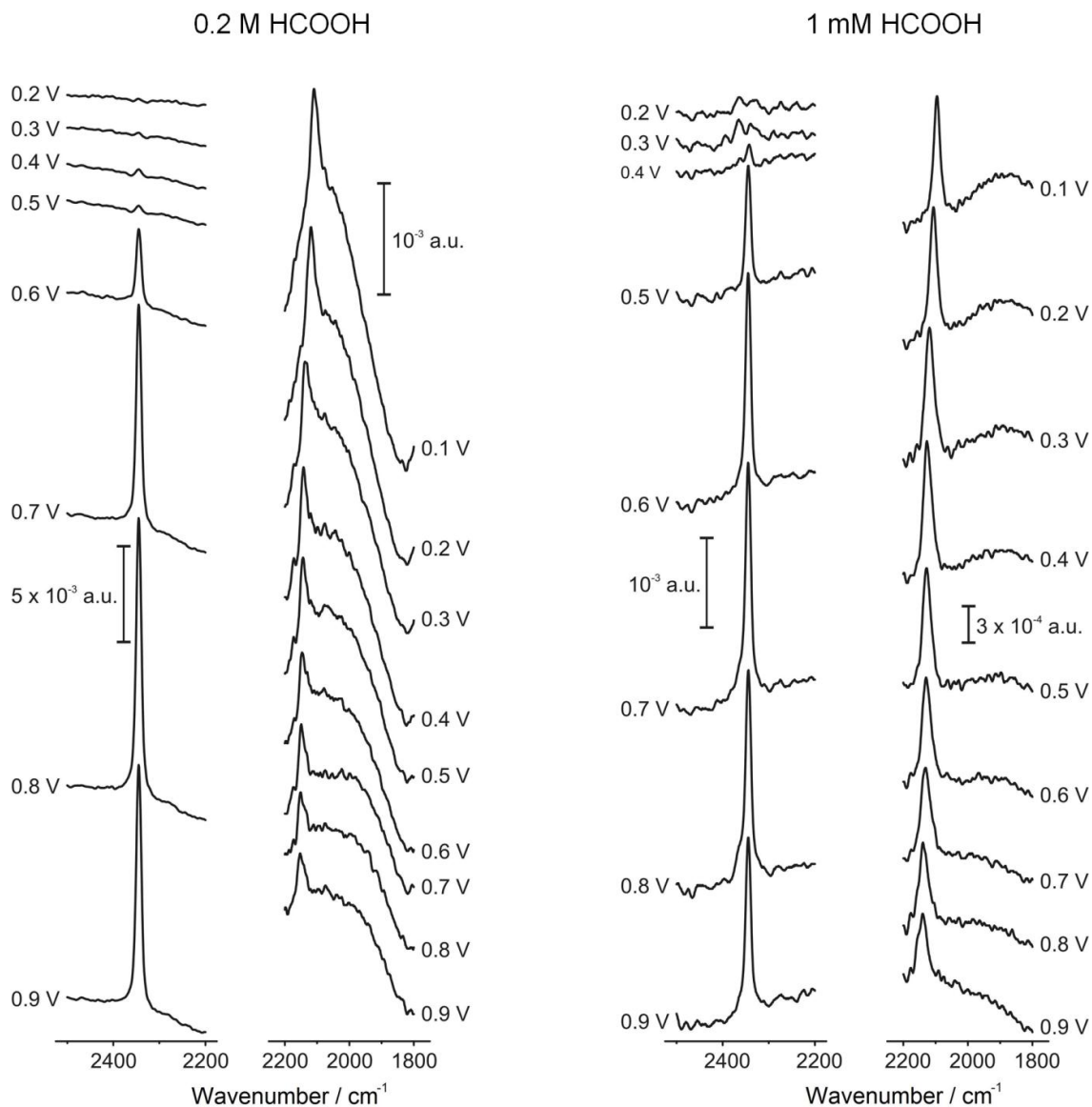
Figure 4.10 also shows that, in the negative-going sweep, the current increases sharply at 0.90 V, coinciding with OH desorption. This is a clear indication that  $\text{OH}_{\text{ads}}$  is a poison for formic acid oxidation, in agreement with the hypothesis according to which adsorbed formate is the intermediate in the reactive pathway of formic acid oxidation [54-58,60], and can decompose to  $\text{CO}_2$  without reacting with co-adsorbed OH. Since adsorbed formate already contains two oxygen atoms,  $\text{OH}_{\text{ads}}$  most likely blocks the sites necessary for the reaction between two adjacent formate species [60].





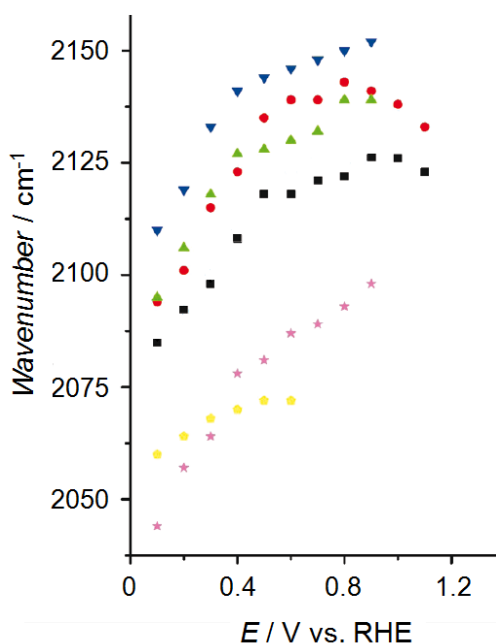
**Figure 4.10.** Cyclic voltammograms at  $50 \text{ mV s}^{-1}$  of a cyanide-modified Pt(111) electrode in  $0.1 \text{ M HClO}_4 + x \text{ M HCOOH}$ ;  $x = 10^{-3}$  (black),  $0.01$  (red),  $0.02$  (green),  $0.1$  (blue) and  $0.2$  (cyan). The scan starts at  $0.20 \text{ V}$  in the negative direction.

Figure 4.11 shows a series of FTIR spectra at increasing potentials recorded during formic acid oxidation on a cyanide-modified Pt(111) electrode in  $0.1 \text{ M HClO}_4$  containing either  $0.2 \text{ M HCOOH}$  (left) or  $1 \text{ mM HCOOH}$  (right). The spectra in the frequency region between  $2500 \text{ cm}^{-1}$  and  $2200 \text{ cm}^{-1}$  were calculated using the spectrum at  $0.10 \text{ V}$  as reference, in order to monitor the potential at which  $\text{CO}_2$  starts to appear, while the spectra in the frequency region between  $2200 \text{ cm}^{-1}$  and  $1800 \text{ cm}^{-1}$  were calculated using the spectrum at  $1.30 \text{ V}$  as reference, in order to obtain positive bands for both  $\text{CN}_{\text{ads}}$  and  $\text{CO}_{\text{ads}}$  and, thus, to better monitor the possible appearance of the latter. The spectra in Figure 4.11 confirm the assumptions made above based on the voltammetric results in Figure 4.10: formic acid electrooxidation, indicated by the positive  $\text{CO}_2$  band at  $2343 \text{ cm}^{-1}$ , starts between  $0.50 \text{ V}$  and  $0.60 \text{ V}$  in  $0.2 \text{ M HCOOH}$ , and around  $0.50 \text{ V}$  in  $1 \text{ mM HCOOH}$ , and no band corresponding to adsorbed CO (the poison intermediate) is observed, confirming that it is not formed at all during formic acid oxidation on cyanide-modified Pt(111) electrodes.



**Figure 4.11.** FTIR spectra at increasing potentials of cyanide-modified Pt(111) in 0.1 M HClO<sub>4</sub> + 0.2 M HCOOH (left) and 0.1 M HClO<sub>4</sub> + 1 mM HCOOH (right). The spectra in the frequency region between 250 cm<sup>-1</sup> and 2200 cm<sup>-1</sup> were calculated using the spectrum at 0.10 V as a reference, while the spectra in the frequency region between 2200 cm<sup>-1</sup> and 1800 cm<sup>-1</sup> were calculated using the spectrum at 1.30 V as a reference.

Additional information can be gained from the dependence of the frequency of the  $\text{CN}_L$  band on the electrode potential in formic acid containing solutions. Figure 4.12 shows the potential dependence of the  $\text{CN}_L$  stretching frequency of the cyanide-modified Pt(111) electrode (black squares), of the  $\text{CN}_L$  and  $\text{CO}_L$  stretching frequencies of cyanide-modified Pt(111) covered by a saturated CO adlayer (red circles and purple stars, respectively), of the  $\text{CN}_L$  stretching frequency of the cyanide-modified Pt(111) electrode in 1 mM (green triangles) and in 0.2 M HCOOH (blue inverted triangles) solutions, and of the  $\text{CO}_L$  stretching frequency of the Pt(111) electrode covered by a saturated CO adlayer in CO-free 0.1 M HClO<sub>4</sub> (yellow pentagons). As explained in Chapter 3, the frequency vs. potential plot of the  $\text{CN}_L$  band of cyanide-modified Pt(111) (Figure 4.12, black squares) shows two clearly different slopes, the higher slope at  $E \leq 0.50$  V being due to the formation of  $\text{CNH}_{\text{ads}}$ . The  $\text{CO}_L$  band of CO adsorbed on cyanide-modified Pt(111) (purple stars in Figure 4.12) also shows a higher Stark tuning rate ( $109 \text{ cm}^{-1} \text{ V}^{-1}$ ) at  $E \leq 0.50$  V (coinciding with the potential region where there is hydrogen adsorption) than at  $E \geq 0.50$  V ( $40 \text{ cm}^{-1} \text{ V}^{-1}$ ), although in this case the difference is smaller. This is most likely also due to the formation of  $\text{CNH}_{\text{ads}}$  at  $E \leq 0.50$  V.



**Figure 4.12.** Dependence on the electrode potential of the frequency of: the  $\text{CN}_L$  band of cyanide-modified Pt(111) in 0.1 M HClO<sub>4</sub> (black squares), the  $\text{CN}_L$  band of CO-covered cyanide-modified Pt(111) in 0.1 M HClO<sub>4</sub> (red circles), the  $\text{CN}_L$  band of cyanide-modified Pt(111) in 0.1 M HClO<sub>4</sub> + 1 mM HCOOH (green triangles), the  $\text{CN}_L$  band of CN-Pt(111) in 0.1 M HClO<sub>4</sub> + 0.2 M HCOOH (blue inverted triangles), the  $\text{CO}_L$  band of CO-covered cyanide-modified Pt(111) in 0.1 M HClO<sub>4</sub> (purple stars) and the  $\text{CO}_L$  band of  $\text{CO}_{\text{ads}}$  on Pt(111) in 0.1 M HClO<sub>4</sub> (yellow pentagons).

Although the spectra in Figure 4.11 clearly show that no adsorbed CO forms on the electrode surface during formic acid electrooxidation, the  $\text{CN}_L$  stretching frequency increases as compared to the case in HCOOH-free solution. The increase in 1 mM HCOOH solution is similar to that observed for a cyanide-modified Pt(111) electrode covered by a saturated CO adlayer, while in 0.2 M HCOOH solutions the increase is clearly larger. Since  $\text{CO}_{\text{ads}}$  cannot be the reason for this increase, it must be concluded that, in formic acid-containing solutions, there is another adsorbate on the surface of the cyanide-modified Pt(111) electrode. This adsorbed species must be the active intermediate in the direct reaction pathway, *i.e.*, adsorbed formate [54-58,60]. Since adsorbed formate must form from formic acid in the solution, its coverage will be the higher the more concentrated the solution, thus explaining the larger increase in the stretching frequency of  $\text{CN}_L$  in 0.2 M HCOOH as compared to 1 mM HCOOH.

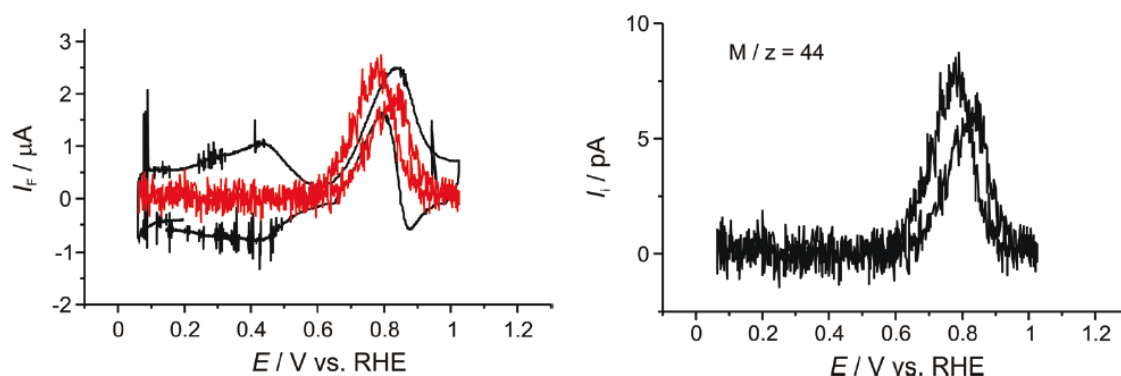
The effect of adsorbed hydrogen on the electrooxidation of formic acid on cyanide-modified Pt(111) is also worth of being discussed. In the  $\text{H}_{\text{upd}}$  region, the CV in HCOOH-containing solutions overlaps that in HCOOH-free solutions, suggesting that neither CO nor any other HCOOH-derived adsorbate forms on the surface within this potential region. This is in contradiction with the FTIR data, which, contrary to what happens in the case of methanol [115], show an increase in the stretching frequency of  $\text{CN}_L$  in 1 mM and in 0.2 M HCOOH even at potentials within the hydrogen adsorption region. This apparent contradiction can only be explained by assuming that adsorbed formate does not block the sites for hydrogen adsorption on cyanide-modified Pt(111), in good agreement with the conclusion reached in Chapter 3 that  $\text{H}_{\text{ads}}$  on cyanide-modified Pt(111) corresponds to  $\text{CNH}_{\text{ads}}$ . Interestingly, if this hypothesis is correct, it implies that  $\text{CNH}_{\text{ads}}$  hinders the decomposition of adsorbed formate to  $\text{CO}_2$ . We suggest here that this might be due to a reduced mobility of adsorbed formate in the presence of  $\text{CNH}_{\text{ads}}$ , and/or to the latter hindering the formation of the transition state.

Figure 4.13 shows the CV and the simultaneously recorded mass spectrometric cyclic voltammogram (MSCV,  $m/z$  44) of cyanide-modified Pt(111) in 0.1 M  $\text{HClO}_4$  + 1 mM HCOOH. The low concentration of formic acid used is due to the fact that, with higher concentrations a continuous increase in the intensity of the  $m/z$  44 signal was observed, which made the quantitative analysis of the DEMS results difficult. The red line in Figure 4.13 (left) is the faradaic current corresponding exclusively to  $\text{CO}_2$  formation, as calculated from the ion current for  $m/z$  44 shown in Figure 4.13 using Equation 4.20 [159], where  $n$ , the number of electrons transferred in the oxidation of CO to  $\text{CO}_2$ , is two. The calibration constant,  $K^*$ , was calculated as the ratio between the faradaic charge,  $Q_f^{\text{CO}}$ , and the charge obtained by

integration of the ion current for  $\text{CO}_2$ ,  $Q_i(44)$ , measured during the stripping of a  $\text{CO}_{\text{ads}}$  monolayer in a calibration experiment (Equation 4.21).

$$I_f^* = \frac{nI_i(44)}{K^*(44)} \quad (4.20)$$

$$K^*(44) = \frac{nQ_i(44)}{Q_f^{\text{CO}}} \quad (4.21)$$



**Figure 4.13.** CV (left, black line) and MSCV (right) recorded simultaneously during the oxidation of formic acid on cyanide-modified Pt(111) in 0.1 M  $\text{HClO}_4$  + 1 mM  $\text{HCOOH}$ . Scan rate:  $10 \text{ mV s}^{-1}$ . The red line (left) corresponds to the faradaic current due to  $\text{CO}_2$  formation, as calculated from the ion current for  $m/z$  44 in the MSCV (right). Adapted from reference [115].

Since  $\text{CO}_2$  is the only possible product in formic acid oxidation, the current efficiency for  $\text{CO}_2$  formation is of 100%. The differences between the current in the CV and the faradaic current calculated from the MSCV are due to the contribution of the double layer charging and the OH adsorption-desorption process to the current in the CV. The results in Figure 4.13 do not throw any light regarding the formation of  $\text{CO}_{\text{ads}}$  during formic acid oxidation on cyanide-modified Pt(111) electrodes. For this reason, after performing the experiment in Figure 4.13, the potential was stopped at 0.2 V, the solution containing 1 mM  $\text{HCOOH}$  was exchanged by a solution containing only 0.1 M  $\text{HClO}_4$ , and new CV and MSCV were recorded. The CV coincided with that recorded before introduction of formic acid into the cell, and no current at  $m/z$  44 could be detected in the simultaneous MSCV, confirming that no  $\text{CO}_{\text{ads}}$  had been formed during the previous CV in the presence of formic acid.

The combination of voltammetric, spectroscopic and mass spectrometry experiments demonstrates that, as in the case of methanol [38], CO formation during formic acid electrooxidation, requires sites composed of three contiguous Pt atoms, and is, hence, inhibited on cyanide-modified Pt(111) surfaces, where all the sites are absent. On the contrary, direct oxidation of formic acid to CO<sub>2</sub> without passing through CO<sub>ads</sub> occurs unhindered on cyanide-modified Pt(111) electrodes, suggesting that in the corresponding transition state adsorbed formate does not need to interact with more than two adjacent Pt atoms, in agreement with recent theoretical calculations by Neurock *et al.* [160].

The suggestion that dehydration of formic acid to adsorbed CO requires a larger atomic ensemble than its electrooxidation to CO<sub>2</sub> can be traced back to the earliest reports of purely geometric effects in electrocatalysis [29,30,33]. However, this conclusion has been recently criticized by Grozovski *et al.* [161-163], who, based on pulsed voltammetry experiments on Pt stepped surfaces, suggested that formation of CO<sub>ads</sub> on Pt(111) electrodes and on stepped Pt single-crystals containing (111) terraces occurs exclusively at steps and other defect sites, in good agreement with previous work by Maciá *et al.* [164-166]. They suggested that CO<sub>ads</sub> should not form on ideal Pt(111) surfaces, and attributed, therefore, the findings obtained using cyanide-modified Pt(111) electrodes to the blockage of the defects by CN<sub>ads</sub> and not to the structure of this chemically-modified Pt electrodes.

Grozovski *et al.* [161-163] also found that dehydration of HCOOH forming CO<sub>ads</sub> on Pt stepped surfaces takes place only in a narrow potential window close to the potential of zero total charge ( $E_{\text{pztc}}$ ). Since the local  $E_{\text{pztc}}$  at steps is lower than at (111) terraces, the  $E_{\text{pztc}}$  of stepped Pt single-crystal electrodes containing (111)-oriented terraces decreases linearly with increasing step density [167,168] and formation of CO<sub>ads</sub> will be therefore expected to occur at lower potentials on stepped surfaces. By extrapolation of the values of the dehydration reaction rate constant obtained with stepped Pt[n(111) x (111)] single-crystal electrodes, Grozovski *et al.* [162] deduced a negligible value for the activity of an ideal Pt(111) surface towards dehydration of formic acid, but the extrapolation was performed at a constant potential of 0.15 V vs. RHE, clearly below the  $E_{\text{pztc}}$  of Pt(111) [132,169]. The highest activity of Pt(111) electrodes for formic acid dehydration (attributed to the small amount of defects always present even in the best possible real Pt(111) electrode) was observed around 0.3 V [162], nearly coinciding with the  $E_{\text{pztc}}$  of Pt(111). Even at the maximum, the activity of Pt(111) for dehydration of formic acid was very low, but it must be noted that all the experiments reported by Grozovski *et al.* were performed in sulphuric acid solutions, and that it is well known that sulphate adsorbs specifically on Pt(111) surfaces occupying trigonal sites, exactly those that, according to our results with cyanide-modified Pt(111) electrodes, are needed for the formation of adsorbed CO from adsorbed formate [115].

It is also worth noting that Chang *et al.* [34] observed a negative shift of the potential at which CO formation starts during formic acid oxidation on a Pt(111) electrode upon deposition of 0.20-0.25 ML of Bi. At this relatively high Bi coverage all the defect sites on a Pt(111) electrode should be blocked by Bi, and the observation reported by Chang *et al.* might be explained by the decrease of the  $E_{\text{pztc}}$  of Pt(111) [170]. Our conclusion is, therefore, that formic acid dehydration requires at least three contiguous atoms, but that defect sites have a higher activity due to their lower local  $E_{\text{pztc}}$ .

It has been very recently suggested [59] that adsorbed formate is not only the reactive intermediate in the direct path of formic acid electrooxidation, but also in the indirect path, *i.e.*, that it is the bifurcation point of the dual-path mechanism, where it is decided which path will be followed. Obviously, if both paths share the same intermediate their corresponding transition states must be different. Since the indirect path is blocked on cyanide-modified Pt(111) electrodes, it must be concluded that the transition state connecting adsorbed formate with adsorbed CO cannot be reached on this surface. Accordingly, this transition state must involve the simultaneous interaction with three contiguous Pt atoms.

## 4.5. Oxygen reduction reaction

The main obstacle to the development of fuel cells as a commercially competitive reality is the high overpotential required for the oxygen reduction reaction (ORR) to proceed at an adequate rate. Due to this fact, the ORR has been the most intensively studied fuel-cell reaction over the last two decades (see, for example, [3,22,23,44,45,61,171,172]). A suitable electrocatalyst for the ORR must be noble enough to minimize adsorption of poisonous 'spectator' species but at the same time, it must be catalytically active enough to break the O-O bond and reduce oxygen at potentials that are as close as possible to the equilibrium potential.

The most active electrocatalysts known for the ORR are all Pt-based materials. In practical fuel-cell catalysts the amount of Pt must be reduced as much as possible for economic reasons, and the production of hydrogen peroxide must be minimized, in order to increase the durability of the membrane and other materials in the cell. Therefore, a catalyst must favor the complete, 4-electron reduction to H<sub>2</sub>O over the partial, 2-electron reduction to H<sub>2</sub>O<sub>2</sub>, must show a measurable oxygen-reduction current at the lowest possible overpotential, and must have the highest possible value of the exchange current density.

The most widely used approach to improve the activity of Pt-based electrocatalysts has been the modification of the electronic properties of the surface atoms by alloying Pt with other metals [23,44,172] or by synthesizing Pt core-shell catalysts [45,65-67]. Although an increase of the affinity of the surface atoms for oxygen will also have the undesired effect of increasing the strength of the interaction with spectators, these strategies have proved themselves successful for the design of electrocatalysts for PEMFCs [43]. However, in environments containing a high concentration of potential spectator species, as in the case of PAFCs, the improvement of the catalyst using this strategy becomes impossible. An alternative strategy to design active catalysts that can work in environments in which the ORR is controlled by the adsorption of spectator anions, such as sulphuric or phosphoric acid anions, might be to engineer the surface at the atomic level with the aim of designing surfaces where the sites necessary for the adsorption of spectator anions have been blocked, while providing the sufficient number of free Pt atoms required for the oxygen molecule to chemisorb and for the O-O bond to be broken. We will illustrate the feasibility of this approach using cyanide-modified Pt(111) electrodes.

#### 4.5.1. Oxygen reduction on cyanide-modified Pt(111) electrodes

Rotating disk electrode (RDE) polarization curves recorded with Pt(111) and cyanide-modified Pt(111) electrodes in oxygen saturated sulphuric acid solutions are shown in Figure 4.14. As can be observed, the curves show the same four regions on both Pt(111) and cyanide-modified Pt(111) electrodes: at the most positive potentials, the surface is inactive and zero current density is detected. This is followed by a potential region where the complete (4-electron, Reaction 4.22) reduction of oxygen to H<sub>2</sub>O occurs under kinetic control, the current increasing exponentially with decreasing potential. Then, when the reaction is so fast that the concentration of oxygen in the electrolyte layer adjacent to the electrode surface is zero, the diffusion-limited current is reached. Finally, at the most negative potentials, there is a change from the 4-electron to the 2-electron reduction, and hydrogen peroxide is formed (Reaction 4.23).



As can be observed in Figure 4.14 (black line), in sulphuric acid solutions there is a high deactivation of the ORR on Pt(111) electrodes, due to the strong adsorption of sulphuric acid anions. However, a considerable decrease in the overpotential and a massive increase in the kinetic current is observed on the cyanide-modified Pt(111) surface. In the case of



reactions that are first order with respect to the concentration of the reactant, the Koutecky-Levich equation,

$$\frac{1}{j} = \frac{1}{j_k} + \frac{1}{j_l} \quad \rightarrow \quad j_k = \frac{j_l \cdot j}{j_l - j} \quad (4.24)$$

can be used to determine the kinetic current,  $j_k$ , *i.e.*, the current in the absence of any mass-transfer effects, from the current experimentally measured in the potential region of mixed kinetic-transport control,  $j$ . At 0.85 V,  $j_k = -0.18 \text{ mA cm}^{-2}$  and  $j_k = -5.2 \text{ mA cm}^{-2}$  on Pt(111) and on cyanide-modified Pt(111) electrodes, respectively, *i.e.*, in spite of having 50% less Pt free atoms, the cyanide-modified Pt(111) surface is 29 times more active than the unmodified Pt(111) electrode. Similarly, in phosphoric acid solutions cyanide-modified Pt(111) electrodes were found to be 10 times more active than Pt(111) electrodes (not shown).

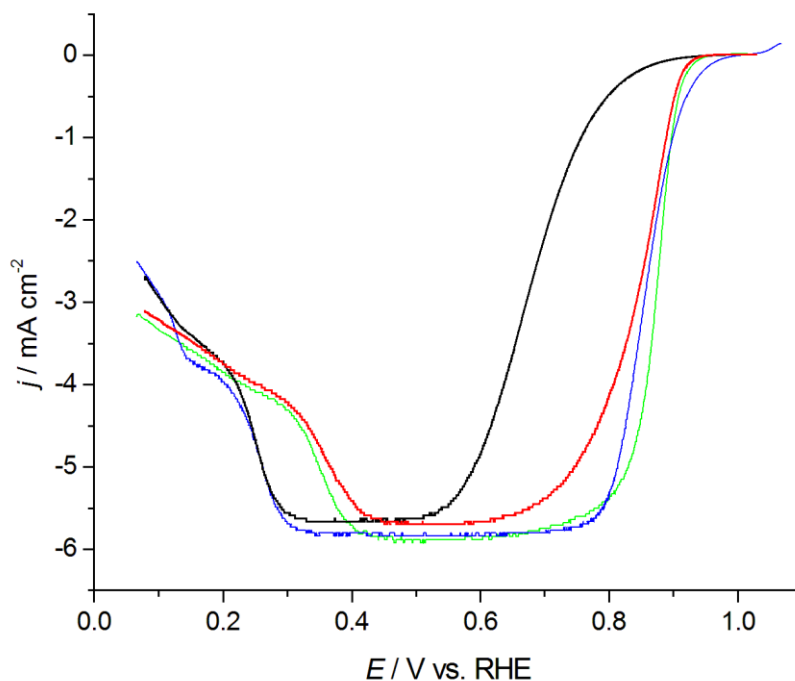


**Figure 4.14.** RDE polarization curve at 1600 rpm and  $50 \text{ mV s}^{-1}$  for the ORR on Pt(111) (black curve) and cyanide-modified Pt(111) (red curve) in oxygen-saturated 0.05 M  $\text{H}_2\text{SO}_4$ . The blue and green lines correspond to the polarization curves for the ORR on Pt(111) and cyanide-modified Pt(111), respectively, in oxygen-saturated 0.1 M  $\text{HClO}_4$ .

Figure 4.14 also shows that the ORR on cyanide-modified Pt(111) in sulphuric acid solution is nearly the same as in perchloric acid solution, suggesting that sulphuric acid anion adsorption is nearly completely inhibited on the cyanide-modified Pt(111) surface, and that the activity is controlled completely by the coverages of  $\text{CN}_{\text{ads}}$  and  $\text{OH}_{\text{ads}}$ . The inhibition of the specific adsorption of anions in sulphuric and phosphoric acid is most likely due to the blockage of the trigonal sites necessary for the specific adsorption of the sulphuric and phosphoric acid anions by cyanide. Oxygen and reaction intermediates are adsorbed to a low coverage and play a rather small role in controlling the rate of the ORR on Pt [175].

The enhancement of the ORR found for cyanide-modified Pt(111) electrodes in sulphuric and phosphoric acid solutions as compared with unmodified Pt(111) is in complete concordance with the idea that the primary role of  $\text{CN}_{\text{ads}}$  is to block selectively the adsorption of sulphuric and phosphoric acid anions, while allowing adsorption of oxygen on the free Pt sites, as represented in Figure 4.15 [176]. On Pt(111) covered by phosphoric or sulphuric acid anions oxygen can access the surface atoms only through a small number of holes in the anion adlayer. As can be observed in Figure 4.15, the number of sites required for oxygen adsorption is significantly increased on the cyanide-modified Pt(111) surface because adsorption of phosphoric or sulphuric acid anions is suppressed by the  $\text{CN}_{\text{ads}}$  adlayer. We note that above 0.70 V the total coverage by  $\text{CN}_{\text{ads}}$  and  $\text{OH}_{\text{ads}}$  on cyanide-modified Pt(111) is lower than the coverage by sulphuric and phosphoric acid anions on unmodified Pt(111).

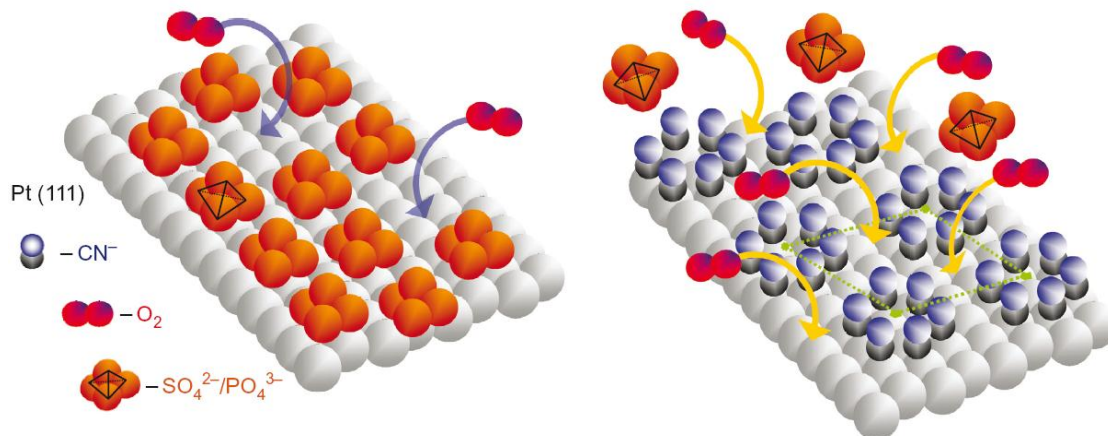


**Figure 4.15.** Proposed model for the selective adsorption of spectator sulphuric or phosphoric acid anions and of reactants and schematic presentation of the availability of Pt atoms for adsorption of  $\text{O}_2$  molecules on cyanide-free (left) and cyanide-covered (right) Pt(111) surfaces. Adapted from reference [176].

Based on all the previous experimental facts, and assuming a small change of the apparent standard free energy of adsorption of O<sub>2</sub> and its reaction intermediates with the surface coverage by adsorbing species, the general rate expression (current density  $j$  at a *constant* electrode potential  $E_1$ ) for the ORR on metal surfaces has been proposed to be given by Equation 4.25, in which the findings in references [3,68] are combined.

$$j_{E_1} = nFk_1c_{O_2} [1 - \theta_{\text{cov}}(\Delta G_{\text{c-spec}}) - \theta_{\text{non-cov}}(\Delta G_{\text{nc-spec}}) ] \quad (4.25)$$

where  $n$  is the number of electrons,  $k_1$  is a kinetic constant,  $c_{O_2}$  is the concentration of O<sub>2</sub> in the solution, and  $(\theta_{\text{cov}} + \theta_{\text{non-cov}} = \theta_{\text{ads}})$  is the fraction of the surface masked by the site-blocking covalently and non-covalently bound species. The surface coverage of covalently bound spectator adsorbates on Pt and Pt-group metals depends on the metal-spectator energetics ( $\Delta G_{\text{c-spec}}$ ), so in Equation 4.25 the rate is strongly dependent on the nature of the metal catalyst. Moreover, the coverage by non-covalently bound species and, thus, the current density  $j$ , is also determined by the free-energy of interaction between the covalently bound spectators and hydrated ions in the OHP, in Equation 4.25 the  $\theta_{\text{non-cov}}(\Delta G_{\text{nc-spec}})$  term. Generally, the relevant covalent adsorbates are strongly adsorbing anions, OH<sub>ads</sub> and H<sub>ads</sub>; and in this particular case, also CN<sub>ads</sub> with a constant coverage between 0.1 V and 1.0 V. In these acidic electrolytes, non-covalently bonded adsorbates are absent.

In order to confirm the hypothesis that cyanide acts as a third body which selectively blocks the adsorption of sulphuric and phosphoric acid anions, while allowing the adsorption of hydrogen and oxygenated species, we studied the ORR in 0.1 M HClO<sub>4</sub>, since perchlorate anions do not adsorb specifically on Pt(111) surfaces. As can be observed in Figure 4.16, the activity for the ORR of cyanide-modified Pt(111) electrodes is similar to that of the unmodified Pt(111) surface, which is also an evidence that cyanide has a negligible effect on the energetics and the rate of the ORR on Pt(111)-CN<sub>ad</sub>. Figure 4.16 also shows that the activity of Pt(111) is higher than that of cyanide-modified Pt(111) above 0.90 V. This result can be explained by the fact that, at these potentials, the coverage by OH<sub>ads</sub> on Pt(111) is slightly smaller than the coverage by OH<sub>ads</sub> and CN<sub>ads</sub> on a cyanide-modified Pt(111) surface. However, at potentials below 0.9 V, cyanide-modified Pt(111) becomes slightly more active than Pt(111) because the coverage by OH<sub>ads</sub> and CN<sub>ads</sub> is smaller. Again, these findings suggest that the rate of the ORR is predominantly controlled by the  $(1 - \theta_{\text{cov}})$  term. This result confirms that the intrinsic activity of Pt for the oxygen reduction is very high, the low activity observed in real catalysts being due to the presence, at relatively low potentials, of OH<sub>ads</sub> or O<sub>ads</sub>.

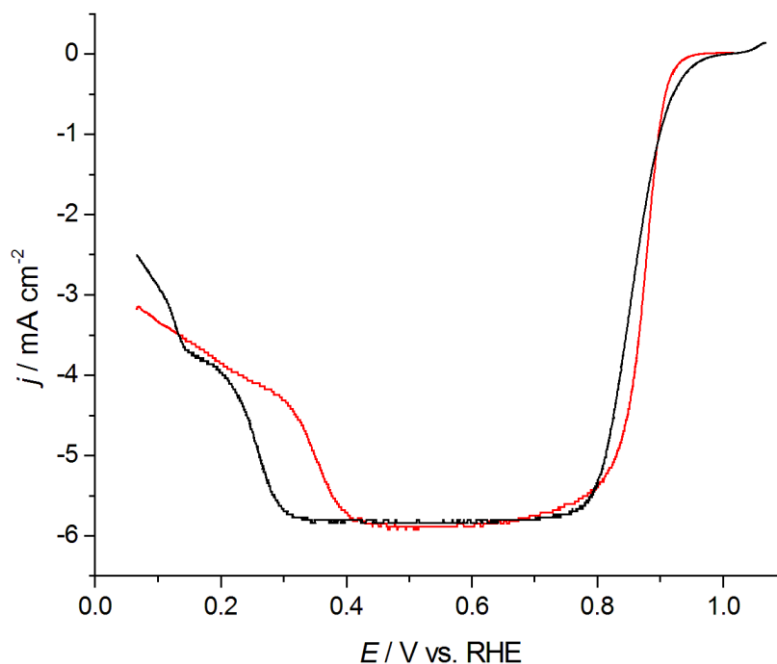


**Figure 4.16.** RDE polarization curve at 1600 rpm and  $50 \text{ mV s}^{-1}$  for the ORR on Pt(111) (black curve) and cyanide-modified Pt(111) (red curve) in oxygen-saturated  $0.1 \text{ M HClO}_4$ .

An analysis of the polarization curves in Figures 4.14 and 4.16 indicates that a series 4-electrons pathway, characteristic for Pt(111) in the kinetically controlled potential region, is operative in all environments (sulphuric, phosphoric and perchloric acid) above 0.30 V on Pt(111) and above 0.40 V on cyanide-modified Pt(111) electrodes. The change from the 4-electron to the 2-electron reaction pathway is due to the formation of  $\text{H}_{\text{upd}}$  [175,176]. The formation of hydrogen peroxide *ca.* 0.10 V more positive on the Pt(111)- $\text{CN}_{\text{ad}}$  surface reflects the earlier formation of adsorbed hydrogen on cyanide-modified Pt(111) surfaces.

In addition to the rotating disk electrode experiments, we carried out ORR experiments using a rotating ring-disk electrode (RRDE), which allows us to monitor the formation of hydrogen peroxide on the ring. The ring was potentiostated at 1.15 V vs. RHE, where oxidation of peroxide arriving at the ring is under diffusion control. Figure 4.17 shows the polarization curves obtained by the RRDE technique, which confirms that hydrogen peroxide is formed on cyanide-modified Pt(111) at potentials 0.1 V more positive than on Pt(111). A comparison of these results with the cyclic voltammogram of cyanide-modified Pt(111) (see Figure 3.3) suggests that, as noted above, this shift in the onset potential of peroxide formation must be related with the shift in the onset potential of hydrogen adsorption, that on cyanide-modified Pt(111) occurs at potentials clearly less negative than

on Pt(111). We have shown in Chapter 3 that the current in the  $H_{\text{upd}}$  region of the CV of a cyanide-modified Pt(111) electrode corresponds to the formation of  $\text{CNH}_{\text{ads}}$ . Accordingly, this result is an indication that access of the  $\text{O}_2$  molecule to two adjacent Pt atoms on the electrode surface is impeded by the formation of  $\text{CNH}_{\text{ads}}$ , the rupture of the O-O bond, necessary for completion of the 4-electron pathway, becoming impossible. This result also suggests that formation of  $\text{HOO}^-$  occurs by reaction of an adsorbed  $\text{O}_2$  molecule with hydrogen from the  $(\text{CN})_x\text{-H}_{\text{ads}}$  clusters.

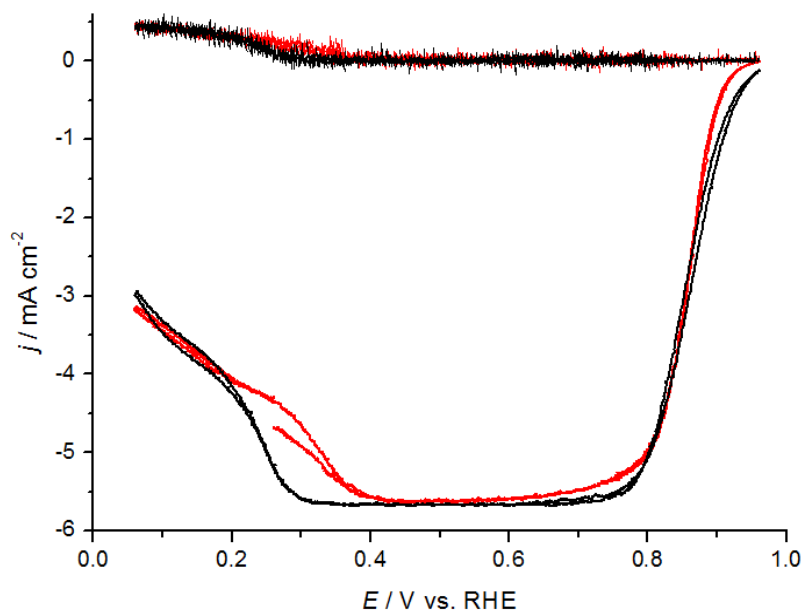


**Figure 4.17.** RRDE polarization curves at 1600 rpm for the ORR on Pt(111) (black lines) and cyanide-modified Pt(111) (red lines) in 0.1 M  $\text{HClO}_4$ . The disk potential was scanned at  $50 \text{ mV s}^{-1}$ , while the ring was potentiostated at 1.15 V.

In contrast to acidic solutions, in alkaline solution the diffusion-limited current is not reached on cyanide-modified Pt(111) electrodes, and the onset of the ORR is shifted negatively by *ca.* 0.20 V, as compared with Pt(111) (Figure 4.18). A strong deactivation is observed in the entire region between 0.10 V and 1.00 V, and at  $E = 0.90 \text{ V}$ , cyanide-modified Pt(111) is 58 times less active than the Pt(111) surface. The adsorption of  $\text{O}_2$  (and  $\text{H}_2\text{O}$ ) is strongly suppressed on cyanide-modified Pt(111) due to non-covalent interactions between  $\text{K}^+$  and  $\text{CN}_{\text{ads}}$ , and the formation of adsorbed spectator  $\text{K}^+(\text{H}_2\text{O})_x\text{-CN}_{\text{ads}}$  clusters, that effectively block the adsorption of  $\text{O}_2$  during the ORR. The role of non-covalent interactions between  $\text{CN}_{\text{ads}}$  and  $\text{K}^+$  on Pt(111) on the ORR is the same as that deduced for  $\text{OH}_{\text{ads}}\text{-K}^+(\text{H}_2\text{O})_x$  clusters in [68], *i.e.*, the reaction rate is controlled by both the  $\theta_{\text{cov}}$  and

$\theta_{\text{noncov}}$  terms in Equation 4.25. The model sketched in Figure 4.19 shows the strong blocking effect of  $\text{K}^+(\text{H}_2\text{O})_x\text{-CN}_{\text{ads}}$  clusters, impeding the access of  $\text{O}_2$  molecules to the Pt surface atoms during the ORR.

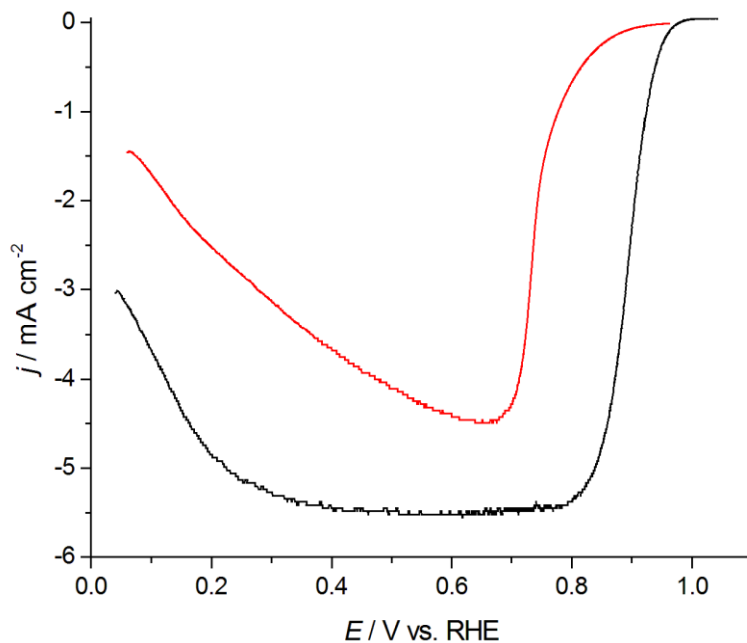


**Figure 4.18.** RDE polarization curves at 1600 rpm and  $50 \text{ mV s}^{-1}$  for the ORR on Pt(111) (black curve) and cyanide-modified Pt(111) (red curve) in oxygen-saturated 0.1 M KOH.

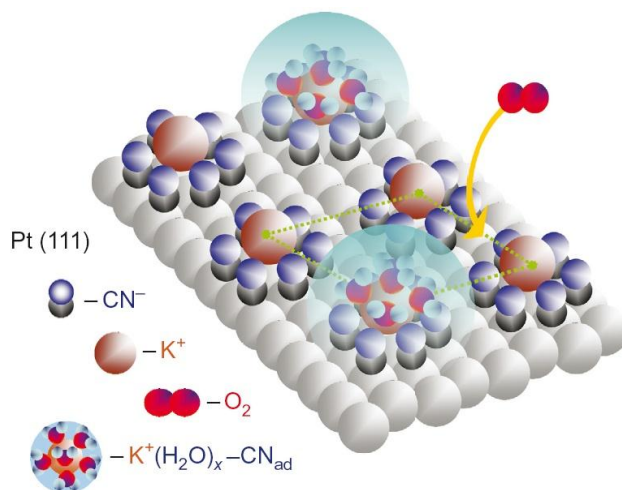


**Figure 4.19.** Schematic presentation of the availability of Pt atoms for adsorption of  $\text{O}_2$  on cyanide-modified Pt(111) in KOH solutions. Adapted from reference [176].

Interestingly, depending on the supporting electrolyte, the surface activity of cyanide-modified Pt(111) surfaces for the ORR can range from a 29-fold increase (in sulphuric acid solutions) to a 58-fold decrease (in potassium hydroxide solutions). As discussed above, the dramatic increase in the activity for the ORR of Pt(111) surfaces in sulphuric and phosphoric acid solutions upon modification with cyanide can be explained by the disappearance from the surface of the sites necessary for the specific adsorption of tetragonal anions, thus cancelling their blocking effect. On the other hand, the huge deactivation observed in alkaline solutions can be explained by the blocking effect of hydrated cations interacting non-covalently with the surface-anchored CN groups on the adsorption of O<sub>2</sub>. The sulphonate groups of the nafion membrane have been shown to adsorb on Pt as sulphuric acid anions do [173,174], and phosphoric acid anions are obviously present in the electrolyte of PAFCs. Hence, this result might be of relevance for the design of cathode catalysts for PEMFCs and PAFCs.

## 4.6. Conclusions and perspectives

Molecular patterning of Pt(111) surfaces with cyanide has been successfully used to study atomic ensemble effects in electrocatalysis in the absence of significant simultaneous electronic effects. Based on the fact that some small molecules can fit within the troughs of the  $(2\sqrt{3} \times 2\sqrt{3})R30^\circ$  structure of cyanide adsorbed on Pt(111), these chemically-modified electrodes have allowed us to get information about the minimum group of atoms required for certain electrocatalytic reactions to take place. The reductive stripping of adsorbed NO was used as a test of the suitability of cyanide-modified Pt(111) electrodes for this purpose [177]. Then, the atomic ensemble requirements of reactions of relevance in fuel-cell electrocatalysis have been investigated.

We have studied hydrogen oxidation reaction on CO-saturated cyanide-modified Pt(111) surfaces and, although a definitive proof cannot be provided, our results suggest that a minimum of two contiguous Pt atoms are required for HOR to take place, which would be an indication that HOR proceeds by a Tafel-Volmer mechanism. Our results also provide an additional proof that hydrogen adsorbed *on-top* of a Pt atom must be the intermediate in the HER and the HOR, H adsorbed at *fcc threefold-hollow* sites of the Pt(111) probably acting as a blocking species.

In those cases in which the reaction proceeds through two parallel pathways, one of them leading to the formation of a poisoning species, the site-knockout strategy, consisting in removing only one kind of sites from the Pt surface without affecting the electronic

properties of the rest of the surface [31], as in cyanide-modified Pt(111) electrodes, can channel the reaction through the desired path [31, 38, 115]. The formation of adsorbed CO during the electrooxidation of formic acid is blocked on cyanide-modified Pt(111) electrodes, because the dehydration of formic acid to form  $\text{CO}_{\text{ads}}$  requires at least three contiguous Pt atoms, and these sites are absent on this surface

In environments containing specifically adsorbing anions, the rate for the oxygen reduction reaction, the cathodic fuel-cell reaction, will be controlled by the coverage of these spectator anions. Modification of Pt(111) with cyanide results in a huge enhancement of the catalytic activity for the ORR in sulphuric and phosphoric acid solutions, because the sites necessary for the adsorption of the tetragonal anions of these acids have been removed from the surface [176].

Although the results presented in this chapter have been obtained using cyanide-modified Pt(111) electrodes, that are obviously of null practical importance, the site-knockout strategy has shown that a detailed knowledge of atomic ensemble effects may be very helpful in designing highly active and selective real anode and cathode electrocatalysts.







## Chapter 5

# Cation-specific non-covalent interactions at the electrochemical double layer

### 5.1. Introduction

Non-covalent interactions [178] play a crucial role in supramolecular chemistry [179-181], that 'chemistry beyond the molecule', as the Chemistry Nobel Prize winner Jean-Marie Lehn [179] defined it. While covalent interactions lead to the formation of classical molecules, non-covalent interactions, that involve energies much lower than the binding energy of covalent bonds, form molecular clusters. Selective non-covalent interactions dominate the formation of nanowires [180], nanomaterials and extended geometrical networks [181] on ordered surfaces. All these supramolecular structures are very promising for emerging technologies such as the fabrication of nanoscale electronic devices.

The influence on the properties of the electrochemical double layer of non-covalent interactions between cations and metal surfaces has traditionally been given little attention. Nevertheless, cations can become attached to the electrode surface through non-covalent interactions with chemisorbed species, affecting the structure and the properties of the electrode-electrolyte interface and, hence, influencing the processes occurring at the electrochemical double layer. The importance of non-covalent interactions with hydrated alkaline-metal cations in some important electrocatalytic processes, such as the methanol oxidation reaction (MOR) and the ORR [68,176] has been recently proved. Markovic and co-workers [68] have demonstrated that non-covalent interactions between hydrated alkaline-metal cations and adsorbed OH may affect the surface reactivity, due to the formation of  $M^+(H_2O)_x-OH_{ads}$  clusters which effectively block oxygen adsorption. Similarly, as explained in Chapter 4, the decrease in the activity for the ORR of cyanide-modified Pt(111) electrodes in KOH solutions was attributed to non-covalent interactions between hydrated cations and the adsorbed cyanide groups, leading to the formation of  $K^+(H_2O)_x-CN_{ads}$  clusters which block the adsorption of reactants during the ORR.

In order to confirm the hypothesis that pH does not play a role in blocking the adsorption of oxygen and other reactants during the ORR in alkaline solutions and, on the contrary, this effect is due to the formation of  $K^+(H_2O)_x-CN_{ads}$  clusters, cyclic voltammetry and *in situ* STM experiments in acidic solutions containing alkali metal cations ( $Li^+$ ,  $Na^+$ ,  $K^+$ , and  $Cs^+$ ) were carried out. In this chapter we present these experimental results combined with theoretical calculations, aimed at deepening our understanding of the factors governing non-covalent interactions in surface electrochemistry.

## 5.2. Experimental studies on the role of alkali cations on cyanide-modified Pt(111) in acidic solutions

### 5.2.1. Voltammetric results

Figures 5.1 to 5.4 show the CVs of cyanide-modified Pt(111) in 0.1 M sulphuric (or perchloric) acid solutions containing different concentrations of  $Li^+$  (Figure 5.1)  $Na^+$  (Figure 5.2)  $K^+$  (Figure 5.3) and  $Cs^+$  (Figure 5.4). As can be observed, both the shape and the position of the hydrogen adsorption region change when cations are present. This behavior can be explained by a competition between protons and cations ( $M^+$ ) for adsorbed cyanide (see Reactions 5.1 and 5.2): the interaction between cations in solution and the negative end of the  $CN_{ads}$  dipole of cyanide-modified Pt(111) provokes that some of the  $CN_{ads}$  groups are not available for the formation of  $(CN_{ads})_x-H$  clusters. As a result, the shape and the position of the hydrogen adsorption region in the CV of cyanide-modified Pt(111) electrodes change.



The charge obtained by integration of the CV in the hydrogen adsorption region is unaffected by the presence of cations in the solution. In all cases, the double layer-corrected voltammetric charge in this region is  $80 \pm 2 \mu C cm^{-2}$ , which shows that, at sufficiently negative potentials,  $(CN_{ads})_y-M^+$  clusters have been displaced from the surface by  $(CN_{ads})_x-H$  clusters. In contrast, the charge obtained by integration of the CV in the OH adsorption region decreases with increasing cation concentration, most likely due to the fact that, in acidic solution, adsorbed OH forms by oxidation of  $H_2O$ , whose access to the CN-free Pt atoms on cyanide-modified Pt(111) might be impeded by  $(CN_{ads})_y-M^+$  clusters.

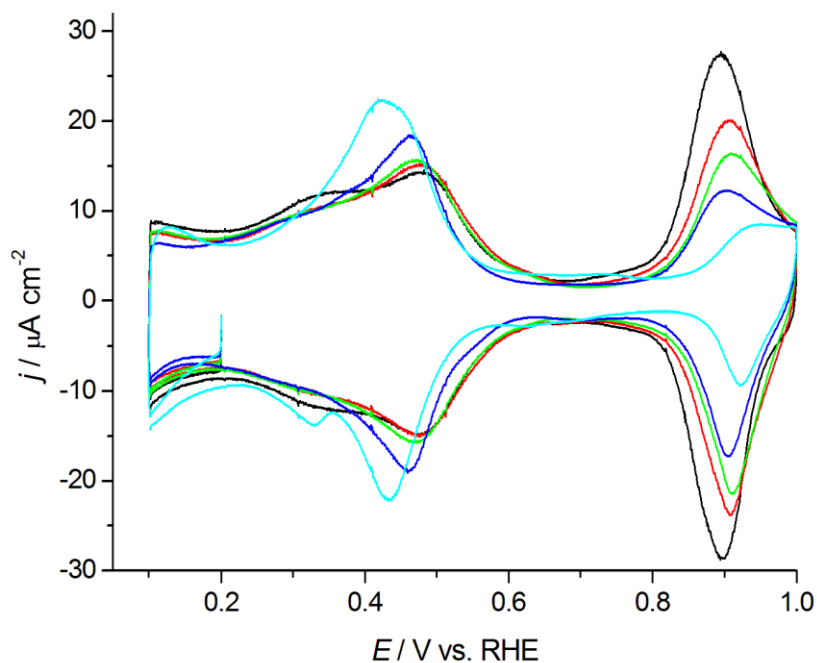


**Figure 5.1.** CVs of a cyanide-modified Pt(111) electrode in 0.1 M HClO<sub>4</sub> + x M LiClO<sub>4</sub>: x = 0 (black), 0.1 (red), 0.5 (green), 1 (blue) and 3 (cyan). Scan rate: 50 mV s<sup>-1</sup>.

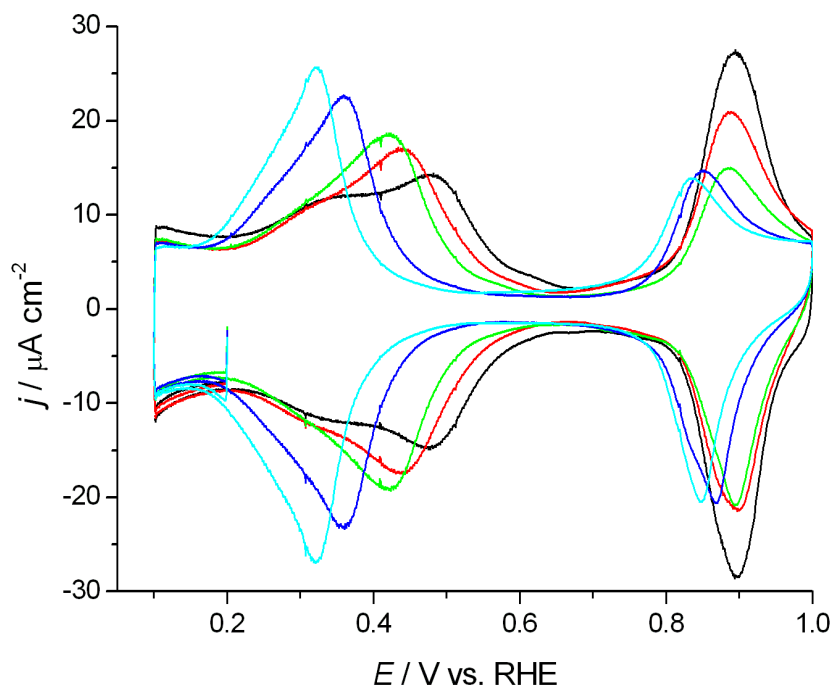


**Figure 5.2.** CVs of cyanide-modified Pt(111) in 0.1 M H<sub>2</sub>SO<sub>4</sub> + x M Na<sub>2</sub>SO<sub>4</sub>: x = 0 (black), 0.05 (red), 0.1 (green), 0.5 (blue) and 1.0 (cyan). Scan rate: 50 mV s<sup>-1</sup>.

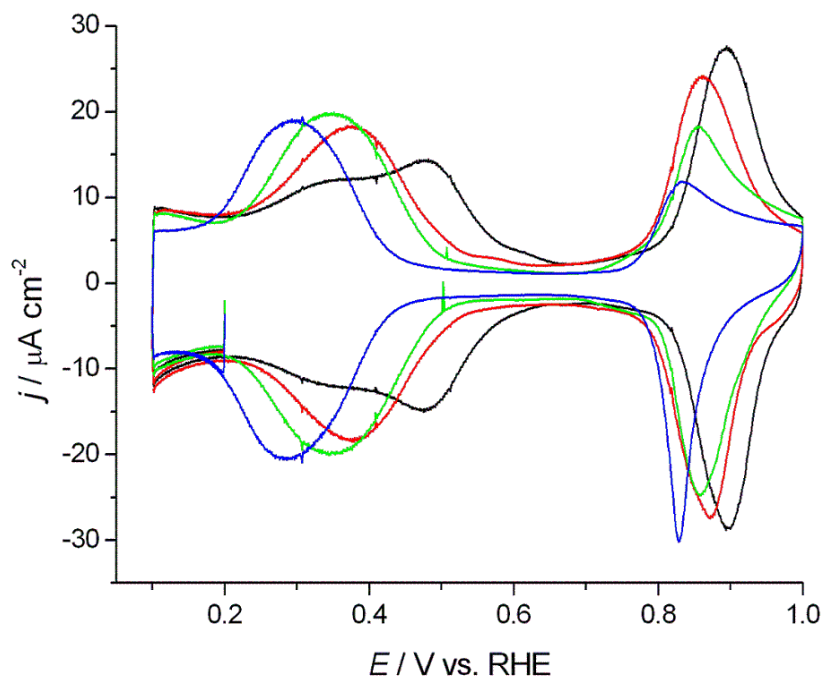


**Figure 5.3.** CVs of cyanide-modified Pt(111) in 0.1 M  $\text{HClO}_4$  ( $\text{H}_2\text{SO}_4$ ) +  $x$  M  $\text{KClO}_4$  ( $\text{K}_2\text{SO}_4$ ):  $x = 0$  (black), 0.05 (red), 0.1 (green), 0.5 (blue). Scan rate:  $50 \text{ mV s}^{-1}$ .

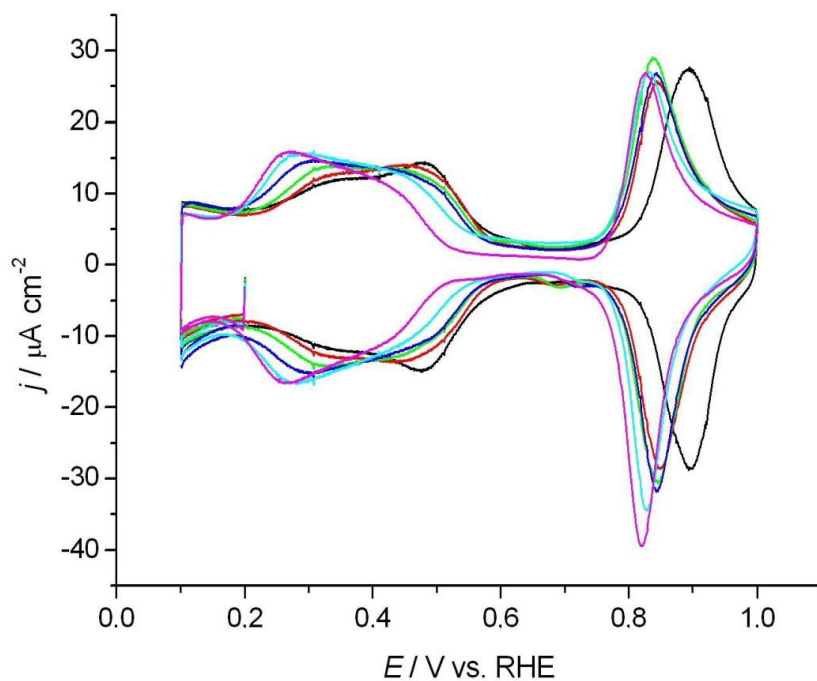
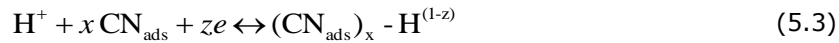


**Figure 5.4.** CVs of cyanide-modified Pt(111) in 0.1 M  $\text{HClO}_4$  ( $\text{H}_2\text{SO}_4$ ) +  $x$  M  $\text{CsClO}_4$  ( $\text{Cs}_2\text{SO}_4$ ):  $x = 0$  (black),  $5 \times 10^{-3}$  (red), 0.01 (green), 0.05 (blue), 0.1 (cyan), 0.2 (magenta). Scan rate:  $50 \text{ mV s}^{-1}$ .

Figure 5.5 shows the potential at which a given adsorption charge (*i.e.*, a given coverage of  $(\text{CN}_{\text{ads}})_x\text{-H}$  clusters) has been achieved as a function of the logarithm of the cation concentration for  $\text{Li}^+$ ,  $\text{Na}^+$ ,  $\text{K}^+$ , and  $\text{Cs}^+$ . It must be noted that, while for the cases of  $\text{Li}^+$ ,  $\text{Na}^+$  and  $\text{K}^+$  we have plotted the variation of the potential of the peak occurring at 0.48 V in the absence of cations (corresponding to a charge of *ca.*  $20 \mu\text{C cm}^{-2}$ ), in the case of  $\text{Cs}^+$  this peak is not clearly defined (see Figure 5.4). For this reason, the peak at 0.32 V in the absence of cations (corresponding to a charge of *ca.*  $50 \mu\text{C cm}^{-2}$ ) was chosen instead.

As can be seen in Figure 5.5, at low cation concentrations the peak potential remains constant in all the cases, and equal to that in cation-free 0.1 M  $\text{H}_2\text{SO}_4$  (or  $\text{HClO}_4$ ) solutions. Above a cation-dependent threshold concentration, the peak potential in the hydrogen adsorption region starts to deviate from the value in the absence of cations and finally, at high enough concentrations, the peak potential decreases linearly with the logarithm of the cation concentration. This Nernstian-like behaviour suggests that cations retained on the surface as  $(\text{CN}_{\text{ads}})_y\text{-M}^+$  clusters are in equilibrium with cations in the solution. This result is remarkable, since, as far as we know, this is the only example of a linear dependence of the equilibrium potential of an electrochemical reaction on the logarithm of the concentration of a species not involved in the reaction, highlighting that non-covalent interactions can dramatically affect the double layer properties.

This behaviour can be modelled assuming (i) that the formation of the  $(\text{CN}_{\text{ads}})_x\text{-H}$  clusters can be represented by Reaction 5.3, in which  $z$  is the number of electrons crossing the interface per every  $(\text{CN}_{\text{ads}})_x\text{-H}$  cluster formed, and (ii) that the formation of the  $(\text{CN}_{\text{ads}})_y\text{-M}^+$  clusters by Reaction 5.2 can be described by the Langmuir isotherm (Equation 5.4).



$$\theta_{(\text{CN}_{\text{ads}})_y\text{-M}^+} = \frac{K_{\text{M}^+} \cdot c_{\text{M}^+}}{K_{\text{M}^+} \cdot c_{\text{M}^+} + 1} \quad (5.4)$$

where  $K_{\text{M}^+}$  is the equilibrium constant for the formation of the  $(\text{CN}_{\text{ads}})_y\text{-M}^+$  clusters, and  $c_{\text{M}^+}$  is the cation concentration in the solution. According to this, the potential at which a given coverage of  $(\text{CN}_{\text{ads}})_x\text{-H}^{(1-z)}$  is attained, *i.e.*, at which a given charge density has crossed the interface, will be given by Equation 5.5.

$$E = E^0 + \frac{RT}{zF} \ln c_{\text{H}^+} + \frac{RT}{zF} \ln \theta_{\text{CN}_{\text{ads}}} \quad (5.5)$$

where  $E^0$  is the potential at which a given coverage of  $(\text{CN}_{\text{ads}})_x\text{-H}$  clusters is attained in the absence of cations at pH 0,  $R$ ,  $T$  and  $F$  have their usual meanings, and  $c_{\text{H}^+}$  is the concentration of protons in the solution ( $c_{\text{H}^+} = 0.1 \text{ M}$ ). In the presence of a cation in the solution  $\theta_{\text{CN}_{\text{ads}}}$  will be determined by the cation concentration. Assuming that the interaction between the cation and the adsorbed cyanide groups to form  $(\text{CN}_{\text{ads}})_y\text{-M}^+$  clusters can be described by a Langmuir isotherm, the coverage by this clusters will be given by Equation 5.4 and the coverage by  $\text{CN}_{\text{ads}}$  may be calculated by Equation 5.6.

$$\theta_{\text{CN}_{\text{ads}}} = 1 - \theta_{\text{M}^+(\text{CN}_{\text{ads}})_y} = \frac{1}{1 + K_{\text{M}^+} c_{\text{M}^+}} \quad (5.6)$$

Accordingly,

$$E = E^0 + \frac{RT}{zF} \ln c_{\text{H}^+} - \frac{RT}{zF} \ln(1 + K_{\text{M}^+} c_{\text{M}^+}) \quad (5.7)$$

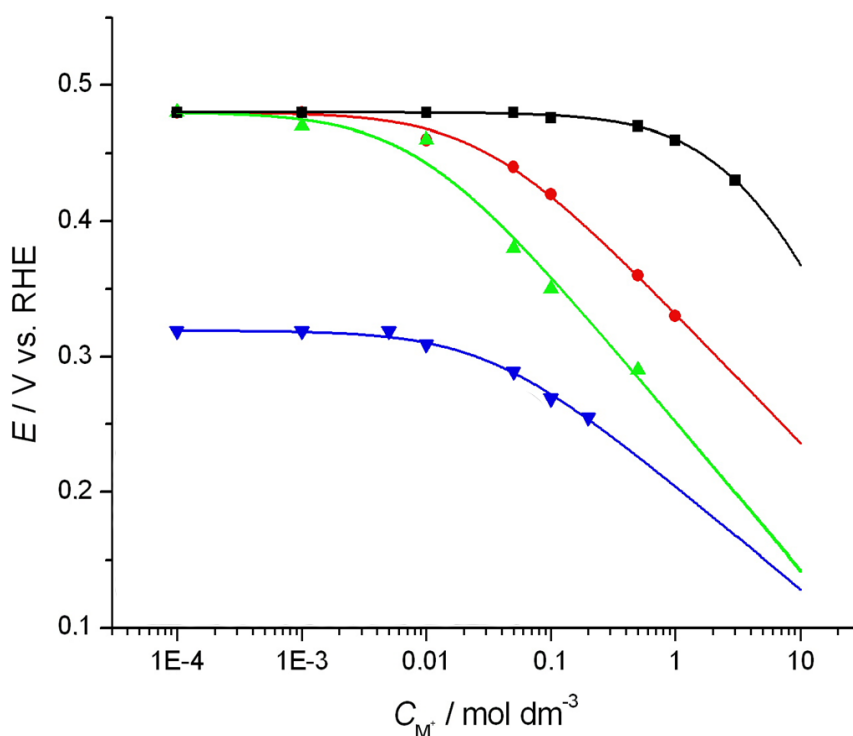


**Figure 5.5.** Semilogarithmic plot of the dependence on the cation concentration of the peak potential for hydrogen adsorption on cyanide-modified Pt(111) in 0.1 M  $\text{H}_2\text{SO}_4$  or  $\text{HClO}_4$ , as obtained from CVs at  $50 \text{ mV s}^{-1}$ . Black squares:  $\text{Li}^+$ ; red circles:  $\text{Na}^+$ ; green up triangles:  $\text{K}^+$ ; blue down triangles:  $\text{Cs}^+$ . The lines correspond to the fit of the experimental data to Equation 5.7.



The model predicts that if  $K_{M^+} c_{M^+} \ll 1$  (equivalently,  $\theta_{(\text{CN}_{\text{ads}})_x - M^+} \ll 1$ ), the peak potential is independent on the cation concentration. According to Equation 5.7, the threshold concentration, above which the peak potential starts to decrease below that observed in the absence of cations will be the lower the higher the value of  $K_{M^+}$ , *i.e.*, it will be a measure of the affinity of the cation for the  $\text{CN}_{\text{ads}}$  groups. When  $c_{M^+}$  is high enough,  $K_{M^+} c_{M^+} \gg 1$  (equivalently  $\theta_{(\text{CN}_{\text{ads}})_x - M^+} \approx 1$ ), and the potential decreases linearly with  $\log c_{M^+}$ , with slope  $2.3 RT/zF$ . As can be seen in Figure 5.5, the fit of the experimental data to this model is excellent.

**Table 5.1.** Equilibrium constants for the formation of the  $(\text{CN}_{\text{ads}})_3 - M^+$  clusters ( $K_M$ ) and apparent number of electrons crossing the interface per every  $(\text{CN}_{\text{ads}})_x - \text{H}$  cluster formed ( $z$ ), as obtained from the fit of the experimental data in Figure 5.5 to the model described by Equation 5.7. The last two columns show the Gibbs energy of hydration ( $\Delta G^0$ ) and the ionic diameter of the cations.

	$K_M / M^{-1}$	$z$	$\Delta G^0 / \text{eV}^{[a]}$	ionic diameter / Å <sup>[a]</sup>
<b>Li<sup>+</sup></b>	0.24 ± 0.07	0.28 ± 0.07	- 5.3	1.56
<b>Na<sup>+</sup></b>	34 ± 6	0.61 ± 0.04	- 4.3	1.96
<b>K<sup>+</sup></b>	120 ± 50	0.54 ± 0.08	- 3.5	2.66
<b>Cs<sup>+</sup></b>	31 ± 11	0.8 ± 0.1	- 2.9	3.30

[a] Values taken from reference [183].

Table 5.1 shows the values of  $K_{M^+}$  and  $z$  for these four alkali metal cations, as obtained from the corresponding fits to Equation 5.7. Based on the values of  $K_{M^+}$ , the following affinity series,  $\text{Li}^+ \ll \text{Cs}^+ \approx \text{Na}^+ < \text{K}^+$ , can be constructed. A similar series ( $\text{Li}^+ \ll \text{H}^+ < \text{Cs}^+ \approx \text{Na}^+ < \text{K}^+ \ll \text{Mg}^{2+} \ll \text{Ca}^{2+} < \text{Ba}^{2+} \ll \text{La}^{3+}$ ) was deduced by Rosasco *et al.* [182], who also demonstrated, using *ex-situ* Auger spectra, that cation exchange proceeds without loss or rearrangement of the cyanide adlayer. The deviation of  $z$  from the expected value of unity apparently suggests that less than one electron crosses the interface per  $(\text{CN}_{\text{ads}})_x - \text{H}$  formed in the presence of  $\text{Li}^+$ ,  $\text{Na}^+$ ,  $\text{K}^+$  and  $\text{Cs}^+$ . However, due to the high ionic strengths used (particularly in the case of  $\text{Li}^+$ ), we cannot discard that  $z$  obtained from a fit

of the experimental data to Equation 5.7 includes the activity coefficient, thus explaining the low values of  $z$  in Table 5.1.

The formation of the  $(\text{CN}_{\text{ads}})_y\text{-M}^+$  clusters must be due to non-covalent electrostatic interactions of the charge-dipole or charge-induced dipole type between the negative end of the  $\text{CN}_{\text{ads}}$  dipole and the oppositely charged  $\text{M}^+$ . These interactions would be expected to be stronger the smaller the cation radius. On the contrary, as can be observed,  $K_{\text{M}^+}$  increases strongly from  $\text{Li}^+$  to  $\text{K}^+$  and decreases again for  $\text{Cs}^+$ . This observation cannot be explained only by the decrease in the hydration energy with increasing cation radius (see Table 5.1), and suggests that additional stability of the  $(\text{CN}_{\text{ads}})_y\text{-M}^+$  cluster is provided by an optimal fit of the cation into the cavity formed by the CN groups, as in some [2]-cryptate inclusion complexes formed by macrobicyclic ligands and alkali metals [183]. The size of the cavity formed by the CN groups must be close to the atomic diameter of Pt (2.77 Å), and  $\text{K}^+$  (atomic diameter 2.66 Å) must therefore fit particularly well inside it. Although  $\text{Cs}^+$  has a lower hydration energy than  $\text{K}^+$ , it is too big to fit in the cavity, and therefore its  $K_{\text{M}^+}$  is smaller. A similar dependence of the stability constant of [2]-cryptates complexes, with a maximum for  $\text{K}^+$ , was found when cryptand [2.2.2] (cavity diameter of 2.8 Å) was used as ligand [183].

The effect of alkaline-metal cations on the cyclic voltammogram of Pt(111) electrodes in sulphuric acid solutions had already been studied by Feliu and co-workers [107,184], but they did not provide a quantitative interpretation. Recently, Koper and co-workers [185] have studied the influence of alkali metal cations on the CO oxidation in alkaline solutions using stepped Pt electrodes. Their results show that small alkali cations such as  $\text{Li}^+$  and  $\text{Be}^{2+}$  have a significant promoting effect on the oxidation of  $\text{CO}_{\text{ads}}$  both on terraces and on steps, due to the promoting effect that these cations have on the formation of  $\text{OH}_{\text{ads}}$  on Pt surfaces, which makes this  $\text{OH}_{\text{ads}}$  available for CO oxidation at lower oxidation potentials. The size of these cations plays a crucial role in this promoting action, smaller cations giving rise to stronger non-covalent interactions with  $\text{OH}_{\text{ads}}$  than bigger cations. The model developed here to describe the interaction of alkali metal cations with surface anchored CN groups might be of general applicability to explain previously observed cation effects on the properties of the electrochemical double layer [107,184,185].

### 5.2.2. Visualization of cations by electrochemical STM

We have visualized the alkali-metal cations adsorbed on the  $\text{CN}_{\text{ads}}$  groups by *in situ* high-resolution electrochemical STM, but only in solutions containing the cation in concentrations lying on the linear region of Figure 5.5. This was to be expected, since

although the cations retained on the surface in the  $(\text{CN}_{\text{ads}})_y\text{-M}^+$  clusters are in equilibrium with the cations in solution, in this concentration region the coverage by these clusters is *ca.* 1, and hence the STM tip will always see a cation occupying those sites. At concentrations below the linear region in Figure 5.5, the cations change positions too fast for the scan rate typical of constant-current STM.

Figures 5.6 to 5.8 show STM images of cyanide-modified Pt(111) electrodes in acidic solutions containing  $\text{K}^+$  (Figures 5.6 and 5.8, left) and  $\text{Na}^+$  (Figures 5.7 and 5.8, right). The honeycomb structure shown in Figures 5.6 to 5.8 could only be observed for  $\text{K}^+$  and  $\text{Na}^+$  concentrations above 0.05 M and 0.5 M, respectively. We can clearly observe six tunneling maxima surrounding the CN rings, that we have attributed to six cations forming the hexagons of the honeycomb structure. The distance between the centres of two adjacent hexagons is *ca.* 0.96 nm, corresponding to the distance expected if the cation is adsorbed above the Pt atoms surrounding the CN rings ( $2\sqrt{3}d_{\text{Pt}} = 2\sqrt{3} \times 0.277 \text{ nm}$ ) of the cyanide-modified Pt(111) electrode. Accordingly, the distances between two opposite corners ( $4d_{\text{Pt}}$ ) and two opposite sides ( $2\sqrt{3}d_{\text{Pt}}$ ) are *ca.* 1.11 and 0.96 nm, respectively. The honeycomb structures formed by potassium (Figures 5.6 and 5.8, left) and sodium (Figures 5.7 and 5.8, right) extend over the whole electrode surface.

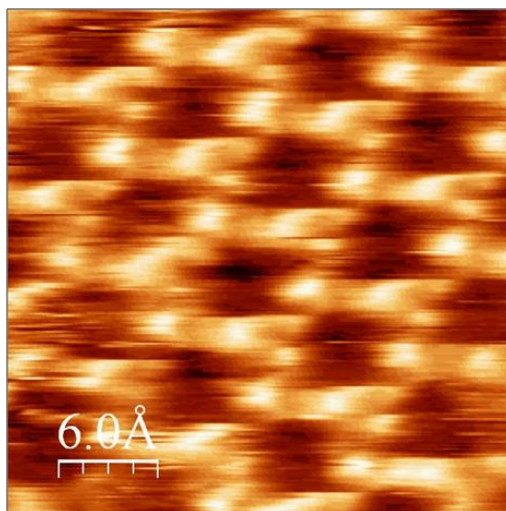


**Figure 5.6.**  $3.0 \times 3.0 \text{ nm}^2$  STM image of a cyanide-modified Pt(111) electrode in 0.1 M  $\text{HClO}_4 + 0.05 \text{ M KClO}_4$  at 0.60 V;  $U_{\text{T}} = 0.45 \text{ V}$  (tip negative);  $I_{\text{T}} = 2 \text{ nA}$ .

In some cases, and for unknown reasons, the  $\text{CN}_{\text{ads}}$  groups of the cyanide-modified Pt(111) surface were imaged instead of the cation interacting with them (see the bottom part of Figure 5.7, right). As shown in Figure 5.7, right, the STM image

changes when the potential is stepped into the hydrogen adsorption region, as expected if cations are removed and  $(\text{CN})_x\text{-H}_{\text{ad}}$  is formed. Unfortunately, we could not obtain high-resolution STM images of the structure in the  $\text{H}_{\text{upd}}$  potential region, most likely because hydrogen bonds in the  $(\text{CN})_x\text{-H}_{\text{ad}}$  adlayer make the images noisy.

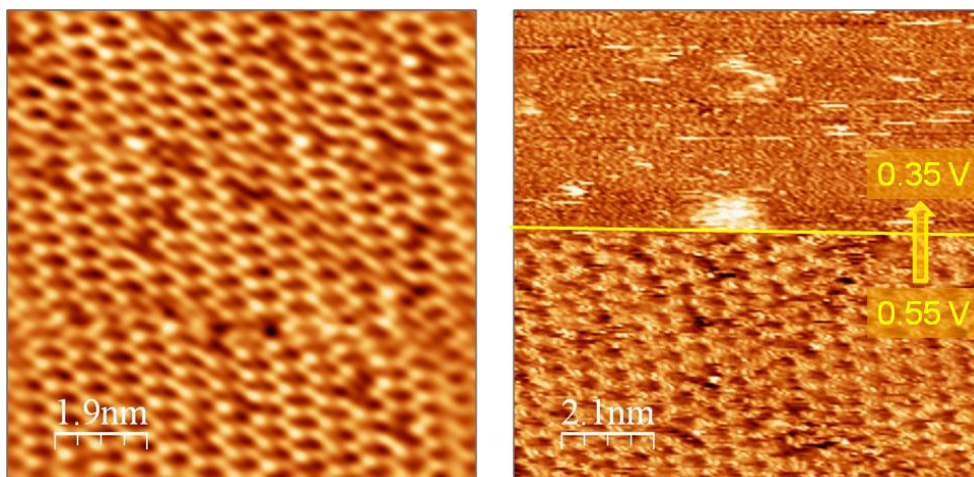


**Figure 5.7.** STM images of a cyanide-modified Pt(111) electrode in 0.1 M  $\text{HClO}_4$  + 0.5 M  $\text{NaClO}_4$  ( $I_T = 2$  nA). Left:  $9.5 \times 9.5$  nm<sup>2</sup> image at 0.55 V;  $U_T = 0.30$  V (tip negative). Right:  $10.5 \times 10.5$  nm<sup>2</sup> image. The yellow line indicates the moment at which the sample potential was stepped from 0.55 V ( $U_T = 0.30$  V, tip negative) to 0.35 V ( $U_T = 0.10$  V, tip negative).

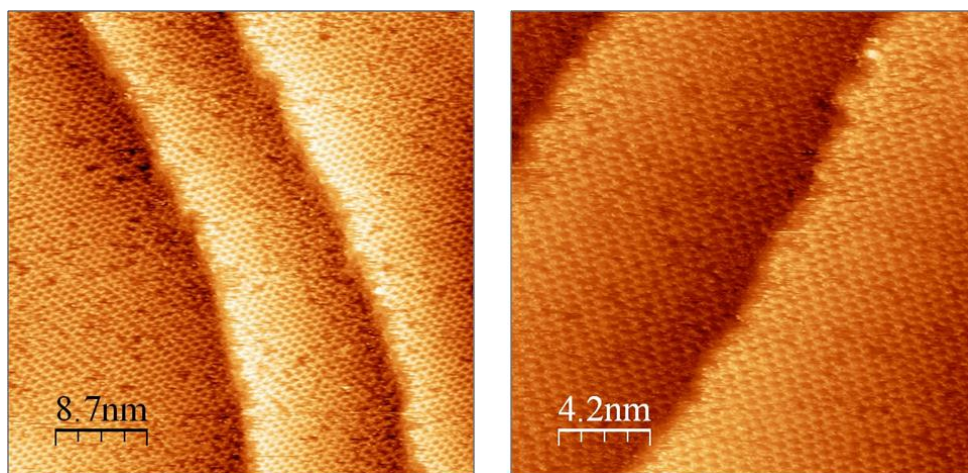


**Figure 5.8.** Images of the honeycomb cation structure surrounding the CN rings ( $I_T = 2$  nA). Left:  $43.5 \times 43.5$  nm<sup>2</sup> image of a cyanide-modified Pt(111) electrode in 0.1 M  $\text{HClO}_4$  + 0.05 M  $\text{KClO}_4$  at 0.60 V;  $U_T = 0.42$  V (tip negative). Right:  $21 \times 21$  nm<sup>2</sup> image of a cyanide-modified Pt(111) electrode in 0.1 M  $\text{HClO}_4$  + 0.5 M  $\text{NaClO}_4$  at 0.55 V;  $U_T = 0.30$  V (tip negative).

The three possible kinds of sites available for the adsorption of metal cations on the cyanide-modified Pt(111) surface are represented in Figure 5.9. The observation of six tunnelling maxima forming a honeycomb structure indicates that sites surrounded by three CN groups are occupied, and  $(\text{CN}_{\text{ads}})_3\text{-M}^+$  clusters are formed according to Reaction 5.7.

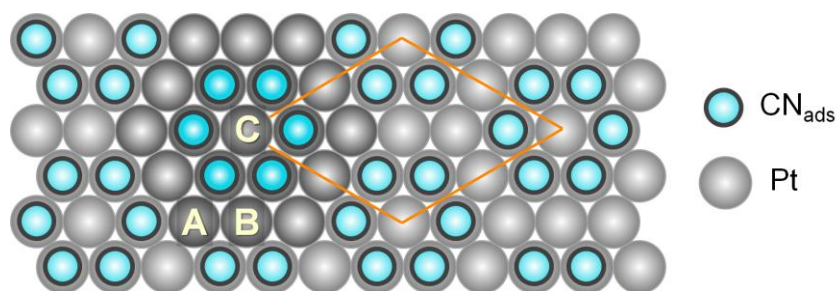


**Figure 5.9.** Ball model of the structure of the cyanide-modified Pt(111) surface indicating the three possible kinds of sites available for cation adsorption. Cations can adsorb at sites surrounded by three (A), four (B) or six CN groups (C).

### 5.3. Theoretical calculations

The adsorption of  $\text{Na}^+$  and  $\text{K}^+$  onto the cyanide-modified Pt(111) surface has been investigated by means of DFT calculations by Zoloff-Michoff and Leiva at the Universidad Nacional de Córdoba (Argentina). In this section I will briefly show, for the sake of clarity and completeness, the most relevant results regarding the stability of  $\text{Na}^+$  and  $\text{K}^+$  adsorbed onto cyanide-modified Pt(111) surfaces forming different structures. As shown in Chapter 3, adsorbed cyanide groups are negatively charged and the work function of the cyanide-modified Pt(111) is higher than that of Pt(111), which explains the avidity of the chemically-modified surface for positively charged particles, such as the alkali metal cations present in solution.

In a first approximation, the adsorption energies of the cations on the different adsorption sites were calculated on a  $3 \times 3$  Pt(111) slab, and three distinct *on-top* adsorption sites were examined (see Figure 5.9): a site surrounded by three CN molecules, giving rise to  $(\text{CN}_{\text{ads}})_3\text{-M}^+$ , a site surrounded by four CN molecules, labeled as  $(\text{CN}_{\text{ads}})_4\text{-M}^+$ , and the centre of the CN rings, to which we will refer to as  $(\text{CN}_{\text{ads}})_6\text{-M}^+$ .  $(\text{CN}_{\text{ads}})_3$  and  $(\text{CN}_{\text{ads}})_4$  sites are more favoured than a  $(\text{CN}_{\text{ads}})_6$  site. Figure 5.10 shows that the three possible cavities for



adsorption of cations have different sizes, and the results obtained for the  $(\text{CN}_{\text{ads}})_6$  site are an indication that the corresponding cavity is the less favoured one.

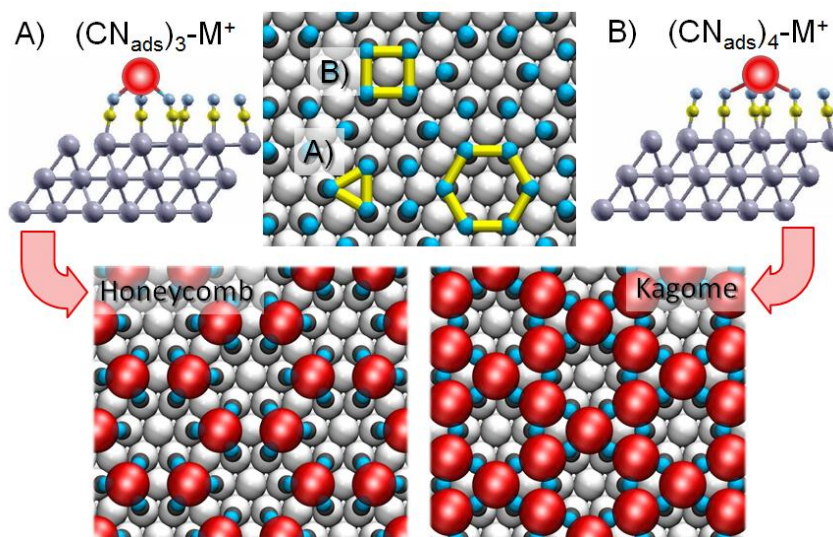


**Figure 5.10.** Top and side views of the  $(\text{CN}_{\text{ads}})_3$  and  $(\text{CN}_{\text{ads}})_4$  cavity sites of cyanide-modified Pt(111) surfaces. Formation of  $(\text{CN}_{\text{ads}})_3\text{-M}^+$  clusters yields a honeycomb structure, while formation of  $(\text{CN}_{\text{ads}})_4\text{-M}^+$  clusters yields a kagome structure.

According to the calculations performed including only one cation per unit cell, the  $(\text{CN}_{\text{ads}})_4$  site is slightly more favoured than the  $(\text{CN}_{\text{ads}})_3$  site [116]. However, location of the metal cation centred on the side of a hexagonal  $\text{CN}_{\text{ad}}$  ring, interacting with four  $\text{CN}_{\text{ad}}$  groups and forming  $(\text{CN}_{\text{ads}})_4\text{-M}^+$  clusters (see Figure 5.10), would yield a kagome structure, which is not experimentally observed. For this reason, honeycomb and kagome structures were constructed and optimized (Figure 5.10). Table 5.2 summarizes the calculated adsorption energies, the averaged distances between atoms and the Mulliken charge analysis for these optimized structures. The adsorption energy of an atom on Pt(111) is notably increased by the presence of the cyanide adlayer. This is mostly due to the higher energy gain incurred by the electron withdrawn from the neutral atom upon its falling to the Fermi level of the metal, which is 2.86 eV lower for cyanide-modified Pt(111) than for Pt(111). As can be seen in Table 5.2, for potassium the calculated adsorption energies per cation are -5.62 eV and -5.42 eV for the optimized honeycomb and kagome structures, respectively. In the case of sodium, the adsorption energies per cation are -5.59 eV and -5.31 eV for the honeycomb and kagome geometries, respectively. The 0.2 eV – 0.3 eV gain in adsorption energy of the honeycomb structure results, at least in part, from avoiding  $\text{M}^+\text{-M}^+$  repulsions. The higher

stability of the honeycomb structure concluded from these theoretical calculations is in agreement with the experimental observations.

**Table 5.2.** Adsorption energies, distances and Mulliken charge analysis for the kagome and honeycomb structures for sodium and cation adsorbed onto a cyanide-modified Pt(111) electrode.

Structure	$E_{ad} / eV$ <sup>[a]</sup>	$d(M^+-Pt) / \text{\AA}$ <sup>[b]</sup>	$d(N-M^+) / \text{\AA}$ <sup>[c]</sup>	$d(N-Pt) / \text{\AA}$ <sup>[d]</sup>	$\delta_{M^+} / e$ <sup>[e]</sup>	$\delta_{CN} / e$ <sup>[e]</sup>
<b>M = Na</b>						
Kagome	- 5.31	3.69	2.59	3.14	+ 0.88	- 0.42
Honey-comb	- 5.59	4.23	2.43	3.14	+ 0.88	- 0.32
<b>M = K</b>						
Kagome	- 5.42	3.86	2.65	3.14	+ 0.85	- 0.40
Honey-comb	- 5.62	4.44	2.61	3.14	+ 0.90	- 0.32

[a] Adsorption energy referred to the optimized  $(2\sqrt{3} \times 2\sqrt{3})R30^\circ$  CN adlayer and a M atom in the vacuum.

[b] Distance between the cation and the Pt surface in the optimized structure.

[c] Averaged distance between  $M^+$  and the N atom of the CN groups surrounding the adsorption site.

[d] Average distance from the N atoms of the adsorbed CN groups to the Pt surface.

[e] Mulliken charge of the species in the optimized structure.

## 5.4. Conclusions

In conclusion, we have used cyanide-modified Pt(111) electrodes to illustrate the importance of non-covalent interactions in governing site-selective adsorption of alkali metal cations. Non-covalent interactions have been proved to dramatically affect the properties and structure of the electrochemical double layer. Remarkably, non-covalent interactions can induce a Nernstian-like dependence of the equilibrium potential on the concentration of a species not involved in the electrochemical reaction and which does not interact with the electroactive species. Furthermore, we have been able to visualize cations retained on the electrode surface by non-covalent interactions using high-resolution *in situ* EC-STM. *In situ* STM images indicate that cations are adsorbed forming  $(CN_{ads})_3-M^+$  clusters, resulting in a honeycomb structure which extends over the whole electrode surface, and theoretical calculations have allowed us to understand why this structure is preferred over the other possible ones.





## Chapter 6

# Electrochemical surface nanostructuring using a molecular pattern

### 6.1. Introduction

Electrochemical methods are very promising for surface nanostructuring due to their ability to easily create and control intense electric fields at the electrochemical interface. One of the aims of this work was to use of chemically-modified Pt electrodes to fabricate periodic metallic nanostructures with feature sizes of one atomic diameter. This limit is currently only achievable when nanostructures are formed locally, for instance, using scanning probe microcopies (SPM) nanostructuring and nanomanipulation techniques. In contrast, nanostructures fabricated on surfaces using a molecular pattern would extend over the whole electrode surface and several samples could be prepared simultaneously.

Cyanide-modified Pt(111) electrodes may be used as molecular patterns for surface decoration. The use of a molecular pattern to design and control nanostructures has already been reported [186-188]. However, with cyanide-modified Pt(111) electrodes we aimed at fabricating periodic networks of atomic dimensions following the pattern formed by adsorbed cyanide groups on Pt(111) surfaces. For this purpose, we have studied the adsorption and the electrodeposition of copper, as well as the polymerization of aniline, on cyanide-modified Pt(111). Electrochemical techniques, in particular cyclic voltammetry, have been used for the fabrication of the nanostructures, and non-electrochemical techniques, such as EC-STM and FTIRS, have been used for the characterization of the resulting surfaces at the atomic or molecular level.

## 6.2. Cyclic voltammetry, FTIRS and EC-STM studies of copper adsorption on cyanide-modified Pt(111) electrodes

We chose copper for the first experiments for three reasons: i) its atomic diameter ( $d_{\text{Cu}} = 2.56 \text{ \AA}$ ) is small enough to fit in the troughs between the rings of CN groups ( $d_{\text{Pt}} = 2.78 \text{ \AA}$ ), ii) it deposits reversibly at underpotentials (*upd*) on Pt(111) (see, for example, [189]), thus allowing to very easily stop the process just when one Cu atom has been deposited on every free Pt atom, and iii) it forms very stable Cu(I) coordination complexes with cyanide.

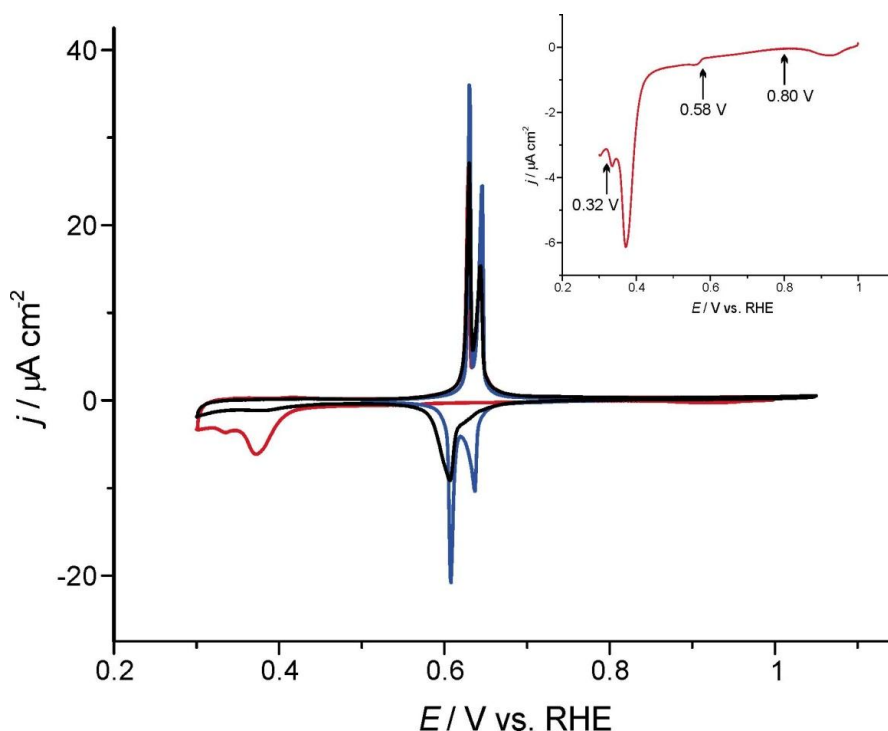


**Figure 6.1.** First (red curve) and second (black curve) cyclic voltammograms of cyanide-modified Pt(111). Blue curve: CV of Pt(111). The electrolyte was 0.1 M  $\text{H}_2\text{SO}_4$  + 1 mM  $\text{CuSO}_4$  in all cases. The inset shows the first negative sweep in an expanded scale. Scan rate:  $1 \text{ mV s}^{-1}$ .

Figure 6.1 shows the first (red curve) and second (black curve) CVs of a cyanide-modified Pt(111) electrode in cyanide-free 0.1 M  $\text{H}_2\text{SO}_4$  + 1 mM  $\text{CuSO}_4$  at  $1 \text{ mV s}^{-1}$ . The CV of copper *upd* on Pt(111) (blue curve) [190,191] is shown for comparison. As can be observed, on unmodified Pt(111) electrodes both the deposition and dissolution of a Cu

monolayer occur in two different peaks, the first underpotential deposition peak appearing at 0.64 V and the second one at 0.61 V. The most positive peak of the Cu *upd* process has been attributed to the formation of a  $(\sqrt{3} \times \sqrt{3})R30^\circ$  structure consisting of both Cu and (bi)sulphate ions [191,192].

The total charge obtained by integration of the CV between 0.80 V (where a small negative, continuously increasing, current starts to be observed, see inset in Figure 6.1) and 0.32 V amounts to  $-508 \mu\text{C cm}^{-2}$ , indicating deposition of a full monolayer of metallic copper. It should be noted that Cu *upd* ( $-480 \mu\text{C cm}^{-2}$  for a two electrons process) is accompanied by desorption of cyanide (0.5 ML,  $-120 \mu\text{C cm}^{-2}$ ) and by adsorption of 0.22 ML of sulphate onto the Cu *upd* adlayer ( $+105.6 \mu\text{C cm}^{-2}$  for 0.22 ML onto 1 ML of Cu on Pt(111)), as suggested by the fact that the subsequent positive sweep is nearly identical to that of unmodified Pt(111) in 0.1 M  $\text{H}_2\text{SO}_4$  + 1 mM  $\text{CuSO}_4$  (compare the black and blue positive sweeps in the CVs in Figure 6.1), but for a slightly smaller charge under the peak. In the subsequent negative sweep, Cu *upd* occurs at the same potential as with unmodified Pt(111) in 0.1 M  $\text{H}_2\text{SO}_4$  + 1 mM  $\text{CuSO}_4$  (compare the black and blue negative sweeps in the CVs in Figure 6.1), although the charge is smaller and the most positive peak has nearly disappeared, which suggests that the absence of this peak in the second negative sweep (black line in Figure 6.1) is due to the presence of a small amount of  $\text{CN}_{\text{ads}}$  groups hindering the formation of large domains of the  $(\sqrt{3} \times \sqrt{3})R30^\circ$  structure.

We have used *in situ* EC-STM to study cyanide-modified Pt(111) electrodes in copper-containing solutions. In the region between 0.80 V and 0.58 V (see Figure 6.1), a honeycomb structure with one-atom wide walls, similar to that observed on cyanide-modified Pt(111) in the presence of high concentrations of  $\text{Na}^+$  or  $\text{K}^+$  (Chapter 5) is observed (see Figure 6.2). Based on the well-known stabilization of  $\text{Cu}^+$  complexes when cyanide is used as a ligand, we identify each of the bright tunneling maxima in the STM images of Figure 6.1 to a  $\text{Cu}^+$  cation. This assignment is supported by *ex situ* XPS measurements with a cyanide-modified Pt(111) electrode emersed from a 0.1 M  $\text{H}_2\text{SO}_4$  + 1 mM  $\text{CuSO}_4$  solution at 0.68 V [193] (Figures 6.3 and 6.4). As in the case of the alkali metal cations, we attribute the formation of this structure to non-covalent interactions between  $\text{Cu}^+$  and the surface-anchored CN groups.

We can observe at least six tunneling maxima forming each honeycomb hexagon. A detailed examination of Figure 6.2 shows that some hexagonal rings forming the honeycomb structure are composed of one  $\text{Cu}^+$  per free Pt atom surrounding the  $\text{CN}_{\text{ads}}$  ring (*i.e.*, both the sites surrounded by three CN groups and the sites surrounded by 4 CN groups are occupied by copper cations). This might be again due to the well-known high affinity of cyanide for the +1 valence state of copper. Moreover, we can clearly also observe a dimmer tunneling

maximum located at the centre of each  $\text{CN}_{\text{ads}}$  hexagonal ring (see Figure 6.2, unfiltered image). Since the experiments were performed in copper-containing acidic solutions, a proton or a copper cation (either  $\text{Cu}^+$  or  $\text{Cu}^{2+}$ ) could be adsorbed at the centre of the hexagonal ring. The possibility that the tunneling maximum corresponds to adsorbed  $\text{Na}^+$  or  $\text{K}^+$  from the NaCN or KCN solution in which cyanide-modified Pt(111) electrodes were prepared cannot be discarded.

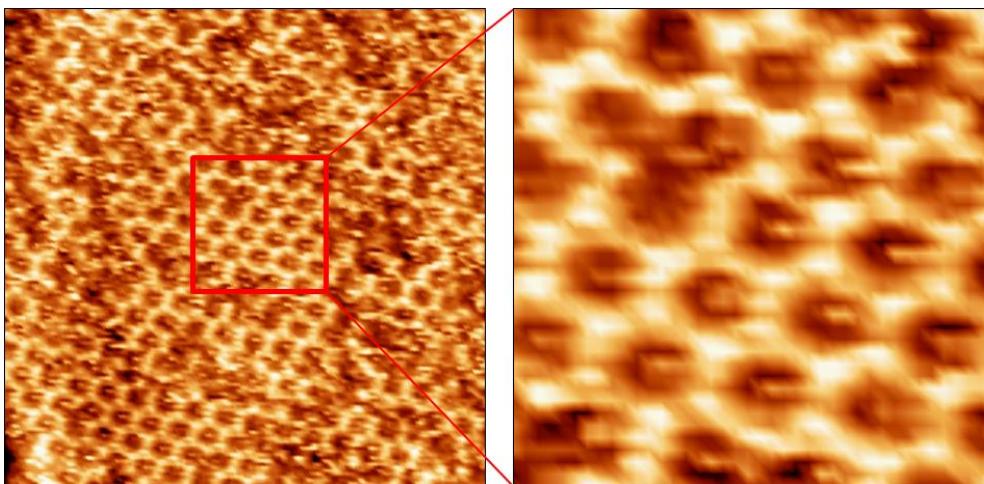


**Figure 6.2.**  $14 \times 14 \text{ nm}^2$  (left) and  $3.8 \times 3.8 \text{ nm}^2$  (right) STM images of cyanide-modified Pt(111) in  $0.1 \text{ M H}_2\text{SO}_4 + 0.1 \text{ M CuSO}_4$  at  $0.85 \text{ V}$ ;  $U_{\text{T}} = 0.55 \text{ V}$  (tip negative);  $I_{\text{T}} = 2 \text{ nA}$ .

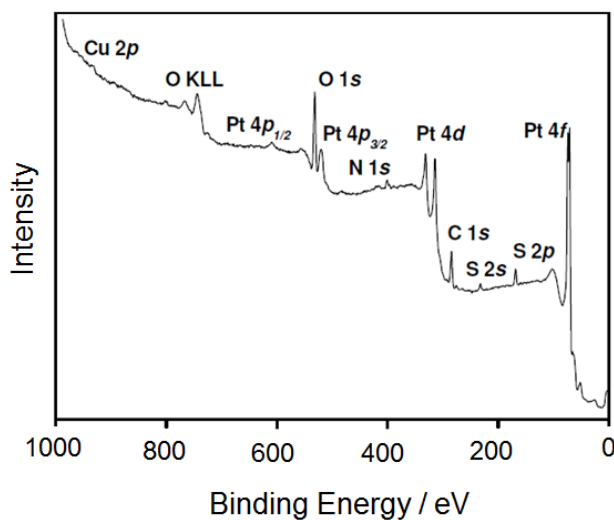


**Figure 6.3.** Wide scan spectrum recorded from a cyanide-modified Pt(111) electrode emerged from a  $0.1 \text{ M H}_2\text{SO}_4 + 1 \text{ mM CuSO}_4$  solution at  $0.68 \text{ V}$ . Courtesy of J.M. Marco, Mössbauer and Surface Spectroscopy Group, Institute of Physical Chemistry 'Rocasolano'.

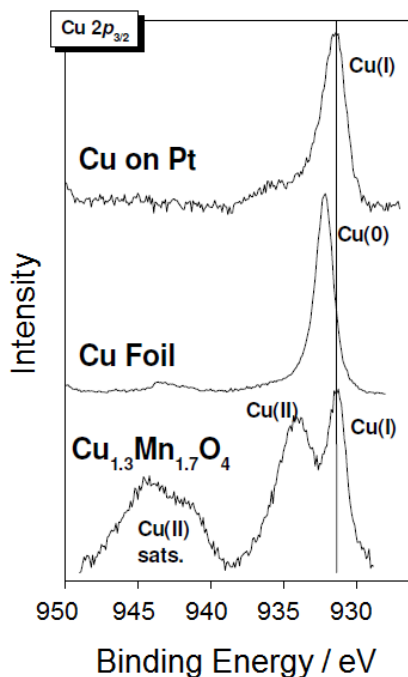


**Figure 6.4.** *Cu 2p<sub>3/2</sub> spectra recorded from a cyanide-modified Pt(111) electrode emersed from a 0.1 M H<sub>2</sub>SO<sub>4</sub> + 1 mM CuSO<sub>4</sub> solution at 0.68 V (top), recorded from metallic Cu (middle), and recorded from Cu<sub>1.3</sub>Mn<sub>1.7</sub>O<sub>4</sub> (bottom). Courtesy of J.M. Marco, Mössbauer and Surface Spectroscopy Group, Institute of Physical Chemistry 'Rocasolano'.*

As in the case of the alkali metal cations, the honeycomb pattern formed by copper extends over the whole electrode surface (see Figures 6.5 and 6.6), although it shows vacancies which are probably due to defects within the cyanide template. Figure 6.6 shows two different ordered structures on different terraces. While one of these structures (A) corresponds to the copper honeycomb superstructure, the other one (B) has the typical appearance of the  $(2\sqrt{3} \times 2\sqrt{3})R30^\circ$  formed by the cyanide adlayer. We ignore the reason why, apparently, in this particular case the copper ions surrounding the CN rings are imaged in the upper terrace, the CN rings remaining invisible, while, on the contrary, in the lower terrace the CN rings are imaged and the copper ions surrounding them remain invisible. This highlights the complexity of STM imaging, particularly at the electrode-electrolyte interface, and is a clear example of how very subtle electronic effects can alter the appearance of STM images of the same system.

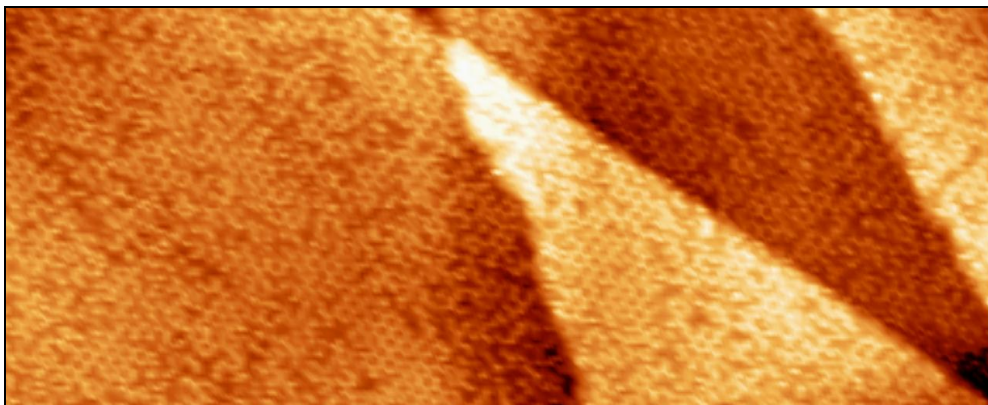


**Figure 6.5.**  $57 \times 23 \text{ nm}^2$  image of cyanide-modified Pt(111) in  $0.1 \text{ M H}_2\text{SO}_4 + 0.1 \text{ M CuSO}_4$  at  $0.85 \text{ V}$ ;  $U_T = 0.55 \text{ V}$  (tip negative);  $I_T = 2 \text{ nA}$ .

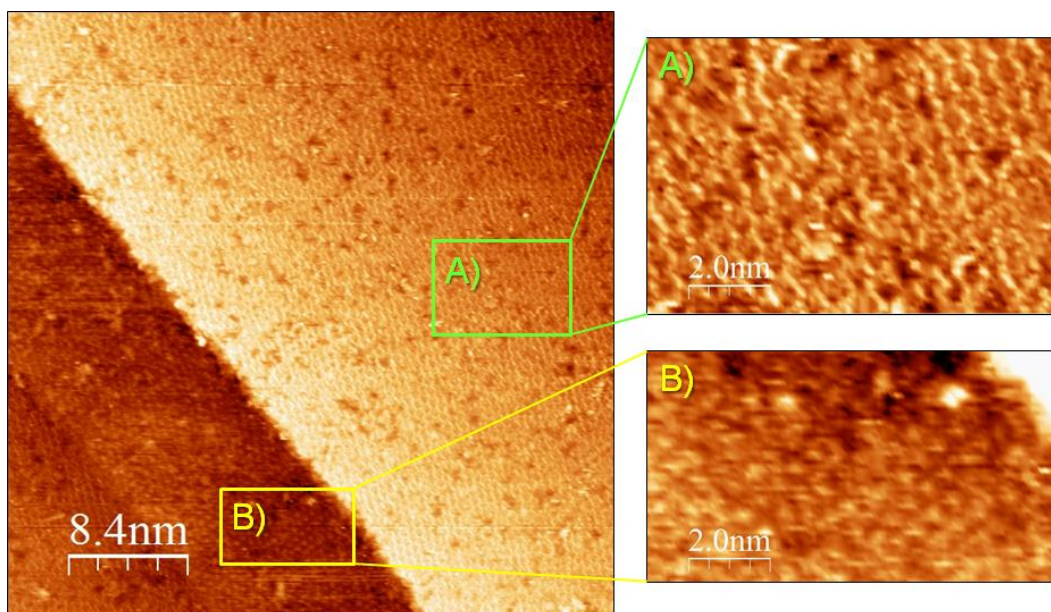


**Figure 6.6.**  $42 \times 42 \text{ nm}^2$  image of cyanide-modified Pt(111) in  $0.1 \text{ M H}_2\text{SO}_4 + 0.1 \text{ M CuSO}_4$  at  $0.95 \text{ V}$ ;  $U_T = 0.65 \text{ V}$  (tip negative);  $I_T = 2 \text{ nA}$ . Two ordered structures can be observed: on the upper terrace (A) the typical honeycomb structure of  $\text{Cu}^+$  adsorbed on cyanide-modified Pt(111) is obtained, while in the lower terrace (B) tunneling maxima corresponding to the CN rings of the cyanide structure are observed instead.



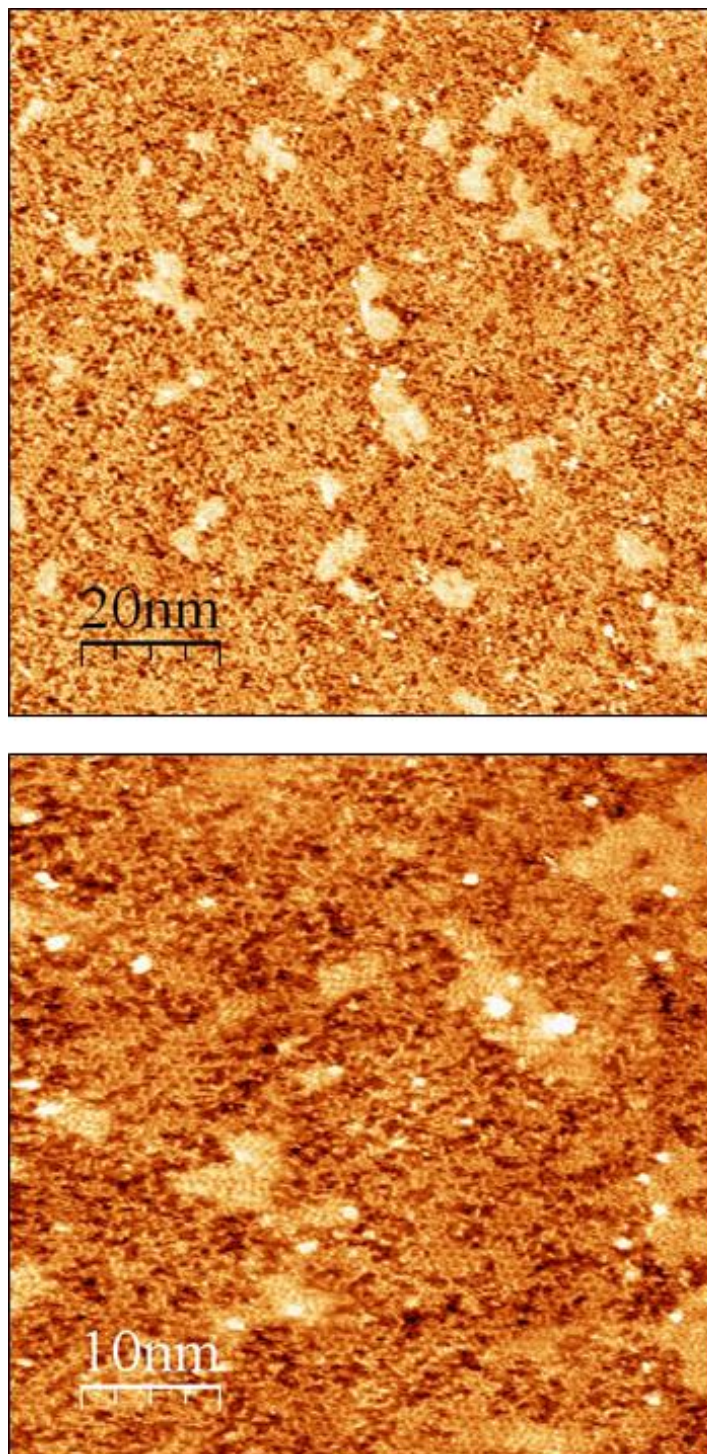


**Figure 6.7.** STM images (top:  $100 \times 100 \text{ nm}^2$ ; bottom:  $50 \times 50 \text{ nm}^2$ ) of the cyanide-modified Pt(111) electrode in  $0.1 \text{ M H}_2\text{SO}_4 + 1 \text{ mM CuSO}_4$  at  $E = 0.52 \text{ V}$ ;  $U_T = 0.22 \text{ V}$  (tip negative).

When the potential is decreased below the shoulder at 0.58 V in the corresponding CV (see inset in Figure 6.1), the honeycomb structure coexists with islands onto which a different structure can be observed (Figure 6.7). Although we could not resolve the latter structure clearly, the observation on some of the islands of three rotational domains, as expected for the  $(\sqrt{3} \times \sqrt{7})R30^\circ$  sulphate structure, suggests that they correspond to epitaxial copper *upd* islands on the Pt surface.

As we reach the potential of the peak at 0.37 V in the first negative sweep in the CV (Figure 6.1, red line and inset), a nearly complete copper *upd* monolayer is formed concomitantly with the desorption of the cyanide adlayer and the adsorption of sulphate onto the Cu *upd* adlayer, as indicated by the observation over the whole electrode surface of the well-known  $(\sqrt{3} \times \sqrt{7})R30^\circ$  structure, characteristic of sulphate adsorbed on the (111) faces of most *fcc* metals (see, for example, [194-196]) (Figure 6.8). This Cu *upd* adlayer is stripped coinciding with the anodic peaks in the subsequent positive sweep (Figure 6.1). The dissolution of the Cu *upd* adlayer can be observed in the upper third of Figure 6.9.

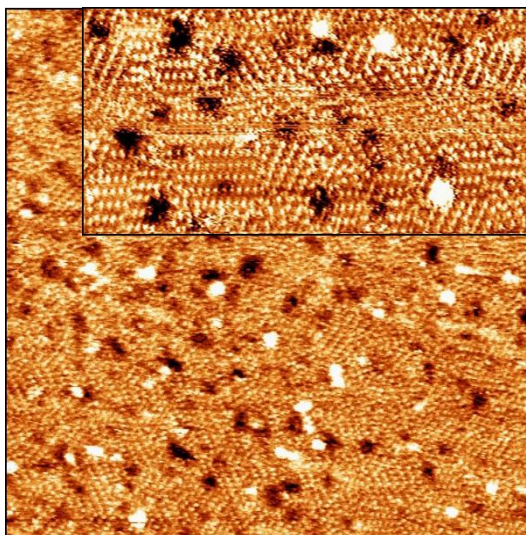


**Figure 6.8.**  $46 \times 46 \text{ nm}^2$  STM image of cyanide-modified Pt(111) in  $0.1 \text{ M H}_2\text{SO}_4 + 1 \text{ mM CuSO}_4$  at  $E = 0.35 \text{ V}$ ;  $U_T = 0.05 \text{ V}$  (tip negative). The inset shows a molecularly resolved image of the same surface ( $24 \times 12 \text{ nm}^2$ ).



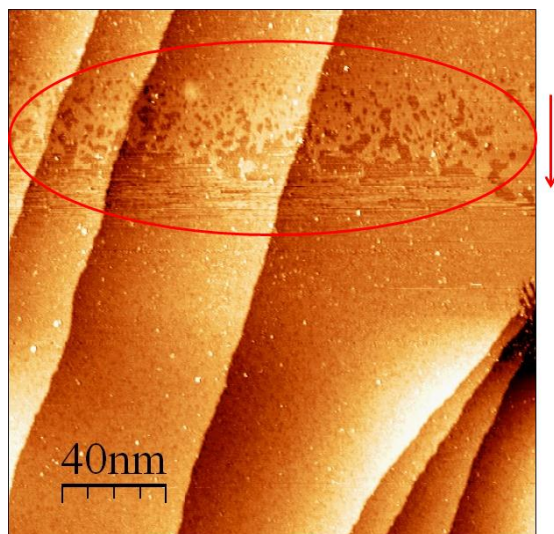


**Figure 6.9.**  $200 \times 200 \text{ nm}^2$  STM image recorded during a positive potential sweep from 0.35 V to 0.85 V.  $U_T = 0.05 \text{ V}$  to 0.50 V (tip negative). The scan direction is from top to bottom and from left to right.

We have carried out *in situ* FTIRS experiments with a cyanide-modified Pt(111) electrode in Cu-containing 0.1 M  $\text{H}_2\text{SO}_4$  solutions. FTIR spectra recorded at potentials between 1.00 V and 0.30 V confirm the conclusions reached from the EC–STM data. At  $E > 0.60 \text{ V}$ , bands corresponding to carbon-bonded, linearly adsorbed CN can be observed, in the same frequency region and with a similar intensity as that observed in the absence of Cu(II) in the solution (Figures 6.10 (A) and (B)), confirming that the cyanide adlayer remains essentially intact in the potential region where the copper honeycomb is observed (Figure 6.2). No other band indicating the formation of another carbon- or nitrogen-containing species during the experiment could be observed in the spectra. At  $E \leq 0.60 \text{ V}$ , the intensity of the CN stretching band decreases as compared with that observed in the same potential region in the absence of Cu(II) (Figure 6.10 (A)), and a band around  $1220 \text{ cm}^{-1}$ , corresponding to adsorbed sulphate, starts to appear (Figure 6.10 (C)), confirming the formation of a sulphate-covered Cu *upd* adlayer on Pt(111) in this potential region, and the destruction of the CN pattern, as deduced from the CV (Figure 6.1) and the EC–STM images (Figures 6.7 and 6.8).

Our results are in agreement with an earlier work by White and Abruña [197], who studied Cu *upd* on Pt(111) electrodes pretreated with, or in the presence of, several anions and molecules, amongst them cyanide. However, since their study was restricted to voltammetric measurements, they could not detect the presence on the surface, at potentials

between 1.00 V and 0.58 V, of copper adsorbed on the cyanide-modified Pt(111) electrode, exactly following the pattern created by the CN groups.

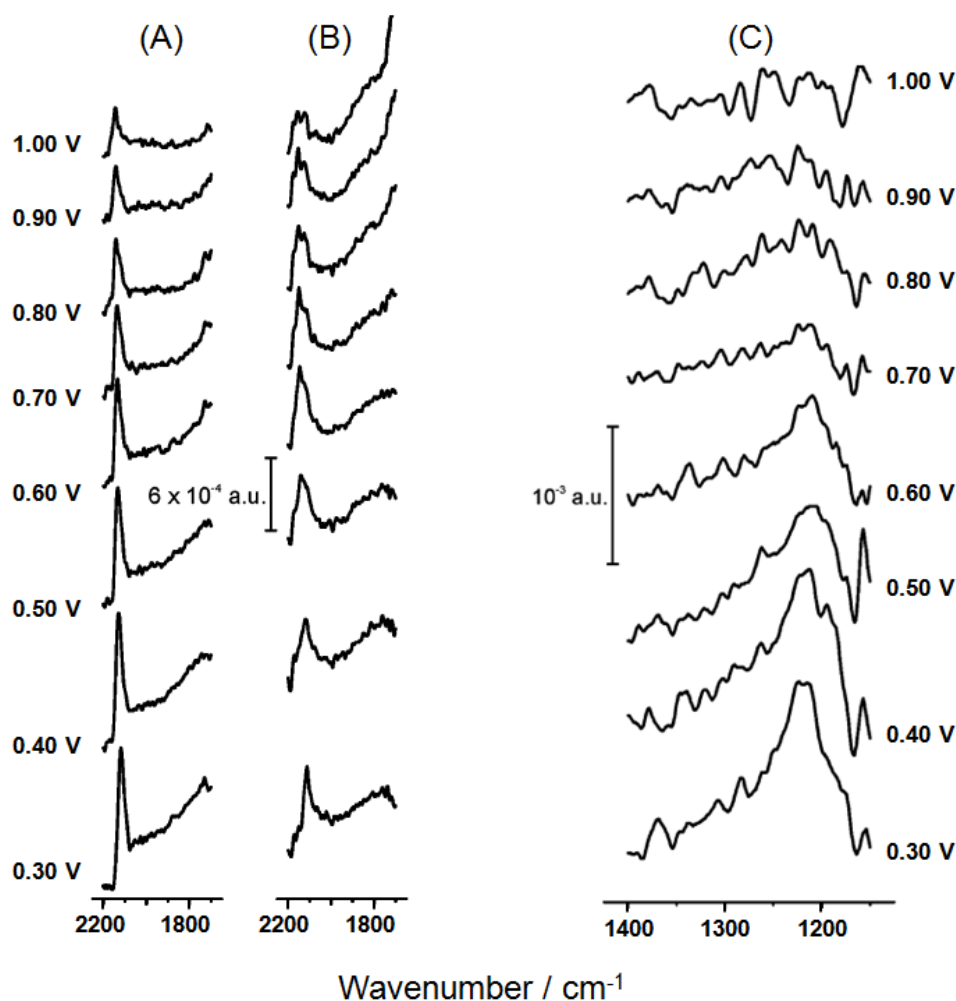


**Figure 6.10.** Potential difference FTIR spectra at decreasing potentials of cyanide-modified Pt(111) in 0.1 M H<sub>2</sub>SO<sub>4</sub> (A) and in 0.1 M H<sub>2</sub>SO<sub>4</sub> + 1 mM CuSO<sub>4</sub> (B, C). The spectra in the frequency region between 2200 cm<sup>-1</sup> and 1700 cm<sup>-1</sup> (A, B) were calculated using the spectrum recorded at 1.30 V as reference, while the spectra in the frequency region between 1400 cm<sup>-1</sup> and 1100 cm<sup>-1</sup> (C) were calculated using the spectrum at 1.00 V as reference.

These results suggest that, if the metallic cation is present in the solution, non-covalent interactions with surface-anchored species cannot be used to obtain extended surface nanostructures following a predefined motif, because deposition of the metal will

strip the cyanide adlayer and destroy the pattern. For this reason, we attempted to electrodeposit copper preadsorbed via non-covalent interactions on a cyanide-modified Pt(111) electrodes in copper-free sulphuric acid solutions, a procedure that has proven successful for metallizing SAMs of mercaptopyridine [198,199] and 4-aminotiophenol [200]. The cyanide-modified Pt(111) electrode was immersed in 0.1 M H<sub>2</sub>SO<sub>4</sub> + 1 mM CuSO<sub>4</sub> for 5 min, after which the electrode was rinsed with ultrapure water and transferred to the electrochemical cell containing sulphuric acid. Figure 6.11 shows the cyclic voltammogram in 0.1 M H<sub>2</sub>SO<sub>4</sub> of a cyanide-modified Pt(111) electrode onto which copper had been preadsorbed. The CV of cyanide-modified Pt(111) in the same solution is shown for comparison. As can be seen, when copper has been preadsorbed on the surface of cyanide-modified Pt(111) but copper is absent from the solution, the voltammetric profile (Figure 6.11, red line) is very different from the CV obtained in copper-containing solutions (Figure 6.1, red line). A new reversible process appears at 0.38 V, no change being observed in the CV upon repetitive cycling between 0.10 V and 1.00 V. The voltammetric charges under the corresponding cathodic and anodic peaks (marked in Figure 6.11) amount to 4 μC cm<sup>-2</sup> and 7 μC cm<sup>-2</sup>, respectively. The double layer-corrected charge in the potential region from 0.64 V to 0.10 V amounts to 101 μC cm<sup>-2</sup> (cathodic charge) and 94 μC cm<sup>-2</sup> (anodic charge). These values are larger than the charge obtained for cyanide-modified Pt(111) electrodes in 0.1 M H<sub>2</sub>SO<sub>4</sub> in the absence of preadsorbed copper (*ca.* 80 μC cm<sup>-2</sup>, see Chapter 3), which is an indication that both H<sub>upd</sub> and Cu<sub>upd</sub> are adsorbed in this potential region and that the reversible peak at *ca.* 0.38 V corresponds to Cu electrodeposition. These results would be in agreement, if Cu<sup>+</sup> is reduced to metallic copper, with the deposition of *ca.* (1/6) ML of Cu, the coverage expected if all the copper cations in the honeycomb structure are reduced to Cu.

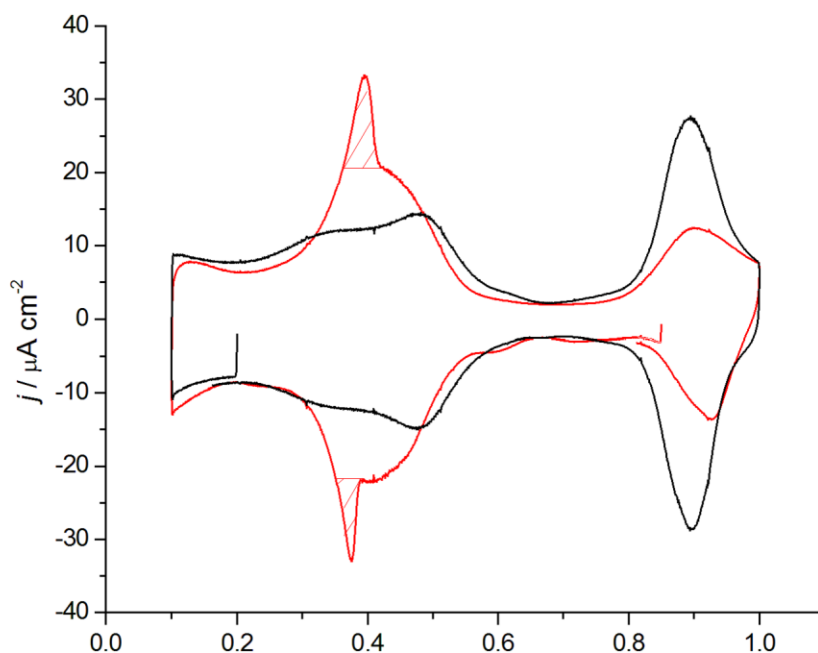


**Figure 6.11.** CV in copper-free 0.1 M  $H_2SO_4$  of a cyanide-modified Pt(111) electrode (red curve) onto which copper had been pre-adsorbed by immersion in a copper-containing 0.1 M  $H_2SO_4$  solution. The black curve corresponds to the CV of a cyanide-modified Pt(111) in the same solution, and is shown for comparison. Scan rate =  $50 \text{ mV s}^{-1}$ .

EC-STM was used to study cyanide-modified Pt(111) electrodes onto which  $Cu^+$  had been preadsorbed in Cu-free 0.1 M  $H_2SO_4$ . In spite of the absence of Cu ions in the solution, at 0.7 V the honeycomb structure can still be observed (Figure 6.12), although with more defects than in copper-containing solutions (Figures 6.2, 6.5 and 6.6).

If the potential is decreased below 0.64 V, coinciding with the onset of hydrogen adsorption, some changes can be observed on the surface: small protrusions *ca.* 0.4 nm in diameter and less than 0.1 nm in height start to appear (see Figure 6.13). These protrusions show a tendency to arrange themselves hexagonally, although with a very short range order. They also show some internal structure, which we have not been able to resolve. The images also show some frizziness, a typical indication of a high surface mobility.

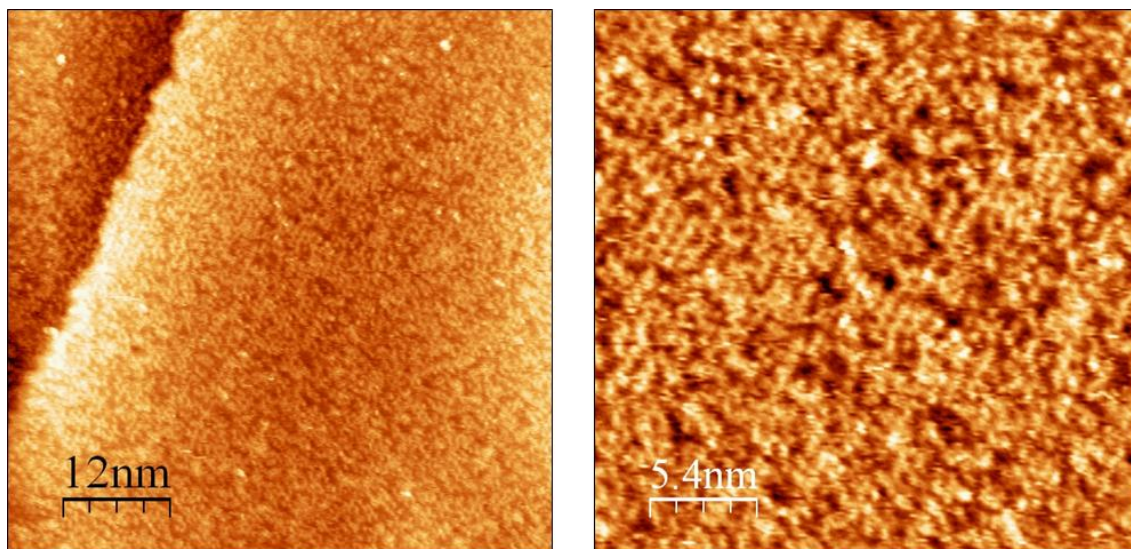


**Figure 6.12.**  $60 \times 60 \text{ nm}^2$  (left) and  $27 \times 27 \text{ nm}^2$  (right) images of preadsorbed copper on cyanide-modified Pt(111) in  $0.1 \text{ M H}_2\text{SO}_4$  at  $0.70 \text{ V}$ ;  $U_T = 0.40 \text{ V}$  (tip negative);  $I_T = 2 \text{ nA}$ .

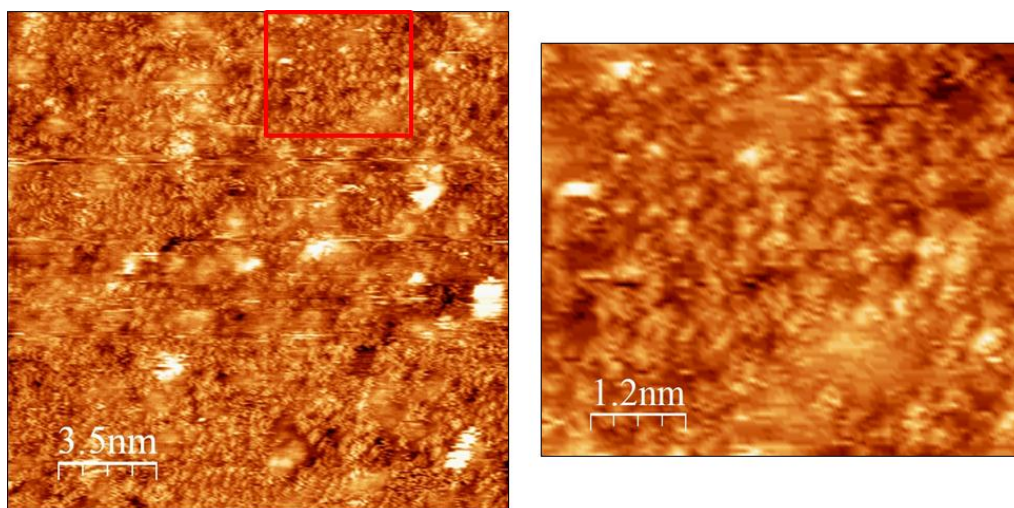


**Figure 6.13.**  $18 \times 18 \text{ nm}^2$  (left) and  $6 \times 5 \text{ nm}^2$  (right) images of preadsorbed copper on cyanide-modified Pt(111) in  $0.1 \text{ M H}_2\text{SO}_4$  at  $0.47 \text{ V}$ ;  $U_T = 0.17 \text{ V}$  (tip negative);  $I_T = 2 \text{ nA}$ .

When the potential is decreased below  $0.40 \text{ V}$ , a potential that coincides with the foot of the cathodic peak that we have assigned to the reduction of adsorbed  $\text{Cu}^+$  to  $\text{Cu}$ , frizzy islands surrounded by the structure observed around  $0.5 \text{ V}$  (see Figure 6.13) start to appear (Figure 6.14), the size of the islands growing if the potential is kept more negative than the reduction peak at  $0.38 \text{ V}$ . Based on the fact that no sign of destruction of the cyanide adlayer



is observed in the corresponding CV, that remains unaltered even after 18 hours (see below), we assign these islands to metallic Cu deposited on top of the cyanide adlayer, in contrast with the Cu-upd adlayer in direct contact with the Pt surface formed in the presence of  $\text{Cu}^{2+}$  in the solution. As can be seen in the upper part of the STM image on the right of Figure 6.14, these islands show a square symmetry, this being another indication that they are not deposited on the Pt surface, because in this case a hexagonal symmetry should be observed, as is indeed the case when a Cu-upd adlayer is formed (see Figure 6.5).

As can be observed in Figure 6.14 (right), these islands disappear at the double-layer region during the positive scan. However, the honeycomb structure is not recovered, and only dispersed islands are observed (see Figure 6.15). More EC-STM and FTIRS experiments are needed in order to reach a complete description of the metallization of the cyanide adlayer upon reduction of preadsorbed  $\text{Cu}^+$ .

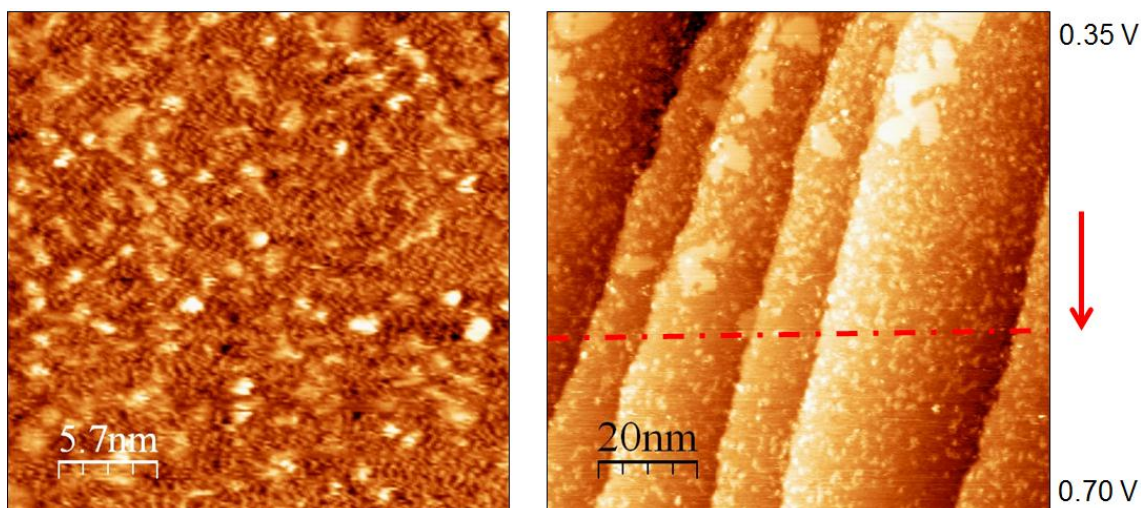


**Figure 6.14.** STM images recorded during the reduction of preadsorbed  $\text{Cu}^+$  on cyanide-modified Pt(111) in 0.1 M  $\text{H}_2\text{SO}_4$ . Left:  $28.5 \times 28.5 \text{ nm}^2$  at 0.40 V;  $U_T = 0.10 \text{ V}$  (tip negative). Right:  $100 \times 100 \text{ nm}^2$  image recorded during a positive potential sweep from 0.35 V to 0.70 V;  $U_T = 0.05 \text{ V}$  to 0.40 V (tip negative). The scan direction is from top to bottom and from left to right.  $I_T = 2 \text{ nA}$  in both cases.

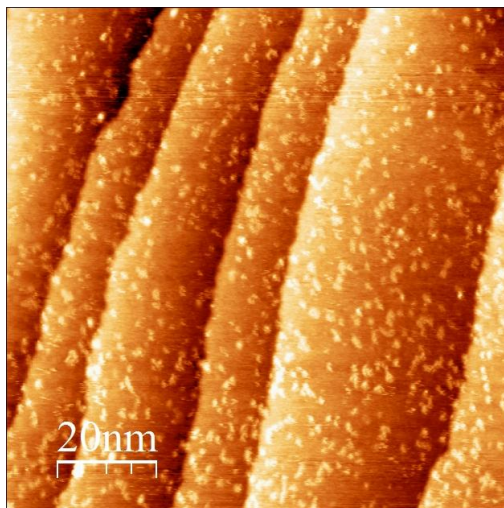


**Figure 6.15.**  $100 \times 100 \text{ nm}^2$  STM image of a cyanide-modified Pt(111) onto which  $\text{Cu}^+$  had been preadsorbed in  $0.1 \text{ M H}_2\text{SO}_4$  at  $0.70 \text{ V}$ , after a potential excursion into the region where metallization of the cyanide adlayer occurs;  $U_T = 0.40 \text{ V}$  (tip negative);  $I_T = 2 \text{ nA}$ .

In order to check the stability of preadsorbed copper on cyanide-modified Pt(111), we left a cyanide-modified Pt(111) electrode onto which  $\text{Cu}^+$  had been preadsorbed 18 hours in contact with the  $\text{N}_2$  atmosphere in the electrochemical cell, and then recorded a new CV. Figure 6.16 shows the cyclic voltammogram of the fresh electrode and the first 10 cycles after 18 hours in contact with the  $\text{N}_2$  atmosphere. Remarkably, only a small decrease in the intensity of the peaks corresponding redox couple at  $0.38 \text{ V}$  and of the features corresponding to OH adsorption-desorption can be observed and, in addition, the initial profile is almost recovered after a few cycles. This supports our assignment of the redox process to the metallization of the cyanide adlayer, and indicates that both the surface with the attached cations and the metallized adlayer are very robust.

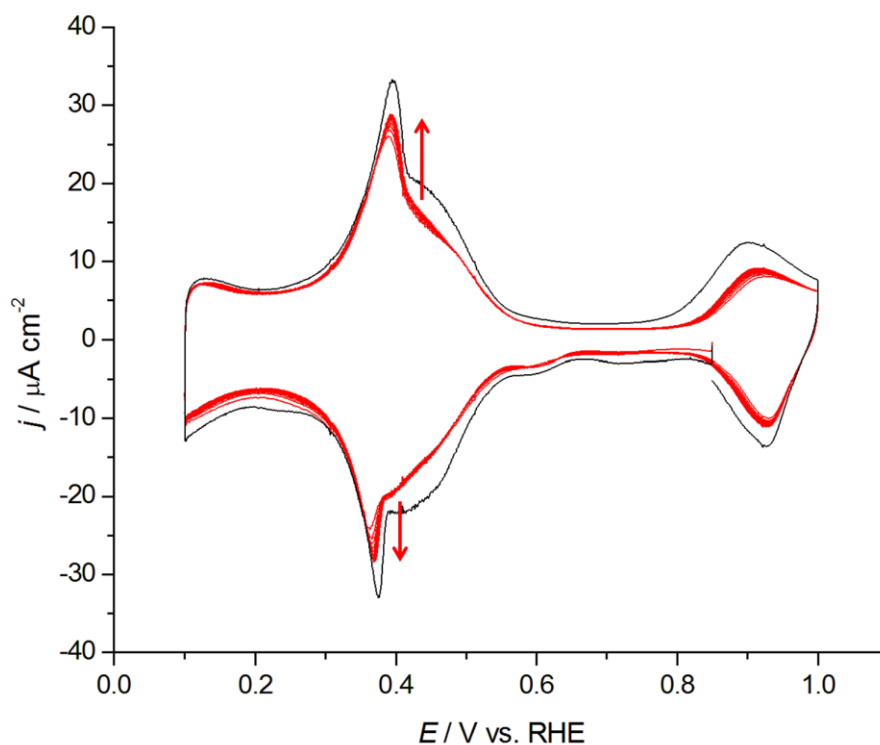


**Figure 6.16.** CVs of cyanide-modified Pt(111) in 0.1 M  $\text{H}_2\text{SO}_4$  18 hours after the preadsorption of  $\text{Cu}^+$  (red lines). The evolution during the first 10 cycles is shown. The black line corresponds to the CV of a fresh electrode, just after preadsorption of  $\text{Cu}^+$ . The arrows indicate the evolution of the CVs upon repetitive cycling. Scan rate =  $50 \text{ mV s}^{-1}$ .

Although we have not been able to fabricate the searched-for network of one-atom wide metallic wires, these preliminary results clearly show that the reduction of metallic cations retained non-covalently on the surface of a cyanide-modified Pt(111) can lead to the metallization of the cyanide adlayer, resulting in a sandwich metal-molecular adlayer-metal configuration. We expect that the particular structure of the cyanide adlayer will provide a playground onto which to attempt the metallization of the molecular adlayer with a regular array of bidimensional metallic islands of a well-defined size. Taking into account that bidimensional metallic islands of just some nanometers in diameter have been predicted to be ferromagnetic [201,202], this offers exciting perspectives for future work.



### 6.3. Polymerization of aniline on cyanide-modified Pt(111) electrodes

We aim at using cyanide-modified Pt(111) surfaces to guide the adsorption and polymerization of aniline in order to fabricate a network of molecular fibers of a conducting polymer. Conducting polymers can be readily synthesized from aqueous electrolytes and they can have high conductivities. Polyaniline is among the most studied conducting polymers due to its interest for many technological applications, such as molecular electronics [203], intelligent windows [204,205] or artificial muscles [206].

Aniline molecules adsorb on Au(111) electrodes in acidic solutions adopting a highly ordered structure that incorporates sulphate (in  $\text{H}_2\text{SO}_4$  solutions) or perchlorate (in  $\text{HClO}_4$  solutions) anions [79,80,207,208]. According to STM results, this molecular arrangement of aniline molecules polymerizes into 'metallic' polyaniline (PANI), which are initially monomolecular chains, with well-defined, potential-dependent molecular conformations [79,80].

We have studied using cyclic voltammetry the adsorption and polymerization of aniline on cyanide-modified Pt(111) electrodes. Figure 6.17 shows the first (black curve) and second (red curve) CVs of cyanide-modified Pt(111) in  $0.1 \text{ M H}_2\text{SO}_4 + 10 \text{ mM C}_6\text{H}_5\text{NH}_2$ . The CV of cyanide-modified Pt(111) in  $0.1 \text{ M H}_2\text{SO}_4$  (blue curve) is shown for comparison. Starting from  $0.8 \text{ V}$ , a cathodic peak appears at  $0.47 \text{ V}$  in the first negative sweep in the presence of polyaniline, but is absent in the second and subsequent cycles, in which a slow adsorption-desorption process can be guessed, with adsorption and desorption peaks at  $0.8 \text{ V}$  and  $0.6 \text{ V}$ , respectively. The charge in the OH adsorption region decreases significantly in the presence of aniline. After the first negative sweep, the CV remains unchanged as far as the positive potential limit is kept below  $1.0 \text{ V}$ .

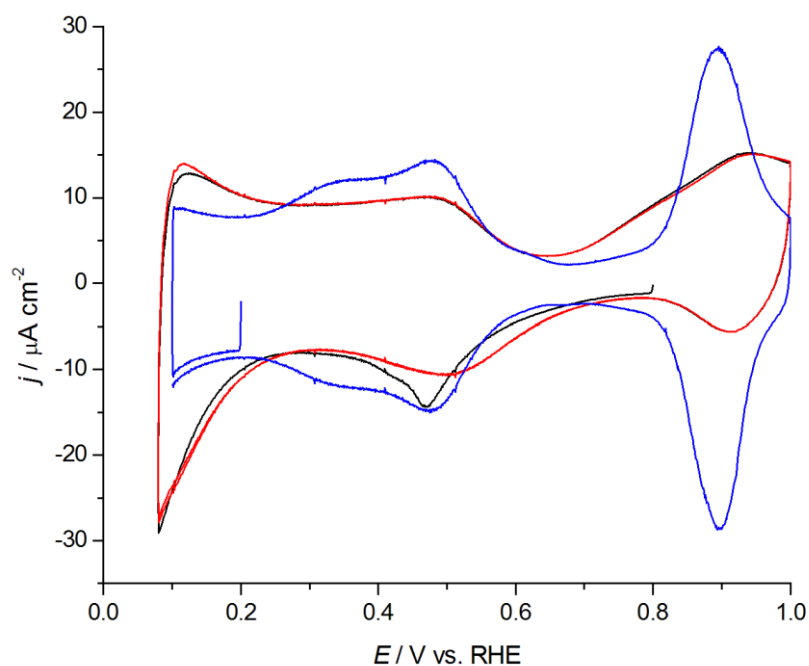


**Figure 6.17.** First (black curve) and second (red curve) CVs of cyanide-modified Pt(111) in 0.1 M  $H_2SO_4 + 10\text{ mM } C_6H_5NH_2$ . The first sweep begins at 0.8 V in the negative direction. The CV of cyanide-modified Pt(111) in 0.1 M  $H_2SO_4$  (blue curve) is shown for comparison. Scan rate:  $50\text{ mV s}^{-1}$ .

We attribute the changes in the CV of cyanide-modified Pt(111) in the presence of aniline to the adsorption of aniline on the electrode surface. A new reversible redox couple appears around 0.75 V in the CV if the positive potential limit is made more positive than 1.04 V vs. RHE (Figure 6.18). We attribute this redox couple to the oxidation and reduction of PANI formed on the electrode surface upon polymerization of aniline at potentials above 1.04 V. Interestingly, the hydrogen adsorption-desorption region does not change during the polymerization process, suggesting that PANI is formed without destroying the cyanide adlayer. The peaks corresponding to the redox couple at ca. 0.75 V increase upon repetitive potential excursions beyond 1.04 V (Figure 6.19), this being typical of a continuous growth of the PANI film. If, after polymerization, the CV is again restricted to the potential region between 0.10 V and 1.00 V, where no indication of aniline polymerization can be observed, the redox process at ca. 0.75 V can still be observed, and its intensity does not increase further (Figure 6.20). A similar redox process appears at the same potential after polymerization of aniline on unmodified Pt(111) electrodes (not shown), which supports the idea that it is due to the reduction-oxidation of PANI.

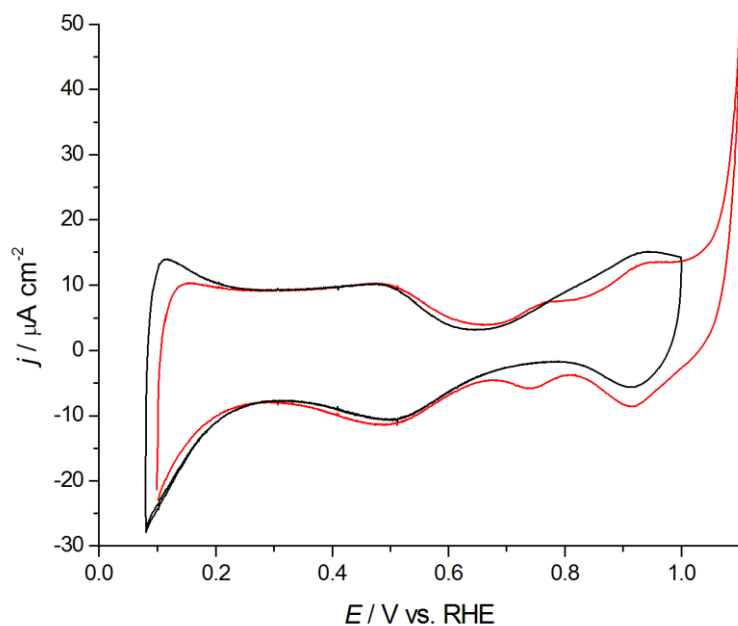


**Figure 6.18.** CV of cyanide-modified Pt(111) in 0.1 M  $H_2SO_4$  + 1 mM  $C_6H_5NH_2$ . The positive potential limits are 1.00 V (black curve) and 1.10 V (red curve) and the scan rate is  $50 \text{ mV s}^{-1}$ .

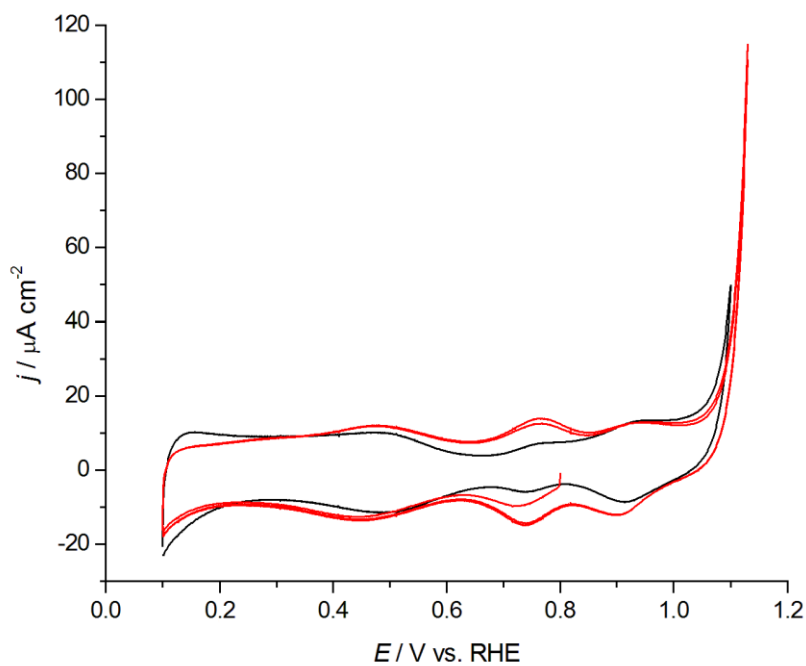


**Figure 6.19.** CV of cyanide-modified Pt(111) in 0.1 M  $H_2SO_4$  + 1 mM  $C_6H_5NH_2$ . The positive potential limits are 1.10 V (black curve) and 1.13 V (red curve) and the scan rate is  $50 \text{ mV s}^{-1}$ .

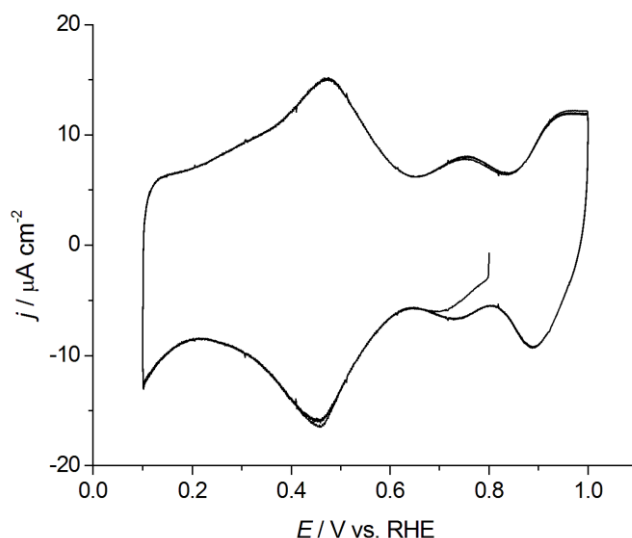


**Figure 6.20.** CV of cyanide-modified Pt(111) in 0.1 M  $\text{H}_2\text{SO}_4$  + 1 mM  $\text{C}_6\text{H}_5\text{NH}_2$  after PANI formation. Scan rate: 50  $\text{mV s}^{-1}$ .

These preliminary results make us be very optimistic regarding the possibility of fabricating a periodic network of monomolecular conducting polymer fibres, although in the absence of crucial STM experiments we cannot know, yet, if PANI is being formed within the troughs of the cyanide structure or on top of it.

## 6.4. Conclusions and perspectives

In an attempt to develop a procedure with which periodic metallic nanostructures could be fabricated, we have first studied the adsorption of copper from the solution on cyanide-modified Pt(111) electrodes. We have shown that copper adsorbs on cyanide-modified Pt(111), perfectly following the molecular pattern created by the cyanide adlayer and without disrupting it, forming a honeycomb structure that extends over the entire electrode surface.

*Ex situ* XPS measurements have revealed the presence of  $\text{Cu}^+$  on the surface of a cyanide-modified Pt(111) electrode after exposing it to a solution containing 1 mM  $\text{CuSO}_4$ , suggesting that the high affinity of cyanide-modified Pt(111) electrodes for copper might be

related to the tendency of cyanide to stabilize the +1 oxidation state of copper. Moreover, it has been shown that preadsorbed copper is very robustly attached to cyanide-modified Pt(111) surfaces, resisting emersion even after 18 hours. Reduction of preadsorbed copper leads to the metallization of the cyanide adlayer, and to the formation of a metal-molecular adlayer-bidimensional metallic island sandwich, although a deeper and systematic STM study is still necessary for a correct characterization of the system.

Preliminary results regarding the adsorption and polymerization of aniline on cyanide-modified Pt(111) electrodes show that aniline can polymerize on cyanide-modified Pt(111) surfaces without destroying the cyanide adlayer. Again, a deep and systematic *in situ* STM study is necessary in order to characterize the structure and morphology of the PANI films.



# Chapter 7

## General conclusions

The most relevant conclusions drawn from the results obtained in this Doctoral Thesis are summarised below.

### 1. Adsorption of hydrogen on cyanide-modified Pt(111) surfaces. Electronic structure of the Pt atoms not directly bonded to CN

According to DFT calculations, hydrogen adsorbed on the nitrogen atoms of the CN groups of the cyanide-modified Pt(111) ( $2\sqrt{3} \times 2\sqrt{3}$ )R30° structure is much more stable than  $H_{\text{upd}}$  on the free Pt atoms of the surface. This result supports the hypothesis that the hydrogen adsorption region on cyanide-modified Pt(111) electrodes is due to the formation of  $CN_{\text{ads}}H$ . DFT calculations of the LDOS projected onto those Pt atoms that are not directly bonded to CN show that the electronic structure of these atoms remains essentially unaltered.

### 2. Atomic ensemble effects in electrocatalysis

The cyanide groups of the cyanide-modified Pt(111) ( $2\sqrt{3} \times 2\sqrt{3}$ )R30° structure act as a third body which selectively blocks only one kind of sites on the Pt surface, leaving the cyanide-free Pt atoms essentially unaltered. This makes cyanide-modified Pt(111) surfaces ideal to study atomic ensemble effects in electrocatalysis using the site-knockout strategy.

In the case of the electrooxidation of formic acid, that proceeds through two parallel paths, one of them leading to the formation of adsorbed CO (a catalytic poison), the reaction proceeds on cyanide-modified Pt(111) electrodes exclusively through the reactive pathway. This proves that formation of adsorbed CO requires the presence on the electrode surface of sites composed at least of three contiguous Pt atoms, and that, in the absence of these sites, the reaction can be channelled through the reactive pathway.

Using cyanide-modified Pt(111) electrodes we have shown that the activity of Pt-based electrocatalysts for the ORR can be dramatically enhanced by simply blocking the sites necessary for the adsorption of specifically adsorbing 'spectator' anions. This was

demonstrated for the ORR in sulphuric and phosphoric acid solutions, that contain tetrahedral anions whose specific adsorption requires a trigonal site, absent on the surface of cyanide-modified Pt(111) electrodes. In these solutions, the activity of cyanide-modified Pt(111) can be up to 29 times higher than that of a clean Pt(111) electrode, even though CN blocks 50% of the Pt atoms on the surface. Interestingly, in perchloric acid solutions, that do not contain specifically adsorbing anions, the activity of a cyanide-modified Pt(111) electrode for the ORR is practically identical to that of a clean Pt(111) electrode, although in the former case 50% of the surface Pt atoms are blocked by adsorbed CN. This is a clear evidence that the intrinsic activity of Pt for the oxygen reduction is very high, and that the low activity observed in real catalysts is due to the presence, at relatively low potentials, of adsorbed OH or adsorbed O, that block an excessive fraction of surface atoms.

### 3. Quantitative study of non-covalent interactions at the electrochemical double layer and electrochemical surface nanostructuring

Non-covalent interactions between cations at the outer Helmholtz plane and surface anchored species, like CN in cyanide-modified Pt(111) electrodes, can affect the structure and the properties of the electrochemical double layer. A detailed study of the changes in the voltammetric profile of cyanide-modified Pt(111) electrodes in the presence of alkali-metal cations has allowed us to develop a quantitative model that describes very well non-covalent interactions in this system, and that very likely can be extended to other systems in which the effect of non-covalent interactions has been previously reported. Furthermore, cations non-covalently attached to the electrode surface have been imaged with atomic resolution for the first time using *in situ* STM, and they have been shown to adopt a honeycomb structure that extends over the entire electrode surface.

Copper ions adsorb on cyanide-modified Pt(111) exactly as alkali-metal cations do, but much lower  $\text{Cu}^{2+}$  concentrations are needed in order to reach the maximum possible copper coverage on the surface. Reduction of preadsorbed copper ions leads to the metallization of the cyanide adlayer, and to the formation of a metal-molecular adlayer-bidimensional metallic island sandwich, demonstrating that non-covalent interactions can be used to metallize molecular films. We expect that, if controlled wisely and adequately, attachment through non-covalent interactions and subsequent reduction of transition metal cations might allow nanometer or subnanometer scale patterned metallization of molecular films.

Cyclic voltammetry experiments on cyanide-modified Pt(111) electrodes in aniline-containing acidic solutions show that aniline molecules can polymerize on these surfaces without destroying the cyanide adlayer.



## 7.1. Conclusiones generales

A continuación se muestran las conclusiones más relevantes que se extraen de los resultados obtenidos en esta Tesis Doctoral.

### 1. Adsorción de hidrógeno sobre superficies de Pt(111) modificadas con cianuro. Estructura electrónica de los átomos de Pt no enlazados al CN

Según los cálculos DFT, el hidrógeno adsorbido sobre los átomos de nitrógeno de los grupos CN es mucho más estable que el  $H_{upd}$  que se adsorbe sobre los átomos de Pt libres. Este resultado apoya la hipótesis de que la región de adsorción de hidrógeno en electrodos de Pt(111) modificados con cianuro se debe a la formación de  $CN_{ads}H$ . Los cálculos DFT de la LDOS proyectada sobre los átomos de Pt que no están directamente enlazados al CN muestran que la estructura electrónica de estos átomos permanece prácticamente inalterada.

### 2. Efectos geométricos en electrocatálisis

Los grupos cianuro de la estructura  $(2\sqrt{3} \times 2\sqrt{3})R30^\circ$  del Pt(111) modificado con cianuro actúan como un tercer cuerpo que bloquea de forma selectiva únicamente un tipo de sitios de la superficie de Pt, mientras que deja prácticamente sin alterar los átomos de Pt no enlazados al CN. Este hecho hace que las superficies de Pt(111) sean idóneas para estudiar los efectos geométricos en electrocatálisis mediante la estrategia "site-knockout".

En el caso de la electrooxidación de ácido fórmico, que ocurre a través de dos caminos paralelos, en uno de los cuales se forma CO adsorbido (un veneno catalítico), la reacción tiene lugar únicamente a través del camino reactivo sobre electrodos Pt(111) modificados con cianuro. Este resultado demuestra que la deshidratación de ácido fórmico a CO adsorbido requiere la presencia en la superficie del electrodo de sitios compuestos por tres átomos de Pt contiguos y que, en ausencia de dichos sitios, la reacción se puede canalizar por el camino reactivo.

Los electrodos de Pt(111) modificados con cianuro nos han permitido demostrar que la estrategia de bloquear los sitios necesarios para la adsorción específica de aniones "espectadores" puede producir un enorme incremento en la actividad para la ORR de los electrocatalizadores basados en Pt. En disoluciones de ácidos sulfúrico y fosfórico, que contienen aniones tetraédricos que se adsorben específicamente ocupando sitios trigonales (ausentes en la superficie de los electrodos de Pt(111) modificados con cianuro), la actividad del Pt(111) modificado con cianuro puede ser hasta 29 veces mayor que la de un electrodo de Pt(111) sin modificar, aunque el cianuro bloquea el 50% de los átomos de Pt de la

superficie. En disoluciones de ácido perclórico (cuyos aniones no se adsorben específicamente), curiosamente, la actividad de un electrodo de Pt(111) modificado con cianuro para la ORR es prácticamente idéntica a la de un electrodo de Pt(111) sin modificar, aunque en el primer caso el 50% de los átomos de Pt de la superficie están bloqueados por el CN adsorbido. Este resultado demuestra que la actividad intrínseca del Pt para la ORR es muy alta, y que la baja actividad observada en catalizadores reales se debe a la presencia, a potenciales relativamente bajos, de OH u O adsorbidos, que bloquean gran parte de los átomos de la superficie.

### 3. Estudio cuantitativo de las interacciones no-covalentes en la doble capa electroquímica y nanoestructurado electroquímico de superficies

Las interacciones no-covalentes entre cationes situados en el plano exterior de Helmholtz y especies ancladas en la superficie, como los grupos CN en los electrodos de Pt(111) modificados con cianuro, pueden afectar a la estructura y a las propiedades de la doble capa electroquímica. Hemos estudiado los cambios en el perfil voltamétrico de los electrodos de Pt(111) modificados con cianuro en presencia de cationes de metales alcalinos en disolución y hemos desarrollado un modelo cuantitativo que describe las interacciones no-covalentes en este sistema, y que probablemente pueda extenderse a otros sistemas en los que también se ha observado el efecto de las interacciones no-covalentes. Además, hemos obtenido, por primera vez, imágenes STM *in situ* con resolución atómica de los cationes interaccionando no-covalentemente con la superficie del electrodo. Estos cationes adoptan una estructura en panal de abeja que se extiende sobre toda la superficie del electrodo.

Los iones de cobre se adsorben sobre Pt(111) modificado con cianuro de la misma forma que lo hacen los cationes de metales alcalinos, aunque se necesitan concentraciones de  $\text{Cu}^{2+}$  mucho menores para alcanzar el recubrimiento máximo posible de cobre sobre la superficie. La reducción de iones cobre preadsorbidos da lugar a la metalización de la adcapa de cianuro y a la formación de un sándwich metal-adcapa molecular-isla metálica bidimensional, lo cual demuestra que las interacciones no-covalentes se pueden utilizar para metalizar películas moleculares. Esperamos que, si se controla racional y adecuadamente, la fijación a la superficie mediante interacciones no-covalentes de cationes de metales de transición seguida de su reducción permita metalizar películas moleculares con patrones de escala nanométrica o subnanométrica.

Los experimentos de voltametría cíclica con electrodos de Pt(111) modificados con cianuro en presencia de anilina en disolución muestran que las moléculas de anilina pueden polimerizar sobre estas superficies sin que se destruya la adcapa de cianuro.



## 8. References

- [1] W. Schmickler, E. Santos, *Interfacial Electrochemistry*, Springer-Verlag Berlin Heidelberg, **2010**.
- [2] D. M. Kolb, *Surf. Sci.* **2002**, *500*, 722.
- [3] N. M. Markovic, P. N. Ross, *Surf. Sci. Rep.* **2002**, *45*, 117.
- [4] J. Clavilier, R. Faure, G. Guinet, R. Durand, *J. Electroanal. Chem.* **1980**, *107*, 205.
- [5] J. L. Stickney, S. D. Rosasco, G. N. Salaita, A. T. Hubbard, *Langmuir* **1985**, *1*, 66.
- [6] C. Stuhlmann, I. Villegas, M. J. Weaver, *Chem. Phys. Lett.* **1994**, *219*, 319.
- [7] Y.-G. Kim, S.-L. Yau, K. Itaya, *J. Am. Chem. Soc.* **1996**, *118*, 393.
- [8] V. B. Paulissen, C. Korzeniewski, *J. Phys. Chem.* **1992**, *96*, 4563.
- [9] C. S. Kim, C. Korzeniewski, *J. Phys. Chem.* **1993**, *97*, 9784.
- [10] F. Huerta, E. Morallón, C. Quijada, J. L. Vázquez, A. Aldaz, *Electrochim. Acta* **1998**, *44*, 943.
- [11] F. Huerta, E. Morallón, J. L. Vázquez, A. Aldaz, *Surf. Sci.* **1998**, *396*, 400.
- [12] F. Huerta, E. Morallón, C. Quijada, J. L. Vázquez, L. E. A. Berlouis, *J. Electroanal. Chem.* **1999**, *463*, 109.
- [13] F. Huerta, E. Morallón, J. L. Vázquez, *Surf. Sci.* **1999**, *431*, L577.
- [14] F. Huerta, E. Morallón, C. Quijada, J. L. Vázquez, *Electrochem. Commun.* **2002**, *4*, 251.
- [15] W. T. Grubb, *Nature*, **1963**, *198*, 833.
- [16] E. Herrero, J. M. Feliu, A. Aldaz, in *Encyclopedia of Electrochemistry, Vol. 2* (Eds.: A. J. Bard, M. Stratmann, E. J. Calvo), Wiley Publishers, **2003**.
- [17] T. Bligaard, J. K. Nørskov, *Electrochim. Acta* **2007**, *52*, 5512.
- [18] V. Climent, N. García-Aráez, J. M. Feliu, in *Fuel Cell Catalysis. A Surface Science Approach*, (Ed.: M. T. M. Koper), John Wiley & Sons, Inc., Hoboken, **2009**.
- [19] W. N. Hansen, D. M. Kolb, *J. Electroanal. Chem.* **1979**, *100*, 493.
- [20] B. Hammer, J. K. Nørskov, *Surf. Sci.* **1995**, *343*, 211.

- [21] J. G. Chen, C. A. Menning, M. B. Zellner, *Surf. Sci. Rep.* **2008**, 63, 201.
- [22] H. A. Gasteiger, S. S. Kocha, B. Sompalli, F. T. Wagner, *Applied Catalysis B-Environmental*, **2005**, 56, 9.
- [23] V. R. Stamenkovic, B. Fowler, B. S. Mun, G. Wang, P. N. Ross, C. A. Lucas, N. M. Markovic, *Science* **2007**, 315, 493.
- [24] M. Mavrikakis, B. Hammer, J. K. Norskov, *Phys. Rev. Lett.* **1998**, 81, 2819.
- [25] L. A. Kibler, A. M. El-Aziz, R. Hoyer, D. M. Kolb, *Angew. Chem. Int. Ed.* **2005**, 44, 2080.
- [26] W. M. H. Sachtler, P. Van Der Plank, *Surf. Sci.* **1969**, 18, 62.
- [27] V. Ponec, W. M. H. Sachtler, *J. Catal.* **1972**, 24, 250.
- [28] C. Xu, B. E. Koel, *Surf. Sci.* **1994**, 310, 198.
- [29] H. Angerstein-Kozłowska, B. MacDougall, B. E. Conway, *J. Electrochem. Soc.* **1973**, 120, 756.
- [30] R. R. Adzic, D. N. Simic, A. R. Despic, D. M. Drazic, *J. Electroanal. Chem.* **1975**, 65, 587.
- [31] A. Cuesta, *ChemPhysChem* **2011**, 12, 2375.
- [32] A. Fernández-Vega, J. M. Feliu, A. Aldaz, J. Clavilier, *J. Electroanal. Chem.* **1989**, 258, 101.
- [33] Clavilier, A. Fernández-Vega, J. M. Feliu, A. Aldaz, *J. Electroanal. Chem.* **1989**, 258, 89.
- [34] S.-C. Chang, Y. Ho, M. J. Weaver, *Surf. Sci.* **1992**, 265, 81.
- [35] E. Leiva, T. Iwasita, E. Herrero, J. M. Feliu, *Langmuir* **1997**, 13, 6287.
- [36] F. Maroun, F. Ozanam, O. M. Magnussen, R. J. Behm, *Science* **2001**, 293, 1811.
- [37] S. Kozuch, J. M. L. Martin, *ChemPhysChem* **2011**, 12, 1413.
- [38] A. Cuesta, *J. Am. Chem. Soc.* **2006**, 128, 13332.
- [39] W. R. Grove, *Philos. Mag.*, **1839**, 14, 127.
- [40] *Fuel Cell Handbook*, U.S. Department of Energy, 7<sup>th</sup> edition, **2004**.
- [41] U. Eberle, R. von Helmholt, *Energy Environ. Sci.* **2010**, 3, 689.
- [42] E. Herrero, L. J. Buller, H. D. Abruña, *Chem. Rev.* **2001**, 101, 1897.
- [43] H. A. Gasteiger, N. M. Markovic, *Science*, **2009**, 324, 48.

- [44] J. Greeley, I. E. L. Stephens, A. S. Bondarenko, T. P. Johansson, H. A. Hansen, T. F. Jaramillo, J. Rossmeisl, I. Chorkendorff, J. K. Nørskov, *Nature Chem.* **2009**, *1*, 552.
- [45] P. Strasser, K. Shirlaine, T. Anniyev, J. Greeley, K. More, C. Yu, Z. Liu, S. Kaya, D. Nordlund, H. Ogasawara, M. F. Toney, A. Nilsson, *Nature Chem.* **2010**, *2*, 454.
- [46] L. Carrette, C. A. Friedrich, U. Stimming, *Fuel Cells* **2001**, *1*, 5.
- [47] A. Serov, C. Kwak, *Appl. Catal. B* **2010**, *98*, 1.
- [48] J. Sanabria-Chinchilla, K. Asazawa, T. Sakamoto, K. Yamada, H. Tanaka, P. Strasser, *J. Am. Chem. Soc.* **2011**, *133*, 5425.
- [49] J. Ma, N. A. Choudhury, Y. Sahai, *Ren. Sust. Energy Rev.* **2010**, *14*, 183.
- [50] R. Parsons, T. VanderNoot, *J. Electroanal. Chem.* **1988**, *257*, 9.
- [51] E. Herrero, W. Chrzanowski, A. Wieckowski, *J. Phys. Chem.* **1995**, *99*, 10423.
- [52] B. Beden, C. Lamy, A. Bewick, K. Kunimatsu, *J. Electroanal. Chem.* **1981**, *121*, 343.
- [53] B. Beden, A. Bewick, C. Lamy, *J. Electroanal. Chem.* **1983**, *148*, 147.
- [54] A. Miki, S. Ye, M. Osawa, *Chem. Commun.* **2002**, 1500.
- [55] G. Samjeské, A. Miki, S. Ye, M. Osawa, *J. Phys. Chem. B* **2005**, *109*, 23509.
- [56] G. Samjeské, A. Miki, S. Ye, M. Osawa, *J. Phys. Chem. B* **2006**, *110*, 16559.
- [57] M. Osawa, K. Komatsu, G. Samjeské, T. Uchida, T. Ikeshoji, A. Cuesta, C. Gutiérrez, *Angew. Chem. Int. Ed.* **2011**, *50*, 1159.
- [58] Y. X. Chen, A. Miki, S. Ye, H. Sakai, M. Osawa, *J. Am. Chem. Soc.* **2003**, *125*, 3680.
- [59] A. Cuesta, G. Cabello, C. Gutiérrez, M. Osawa, *Phys. Chem. Chem. Phys.* **2011**, *13*, DOI: 10.1039/C1CP22498K.
- [60] A. Cuesta, G. Cabello, F. Hartl, M. Escudero-Escribano, C. Vaz-Domínguez, L. Kibler, C. Gutiérrez, M. Osawa, *J. Am. Chem. Soc.* **2011**, submitted.
- [61] J. K. Nørskov, J. Rossmeisl, A. Logadottir, L. Lindqvist, J. R. Kitchin, T. Bligaard, H. Jonsson, *J. Phys. Chem. B* **2004**, *108*, 17886.
- [62] F. T. Wagner, B. Lakshmanan, M. F. Mathias, *J. Phys. Chem. Lett.* **2010**, *1*, 2204.
- [63] <http://www.liv.ac.uk/researchintelligence/issue17/fuelcells.html>
- [64] R. Srivastava, P. Mani, N. Hahn, P. Strasser, *Angew. Chem. Int. Ed.* **2007**, *46*, 8988.
- [65] A. U. Nilekar, Y. Xu, J. L. Zhang, M. B. Vukmirovic, K. Sasaki, R. R. Adzic, M. Mavrikakis, *Top.Catal.* **2007**, *46*, 276.

- [66] Y. Xing, Y. Cai, M. B. Vukmirovic, W-P Zhou, H. Karan, J. X. Wang, R. R. Adzic, *J. Phys. Chem. Lett.* **2010**, *1*, 3238.
- [67] K. Sasaki, H. Naohara, Y. Cai, Y. M. Choi, P. Liu, M. B. Vukmirovic, J. X. Wang, R. R. Adzic, *Angew. Chem. Int. Ed.* **2010**, *49*, 8602.
- [68] D. Strmcnik, K. Kodama, D. Van der Vliet, J. Greeley, V. R. Stamenkovic, N. M. Markovic, *Nature Chem.* **2009**, *1*, 466.
- [69] S. Peercy, *Nature* **2000**, *406*, 1023.
- [70] R. P. Feynman, *Eng. Sci.* **1960**, *23*, 22.
- [71] G. Binning, H. Rohrer, C. Gerber, *Phys. Rev. Lett.* **1982**, *49*, 57.
- [72] R. S. Becker, J. A. Golovchenko, B. S. Schwarzenruber, *Nature* **1987**, *325*, 419.
- [73] D. M. Eigler, E. K. Schweizer, *Nature* **1990**, *344*, 524.
- [74] M. F. Crommie, C. P. Lutz, D. M. Eigler, *Science* **1993**, *262*, 218.
- [75] E. C. Walter, B. J. Murray, F. Favier, G. Kaltepoth, M. Grunze, R.M. Penner, *J. Phys. Chem. B* **2002**, *106*, 11407.
- [76] X. Xiao, M. Nielinger, H. Baltruschat, *Electrochim. Acta* **2003**, *48*, 3093.
- [77] M. D. Lay, J. L. Stickney, *J. Am. Chem. Soc.* **2003**, *125*, 1352.
- [78] D. M. Kolb, R. Ullmann, T. Will, *Science* **1997**, *275*, 1097.
- [79] S. Yau, Y. Lee, C. Chang, L. Fan, Y. Yang, W.-P. Dow, *J. Phys. Chem. C* **2009**, *113*, 13758.
- [80] Y. Lee, C. Chang, S. Yau, L. Fan, Y. Yang, L. O. Yang, K. Itaya, *J. Am. Chem. Soc.* **2009**, *131*, 6468.
- [81] R. Kaischew and B. Mutaftschiew, *Z. Phys. Chem.* **1955**, *204*, 334.
- [82] J. Clavilier, J.P. Chatlvineau, *J. Electroanal. Chem.* **1978**, *100*, 461.
- [83] J. Clavilier, in *Interfacial Electrochemistry*, (Ed.: A. Wieckowski), Marcel Dekker, Inc. New York, **1999**.
- [84] A. J. Bard, L. R. Faulkner, *Electrochemical Methods. Fundamentals and Applications*, John Wiley and Sons, New York, **2001**.
- [85] G. Binning, H. Rohrer, *Rev. Mod. Phys.* **1987**, *56*, 615.
- [86] G. Binnig, D. P. E. Smith, *Rev. Sci. Instrum.* **1986**, *57*, 1688.
- [87] C. J. Chen, *Appl. Phys. Lett.* **1992**, *60*, 132.

- [88] D. M. Kolb, *Electrochim. Acta* **2000**, *45*, 2387.
- [89] [http://nobelprize.org/nobel\\_prizes/physics/laureates/1986/press.html](http://nobelprize.org/nobel_prizes/physics/laureates/1986/press.html)
- [90] T. Iwasita, F. C. Nart, *Prog. Surf. Sci.* **1997**, *55*, 271.
- [91] D. K. Lambert, *Electrochim. Acta*, **1996**, *41*, 623.
- [92] B. Beden, C. Lamy, in *Infrared reflectance spectroscopy, in Spectroelectrochemistry – theory and practice*, (Ed.: R. J. Gale), Plenum Press. **1988**.
- [93] R. G. Greenler, *J. Chem. Phys.* **1966**, *44*, 310.
- [94] P. A. Christensen, in *Encyclopedia of Electrochemistry, Vol. 3* (Eds.: A. J. Bard, M. Stratmann, E. J. Calvo), Wiley Publishers, **2003**.
- [95] P. Hohenberg, W. Kohn, *Phys. Rev. B* **1964**, *136*, 864.
- [96] W. Kohn, *Rev. Mod. Phys.* **1999**, *71*, 1253.
- [97] C. Kittel, *Introduction to solid state physics*, 3<sup>rd</sup> ed., New York, **1967**.
- [98] B. Hammer, L. B. Hansen, J. K. Nørskov, *Phys. Rev. B* **1999**, *59*, 7413.
- [99] David Vanderbilt, *Phys. Rev. B* **1990**, *41*, 7892.
- [100] Y. Wang, J. P. Perdew, *Phys. Rev. B* **1991**, *44*, 13298.
- [101] J. P. Perdew, J. A. Chevary, S. H. Vosko, K. A. Jackson, M. R. Pederson, D. J. Singh, C. Fiolhais, *Phys. Rev. B* **1992**, *46*, 6671.
- [102] J. H. Monkhorst, D. J. Pack, *Phys. Rev. B* **1976**, *13*, 5188.
- [103] I. Morales-Moreno, A. Cuesta, C. Gutiérrez, *J. Electroanal. Chem.* **2003**, *560*, 135.
- [104] F. Huerta, E. Morallón, J. M. Pérez, J. L. Vázquez, A. Aldaz, *J. Electroanal. Chem.* **1999**, *469*, 159.
- [105] F. Huerta, E. Morallón, F. Cases, A. Rodes, J. L. Vázquez, A. Aldaz, *J. Electroanal. Chem.* **1997**, *421*, 179.
- [106] F. Huerta, E. Morallón, F. Cases, A. Rodes, J. L. Vázquez, A. Aldaz, *J. Electroanal. Chem.* **1997**, *431*, 269.
- [107] N. García, V. Climent, J. M. Orts, J. M. Feliu, A. Aldaz, *ChemPhysChem* **2004**, *5*, 1221.
- [108] B. C. Schardt, J. L. Stickney, D. A. Stern, D. G. Frank, J. Y. Katekaru, S. D. Rosasco, G. N. Salaita, M. P. Soriaga, A. T. Hubbard, *Inorg. Chem.* **1985**, *24*, 1419.



- [109] P. Ramírez, A. Granero, R. Andreu, A. Cuesta, C. J. Calzado, J. J. Calvente, *Electrochem. Commun.* **2008**, *10*, 1548.
- [110] K. A. Friedrich, W. Daum, C. Klünker, D. Knabben, U. Stimming, H. Ibach, *Surf. Sci.* **1995**, *335*, 315.
- [111] W. Daum et al., *App. Phys. A* **1994**, *59*, 553.
- [112] F. Huerta, F. Montilla, E. Murallón, J. L. Vázquez, *Surf. Sci.* **2006**, *600*, 1221.
- [113] A. Tadjeddine, A. Peremans, A. Le Rille, W. Q. Zheng, M. Tadjeddine, J. P. Flament, *J. Chem. Soc., Faraday Trans.* **1996**, *92*, 3823.
- [114] M. Tadjeddine, J. P. Flament, *Chem. Phys.* **1999**, *240*, 39.
- [115] A. Cuesta, M. Escudero, B. Lanova, H. Baltruschat, *Langmuir* **2009**, *25*, 6500.
- [116] M. Escudero-Escribano, M. E. Zoloff-Michoff, E. P. M. Leiva, N. M. Markovic, C. Gutiérrez, A. Cuesta, *ChemPhysChem* **2011**, *12*, 2230.
- [117] W. Daum, F. Dederichs, J. E. Müller, *Phys. Rev. Lett.* **1998**, *80*, 766.
- [118] F. Ample, D. Curulla, F. Fuster, A. Clotet, J. M. Ricart, *Surf. Sci.* **2002**, *497*, 139.
- [119] F. Ample, A. Clotet, J. M. Ricart, *Surf. Sci.* **2004**, *558*, 111.
- [120] B. E. Hayden, *Surf. Sci.* **1983**, *131*, 419.
- [121] V. K. Agrawal, M. Trenary, *Surf. Sci.* **1991**, *259*, 116.
- [122] S. Ye, H. Kita, *J. Electroanal. Chem.* **1993**, *346*, 489.
- [123] A. Rodes, R. Gómez, J. M. Orts, J. M. Feliu, A. Pérez, A. Aldaz, *J. Electroanal. Chem.* **1993**, *359*, 315.
- [124] A. Rodes, R. Gómez, J. M. Orts, J. M. Feliu, A. Pérez, A. Aldaz, *Langmuir* **1995**, *11*, 3549.
- [125] I. Villegas, R. Gómez, M. J. Weaver *J. Phys. Chem.* **1995**, *99*, 14832.
- [126] A. Rodes, R. Gómez, A. Pérez, J. M. Feliu, A. Aldaz, *Electrochim. Acta* **1996**, *41*, 729.
- [127] K. Momoi, M. B. Song, M. Ito, *J. Electroanal. Chem.* **1999**, *473*, 43.
- [128] W. A. Brown, D. A. King, *J. Phys. Chem. B* **2000**, *104*, 2578.
- [129] R. Gómez, A. Rodes, J. M. Orts, J. M. Feliu, J. M. Pérez, *Surf. Sci.*, **1995**, *342*, L1104.
- [130] G. L. Beltramo, M. T. M. Koper, *Langmuir*, **2003**, *19*, 8907.
- [131] V. Rosca, G. L. Beltramo, M. T. M. Koper, *Langmuir*, **2005**, *21*, 1448.

- [132] V. Climent, R. Gómez, J. M. Orts, A. Rodes, A. Aldaz, J. M. Feliu, in *Interfacial Electrochemistry* (Ed. A. Wieckowski), Marcel Dekker, New York, **1999**.
- [133] E. Casero et al., *Surf. Sci.* **2002**, 507-510, 688.
- [134] M. J. Weaver, S. Zou, C. Tang, *J. Chem. Phys.* **1999**, 111, 368.
- [135] P. J. Bruna, *Chem. Phys.* **1980**, 49, 39.
- [136] A. C. A. de Vooy, M. T. M. Koper, R. A. van Santen, J. A. R. van Veen, *Electrochim. Acta* **2001**, 46, 923.
- [137] W. Vogel, J. Lundquist, P. Ross, P. Stonehart, *Electrochim. Acta* **1975**, 20, 79.
- [138] H. F. Oetjen, V. M. Schmidt, U. Stimming, F. Trila, *J. Electrochem. Soc.* **1996**, 143, 3838.
- [139] T. E. Springer, T. Rockward, T. A. Zawodzinski, S. Gottesfeld, *J. Electrochem. Soc.* **2001**, 148, A11.
- [140] H.A. Gasteiger, N. Markovic, P.N. Ross, *J. Phys. Chem.* **1995**, 99, 8945.
- [141] M. Arenz, V. Stamenkovic, B. B. Blizanac, K. J. Mayrhofer, N. M. Markovic, P. N. Ross, *J. Catal.* **2005**, 232, 402.
- [142] S. Alayoglu, A.U. Nilekar, M. Mavrikakis, B. Eichhorn, *Nat. Mater.* **2008**, 7, 333.
- [143] J. Clavilier, A. Rodes, K. El Achi, M. A. Zamakhchari, *J. Chim. Phys.* **1991**, 88, 1291.
- [144] H. Kita, S. Ye, Y. Gao, *J. Electroanal. Chem.* **1992**, 334, 351.
- [145] N. M. Markovic, T. S. Sarraf, H. A. Gasteiger, P. N. Ross, *J. Chem. Soc., Faraday Trans.* **1996**, 92, 3719.
- [146] N. M. Markovic, B. N. Grgur, P. N. Ross, *J. Phys. Chem. B* **1997**, 101, 5405.
- [147] D. Strmcnik, D. Tripkovic, D. van der Vliet, V. Stamenkovic, N. M. Markovic, *Electrochem. Commun.* **2008**, 10, 1602.
- [148] B.E. Conway, B. Tilak, *Electrochim. Acta* **2002**, 47, 3571.
- [149] K. Kunimatsu, H. Uchida, M. Osawa, M. Watanabe, *J. Electroanal. Chem.* **2006**, 587, 299.
- [150] R. J. Nichols, A. Bewick, *J. Electroanal. Chem.* **1988**, 243, 445.
- [151] M. Nakamura, T. Kobayashi, N. Hoshi, *Surf. Sci.* **2011**, 605, 1462.
- [152] C. Rice, S. Ha, R. I. Masel, P. Waszczuk, A. Wieckowski, T. Barnard, *J. Power Sources*, **2002**, 111, 83.

- [153] A. Capon, R. Parsons, *J. Electroanal. Chem.* **1973**, *44*, 1.
- [154] A. Capon, R. Parsons, *J. Electroanal. Chem.* **1973**, *45*, 205.
- [155] S. Lai, N. Lebedeva, T. Housmans, M. Koper, *Top Catal.* **2007**, *46*, 320.
- [156] A. Miki, S. Ye, T. Senzaki, M. Osawa, *J. Electroanal. Chem.* **2004**, *563*, 23.
- [157] G. Samjeské, A. Miki, M. Osawa, *J. Phys. Chem. C*, **2007**, *111*, 15074.
- [158] M. Bergelin, E. Herrero, J. M. Feliu, M. Wasberg, *J. Electroanal. Chem.* **1999**, *467*, 74.
- [159] H. Baltruschat, *J. Am. Soc. Mass. Spectrom.* **2004**, *15*, 1693.
- [160] M. Neurock, M. Janik, A. Wieckowski, *Faraday Discuss.* **2008**, *140*, 363.
- [161] V. Grozovski, V. Climent, E. Herrero, J. M. Feliu, *ChemPhysChem*, **2009**, *10*, 1922.
- [162] V. Grozovski, V. Climent, E. Herrero, J. M. Feliu, *Phys. Chem. Chem. Phys.* **2010**, *12*, 8822.
- [163] V. Grozovski, J. Solla-Gullon, V. Climent, E. Herrero, J. M. Feliu, *J. Phys. Chem. C* **2010**, *114*, 13802.
- [164] M. D. Maciá, E. Herrero, J. M. Feliu, A. Aldaz, *Electrochem. Commun.* **1999**, *1*, 87.
- [165] M. D. Maciá, E. Herrero, J. M. Feliu, A. Aldaz, *J. Electroanal. Chem.* **2001**, *500*, 498.
- [166] M. D. Maciá, E. Herrero, J. M. Feliu, *J. Electroanal. Chem.* **2003**, *554-555*, 25.
- [167] V. Climent, R. Gómez, J. M. Feliu, *Electrochim. Acta* **1999**, *45*, 629.
- [168] R. Gómez, V. Climent, J. M. Feliu, M. J. Weaver, *J. Phys. Chem. B* **2000**, *104*, 597.
- [169] A. Cuesta, *Surf. Sci.* **2004**, *572*, 11.
- [170] M. T. Paffett, C. T. Campbell, T. N. Taylor, *J. Chem. Phys.* **1986**, *85*, 6176.
- [171] N. M. Markovic, R. R. Adzic, B. D. Cahan, E. B. Yeager, *J. Electroanal. Chem.* **1994**, *377*, 249.
- [172] I. E. L. Stephens, A. S. Bondarenko, F. J. Perez-Alonso, F. Calle-Vallejo, L. Bech, T. P. Johansson, A. K. Jepsen, R. Frydendal, B. P. Knudsen, J. Rossmeisl, I. Chorkendorff, *J. Am. Chem. Soc.* **2011**, *133*, 5485.
- [173] R. Subbaraman, D. Strmcnik, A. P. Paulikas, V. R. Stamenkovic, N. M. Markovic, *ChemPhysChem* **2010**, *11*, 2825.
- [174] R. Subbaraman, D. Strmcnik, V. R. Stamenkovic, N. M. Markovic, *J. Phys. Chem. C* **2010**, *114*, 8414.

- [175] N. M. Markovic, H. A. Gasteiger, P. N. Ross, *J. Electrochem. Soc.* **1997**, *144*, 1591.
- [176] D. Strmcnik, M. Escudero-Escribano, K. Kodama, V. R. Stamenkovic, A. Cuesta, N. M. Markovic, *Nature Chem.* **2010**, *2*, 880.
- [177] A. Cuesta, M. Escudero, *Phys. Chem. Chem. Phys.* **2008**, *10*, 3628.
- [178] K. Müller-Dethlefs, P. Hobza, *Chem. Rev.* **2000**, *100*, 143.
- [179] J. M. Lehn, *Angew. Chem. Int. Ed. Engl.* **1988**, *27*, 89.
- [180] J. V. Barth, J. Weckesser, C. Cai, P. Günter, L. Bürgi, O. Jeandupeux, K. Kern, *Angew. Chem. Int. Ed.* **2000**, *39*, 1230.
- [181] J. A. Theobald, N. S. Oxtoby, M. A. Phillips, N. R. Champness, P. H. Beton, *Nature* **2003**, *424*, 1029.
- [182] S. D. Rosasco, J. Stickney, G. N. Salaita, D. G. Frank, J. K. Katekaru, B. C. Schardt, M. P. Soriaga, D. A. Stern, A. T. Hubbard, *J. Electroanal. Chem.* **1985**, *188*, 95.
- [183] J. M. Lehn, J. P. Sauvage, *J. Am. Chem. Soc.* **1975**, *97*, 6700.
- [184] J. M. Feliu, M. J. Valls, A. Aldaz, M. A. Climent, J. Clavilier, *J. Electroanal. Chem.* **1993**, *345*, 475.
- [185] C. Stoffelsma, P. Rodríguez, G. García, N. García-Araez, D. Strmcnik, N. M. Markovic, M. T. M. Koper, *J. Am. Chem. Soc.* **2010**, *132*, 16127.
- [186] J. Lu, S. B. Lei, Q. D. Zeng, S. Z. Kang, C. Wang, L. J. Wan, C. L. Bai, C.L. *J. Phys. Chem. B* **2004**, *108*, 5161.
- [187] S. S. Li, H. J. Yan, L. J. Wan, H. B. Yang, B. H. Northrop, P. J. Stang, *J. Am. Chem. Soc.* **2007**, *129*, 9268.
- [188] Z. Gu, S. Huang, Y. Chen, *Angew. Chem. Int. Ed.* **2009**, *48*, 952.
- [189] B. E. Conway, *Prog. Surf. Sci.* **1984**, *16*, 1.
- [190] D. M. Kolb, R. Kiitz, K. Yamamoto, *Surf. Sci.* **1979**, *87*, 20.
- [191] Y. Shingaya, H. Matsumoto, H. Ogosawara, M. Ito, *Surf. Sci.* **1995**, *335*, 23.
- [192] C. A. Lucas, N. M. Markovic, P. N. Ross, *Phys. Rev. B* **1997**, *56*, 3651.
- [193] M. Escudero, J. F. Marco, A. Cuesta, *J. Phys. Chem. C* **2009**, *113*, 12340.
- [194] O. M. Magnussen, J. Hageböck, J. Hotlos, R. J. Behm, *Faraday Discuss.* **1992**, *94*, 329.
- [195] L.-J. Wan, S. L. Yau, K. Itaya, *J. Phys. Chem.* **1995**, *99*, 9507.

- [196] A. Cuesta, M. Kleinert, D. M. Kolb, *Phys. Chem. Chem. Phys.* **2000**, *2*, 5684.
- [197] J. H. White, H. D. Abruña, *J. Electroanal. Chem.* **1991**, *300*, 521.
- [198] M. Manolova, V. Ivanova, D. M. Kolb, H.-G. Boyen, P. Ziemann, M. Büttner, A. Romanyuk, P. Oelhafen, *Surf. Sci.* **2005**, *590*, 146.
- [199] H.-G. Boyen, P. Ziemann, U. Wiedwald, V. Ivanova, D. M. Kolb, S. Sakong, A. Gross, A. Romanyuk, M. Büttner, P. Oelhafen, *Nature Mater.* **2006**, *5*, 394.
- [200] F. Eberle, M. Saitner, H.-G. Boyen, J. Kucera, A. Gross, A. Romanyuk, P. Oelhafen, M. D'Olieslaeger, M. Manolova, D. M. Kolb, *et al. Angew. Chem. Int. Ed.* **2010**, *49*, 341.
- [201] M. Clemente-Leon, E. Coronado, A. Soriano-Portillo, N. Galvez, J. M. Dominguez-Vera, *J. Mater. Chem.* **2007**, *17*, 49.
- [202] A. Hernando, B. Sampedro, R. Litran, T. C. Rojas, J. C. Sanchez-Lopez, A. Fernandez, *Nanotechnology* **2006**, *17*, 1449.
- [203] A. G. MacDiarmid, Nobel Prize lecture, **2000**.
- [204] M. A. Rodrigues, M. A. De Paoli, M. Mastragostino, *Electrochim. Acta* **1991**, *36*, 2143.
- [205] W. Lu, A. G. Fadeev, B. Qi, E. Smela, B. R. Mattes, *et al. Science* **2002**, *297*, 983.
- [206] K. Kaneto, M. Kaneko, M. Min, A. G. MacDiarmid, *Synth. Met.* **1995**, *71*, 2211.
- [207] L. Y. O. Yang, C. Chang, S. Liu, C. Wu, S. L. Yau, *J. Am. Chem. Soc.* **2007**, *129*, 8076.
- [208] Y. Lee, S. Chen, H. Tu, S. Yau, *Langmuir* **2010**, *26*, 5576.

## Appendix A

## List of acronyms and symbols

Symbol	Meaning	Usual units or value
AE	Auxiliary electrode	
AFC	Alkaline fuel cell	
ATR-SEIRAS	Surface enhanced infrared reflection adsorption spectroscopy in the attenuated total reflection mode	
$b$	Tafel slope	mV
$c_i$	Concentration of species $i$	$\text{mol dm}^{-3}$
CV	Cyclic voltammogram	
$D_i$	Diffusion coefficient of species $i$	$\text{cm}^2 \text{s}^{-1}$
DAFC	Direct alcohol fuel cell	
DEMS	Differential electrochemical mass spectrometry	
DFAFC	Direct formic acid fuel cell	
DFT	Density functional theory	
DOS	Density of states	
$E$	Potential	V
$E_{\text{ads}}$	Adsorption energy	eV
$E_{\text{F}}$	Fermi level	eV
$E_{\text{pzc}}$	Potential of zero charge	V
$E_{\text{pzfc}}$	Potential of zero free charge	V
$E_{\text{pztc}}$	Potential of zero total charge	V
$E_{\text{s}}$	Sample potential	V
$E_{\text{t}}$	Tip potential	V
EC	Reaction mechanism composed of an heterogeneous electron transfer followed by homogeneous chemical reaction, the latter being rate determining	
EC-STM	Electrochemical scanning tunneling microscopy	

EE	Reaction mechanism composed of two successive heterogeneous electron transfers in which the second electron transfer is the rate-determining step	
ER	Eley-Rideal reaction	
$F$	Faraday constant	96 485 C mol <sup>-1</sup>
FAOR	Formic acid oxidation reaction	
FC	Fuel cell	
FTIRS	Fourier transform infrared spectroscopy	
$\Delta G$	Gibbs free energy change	kJ mol <sup>-1</sup>
HOMO	Highest occupied molecular orbital	
HOPG	Highly ordered pyrolytic graphite	
HOR	Hydrogen oxidation reaction	
$i$	Current	A
IHP	Inner Helmholtz plane	
IR	Infrared	
IRRAS	Infrared reflection-absorption spectroscopy	
IRS	Infrared spectroscopy	
$j$	Current density	A cm <sup>-2</sup>
$j_E$	Current density at a constant electrode potential $E$	A cm <sup>-2</sup>
$j_k$	Kinetic current density	A cm <sup>-2</sup>
$j_l$	Diffusion limited current density	A cm <sup>-2</sup>
$k$	Rate constant for a reaction	
LDOS	Local density of states	
LEED	Low-energy electron diffraction	
LH	Langmuir-Hinshelwood reaction	
LUMO	Lowest unoccupied molecular orbital	
MCT	Mercury-cadmium-telluride	
ML	Monolayer	
MO	Molecular orbital	
MOR	Methanol oxidation reaction	
MSCV	Mass spectrometric cyclic voltammetry	
$n_i$	Refractive index of a medium $i$	
OHP	Outer Helmholtz plane	
ORR	Oxygen reduction reaction	
PAFC	Phosphoric acid fuel cell	
PEMFC	Proton exchange membrane fuel cell	

PANI	Polyaniline	
$R$	Universal gas constant	8.314 J mol <sup>-1</sup> K <sup>-1</sup>
RDE	Rotating disk electrode	
<i>rds</i>	Rate-determining step	
RE	Reference electrode	
RHE	Reversible hydrogen electrode	
RRDE	Rotating ring-disk electrode	
SAM	Self-assembled monolayer	
SCE	Saturated calomel electrode	
SPM	Scanning probe microscopy	
<i>opd</i>	Overpotential deposition	
STM	Scanning tunneling microscopy	
SW-FTIRS	Square-wave Fourier transform infrared spectroscopy	
SXS	Surface X-ray scattering	
$U_T$	Tunneling bias or tunneling potential	V
UHV	Ultra-high vacuum	
<i>upd</i>	Underpotential deposition	
WE	Working electrode	
XPS	X-ray photoelectron spectroscopy	



**Greek symbols**

Symbol	Meaning	Usual units
$\alpha$	Transfer coefficient	
$\beta$	Symmetry factor	
$\phi$	Potential barrier	eV
$\nu$	Kinematic viscosity	cm <sup>2</sup> s <sup>-1</sup>
$\nu_i$	Stoichiometric coefficient for species $i$ in a chemical process	
$\eta$	Overpotential, $E-E_{\text{eq}}$	V
$\theta_i$	Coverage of an adsorbate $i$	
$\rho_{(E)}$	Electronic density of states	cm <sup>2</sup> eV <sup>-1</sup>
$\sigma$	Surface energy	eV
$\nu$	Potential scan rate	V s <sup>-1</sup>
$\Phi$	Work function	eV
$\omega$	Angular rotation rate	rad s <sup>-1</sup>

## Appendix B

### Publications and contributions in conferences

Several PhD Thesis results have already been published. A list of publications is shown below.

- **M. Escudero-Escribano**, G. J. Soldano, P. Quaino, W. Schmickler, M. E. Zoloff-Michoff, E. P. M. Leiva, A. Cuesta, "Cyanide-modified Pt(111) electrodes: structure and hydrogen adsorption", in preparation.
- **M. Escudero-Escribano**, M. E. Zoloff-Michoff, E. P. M. Leiva, N. M. Markovic, C. Gutiérrez, A. Cuesta, "Quantitative study of non-covalent interactions at the electrode-electrolyte interface using cyanide-modified Pt(111) electrodes", *ChemPhysChem* **2011**, *12*, 2230.
- D. Strmcnik, **M. Escudero-Escribano**, K. Kodama, V. R. Stamenkovic, N. M. Markovic, A. Cuesta, "Enhanced electrocatalysis of the oxygen reduction reaction based on patterning of platinum surfaces with cyanide", *Nature Chem.* **2010**, *2*, 880.
- **M. Escudero**, J. F. Marco, A. Cuesta, "Surface decoration at the atomic scale using a molecular pattern", *J. Phys. Chem. C*, **2009**, *113*, 12340.
- A. Cuesta, **M. Escudero**, B. Lanova, H. Baltruschat, "Cyclic voltammetry, FTIRS and DEMS study of the electrooxidation of carbon monoxide, formic acid and methanol on cyanide-modified Pt(111) electrodes", *Langmuir*, **2009**, *25*, 6500.
- A. Cuesta, **M. Escudero**, "Electrochemical and FTIRS characterisation of NO adlayers on cyanide-modified-Pt(111) electrodes: The mechanism of nitric oxide electroreduction on Pt" *Phys. Chem. Chem. Phys.* **2008**, *10*, 3628.

Below is listed a selection of contributions presented by the PhD candidate in national and international conferences.

- **M. Escudero-Escribano**, "Modificación de la actividad electrocatalítica con un patrón molecular: reducción de oxígeno sobre Pt(111) modificado con cianuro", *VIII Symposium of Young Researchers of the Spanish Royal Society of Chemistry and Sigma Aldrich*, Torremolinos (Spain), October **2011**. Invited oral contribution.
- **M. Escudero-Escribano**, P. Quaino, G. J. Soldano, W. Schmickler, A. Cuesta, "Adsorption phenomena on cyanide-modified Pt(111): experiment and theory", *62<sup>st</sup> Annual Meeting of the International Society of Electrochemistry*. Niigata (Japan), September **2011**. Oral contribution.
- **M. Escudero-Escribano**, A. Cuesta, D. Strmcnik, N. M. Markovic, "Nueva estrategia para el diseño de catalizadores para la reducción de oxígeno en las pilas de combustible", *VIII National Meeting of Chemical Engineering*. Madrid (Spain), November **2010**. Poster.
- **M. Escudero-Escribano**, A. Cuesta, D. Strmcnik, M. E. Zoloff, E. P. M. Leiva, N. M. Markovic, "Electrocatalysis and surface nanostructuring: atomic ensemble effects and non-covalent interactions", Nice (France), September **2010**. Oral contribution.
- **M. Escudero-Escribano**, A. Cuesta, D. Strmcnik, N. M. Markovic, "Diseño a nivel atómico de superficies electrocatalíticas: reducción de oxígeno sobre Pt(111) modificado con cianuro", *XXXI Meeting of the Electrochemistry Group of the Spanish Royal Society of Chemistry*, Alcalá de Henares (Spain), June **2010**. Oral contribution.
- **M. Escudero**, J. F. Marco, M. E. Zoloff, E. P. M. Leiva, A. Cuesta, "Decoración superficial a escala atómica: adsorción de Cu sobre Pt(111) modificado con CN" *XXX Meeting of the Electrochemistry Group of the Royal Spanish Society of Chemistry*. Tenerife (Spain), July **2009**, Oral contribution.
- **M. Escudero**, A. Cuesta, "Electrodeposition of copper and palladium on cyanide-modified Pt(111) electrodes", *59<sup>th</sup> Annual Meeting of the International Society of Electrochemistry*. Sevilla (Spain), September **2008**. Poster.
- **M. Escudero**, A. Cuesta, "Electrodeposition of copper on cyanide-modified Pt(111) electrodes", *25<sup>th</sup> European Conference on Surface Science*. Liverpool (United Kingdom), July **2008**. Poster.

## Appendix C

### Curriculum Vitae

María Escudero-Escribano was born in Cáceres (Spain) in 1983. She studied Chemical Engineering at the University of Extremadura (2001-2006) and was awarded 'Outstanding student' (best academic record of her promotion). She then moved to Madrid, as she won a FPI Doctoral Fellowship (2007-2011) from the Spanish Ministry of Science and Innovation to do her PhD at the Electrochemistry Group of the Institute of Physical Chemistry 'Rocasolano' (Spanish National Research Council, CSIC) under the supervision of Dr. Ángel Cuesta. She has been living at the 'Residencia de Estudiantes' (Madrid), a European Heritage site, for three years (2008-2011), thanks to a grant from the Madrid City Council to graduate students. During her PhD, M. Escudero-Escribano performed two research stays (each of three months duration), at the Argonne National Laboratory (U.S. Department of Energy, Illinois), under the supervision of Prof. Nenad M. Markovic (2009), and at the University of Ulm (Germany), supervised by Prof. Wolfgang Schmickler (2011).

M. Escudero-Escribano is a member of the International Society of Electrochemistry (ISE) and the Spanish Royal Society of Chemistry (RSEQ). She has already published 5 papers in high impact factor journals. One additional publication has been submitted and two further ones are in preparation. She has been awarded the 'Suschem Young Chemistry Researchers – 2011' National Award, in the Predoc category, from the Spanish Technology Platform for Sustainable Chemistry. She has presented her work on several national and international conferences and meetings both to specialised communities on her research field and also to non-specialised audiences.